THE RELATIONSHIP BETWEEN THE IRRADIATION INDUCED DAMAGE AND THE MECHANICAL PROPERTIES OF SINGLE CRYSTAL NI

THÈSE N^{O} 3177 (2005)

PRÉSENTÉE À LA FACULTÉ SCIENCES DE BASE

CRPP Association Euratom

SECTION DE PHYSIQUE

ÉCOLE POLYTECHNIQUE FÉDÉRALE DE LAUSANNE

POUR L'OBTENTION DU GRADE DE DOCTEUR ÈS SCIENCES

PAR

Zhongwen YAO

M.Sc. in Engineering; Chinese Institute of Atomic Energy, Pekin, Chine
et de nationalité chinoise

acceptée sur proposition du jury:

Dr R. Schäublin, directeur de thèse
Dr W. Hoffelner, rapporteur
Prof. A. Mortensen, rapporteur
Prof. M. Q. Tran, rapporteur
Dr M. Victoria, rapporteur

Lausanne, EPFL
2005

To Huiqing and Jiahe

Abstract

Irradiation is known to lead to a degradation of the mechanical properties of materials. This is particularly crucial in the case of materials that will be used in the future thermonuclear fusion reactor, where extremely high irradiation doses are expected.

In the quest of a better understanding between the irradiation induced defects and the mechanical properties Ni single crystal specimens have been irradiated with 590 MeV protons to doses ranging from 10^{-3} dpa to 0.3 dpa, at room temperature, 250°C and 350°C. The irradiation induced microstructure has been characterized by transmission electron microscopy, and the mechanical properties have been assessed by mechanical testing. Molecular dynamics (MD) simulations have been conducted in Ni and Cu in order to understand the defect formation and accumulation following a displacement cascade. The following conclusions are established.

Following irradiation at room temperature, 43% to 55% of the irradiation induced defects in Ni consist in stacking fault tetrahedra (SFTs), 31%~41% in loops and about 10 % in unidentified black dots. In the case of Ni irradiated at 250 °C, 44%~53% of the irradiation induced defects consists in SFTs, 35%~51% in loops, and less than 5% in black dots. In the case of Ni irradiated at 350 °C, 50% of the irradiation induced defects consists in voids. The remaining 50% include ~ 14% SFTs and 36% loops. Moreover, it appears that these ratios are independent from the irradiation dose, contrary to what was found in the literature. These results allow clarifying a long standing issue, namely that in fact in Ni there is no transition in the ratio between SFTs and loops with increasing dose.

In addition, it appears that in fact the irradiation induced defect density is similar to the one found in other irradiated fcc metals for RT irradiation. The data of the irradiation at 250°C are in agreement with previous published results on a neutron irradiation at 230 °C. It appears that the size of SFTs is independent of the irradiation dose, similar to what is found in irradiated Cu. It depends, however, on the irradiation temperature.

MD simulations have been performed in order to understand the influence of the interatomic potential's parameters on the formation of defects following displacement cascades. Starting with a known defect configuration, namely the SFT, 4 different potentials are tested. Results of the formation of an SFT from a triangular platelet of vacancies show that i) the platelet of 6 vacancies did not collapse to SFT regardless of the annealing conditions, but formed a void above 800K, for all selected potentials; ii) the platelet of 15 vacancies collapsed into an SFT when simulated with Farkas-I and Farkas-II potentials, which have low stacking fault energies; iii) the platelet of 66 vacancies easily collapsed to an SFT at 500K for all applied potentials, even with a high stacking fault energy (SFE) of 300 $mJ \bullet m^{-2}$.

The common neighbor analysis and Wigner-Seitz defects analysis are used for studying the resulting structures after a displacement cascade, and results show that the largest number of stacking faults is surprisingly obtained with the potential giving the highest stacking fault energy (300 $mJ \bullet m^{-2}$). An SFT-like structure appears close to the core of cascades and also an isolated interstitial loop are found with Cleri-Rosato potential. It appears that the defects size, configuration and density relates more to the displacement threshold energy than to the stacking fault energy.

It appears that a significant irradiation hardening occurs starting at the lowest dose of 10^{-3} dpa, at room temperature and 250°C. With increasing dose, the yield shear stress increases. The dose dependence of this increase varies from an irradiation temperature of room temperature to 250°C. In fact the irradiation hardening shows a significant temperature dependence.

The thermal activation energy was calculated by measuring the activation volume, which is obtained from relaxation tests. In unirradiated Ni, an activation energy of about 0.3 eV can be extrapolated at RT. In case of irradiated Ni, the unsuccessful fitting with a linear relationship between the thermal energy and temperature suggests that multiple deformation mechanisms are operating simultaneously or in turn over the considered temperature range of –196 °C to 423 °C.

The dispersion barrier hardening model is used to interpret the irradiation induced hardening in irradiated Ni. According to the equation, $\Delta\tau = \alpha\mu b(Nd)^{1/2}$, with α, the obstacle strength. It appears that α is 0.12 for the room temperature irradiation induced hardening, similar to what was previously found for irradiated Cu, and is 0.22 for the hardening following irradiation at 250°C, which is much larger than previous values. This difference in α is suggested to be related to the presence of voids at high temperatures. It is suggested that voids are stronger obstacles than SFTs or dislocation loops.

In situ TEM observations were made in irradiated Cu, in order to assess the strength of irradiation induced defects as obstacles to gliding dislocations. It appeared that the strength of obstacles is approximately 100 MPa. Considering that 90% of the damage consists in SFTs, it is suggested that the obstacles presenting a resistance of 100 MPa are SFTs. In particular, the pulling out of a string from the interaction between what was assumed to be an SFT and a moving dislocation could be recorded for the first time. This reaction implies that the gliding dislocation is strongly pinned by SFTs.

TEM observation of the microstructure of the irradiated Ni following plastic deformation shows that defect-free channel formation is the deformation mechanism at the beginning of yielding. The channeling explains the observed softening.

As deformation proceeds, a dislocation cell structure is initiated. It takes different forms depending on whether the sample is irradiated or not. In the irradiated case, cell formation initiates from mobile dislocation in the defect free channels. This implies that the eventual cell configuration will retain part of the dimensionality of the channels, for the least their width of 100 nm for the cell size, because of the geometrical constraint. In the unirradiated case the dislocation cell size is larger. The higher flow stress observed in the irradiated case is thus related to the dislocation cell size.

Résumé

L'irradiation est connue pour mener à une dégradation des propriétés mécaniques des matériaux. C'est particulièrement crucial dans le cas des matériaux qui seront utilisés dans le futur réacteur à fusion thermonucléaire, où des doses d'irradiation extrêmement élevées sont prévues.

À la recherche d'une meilleure compréhension entre les défauts induits par irradiation et les propriétés mécaniques des monocristaux de Ni ont été irradiés avec des protons de 590 MeV à des doses entre 10^{-3} dpa à 0.3 dpa, à température ambiante, 250°C et 350°C. La microstructure induite par irradiation a été caractérisée par microscopie électronique à transmission, et les propriétés mécaniques ont été évaluées par des tests mécaniques. Des simulations de dynamique moléculaire (MD) ont été conduites dans le Ni et le Cu afin de comprendre la formation et l'accumulation de défaut suivant une cascade de déplacement. Les conclusions suivantes sont établies.

Après irradiation à la température ambiante, il s'avère que 43% à 55% des défauts induits par irradiation en Ni consistent en tetrahèdres de faute d'empilement (SFTs), 31%~41% en des boucles de dislocation et environ 10 % dans des 'black dots' non identifiés. Dans le cas du Ni irradié à 250°C, 44%~53% des défauts induits par irradiation consistent en des SFTs, 35%~51% dans les boucles, et moins de 5% dans les 'black dots'. Dans le cas du Ni irradié à 350°C, 50% des défauts induits par irradiation consistent en des vides. Les 50% restants incluent ~ 14% de SFTs et 36 % de boucles. Il s'avère que ces taux sont indépendants de la dose d'irradiation, contrairement à ce qui a été trouvé dans la littérature. Ces résultats ont permis de clarifier cette question. Il n'y en fait dans le Ni aucune transition dans le rapport des populations SFT/boucle avec l'augmentation de la dose d'irradiation.

En outre, il s'avère qu'en fait la densité de défauts induite par irradiation est semblable à celle trouvée dans d'autres métaux cubiques à face centrée. Les résultats obtenus après irradiation à 250°C sont en accord avec des résultats publiés concernant une irradiation aux neutrons à une temperature de 230°C. Il s'avère que la taille de SFTs est indépendant de la dose d'irradiation, semblable à ce qui est trouvé dans le Cu irradié. Il dépend, cependant, de la température d'irradiation.

Des simulations de MD ont été exécutées afin de comprendre l'influence des paramètres du potentiel interatomique sur la formation des défauts après des cascades de déplacement. Commençant par une configuration connue de défaut, à savoir le SFT, 4 potentiels différents sont testés. Les résultats de la formation d'un SFT à partir d'unee plaquette triangulaire de lacunes prouvent que i) une plaquette de 6 lacunes ne s'effondre pas en SFT, indépendamment des conditions de recuit, mais forme un vide au-dessus de 800K, pour tous les potentiels choisis ; ii) la plaquette de 15 lacunes s'est effondrée en un SFT avec les potentiels de Farkas-I et de Farkas-II, qui ont des énergies de défaut d'empilement faibles ; iii) la plaquette de 66 lacunes s'est facilement effondrée en un SFT à 500K pour tous les potentiels appliqués, même avec ceux donnant une énergie élevée pour la faute d'empilement.

L'analyse des défauts par les méthodes des 'voisins communs' et par la 'cellule de Wigner-Seitz' est faite pour étudier les structures résultantes d'une cascade de déplacement. Les résultats prouvent que le plus grand nombre de défauts d'empilement est étonnamment obtenu avec le potentiel de Cleri-Rosato donnant l'énergie la plus élevée de défaut d'empilement (300 mJ m^{-2}). Des structures similaires aux SFT apparaissent près du noyau des cascades et

également une boucle interstitielle sont trouvées avec le potentiel de Cleri-Rosato. Il s'avère que la taille, la densité et la configuration des défauts induits par la cascade déplacement dépendent plus du seuil de déplacement atomique que de l'énergie de faute d'empilement donnés par le potentiel.

Il s'avère qu'un durcissement significatif et observé, et ce à partir des plus faibles doses, de 10^{-3} dpa, à la température ambiante et à 250°C. Avec l'augmentation de la dose, la contrainte critique de cisaillement augmente. La dépendance en dose de cette augmentation change d'une température d'irradiation de la température ambiante à 250°C. En fait le durcissement du à l'irradiation présente une dépendance significative à la température.

L'énergie d'activation thermique a été calculée en mesurant le volume d'activation, qui est obtenu à partir des essais de relaxation. Dans le Ni non irradié, une énergie d'activation d'environ 0.3 eV a pu être déduite. Dans le cas du Ni irradié, le manque de linéarité dans la dépendance entre l'énergie thermique et la température suggère que de multiples mécanismes de déformation sont actifs, simultanément ou consécutivement sur la gamme de température considérée.

Le modèle de dispersion durcissante est employé pour interpréter le durcissement induit par irradiation dans le Ni irradié. L'équation $\Delta\sigma = \alpha\mu b(Nd)1/2$, avec α, la force d'obstacle, est employée. Il apparaît que α vaut 0.12 pour le durcissement induit par irradiation à température ambiante, semblable à ce qui a été précédemment trouvé pour le Cu irradié, et est 0.22 pour le durcissement après irradiation à 250°C, qui est beaucoup plus grand que les valeurs précédentes. Cette différence suggère que les vides, possiblement présents à 250°C, soient des obstacles plus forts que les SFTs ou les boucles de dislocation.

Des déformations in situ dans le TEM ont été conduites avec du Cu irradié, afin d'évaluer la force des défauts induits par irradiation comme obstacle aux dislocations. Il s'est avéré que la force des obstacles est approximativement 100 MPa. Considérant que 90% du dommage induit par irradiation consiste en des SFTs, on suggère que ces obstacles présentant une résistance de 100 MPa soient des SFTs. En particulier, retirer d'une chaîne de caractères de l'interaction entre on a assumé que ce qui est un SFT et une dislocation mobile pourrait être enregistré pour la première fois. Cette réaction implique que la dislocation est fortement épinglée par SFTs.

L'observation en TEM de la microstructure de déformation du Ni irradié montre que la formation de canaux libres de défauts est le mécanisme de déformation initial. La formation de ces canaux permet d'expliquer l'adoucissement observé.

Lorsque la déformation augmente une structure de cellules de dislocation est observée. Elle prend différentes formes selon que l'échantillon est irradié ou pas. Dans le cas irradié, la formation de cellules de dislocation commencent dans les canaux. Ceci implique que la configuration finale des cellules maintiendra une partie de la dimensionnalité des canaux. Dans le cas non irradié la taille de cellules de dislocation est plus grande. La contrainte d'écoulement plus élevée observée dans le cas irradié est ainsi liée à la taille de cellules de dislocation.

CONTENTS

Introduction

Thermonuclear fusion of light atoms is considered since decades as an unlimited, safe and reliable source of energy that could eventually replace classical sources based on fossile fuel or nuclear fuel. Indeed, the fusion reaction products are light atoms, such as helium, that are harmless to the environment. However, the structural components of the fusion reactor will be exposed to extremely high fluxes of 14 MeV neutrons, which are produced in, typically, the deuterium-tritium nuclear fusion reaction. These high energy neutrons will produce changes in the properties of the irradiated material, in particular metals, generally in a detrimental way. Mechanical properties are altered, with a significant hardening, loss of ductility and fracture toughness starting at the lowest irradiation doses. At higher doses, a dimensional instability is observed, which is due to the formation of gas bubbles or voids in the irradiated material. The loss in mechanical resistance of metals by irradiation is one of the life determining factors of the future fusion reactor.

While there are abundant data on that subject since more than forty years, there is still a lack of understanding on the basic mechanisms underlying these changes. It appears that irradiation with high energy particles induces atomic displacement cascades that result in a high density of nanometric crystal defects, which in face centred cubic (FCC) metals consist typically in stacking fault tetrahedra (SFT) and interstitial loops, as observed in transmission electron microscopy. These defects are obstacles to mobile dislocations, vectors of the plastic deformation, and are thus at the origin of the mechanical properties degradation. However, the origin of the defect microstructure and its implication on the mechanical properties are not yet clearly understood.

In this work the focus is given to pure single crystal nickel. Metallic single crystals are useful candidates to study basic processes in irradiated metals associated with mechanical properties because of the absence of grain boundary effects. In addition, the interpretation of mechanical tensile testings is simplified as the applied stress can be expressed as a resolved shear stress on the dislocation gliding direction, which is helpful to detail the dislocation-defect interaction.

The 590 MeV proton accelerator at the Paul Scherrer Institute was used for the irradiation of the samples. Indeed, because of the present lack of a fusion neutron source on earth, this proton irradiation proved to be instrumental in simulating the real fusion irradiation conditions. It should be noted however that the interaction of 590 MeV protons with a solid gives rise to a recoil energy spectrum which is harder than that produced by 14 MeV fusion neutrons. Furthermore, it produces helium and other transmutation atoms in larger amounts that the ones produced by fusion neutrons.

In the past a number of irradiation and simulation experiments have already been performed by the materials group of CRPP in order to understand and model the evolution and the influence on the mechanical properties of the defects produced by the 590 MeV protons. Starting with polycrystalline Al (Gavillet 1986, Paschoud 1990), martensitic steel (Marmy 1991), followed by single crystalline Cu, Pd and Au, (Proennecke 1992, Dai 1995), together with molecular dynamics simulations of high energy displacement cascades in ordered intermetallics (Proennecke 1992, Spaczer 1995) these studies established solid grounds to the understanding of these mechanisms.

In the literature Ni appears to be a peculiar fcc metals with respect to its response to irradiation (Zinkle and Snead 1995, Kojima et al. 1992). It exhibits a lower defect production rate than the one observed in other fcc metals, such as Cu, Au and Pd (Fig. 1), but higher than bcc metals such as Fe, and the ratio of SFTs to dislocation loops seems to evolve with dose while in Cu and Au it is constant (Dai 1995). In addition, it has been found that there is a large discrepancy in published results on Ni irradiated by neutrons, ions or protons.

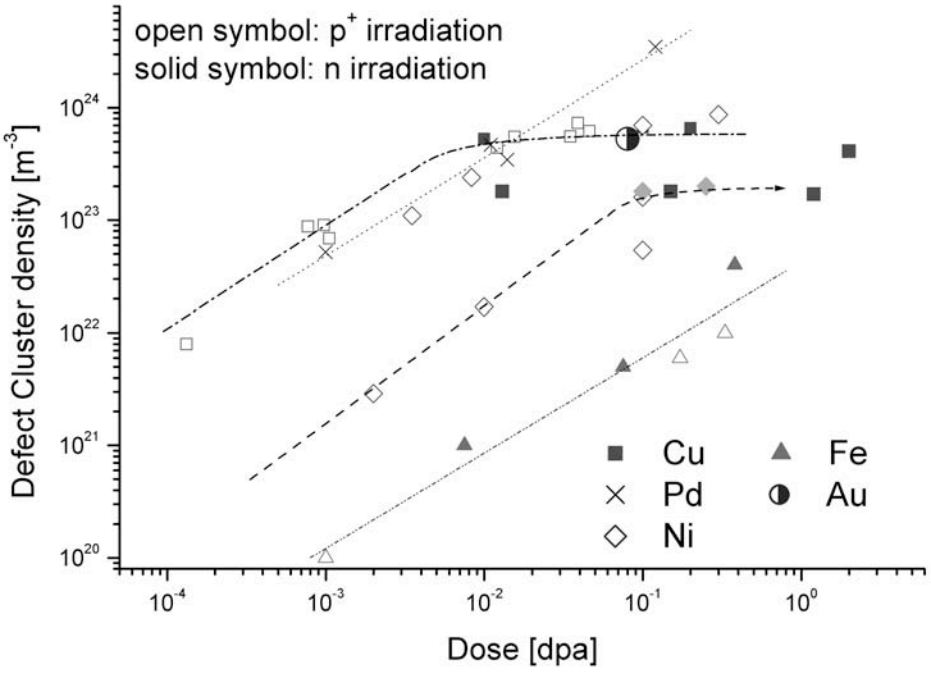

Figure 1 The dose dependence of defect density, including fcc Cu (Dai 1995), Ni (Zinkle and Snead 1992), Pd (Baluc et al. 1999), Au (Dai 1995) and bcc Fe (Luppo et al. 2000).

In the last decade, molecular dynamics simulations performed in the group and in other groups around the world allowed for the first time presenting a scenario for the time evolution of the high energy atomic displacement cascade and the subsequent defect formation (Diaz de la Rubia and Guinan 1990, Bacon et al. 1995). It should be noted that there is until now no direct experimental evidence on that. Simulations highlighted the fact that the atomic mass and the crystalline structure of the target are key parameters in the understanding of the resulting damage. Molecular dynamics simulations appear then crucial in the understanding of the irradiation induced damage formation in Ni, as the atomic mass and the structure are close to those of Cu or Au while experimental data reveal large differences. Ni is thus a good candidate to unveil, first, the basic mechanisms of irradiation effects in fcc metals and second, the materials parameters, such as the stacking fault energy or the shear modulus, that may play a key role in those.

These defects affect the mechanical properties and Ni shows in tension a significant hardening starting at the lowest doses (Zinkle and Snead 1995), similarly to other fcc metals such as Cu, Au and Pd (Dai 1995). Also, it has been demonstrated that deformation of such metals leads to the presence of defect free channels in the microsctucture. This strain

localisation is believed to be at the origin of the significant loss of ductility and premature cracking observed in irradiated technological alloys such as ferritic (Spätig et al. 1998, Gelles and Schäublin 2001) and austenitic steels (Bailat 1999, Bailat et al. 2000). Interestingly, in single crystal metals no significant loss of ductility is observed after irradiation. In this work the formation as well as the evolution of the defect free channels in Ni is investigated in order to reveal the influence of such a peculiar microstructure feature on the mechanical properties.

In order to relate the irradiation induced damage to the change in the mechanical properties, the well-known dispersion barrier hardening model is commonly applied. It expresses the increase in yield stress as a function of the observed defect density and mean size. It is satisfactorily applied to the case of pure single crystal metals (e.g. Dai 1995) but proves unsuccessful in the case of technological alloys, such as ferritic steels (Schäublin et al. 2002a), although the irradiation induced microstructure in the latter case is well characterized over a range of irradiation conditions (Schäublin and Victoria 2000). The difference between these two extreme cases stresses the need for a solid understanding in the simplest cases of the basic mechanisms of the formation of irradiation induced damage and its influence on the mechanical properties.

While transmission electron microscopy is commonly used to characterize the irradiation induced microstructure, mechanical testing can be applied as a probe to it at a microscopical level. In particular, stress relaxation techniques allow obtaining the so-called activation volume and activation energy that relate to microscopical deformation mechanisms. In this work they are measured in the deformed irradiated Ni and Cu and are correlated to transmission electron microscopy observations in order to gain insights on the dislocation-defect mechanisms. In addition, transmission electron microscopy in-situ tensile testing of irradiated Cu allow shedding new lights on these mechanisms.

The next chapter presents a review on the basic mechanisms of irradiated induced damage formation and accumulation, as well as existing models on dislocation-defect interactions that explain hardening.

Chapter I

Literature review

Radiation induced effects in metals have been studied for more than forty years. Radiation damage in metals and particularly its induced mechanical properties degradation is the main frame in the present work. In this chapter, theories and experimental studies on radiation damage will be briefly reviewed. The mechanical property measurements on irradiated Ni will be discussed as well as their theories.

I. LITERATURE REVIEW

The research in the field of radiation induced defects is going on for the past four decades. In the present work, we tried to investigate the influence of the radiation-induced defects on the mechanical properties of single crystal Ni. In this chapter, a literature review on the radiation-induced defects on single crystal metals, and in particular Ni and Cu, is presented.

1.1 Radiation damage in metals

1.1.1 Elementary Theories of Radiation Damage

In general three types of interactions between the incident high energy particle with the target material are given (Schilling and Ullmaier 1994):
1) Elastic interaction between the particle and the target material atoms,
2) Inelastic interaction between the particle and the electrons of the solid, and
3) Inelastic interaction between the particle and the nuclei of the target.
As a result of these interactions, the following defects are induced: i) the displacement of original atoms from their lattice sites leads to the formation of vacancy-interstitial pairs, or Frenkel pairs; ii) the excitation of electrons and iii) the introduction of foreign atoms, either by nuclear transmutations or by the projectile ions stopping in the solid. The damage caused due to electron excitation is unstable. Indeed, if the target is a good conducting material, as metals are, then the energy of eletronic excitation rapidly transforms to thermal energy.

The sequence of basic events of the incident high energy particle bombarding the lattice leading to the formation of defect clusters can be described as follows (Heinisch and Singh 1993, Schilling and Ullmaier 1994, Robinson 1994), At the beginning, within less than 1 fs (10^{-15}s), the primary knock-on event happens and as a result primary knock-on atom (PKA) with a recoil energy T is created. In this time also, transmutation of the knocked atom may occur and may result in the formation of impurities, such as He or H, or heavier elements. Here we are interested in the lattice defect creation. Following the above event after a very short period of time, ~0.2 ps (10^{-12}s), a collision cascade is formed as a result of the slowing down of the PKA and ends with a large number of displaced atoms. Then, in about 3 ps, the energy in the cascade is released to the surroundings and form the so-called thermal spike, which corresponds to the volume within the cascade that has a high temperature, generally much higher than the melting point. In another 7 ps, the cascade will cool down to form a vacancy-rich zone, meanwhile an interstitial shell appears around this depleted zone. Afterwards, a fraction which is temperature dependent of about 70~90% of the interstitials and vacancies will annihilate by thermal intracascade recombination. The surviving vacancies and interstitials agglomerate to form small clusters or annihilate with other existing defects, or move as free point defects. Table 1.1.1 gives a summary of the time evolution of the displacement cascade.

The collision between a particle with mass m and a PKA with mass M and energy E, the maximum recoil energy T_{max} which can be transferred is given by:

$$T_{\max} = \frac{4(mM)}{(m+M)^2} E \qquad (1.1.1.1)$$

Table 1.1.1 Stages in the time evolution of displacement cascade in metals (Schilling and Ullmaier 1994)

Duration(ps)	Event	Result
10^{-3}	Transfer of recoil energy from impinging particle	Primary knock-on atom
10^{-3}~0.2	Slowing down of primary knock-on atom by the generation of a collision cascade, binary collisional phase	Vacancies and low energy recoil collisions, sub-cascades
0.2~0.3	Thermal spike, equipartition of the energy in the cascade volume	Low energy density, hot molten droplet, propagation of a shock wave front in the matrix
0.33	Interstitial ejection, transition from heated to undercooled liquid core	Stable interstitials, atomic mixing
3~10	Cascade core solidification and cooling to ambient temperature	Depleted zone, disordered zone, amorphous zone, vacancy collapse
10 or more	Thermal intra-cascade recombination, thermal escape of SIAs	Surviving defects (SD) escaping interstitials (EI) escaping vacancies (EV) stationary fluxes of EI and EV growth / shrinkage of SIA or vacancy clusters, solute segregation

The energy of PKA lies in the range $0 \le T \le T_{max}$, and can be described by a recoil energy spectrum. A number of codes, e.g., HETC (Coleman and Amstrong 1970) and SPECTER (Greenwood and Smithers 1985), which were developed on the basis of the nuclear reaction theory can be used to calculate recoil energy spectra, and other parameters such as damage energy cross section, helium and transmutation production. Fig. 1.1.1 gives the spectra for the case of Ni.

Kinchin and Pease (1955) were the first to say that when a lattice atom receives a recoil energy larger than the displacement energy threshold, T_d, it will be displaced from its lattice position. However, if $T< T_d$, the atom rapidly returns to its position after a short displacement. T_d is therefore the energy above which a stable Frenkel pair is created. Kinchin and Pease gave the number of displaced atoms produced by a PKA with an energy T as:

$$N_d(T) = \frac{T}{2T_d} \qquad (1.1.1.2)$$

In order to take into account the electronic stopping, Lindhard et al (1963) studied the process of slowing down of energetic PKA by using Thomas-Fermi atomic theory, deduced the well known LSS theory and obtained that the damage energy (T_d) for displacing lattice atoms is a function of the energy of the PKA (T), the mass and atomic number of the PKA (m_1, Z_1) and of the lattice atoms (m_2, Z_2):

$$T_d = f(m_1, Z_1\, m_2, Z_2) \qquad (1.1.1.3)$$

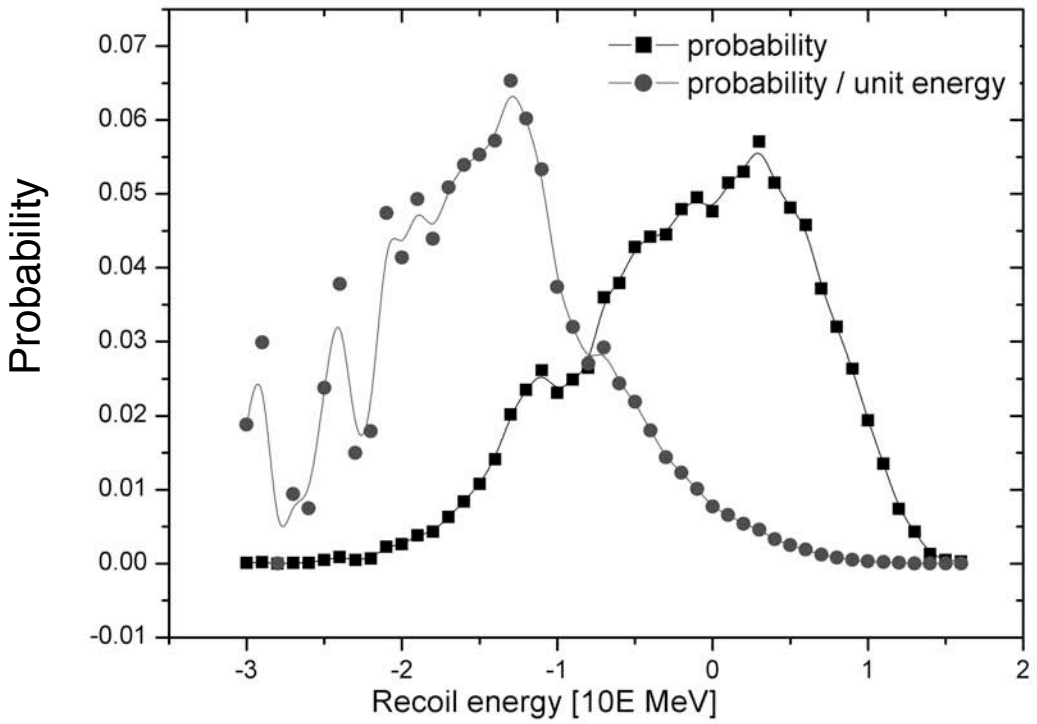

Figure 1.1.1 Recoil energy spectra in terms of probability as a function of recoil energy produced by 590 MeV protons in Ni (Dai 1995).

Figure 1.1.2 gives the spectrum of damage energy in Ni, which is the fraction of the recoil energy which contributes to the effective lattice damage. The ratio, T_d/T, is defined as the damage efficiency. Norgett, Robinson and Torrens (NRT) (1974) modified the Kinchin-Pease model by taking the electronic stopping power into account and got the following relationship:

$$N_d = \begin{cases} 0 & for \quad T < T_d \\ 1 & for \quad T_d < T < 2.5T_d \\ 0.8T_D/(2T_d) & for \quad T > 2.5T_d \end{cases} \qquad (1.1.1.3)$$

This is the widely used NRT approximation for the calculation of displacement damage, quoted in dpa (displacement per atom), which is currently used as a dose unit.

The NRT value corresponds to the displacements produced in the collisional phase. Experimental results (Theis and Wollenberg 1980, Zinkle 1988), as well as molecular dynamics simulation (Hsieh et al, 1989, English et al 1992) show that the number of defects surviving at the end of the cascade evolution, is only a small fraction (~10-30 %, temperature dependent) of the NRT displacement approximation.

By considering the generated number of Frenkel pairs in several metals, Bacon et al. (1995) have shown that a new empirical relationship between N_d and T fits well with the simulation data for energy between 5 and 10 keV:

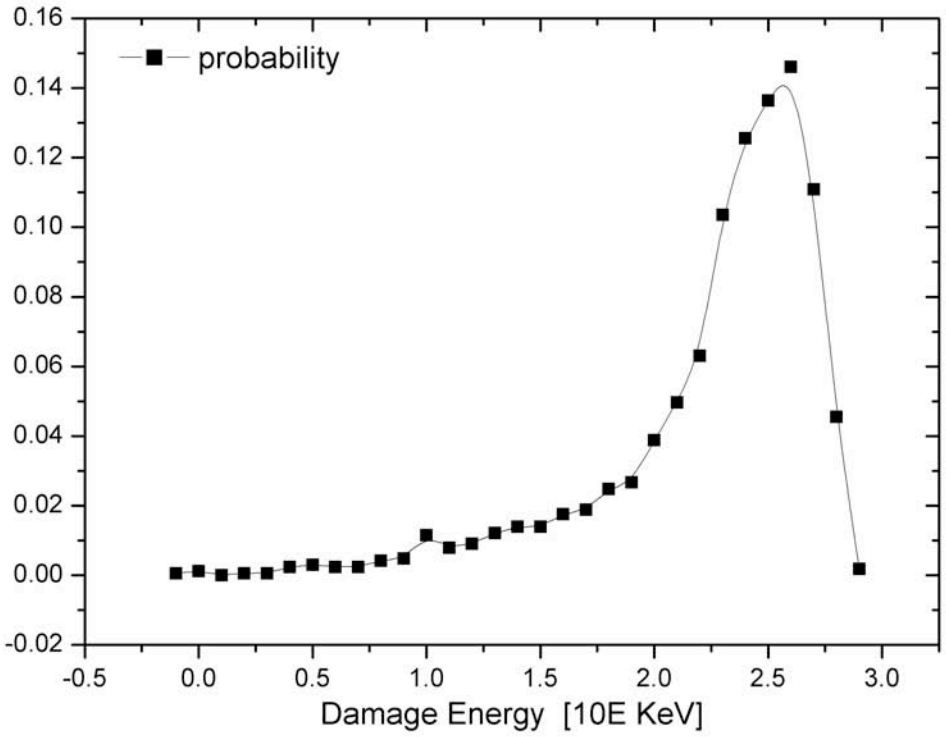

Figure 1.1.2 The damage energy spectra produced by 590 MeV protons in Ni (Dai 1995).

$$N_d = A(T)^m, \qquad (1.1.1.4)$$

where A and m are constants which depend on the material and irradiation temperature. For Al, Almazouzi (1999) has found $A = 8.07$ and $m = 0.83$. These data show that the differences in N_d among different metals are due to their atomic mass, N_d decreases with increasing mass of the target atoms. Since one cascade produces less defects in average than that produced by two separate cascades of the same total energy, subcascade formation leads to an increase in the number of formed Frenkel pairs.

Fundamental findings of the MD simulations of displacement cascades are that the core region undergoes local melting that has pronounced influence on the number of displaced atoms in the cascade and on the primary state of damage. The observation of local melting, with its attendant features of high pressure, liquid-like diffusion, and resolidification provides the basis for understanding many aspects of cascade damage. In most materials the high pressure developed in cascades does not cause plastic deformation. This is largely because the spherical stress state created by a cascade is nearly hydrostatic.

1.2 Computer Simulation of Displacement Cascades in Ni

Since, it is difficult to experimentally investigate the cascades formation in a short interval of time (several ps), computer simulation has been extensively performed in the last fifteen years.

1.2.1 Simulation Tools

Given the short time evolution of the cascade, molecular dynamics (MD) methods have been used to study its behaviour. With present computing power it is not possible to follow with MD the evolution of the resulting defect microstructure in times large enough (ns or more). Other (stochastic) methods are used for this purpose. There are several simulation methods based on different theories.

In present time, the so called 'ab initio' method, the MD method, the kinetic Monte Carlo (KMC) method, the kinetic rate theory, the dislocation dynamics simulation and the finite element method are generally used to simulate the radiation induced defects.

'Ab initio' method, is based on a quantum mechanical description, i.e. solving Schrodinger's equation in some adequate approximation such as the density functional theory. The information that has to be provided is the atomic number and position of the atoms within the system. The approximations for 'ab initio' calculation are based on general physical principles and are not based on the specific nature of the system under investigation. The use of 'ab initio' techniques for predictive calculations offers greater reliability. However, the high computational cost of this methods implies that they are most profitably used for simulating the detailed electronic structure of a system or mechanism of a reaction or the formation and migration energies of defects and their most stable configuration(s), for a reduced number of atoms, at most about 100 atoms.

MD method will be detailed in chapter III. In an MD simulation the time evolution of a system described by interacting atoms is followed using Newtonian mechanics, and the potential energy is represented with empirical or semi-empirical interatomic potentials, such as embedded atom potentials which are used extensively at present. It also needs the atomic number and positions of atoms as input information. MD can calculate systems with large number of atoms, nowadays about milions in a single processor computer, within picoseconds. The KMC method is used to model defect diffusion during irradiation of materials. This method is able to get the density and size of clusters in irradiated samples up to seconds for cubic microns of material. Thus, it is a complementary tool for obtaining the aged structure using MD results on cascade induced damage.

'Ab initio', MD and kMC methods provide the irradiation induced microstructure. To couple these atomistic simulations to the irradiation hardening observed in experiments, dislocation dynamics (DD) simulations are used. In this case the simulation box, only contains the Frank-Read dislocation sources and irradiation induced defects that may act as obstacles to dislocations. Dislocations are discrete and described by straight-line segments. The Peach-Koehler force F acting on a dislocation segment inside the computational cell is calculated from the stress fields that are caused by immediate neighbouring segments, other dislocations segments, defect clusters and the applied stress.

1.2.2 Review of MD computer simulations of cascade evolution

Molecular dynamics (MD) simulation is the usual method to model cascades generated by a PKA. The energy of PKA that can be simulated is limited by the simulation box size, which is related to the computer power. Due to limited computer time, MD simulation can be performed for PKA energies up to hundreds of eV.

Apart from MD method, to simulate the collision phase of cascades induced by high energy recoils, TRIM (Biersack and Haggmark 1980) and MARLOWE (Robinson and Torrens 1974), are the most widely used codes. Both codes use the binary collision approximation where the trajectories of energetic particles are represented as a series of two-body collisions. TRIM uses a structureless target, the next collision is found by a random selection process using Monte Carlo calculation. Therefore it does not need a list of target atom positions. It is clear that TRIM is less realistic. The advantage of the method is that it usually requires less computing time and the energy treated can be up to 1 GeV. The useful information of 3D cascade, morphology, depth distribution of energy loss, displacement, vacancy and ionisation production can be obtained. MARLOWE is more realistic than TRIM as it treats the cascade evolution in a crystalline target. The PKA energy can be chosen between 1 and 1000 keV. MARLOWE can provide information on the collision sequence, replacement and focus on threshold energies. Both codes can be used to model only the collision stage. To simulate the thermal spike quenching process based on the results, modifications or new models have been developed.

An alternative is to convert the final distribution of kinetic energy into heat and to follow the evolution of the liquid droplet as described by Liquid droplet model (LDM) (Alurralde et al. 1990 and 1991) applied classical thermodynamics to the evolution of cascades. At the end of the collisional phase, the kinetic energy is transformed into heat and the evolution of the cascade is followed by heat propagation. They investigated cascades in Ni, Cu, Ag and Fe. The results of low energy (5 and 25 keV) cascades coincided well with those obtained by MD.

Heinisch and Singh (1993) used the binary collision approximation code MARLOWE to study cascade structure and found a 'regular subcascades' as a region with a higher vacancy density and with a size smaller than their mutual distances. Although these simulations do not yield information regarding the surviving lattice defects in the cascades, they can be used to determine the number and morphology of subcascades produced at the end of the collisional phase. Their results showed that the mutual distance between subcascades has a broad distribution but the average value was about 50 atomic distances, which is independent of the atomic number and the PKA energy (up to 1 MeV). In addition, at a given recoil damage energy, the number of subcascades in different metals decreases with increasing atomic number (e.g., Kiritani et al. 1990, Heinisch and Singh 1993). MARLOWE is very useful to study the collisional phase of the cascade. As many body effects take place in the thermal spike it is intrinsically unable to follow the evolution of the cascade.

King et al. (1981) performed cascades with 500 eV PKA and Diaz de la Rubia et al. (1989) performed 5 keV in Ni and Cu. These studies were still limited by the low PKA energy and the used simple pair potential. Diaz de la Rubia and Guinan (1990) finally developed molecular dynamics simulations with a new program, called MOLDY-CASK. This program was based on the MOLDY6 code developed by Finnis (1989) at Harwell laboratory. They used spherical many-body potentials within the embedded atom method (Daw and Baskes 1984) for face-centred cubic (fcc) metals. This code used the link cell method of Heyes and Smith (1987) that allows to speed up the generation of the neighbour list. With the link cell method, it is possible to carry out simulation in crystals containing up to million atoms and therefore to study displacement cascades with energies up to the subcascade formation energy in most metals, which is about 20 to 40 keV. By using this code they reported the results for a cascade initiated by a 25 keV PKA in Cu, and subcascades appeared at 0.288 ps. After this simulation, Heinisch et al. (1994) used a annealing simulation code ALSOME based on a

Monte Carlo scheme to simulate the diffusion and interaction of defects of the collisional phase extracted from the above MOLDY-CASK calculation for 25 keV cascades generated in Cu at 10 K. It was however unable to simulate all the features of the cascade induced defect distributions.

Almazouzi et al. (1999) reported the long term evolution of the defects produced by displacement cascades in Ni, by using MD code 'MOLDY-CASK' (Diaz de la Rubia and Guinan 1990) and Kinetic Monte Carlo code 'BIGMAG' (Jonsson et al. 1998). They used an interatomic potential developed by Cleri and Rosato (1993) and later modified by Almazouzi (1999) in order to describe high energy scattering properly. They performed displacement cascade simulations for PKA energies ranging from 0.5 keV to 30 keV, with constant volume, periodic boundary and a temperature of 100 K. By fitting their results with the power law (see equation 1.1.1.4), they obtained $A = 4.61$ and $m = 0.74$. Following the methodology outlined by Soneda and Diaz de la Rubia (1998) they calculated the formation energy of defect clusters, as shown in Tables 1.2.1 and 1.2.2.

Table 1.2.1 Migration energies in Ni

	MDCASK		Experimental	
	E_m(eV)	D_0(cm^2/s)	E_m(eV)	D_0(cm^2/s)
V1	0.85	0.44	1.04	0.92
V2	0.57	12.1	0.54	24
I1	0.12	0.15	0.14-0.18	-
I2	0.1	0.12	0.12	-
I3	0.1	0.04	-	-
In	0.1	D_0(I2)/n	-	-

Table 1.2.2 Binding Energy in Ni

	$E_{binding}$(MDCASK)(eV)	$E_{binding}$(experiment)(eV)
V2	1.47	1.47
V3	0.2	-
Vn	1.47-2.16($n^{2/3}$-$(n-1)^{2/3}$)	-
I2	4.16	4.16
I3	1.13	-
I4	1.62	-
In	4.16-5.16($n^{2/3}$-$(n-1)^{2/3}$)	-

These calculated data were used as input to the 'BIGMAG' code to calculate the damage annealing or long term aging. Different annealing stages were found: *stage III* at about 350 K, and *stage V* at about 500 K. Furthermore a *substage* of interstitial recombination (clustering) was found at about 250 K. It should be reminded the significance of annealing stages; stage I: migration of self-interstitials; stage II: migration of interstitials from interstitial clusters, stage III: migration of monovacancies; stage IV: migration of vacancies from vacancy clusters; stage V: evaporation of vacancy clusters.

1.3 The irradiation induced defects

The radiation induced defects in fcc metals, such as Cu, Ni, Pd, Au, Al and Ag, have been extensively studied (Kiritani and Yoshida 1984, Singh and Zinkle 1993, Zinkle and Snead 1995, Dai and Victoria 1996, Baluc et al. 1999, Victoria et al 2000). The radiation induced

defects in these fcc metals consist of vacancy type of defects such as loops, voids and SFT, or interstitial type of loops.

Schule (1981) discussed the interaction volume between vacancy and self-interstitials in Ni under high-energy particle irradiations and the vacancy agglomeration during irradiation, but no SFT was observed. While Robinson and Jenkins (1981) found only Frank loops (Burgers vector 1/3<111>), Kitagawa et al. (1985) reported that the majority (90%) of the clusters were small SFTs. Sasaki et al. (1982) performed 450 keV argon ions irradiation on Ni at 600 °C and observed voids and bubbles in microstructure. Kirk (1987) used heavy ions to irradiate Ni and found a high production rate of vacancy type dislocation loops. Yoshida et al. (1988) reported SFTs and voids, aggregates of vacancies and interstitial loops in pure Ni irradiated with 6.4×10^{22} m^{-2} neutrons at 290 °C. Robertson et al. (1991) finished a series of heavy ions irradiation on pure Ni, with 50 keV to 100 keV ions, at different irradiation temperatures (30 and 300 K). He reported that 40% of total damage consists in SFTs to a dose limit of 0.001 dpa to 0.1dpa (10^{15}–10^{17} ions m^{-2}). It should be noted that this last irradiation was performed in situ on a thin foil, where the foil surface may act as a sink for mobile dislocation loops. Kojima et al. (1992) reported a high concentration of SFTs, about 90 %, in total irradiation defects.

The experiments (Zinkle and Snead 1995) in a mixed spectrum fission reactor at low irradiation temperature, less than 0.3 T_m, showed that 33% of defects are SFTs at 0.1 dpa and 28% at a dose of 0.25 dpa. Combined with the results from Kojima (1992), they concluded that transition from an SFT-dominated microstructure at low doses to interstitial dislocation loops-dominated microstructure at higher doses, with a threshold dose between 0.01 and 0.1 dpa.

1.4 Mechanical properties of Unirradiated and Irradiated Metals

1.4.1 Plastic Deformation of Unirradiated Nickel Single Crystals

Haasen (1958) reviewed the plastic deformation of single crystal of pure fcc metals and performed mechanical tests of nickel single crystals. According to Diehl (1956) and Seeger et al. (1957), three stages can be characterized in strain-stress curves (Fig. 1.4.1): Stage I is called the region of *easy glide* (Andrade and Henderson 1951).

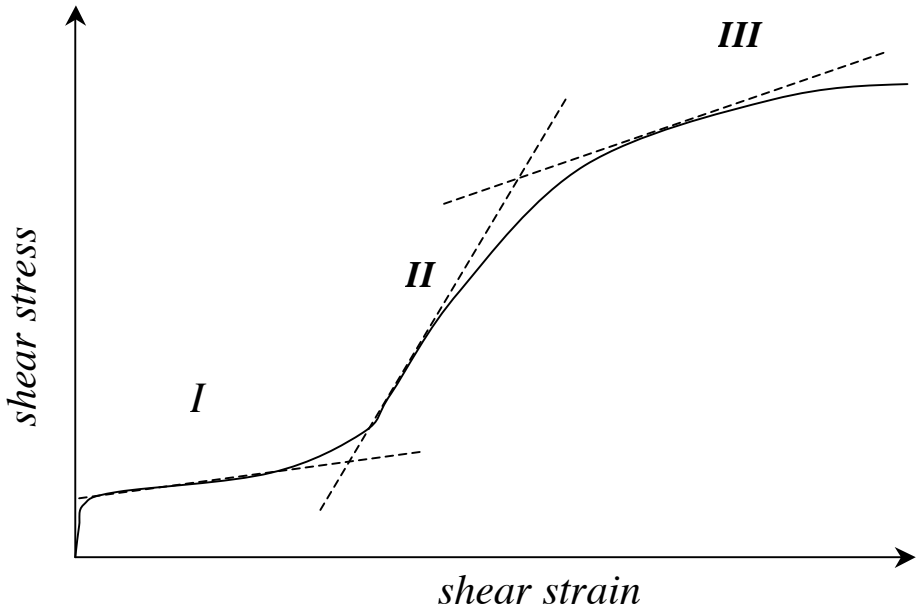

Figure 1.4.1 Schematic shear stress-shear strain curve of face-centred cubic single crystal, with three stages.

Here a low work-hardening rate suggests that most of the dislocations produced during deformation leave the crystal at the surfaces. Stage II, the *rapid hardening* regime which might be related to the formation of piled-up groups of dislocations behind Lomer-Cottrell dislocations or to the blocking of dislocations by forest dislocations (entanglement). At high stresses, some of the slip dislocations become able to by-pass these obstacles by cross-slipping onto another glide plane. This process of *dynamical recovery* reduces the rate of work-hardening and leads to stage III in the stress-strain curve.

Haasen used a tensile sample with gage length 5 cm, with a strain rate between 10^{-4} and 10^{-5} per second. The crystals were deformed along various orientations. He defined the critical resolved shear stress (CRSS), by the intersection of the extrapolated linear easy glide region with the stress axis. In present work, the yield resolved shear stress (YRSS) ($\sigma_{0.2}$) is normally used instead of CRSS. In fact, there is little difference between CRSS and YRSS from experimental measurement. The measured average CRSS values are:

6 ~ 8.5 MPa at 300 K,
7.5 ~ 8.5 MPa at 78 K,
9.0 ~ 11 MPa at 20 K.

These results described a change of 1.5 MPa between 78 K and 300 K. These measurements were higher than the values of 10.4 MPa at 300 K and 13.6 MPa at 93 K given by Andrade and Henderson (1951). The work hardening of stage I increased strongly (some up to 12 MPa) for unfavourable orientations where other slip systems come into early. Andrade and Henderson (1951) also noted that the extent of easy glide was strongly temperature dependent, from 7% at 300 K to 42% at 20 K for a favourable orientation. For unfavourable orientations it was much smaller and less temperature dependent.

At stage II, *rapid hardening*, the stress was somewhat larger for the unfavourable orientations at 300 K than at 20 K. At 300 K, the work hardening rate was from 200 MPa to 240 MPa, much larger than that in stage I. At 20 K and 78 K, this parameter increased to values between

250 MPa and 320 MPa.

Haasen found the extent of the stage III was about 40% ± 10% at all temperatures investigated. The strain at fracture increased from about 85% at 300 K to 130% at 20 K. The fracture stress was independent of orientation within the experimental scattering. Its temperature dependence was predominant that of stress in stage III. The stress at fracture at 20K was about G/400, where G is the shear modulus.

Haasen suggested that the work hardening in the fcc crystals was caused by two mechanisms. In the first case, the dislocations spreading the slip along the main glide planes cut other dislocations, which do not lie in this plane. The production of jogs in screw dislocations required the creation of point defects. In the second case, dislocations are stopped in the crystal by interaction with dislocations of other slip systems leading to the formation of Lomer-Cottrell dislocations. More dislocations piled up behind these obstacles, and the elastic stress fields arising from these groups work-harden the crystal.

The first stage was treated by Seeger (1955) quantitatively. The contribution of dislocation cutting processes depends on temperature in the form

$$\left.\begin{array}{ll} \tau_s(T) = \dfrac{U - kT\log(\dot{\varepsilon}_0/\dot{\varepsilon})}{\upsilon} & for \quad T \le T_0 = \dfrac{U}{k\log(\dot{\varepsilon}_0/\dot{\varepsilon})} \\ \tau_s(T) = 0 & for \quad T \ge T_0 \end{array}\right\} \quad (1.4.1.1)$$

where U is the activation energy of process (jog formation or creation of interstitials and vacancies), υ is bdl, b is strength of the dislocation, d is diameter of the intersected dislocation or of a point defect, l is spacing of dislocation forest or distance between jogs, $\dot{\varepsilon}$ is strain rate. The flow stress $\tau_G = \alpha bG\sqrt{N}$ where N is the dislocation density, α a constant of order of magnitude 1/10 (Seeger 1957)

Thus a CRSS $\tau_0 = \tau_s + \tau_G$ decreases linearly with increasing temperature at low temperatures and is a constant at higher temperatures. Haasen's results on τ_0 (T) by direct measurement on different crystals by temperature change during stage I agree with such a general behaviour, the main rise in τ_0 for Ni being below 100 K. In order to separate τ_G, one has to know the temperature dependence of the shear modulus of as-grown nickel crystals. Andrade and Henderson (1951) showed higher absolute values of τ_0 and also a 30% increase in τ_0 from 300 K to 90 K while Haasen (1958) exhibited only a 10 % change in the same temperature range.

At stress τ_{II} rapid hardening starts and is regarded as the critical shear stress of certain secondary glide systems, the dislocations of which efficiently block the path of dislocations of the main slip system. From equation (1.4.1.1) it follows that the temperature dependence of τ_{II} is stronger than that of τ_0 since υ^{-1} (i.e. the density of dislocation forest) is larger as seen from the secondary systems than seen from the main system. This stronger temperature dependence of τ_{II} explains the strong rise of the strain at the initial phase of stage II at lower temperatures.

As shown in fig. 1.4.1, the work-hardening rate decreases at higher deformation as a

consequence of what has been called 'dynamical recovery'. This stage sets in at a critical shear stress τ_{III}, the strong temperature dependence of which will now be analysed in terms of a dislocation model proposed by Diehl et. al. (1955). These authors ascribed dynamical recovery to the escape of screw dislocations from the main slip planes by means of thermally activated and stress-aided cross-slip. Mader (1957) found essentially no cross slip below a stress level of 41 MPa at 300 K. Haasen identified a τ_{III} of 55 MPa at 300 K. The screw dislocations mobilized in this way from pile-up groups can promote strain and diminish the flow stress thus leading to a reduced rate of work-hardening.

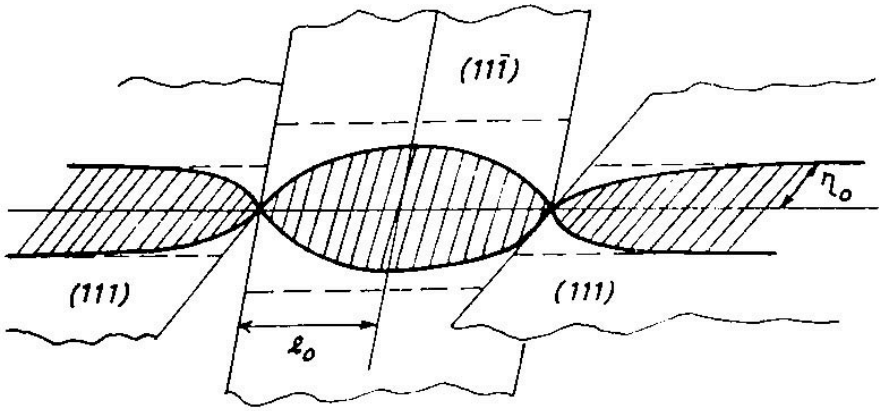

Figure 1.4.2 Cross-slip of extended screw dislocation (Schoeck and Seeger 1955).

Shoeck and Seeger (1955) illustrated the critical step of the cross-slip process. In fig. 1.4.2, an extended dislocation in the main slip plane (111), with 2 η_0 (dissociation width), recombines over a certain length $2l_0$ and separates again into partial dislocations in the cross-slip plane (11$\bar{1}$) where it is now free to move and the activation energy for this process is calculated. For a critical shear stress τ_0 acting in the cross-slip plane the activation energy E_0 turns out to be about 1 eV for aluminium, 10 eV for copper. The difference is caused by the respective widths of the stacking faults in dislocations in these metals, which are determined mainly by stacking fault energies γ. Haasen (1958) estimated E_0 and γ for Ni from their measurement on stage III. The results showed E_0 = 8.1 eV and γ = 90 mJ/ m^{-2} for Ni.

1.4.2 Plastic deformation of irradiated single crystals

In the literature, there is no report on the plastic deformation of irradiated Ni single crystal. However, the plastic deformation of irradiated single crystal Cu was reported more than forty years ago (Blewitt et al. 1960). Blewitt et al. (1960) had investigated the irradiation hardening of Cu single crystal and its temperature dependence. They found that the yield shear stress could be given by a function similar to σ=A-$BT^{1/2}$ above 40 K. Lüders bands with slip lines having large step height were associated to increasing stress.

Plastic deformation of irradiated metals is known to lead to the formation of defect free channels (Smidt 1970). They were observed in a number of metals, starting with steel (Bloom et al. 1967) to pure single crystal Cu (Dai 1995). These defect free channels will lead to a peculiar behavior. This strong strain localisation leads to softening while maintaining a high stress level.

1.4.3 Irradiation hardening

Irradiation hardening is a typical effect induced by irradiation in metals. In the past years, three important concepts were extensively quoted for describing these phenomena, source hardening and friction hardening or lattice hardening and dispersion barrier hardening.

Source hardening is due to the locking of the grown-in dislocations by a heavy decoration of radiation-induced defects. The CRSS is then determined by the stress necessary to break the dislocations away from this locking (Singh et al. 1997).
Friction hardening is due to the defects impeding the motion of dislocations by internal stress fields surrounding the defects (Diehl and Schilling 1965).
Dispersion barrier hardening is due to the defects impeding the motion of dislocations (Bement 1970).

1.4.3.1 Theory of Irradiation Hardening

Seeger's theory

Seeger (1958) analyzed the existing experimental results of irradiation hardening and resisitivity annealing and postulated the theory of radiation hardening, in which he attributed the hardening to the thermally and stress activated cutting of dislocations through a distribution of obstacles, i.e. depleted zones formed during irradiation (Seeger and Essman 1962)

According to them, the strain rate is

$$\dot{\varepsilon} = \frac{N_d}{N_0} b v_0 \exp\left[-\frac{U(\tau)}{kT}\right] \qquad (1.4.3.1)$$

where N_d is the number of dislocations per unit volume hung up against obstacles, N_0 is the number of obstacles per unit area of glide plane, $\boldsymbol{b}$ is the Burgers vector, v_0 is the oscillation frequency of a dislocation $\sim 10^{10}$/s, T is the absolute temperature and $U(\tau)$ is the activation energy to overcome the obstacle under stress τ. Assuming the profile of the energy shown in Fig. 1.4.3a, which can be expressed as

$$U(x) = U_0\left[1 - \frac{1}{1+\exp(x/x_0)}\right] \qquad (1.4.3.2)$$

and under a shear stress τ, the energy profile changes to that of Fig. 1.4.3b and is given by

$$U(x) = U_0\left[1 - \frac{1}{1+\exp(x/x_0)}\right] - b l_0 \tau x \qquad (1.4.3.3)$$

where l_0 is the distance between the obstacles on the dislocation. The activation energy in this case is $U=U(x_2)-U(x_1)$. At a stress level of $U_0/4bl_0x_0$, it gives

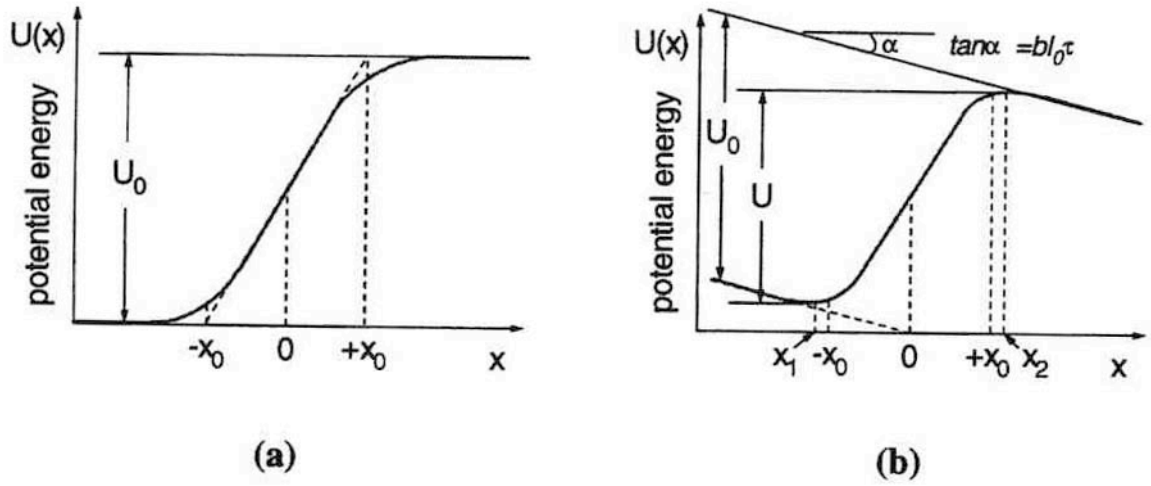

Fig. 1.4.3 Energy profile for the cutting of a dislocation through an obstacle (a) no stress applied, (b) stress τ applied. (Seeger 1958)

$$U = U_0\left[1-\frac{4bl_0x_0\tau}{U_0}\right]^{3/2} \qquad (1.4.3.4)$$

For a fixed obstacle density, the larger the τ, the shorter l_0:

$$l_0^{\,3} = \frac{\mu b}{\tau N_0} \qquad (1.4.3.5)$$

where μ is the shear modulus. From equations (1.4.3.3) and (1.4.3.4) one can obtain that: $\tau^{2/3}$=A-B$T^{2/3}$

$$A = \left(\frac{N_0}{\mu b}\right)^{1/3}\frac{U_0}{4x_0b} \qquad (1.4.3.6)$$

$$B = A\left(\frac{k}{U_0}\ln\frac{Nbv_0}{N_0\dot{\varepsilon}}\right)^{2/3} \qquad (1.4.3.7)$$

Assuming N is proportional to the irradiation dose, this gives a linear relationship between $\tau^{2/3}$ and $T^{2/3}$, and a square root dose dependence of τ.

Fleischer's theory

Fleischer (1962a, 1962b) postulated a theory of hardening due to tetragonal distortions. For a rapid hardening model, Fleischer proposed a force-distance diagram of the obstacle on the dislocation as shown by Fig. 1.4.4. A dislocation passing defects feels a rapidly increasing force, which reaches a critical F_{max} and then rapidly decreases. Under the applied force F_1, the dislocation moves up to x=B. The shaded area in fig 1.4.4, is the thermal activation energy

required to move the dislocation from x=B to x=0.

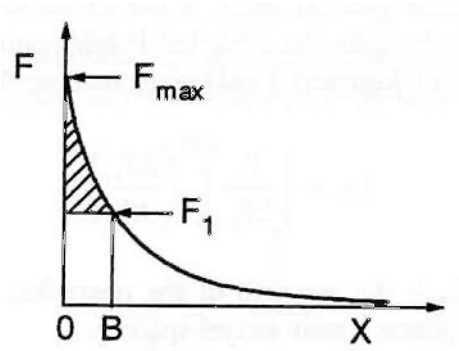

Fig. 1.4.4 Force on a dislocation as a function of distance along a slip plane.

The force F was described as

$$F=F_0[(x/b)+1]^{-2} \qquad (1.4.3.8)$$

where $F_0=G\Delta\varepsilon\, b^2/3.86$, G and b have the same meaning as above, $\Delta\varepsilon$ is the difference between longitudinal and transverse strain of the tetragonal distortion. Thus the activation energy needed to move the dislocation from B to 0 should be

$$U=l_0\int [F_0/l_0 b[(x/b)+1]^{-2}-\tau]dx \qquad (1.4.3.9)$$

where l_0 the distance between the defects on the dislocation. Noting that at B the applied force is $F=\tau l_0 b$, one can obtain

$$U=F_0 b[1-(\tau/\tau_0)^{1/2}]^2 \qquad (1.4.3.10)$$

where $\tau_0 = F_0/bl_0=\mu\Delta\varepsilon(c)^{1/2}/3.3$, is the stress at 0 K, c the concentration of defects. The energy supplied by thermal fluctuations, is therefore proportional to kT. From equation (1.4.3.10) it can be deduced that

$$(\tau/\tau_0)^{1/2}=1-(T/T_0)^{1/2} \qquad (1.4.3.11)$$

where $T_0=F_0 b/\alpha\kappa$. Considering a size distribution for the defects, Fleischer obtained the flow stresses:

$$\tau = \frac{\mu b}{3.7}\left(\sum n_i d_i\right)^{1/2} \qquad (1.4.3.12)$$

where d_i and n_i are the diameter and density of defects. Using the existing data of Markin on defect density and size distribution in neutron irradiated Cu (Makin et al 1961), he found that $\tau \propto (\phi t)^{1/3}$, which was consistent with Blewitt's results (Blewitt et al. 1960).

Theory for particle hardening

For a more general case, if the obstacles are widely-spaced point-like weak obstacles of identical strength, the Fleischer-Friedel point obstacle approximation (Friedel 1964, Fleischer

et al. 1963, Reppich 1994) gives that the flow stress can be expressed as:

$$\tau_{FF} = \left(\frac{F_m}{2T_L}\right)^{3/2}\left(\frac{2T_L}{bL}\right) \qquad (1.4.3.13)$$

where F_m is the strength of the obstacles, T_L is the line tension of the dislocation, L is the average planar square lattice spacing.

Computer simulation with graphical methods performed by Kocks (1966), and Foreman and Makin (1966) shows that for a random obstacle array, the critical flow stress dislocations required to break through the obstacle array is smaller than the value given by eq. (1.4.3.13). For weak obstacles the CRSS, τ_C, is given as (Reppich 1994)

$$\tau_C = 0.9\tau_{FF} = 0.9\left(\frac{F_m}{2T_L}\right)^{3/2}\left(\frac{2T_L}{bL}\right) \qquad (1.4.3.14)$$

The specific obstacle strength, i.e. the breaking angle φ_0, is defined through

$$\cos(\varphi_0/2) = \frac{F_m}{2T_L} \qquad (1.4.3.15)$$

If we assume the line tension to be $1/2\mu b^2$ (Cottrell 1953), then equation (1.4.3.14) is

$$\tau_C = 0.9\cos(\varphi_0/2)^{3/2}\frac{\mu b}{L} \qquad (1.4.3.16)$$

For extended and not widely-spaced obstacles of various strength, Schwarz and Labusch's computer simulation shows that for obstacles with symmetrical force profile (see Fig. 1.4.5) the shear stress is given by:

$$\tau_{SL} = \tau_{FF} \times 0.94(1 + 2.5\eta_{SL})^{1/3} \qquad (1.4.3.17)$$

For obstacle with asymmetrical force profile (see Fig. 1.4.5) on has:

$$\tau_{SL} = \tau_{FF} \times 0.94(1 + C_{SL}\eta_{SL}) \qquad (1.4.3.18)$$

$$\eta_{SL} = \frac{Y_{SL}}{L}\left(\frac{F_m}{2T_L}\right)^{-\frac{1}{2}} \quad << \quad 1 \qquad (1.4.3.19)$$

where Y_{SL} the interaction range illustrated in Fig. 1.4.5, and C_{SL}=2/3.

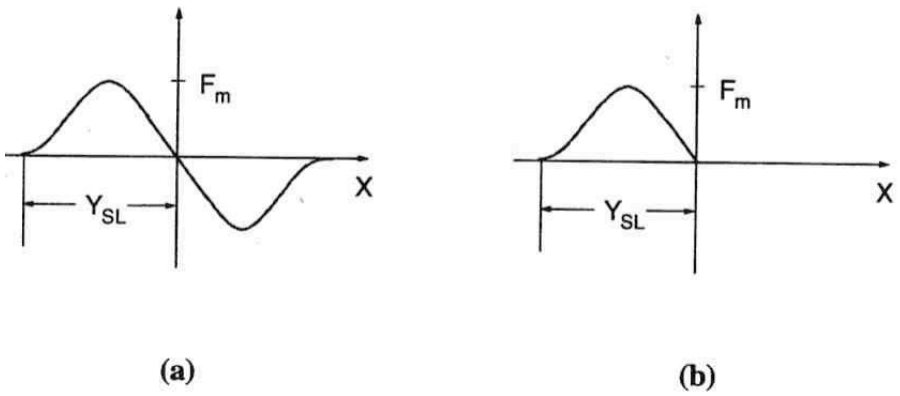

Fig. 1.4.5 Force profile of obstacles (a) symmetrical, and (b) asymmetrical.

In all hardening models, the critical parameter is the effective mean planar obstacle spacing along the dislocation, l_0 which as seen from the above discussion, is obstacle strength, obstacle size and applied stress dependent.

When all above mechanisms are take into account, the microstructure of irradiation defects is not clearly understood, yet. In our present work, the temperature dependence of yield shear stress in Ni irradiated to 0.1 dpa at RT could not be matched with these models.

Dispersion barrier hardening (DBH) model

Bement (1970) proposed a model, namely dispersion barrier hardening (DBH) model, the shear stress is given by

$$\Delta\tau = \alpha\mu b(Nd)^{1/2} \qquad (1.4.2.20)$$

where μ is the shear modulus, l is the average separation of obstacles and α is a parameter representing the obstacle strength. This model will be discussion in Chapter V.

1.5 The interaction between irradiation induced defects and moving dislocation

1.5.1 Interaction with perfect loops

Saada and Washburn (1963) analysed the interaction between prismatic loops and glissile dislocations in quenched and aged pure aluminium.

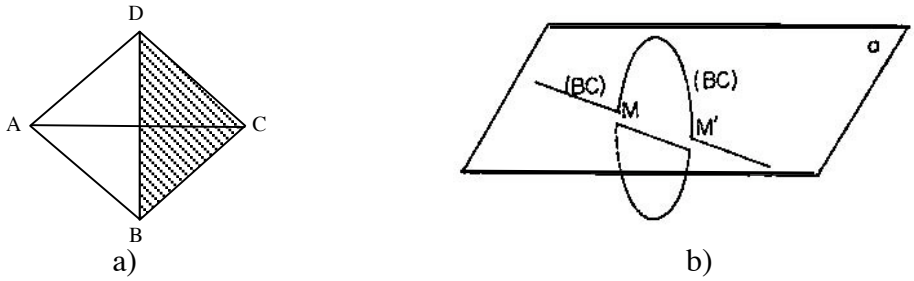

Fig. 1.5.1 a) Thompson tetrahedron. b) Intersection of a prismatic dislocation with a moving dislocation of the same or of opposite Burgers vector. (Saada and Washburn 1963)

As shown in fig. 1.5.1a, perfect prismatic loops can have six possible Burgers vectors, AB, BC, CD, AD, AC, BD. The energy of a perfect loop varies only slightly for small rotations on its glide cylinder away from the plane minimum dislocation length, {110}, which lies at right angles to its Burgers vectors. Therefore, interaction with a moving dislocation may often result in rotation of a prismatic loop.

They assumed four cases on the basis of the angular relationship:

i) Consider the first interaction of a moving dislocation with a prismatic dislocation that has AD as the loop Burgers vector, the moving dislocation are at right angles. Only long range interaction occurs.

ii) If the dislocation loop has BC as its Burgers vectors, the results of intersection will be as depicted in Fig. 1.5.1b. After the cutting, the loop is smaller and the moving dislocation has acquired a loop MM' that does not lie in the original glide plane. If the moving dislocation is not pure screw, these segments will probably be able to slide along the dislocation in the direction of the Burgers vectors and follow it. Therefore, this interaction will cause a progressive destruction of the substructure. If the jogs do not glide, the arms ML and M'L' of the moving dislocation will have to develop into a spiral, meet and annihilate without destroying the loop.

iii) Suppose that the prismatic dislocation has BD or DC as Burgers vectors and lies in a plane cutting the plane a. in fig. 1.5.2a the glide cylinder of the loop, P, is cut by the glide plane α of the dislocation, BC, along two straight lines (shown as dashed lines). Let M be the point of intersection where the configuration of the dislocation lines and their Burgers vectors is such that $\vec{b}_1 \cdot \vec{b}_2 < 0$ at the quadruple node. Then a resultant dislocation M_1M_2 will be formed which must lie along the intersection of the two glide surfaces as shown in fig. 1.5.2a.

It is first assumed that the prismatic loop P lies in a {111} plane. The increase in length and the gain in energy cannot be evaluated with high precision, but the reaction should occur. If the configuration is as depicted in fig. 1.5.2a, there will be a tendency for the loop to rotate toward the plane normal to its Burgers vector. If this happens, it can be seen that the length of the junction dislocation may shrink to zero because it would then cause too much increase in the total length of dislocation.

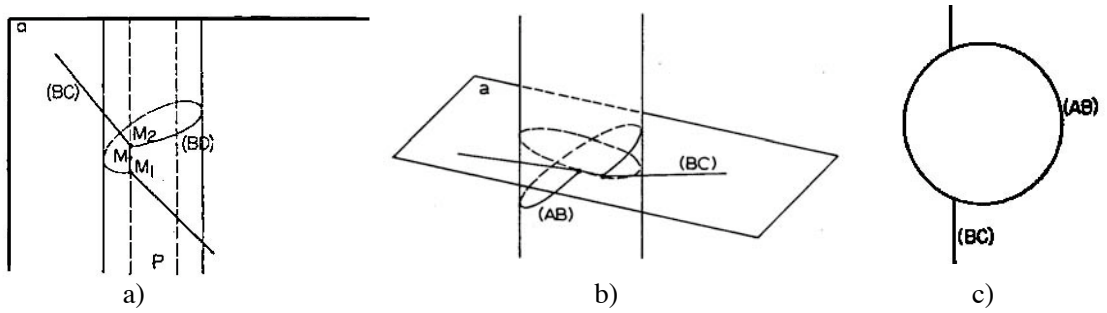

a) b) c)

Fig. 1.5 2 a) Junction reaction at the intersection of a dislocation moving in its glide plane and a perfect prismatic dislocation (glide plane parallel to axis of glide cylinder). b) Junction reaction at the interaction of a dislocation moving on its glide plane and a perfect prismatic dislocation (glide plane at an angle to axis of glide cylinder). c) Change in the Burgers vector of a primatic loop due to interaction with a moving dislocation. (Saada and Washburn 1963)

d) In the last case, if the prismatic loop has AB or AC as Burgers vector, the intersection of the glide plane of the moving dislocation with the glide cylinder of the loop is an ellipse. It can be seen from fig. 1.5.2b that a junction reaction can occur.

It also seems likely that in some cases the prismatic loop can be pushed by the moving dislocation so as to rotate to plane a. if this happens or if the loop lies originally in plane α and near enough to the glide plane of the moving dislocation, then the reaction shown in fig. 1.5.2c will occur when there is attraction. The result is a change in the Burgers vector of the loop. It can be seen that the energy gained by this process can be very large, of the order of $\mu b^2 R$, where R is the radius of the loop.

1.5.2 Interaction with faulted loops

Saada and Washburn (1963) distinguished two cases for this interaction.

a) First, assume that the loop lies in plane α or plane *d* having $A\alpha$ or $D\delta$ as its Burgers vector respectively. If the moving dislocation comes in contact, either by intersecting a loop on plane *d* or by cross-slip contacts a loop on plane α, then it is possible for the partials to recombine and split into two new Shockley partials in the plane of the stacking fault that will sweep away the fault. The final result is the same as that shown in fig. 1.5.2c; two nodes on the moving dislocation line connected by curved dislocation segments that do not lie in the glide plane. For a loop lying in plane *d* the two opposite sides of the loop become segments having Burgers vectors BD and DC. This configuration should act as a strong anchor point on the moving dislocation.

b) The second case occurs when the loop has $C\gamma$ or $B\beta$ as its Burgers vector and lies in plane *c* or *b* respectively. In this case the moving dislocation can also dissociate in the plane of the stacking fault but the result is a Frank sessile dislocation and a Shockley partial. The loop is then separated into two parts. The stacking fault is swept away in only one of the parts and the dislocation line acquires a curved segment that does not lie on the original glide plane. This large jog may glide away in the direction of the Burgers vector. Therefore, both perfect and imperfect loops can be swept away by moving dislocations.

Saada and Washburn also took account of the case where the stacking fault loop is smaller

than a critical size. Neither of these interactions can then occur because the increase in line energy of the Shockley partial associated with sweeping away the stacking fault is larger than the energy of the fault (Saada and Washburn 1962, Saada 1962, Vincotte 1962). This critical radius can be given approximately by

$$R_{critical} = \frac{Gb_{Shockley}^2}{2\gamma} \qquad (1.5.2)$$

where G, $b_{Shockley}$ and γ are the shear modulus, the Shockley Burgers vector and the stacking fault energy, respectively. If γ is taken as 125 mJ•m^{-2} for nickel, then $R_{critical}$ is 6.9 nm.

1.5.3 Interaction with Stacking Fault Tetrahedra

Since 1976 Hirsch studied the interaction between dislocations and prismatic loops, faulted loops and SFT's. He found that, i) when screw (and some other) dislocations interact with loops and SFT's, they will react with the loops or SFT's to form helical and jogged configurations; an example is given in Fig. 1.5.3; ii) The dislocations sweeping process occurs only if the helical and jogged configurations can glide easily. Resistance to glide (hardening) is due to the jogs lying on abnormal slip-planes and in FCC metals to Lomer-Contrell dislocations. iii) At low temperatures, the long jogs are sessile (Orowan obstacle) and athermal processes control the flow stress. The sweeping is limited. At medium temperature, short jogs tend to be glissile and sweeping up will be efficient. The process is thought to be controlled by climb and glide processes. The yield stress will be controlled by the long range repulsive stress from defects before contact. The details are shown as Fig. 1.5.4.

The process of the interaction shown in Fig. 1.5.3 is: the screw EF dissociates on c, and then by combining with the stairs-rods removes the faults on the other planes. Finally, a helical configuration is formed as shown in (c). It should be noted that all segments except for DC are glissile either on c or d, and then the helix will tend to straighten.

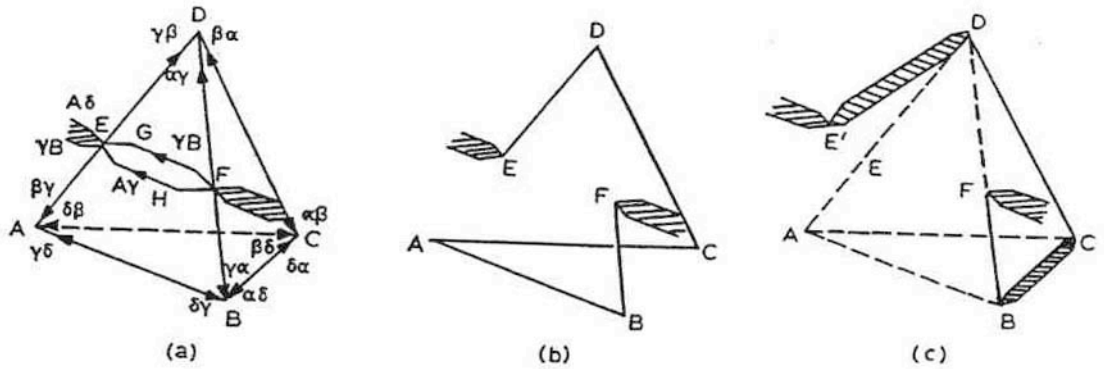

Fig. 1.5.3 Interaction between a screw dislocation EF on slip plane c with Burgers vector AB and a stacking fault tetrahedron. Finally, a helical configuration with a jog DC is formed. (Hirsch 1976).

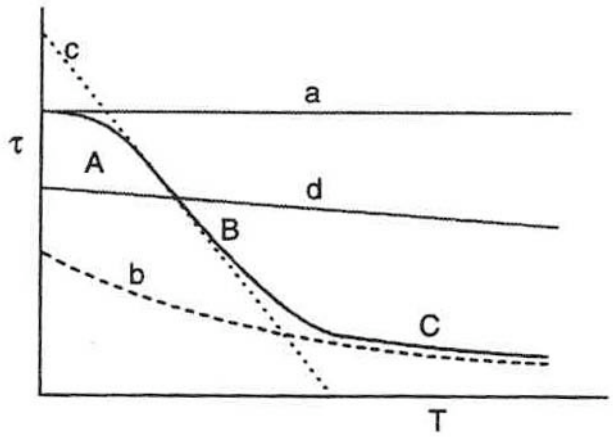

Fig. 1.5.4 Schematic variation of stress with temperature for various processes occurring during deformation of irradiated copper (defects size ≥ ~ 5b, b is burgers vector). 'a', Orowan stress; 'b', elastic repulsion from loops; 'c', climb-glide process for screws with jogs; 'd', sessile-glissile transformation for dislocations with edge components with sessile jogs. (Hirsch 1976).

II Experimental

2.1) Sample Preparation
2.2) Irradiation Facility Description
2.3) Tensile Tests
2.4) TEM

2.1 Preparation of tensile specimens

For the purpose of comparing irradiation induced defects in different fcc materials, single crystal Ni, Cu, Pd and polycrystalline Au were taken into consideration. To get the requested samples for small tensile machine, the raw materials need to be processed in a number of steps, including slice cutting from initial large crystal, mechanical polishing, electro-polishing, high vacuum annealing, and number stamping.

2.1.1 Initial Material

Single crystal rods of nickel of 12 mm in diameter and 25 mm in length, and single crystal rods of Cu of 20 mm in diameter and 40 mm in length, polycrystalline Au and Cu foil in 25×25×0.3 mm were provided by Goodfellow Cambridge Ltd. The purity of all materials is 99.999 % (copper < 2ppm, iron < 5ppm, calcium < 1ppm and magnesium < 1ppm), certified by this company. The crystal was grown along the [110] orientation.

X-ray diffraction was used to determine the orientation of single crystal rods. Fig. 2.1.1a is an example of Laue back reflection pattern.

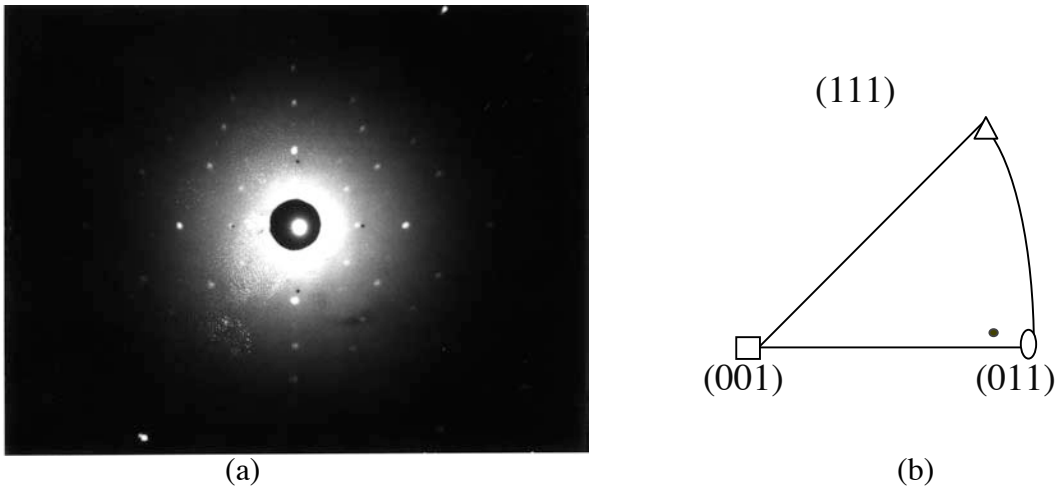

(a) (b)

Fig. 2.1.1 The axial orientations of single crystal tensile specimens. A (left) Laue back reflection patterns. B (right) The position of tensile direction in standard triangle, which is about 5° off 011 towards 001 and 3° off [011] towards [-111].

For X-ray diffraction experiments, the top surface of rod must be mechanically and electro-polished. Fig. 2.1.1b indicates the chosen tensile axis, which is about 5° off [011] towards [001] and 3° off [011] towards [$\bar{1}$11]. The tensile samples are cut to normal PIREX shape in Fig. 2.1.2.

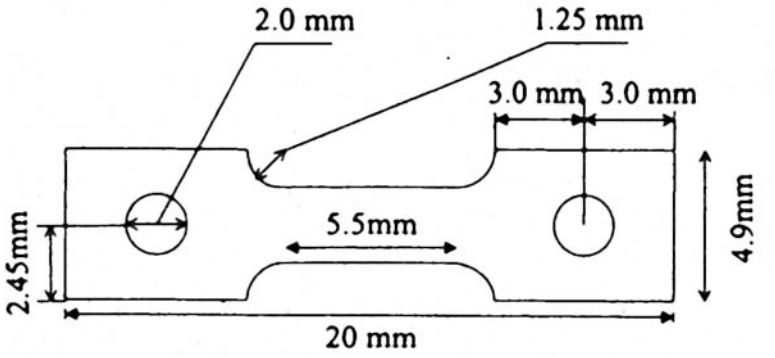

Fig. 2.1.2 The geometry of PIREX samples.

Flat tensile specimens with dimension 5.5×2.5×0.35 mm were cut by spark erosion. The tensile axis is close to [011], where little or no easy glide is expected.

2.1.2 Polishing and annealing

Flat Ni specimens were mechanically polished using silicon carbide paper, down to 320 μm. Then, to remove the work hardening layer on the surface, the specimens were electro-polished to a final thickness of about 300 μm. The electrolyte consists in 12% H_2SO_4 in methanol. Polishing was performed at 0°C at 20 V.

For Cu specimens, the same procedure was applied for the reduction in thickness. Polishing conditions are indicated in table 2.1.

Au and Al polycrystalline foils were supplied with the thickness of 250 μm. Only about 20 μm over the surface layer is removed by electro-polishing. The electrolyte for polishing Au and Al are 10g LiCl in 1 liter Methanol at 20 °C at 40-50V, and 20% $HClO_4$ in methanol at –20 °C at 20 V.

Table 2.1 Electro-polishing conditions for Ni, Cu, Al and Au TEM specimens.

Material	Electrolyte	Condition
Ni	12% H_2SO_4 + methanol	0 °C, 20 V
Cu	25% H_3PO_4+ 25% C_2H_5OH + 50% water	20 °C, 9 V
Al	20% $HClO_4$ + methanol	–20 °C, 20 V
Au	10g LiCl + 1 liter Methanol	20 °C, 40 V

The thickness variation over the gauge length is kept constant within 3%, i.e. within 20 μm.

A slight bending was observed during the specimen cutting and in the case of Ag, Al and Au some cold work might have been introduced additionally due to mechanical polishing. Ni specimens were annealed at 1000 °C for 2 hours in a He atmosphere, then slowly cooled down to room temperature (~25 °C) as illustrated in Fig. 2.1.3. Cu and Au was annealed under high vacuum of 3×10^{-6} mbar at a temperature of 800 °C for 2 hours. Al and Ag were annealed under the same vacuum level at 500 °C and 700 °C, respectively, for 2 hours.

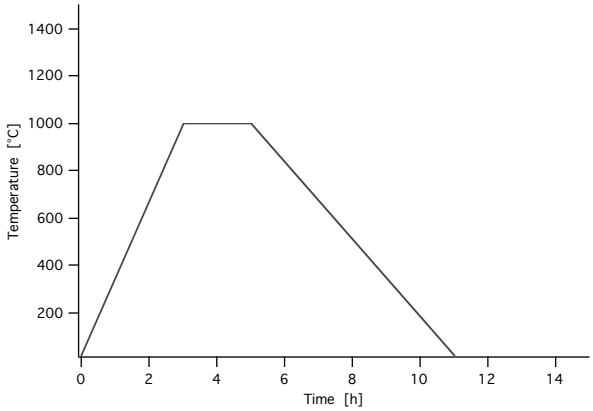

Fig. 2.1.3 Annealing curve of Ni single crystal specimens.

2.2 Irradiation

Tensile specimens were irradiated in the Proton Irradiation Research Experimental (PIREX) facility (Marmy et al. 1990) installed in the 590 MeV proton beam of the accelerator located at the Paul Scherrer Institute in Switzerland, to doses between 10^{-3} and 0.1 dpa, at temperatures from RT to 450 °C.

2.2.1 Irradiation experiment

In PIREX, the typical dose rate is 5×10^{-7}dpa s^{-1}. The irradiation temperature, T_{irr}, from RT to 450 °C represents from $0.2T_M$ to $0.36T_M$, where T_M is the melting temperature of Ni. The beam intensity has a two dimensional Gaussian profile (Gavillet, et al. 1985), the beam size is set to about 3×4 mm^2 ($4\sigma_x\times4\sigma_y$) for most experiments. The proton beam was periodically displaced along the gage length using a wobbler. Its amplitude was about 5 mm along specimens. Because of the use of the wobbler the beam is in principle homogeneously distributed along the specimen gage length.

A special specimen holder has been designed (Fig. 2.2.1). The specimen seats in a slot, in which it is free to move a small distance along the Y-axis. In this case, any possible bending can be avoided and cooling of specimens is more efficient as it is directly exposed to the flowing He cooling gas.

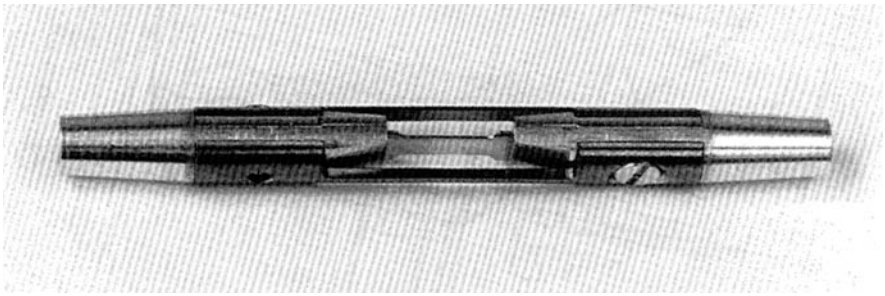

Fig. 2.2.1 PIREX samples holder for supporting two tensile specimens.

Six specimens placed one after the other (Marmy et al. 1990) was irradiated together. A restricted difference of doses for the six specimens can be expected.

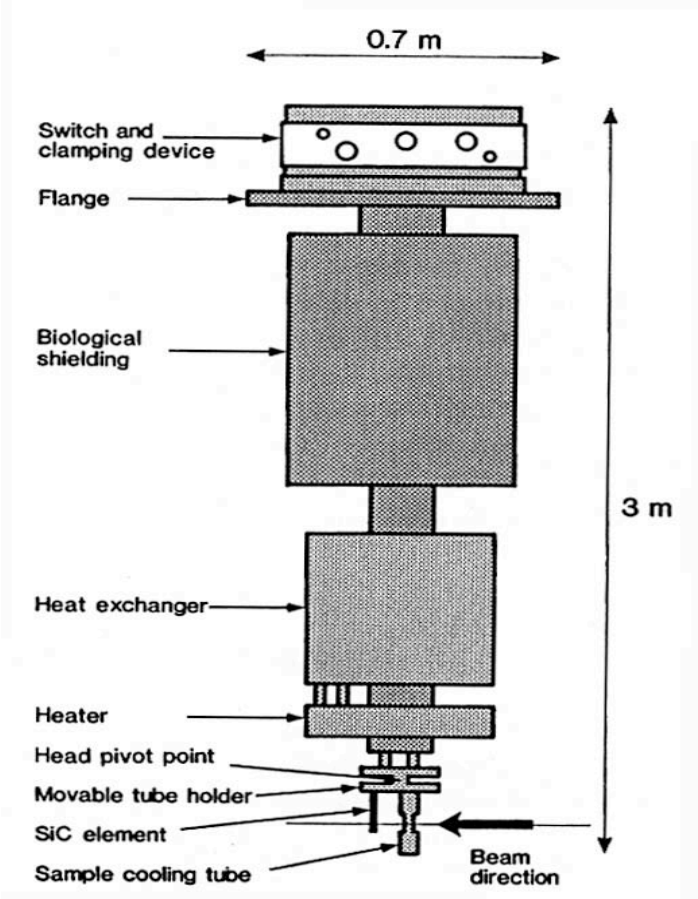

Fig. 2.2.2 Schematic drawing of the PIREX irradiation head.

A large amount of heat, between 2000 and 11000 $W \cdot cm^{-3}$ depending on materials, is deposited in the volume of the irradiated specimen by the proton beam. One of the main problems encountered in using this type of irradiation is the cooling of the specimen. In the PIREX installation, helium gas is used as the cooling medium.

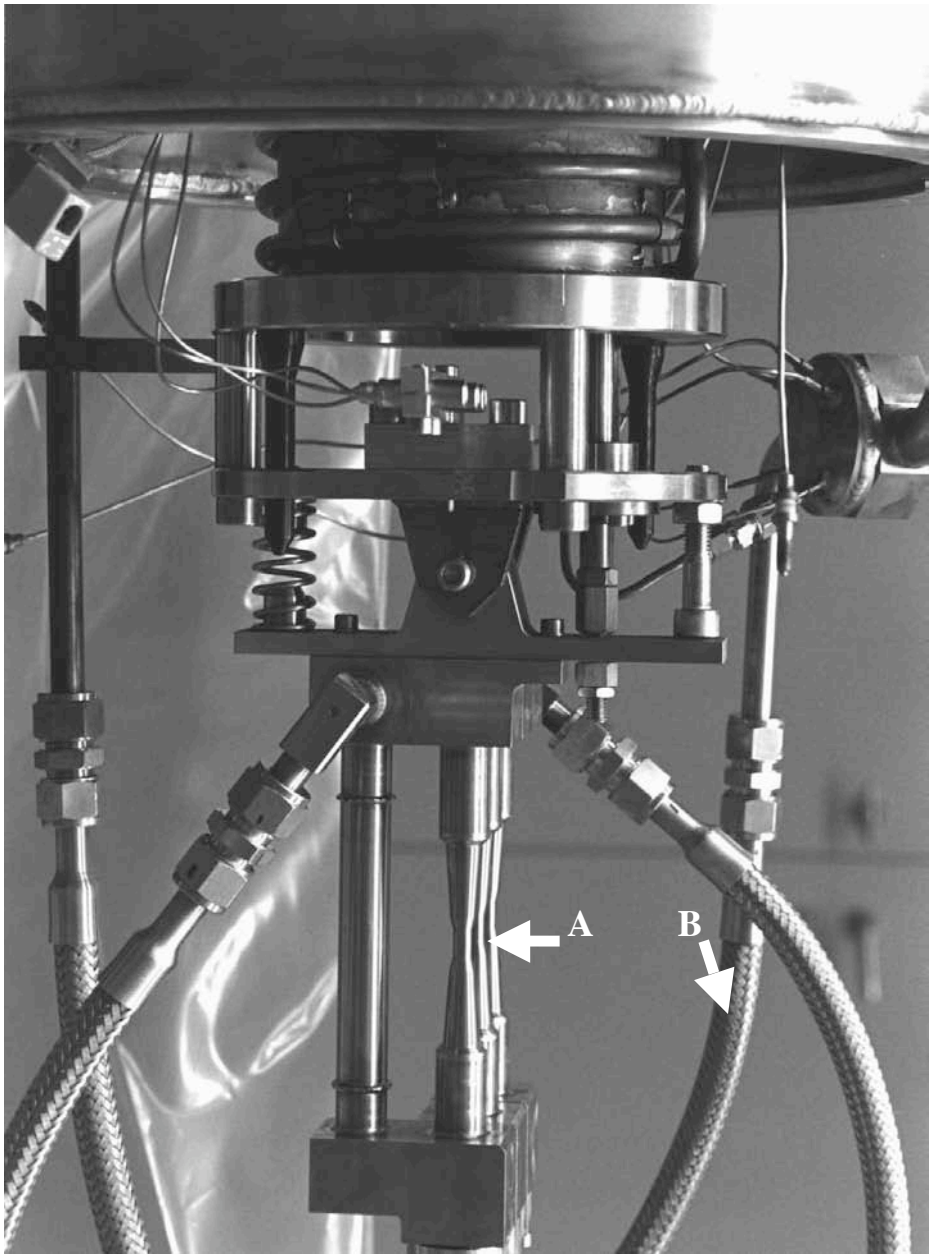

Fig. 2.2.3 The PIREX irradiation head as it seats in the proton beam. A refers to the 3 tubes in which the specimens are mounted. B is the pipe of the helium cooling loop. The proton beam direction is perpendicular to this page.

The general structure of the irradiation head and specimen area is shown in Fig. 2.2.2 and Fig. 2.2.3. Helium gas circulates at pressures of up to 50 bars and its temperature is regulated by a heat exchanger that cools the gas as it exits the specimen region and a 9 kW electrical heater that preheats the input gas. A series of thermo-couples measured the specimen temperature and that of the gas input and output

The helium temperature increases only a few degrees as it extracts the heat deposited in the specimen. Helium is cooled by going through a heat exchanger cooled by liquid nitrogen. In this way the irradiation temperature can be controlled to any desired value between RT and 450 °C with a fluctuation ±20 °C.

In fact the measured temperature of the samples is usually maintained at temperatures about 20 to 50 °C higher than the desired temperature, depending on the proton beam current and size. The proton beam currents used for the irradiation experiment was between 1-15 μA.

Dosimetry

The dose of irradiated samples was measured by a method developed by Gavillet (1991), based on the measurement of the amount of gamma ray emission stemming from radioisotopes formed in the irradiated specimen by transmutation. The isotopes include, ^{56}Co, ^{57}Co, ^{58}Co, ^{60}Co, ^{54}Mn, ^{46}Sc, ^{22}Na, ^{51}Cr for Ni and ^{58}Co, ^{51}Cr, ^{46}Sc, ^{65}Zn for Cu. The corresponding damage is calculated in dpa by using a modified NRT formula:

$$D = \frac{0.8\delta_{ED}\rho_m}{2T_d\rho_a\sigma_i\lambda_i e^{-\lambda_i \Delta t}} \frac{A_{im}}{P_t} \quad \text{[dpa]}$$

D: Displacement dose [dpa]
δ_{ED}: Damage energy cross section [eV cm^2]
E_d: Threshold energy [eV]
σ_i: Isotope production cross section [cm^2]
λ_i: Decay constant of the isotope i [s^{-1}]
Δt: Decay time (time between the end of irradiation and the γ-counting) [s]
ρ_m: Specimens mass density [g cm^{-3}]
ρ_a: Specimens atomic density [cm^{-3}]
A_{im}: Measured activity of the isotope after a cooling time Δt [Bq]
A_i: Activity of isotope after the end of irradiation [Bq]
P_t: Weight of the target [g]

The threshold energy for Ni, Cu, Al and Ag are 40, 25, 16 and 20 eV, respectively.

The variation of dose measurement between the different regions from the gauge of tensile samples is within 20%.

2.3 Mechanical testing

2.3.1 Tensile Test

Tensile tests were performed on a small machine (as illustrated in Fig. 2.3.1), which was specially designed for small load tensile tests (Gavillet 1986) and refurbished in this work. All tests were performed at a crosshead speed of 0.3 μm·s^{-1}, corresponding to a shear strain rate of about 5×10^{-5} s^{-1}. The accuracy of displacement measurement is 1 μm. The machine is equipped with a load cell of 250 N. The load sensitivity is 0.001 N, which is enough to measure the stress drop during the relaxation tests. The machine was instrumented and computer controlled. The tensile test set up is schematically shown in Fig. 2.3.2. The analogue signal of load is converted to the digital signal as input to a computer, by using a DAQ-i218 PCMCIA AD converter card with 1 kHz frequency and 24 bits sampling. The load measurement was calibrated as shown in fig. 2.3.3.

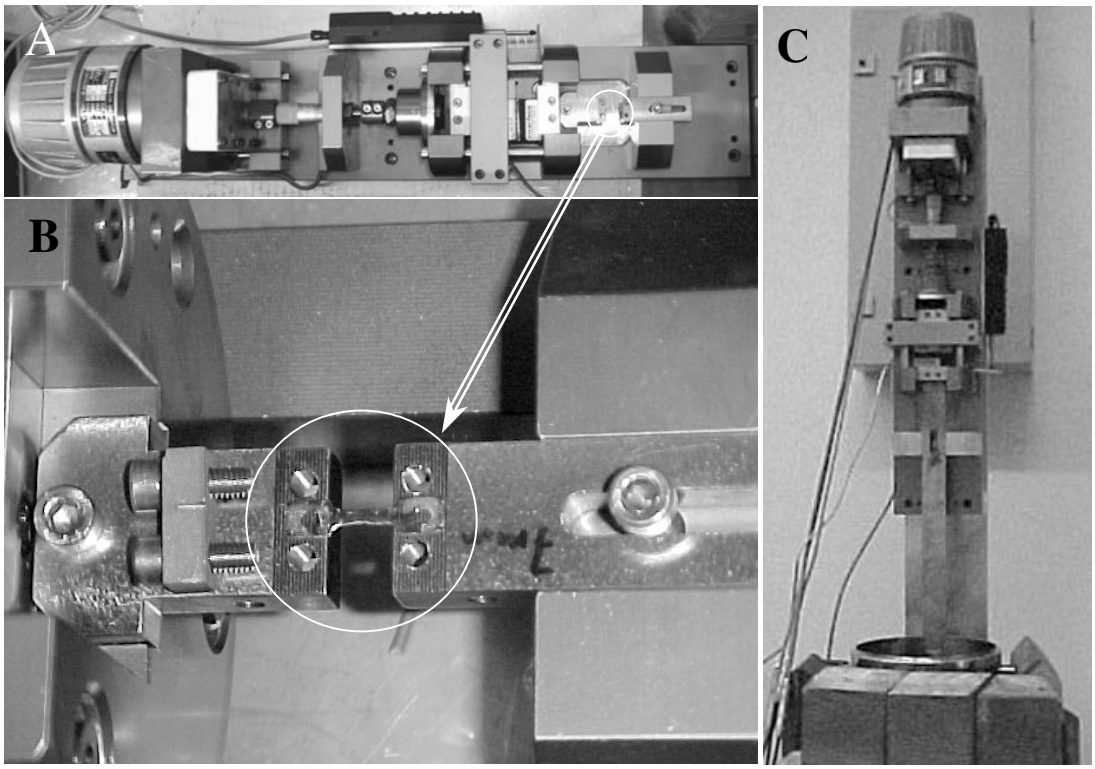

Fig. 2.3.1 The small tensile machine. A) the machine is set up horizontally in a lead shielding against environmental irradiation. B) The tensile test grips with a mounted tensile test specimen (white circle). C) The machine is set up vertically with specially designed elongated grips in the case of testing at low temperature. The specimen is then immersed in a mixture of liquid nitrogen and alcohol.

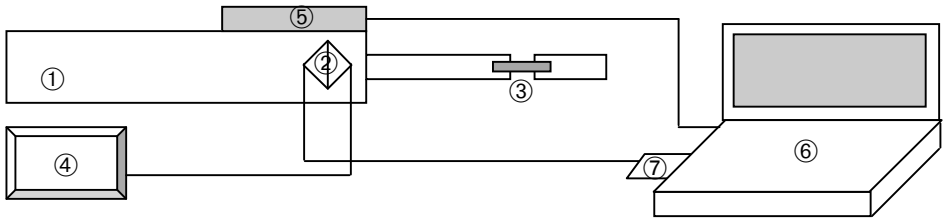

Fig. 2.3.2 The schematic tensile tests. ① the small tensile machine; ② load cell; ③ specimen; ④ electrical power supply for load cell, with a 10 V DC output; ⑤ displacement meter; ⑥ computer for collecting data; ⑦ AD convert card for reading load applied on specimen.

This correlation can be described by following equation:

$$\text{Load (N)} = \text{Current (mV)} \times 17.04 - 0.11$$

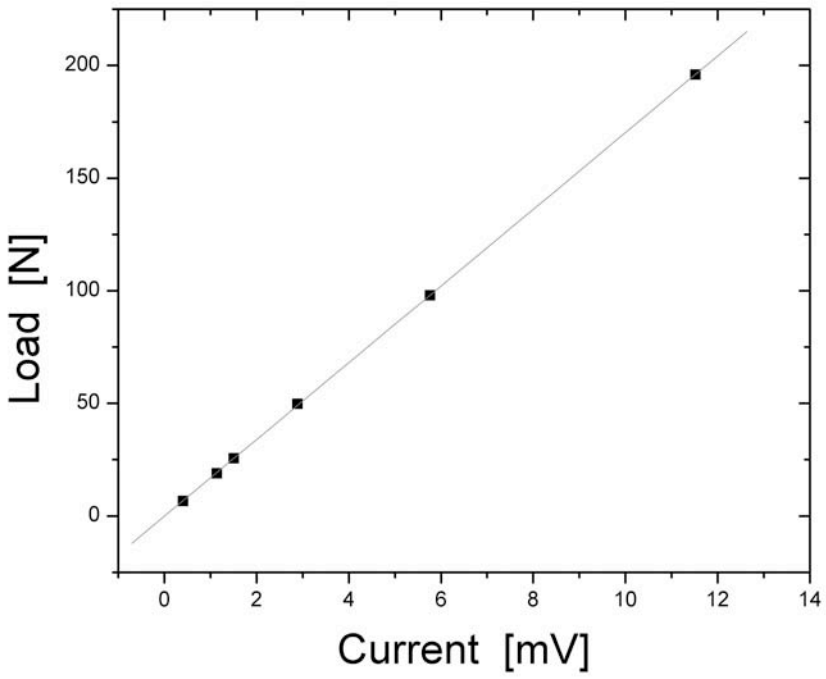

Fig 2.3.3 correlation between the load and current output from load cell.

The elongation of specimens is measured by using a TESA displacement meter with minimum readable distance of 0.5 μm. A program 'stress-strain' developed in LabView software was used to collect testing time, load, and displacement and calculate shear stress. The front panel of the stress-strain programme is shown in Fig 2.3.4 and Fig. 2.3.5 shows the diagramme of function of this programme.

Tensile tests were carried out at RT and at low temperatures using the mixture of alcohol and liquid nitrogen or in pure liquid nitrogen. At low temperatures, during measurement the variation can be controlled within ±5 °C/h.

Tensile tests were performed on irradiated specimens as well as unirradiated specimens. The shear strain (γ) and shear stress (τ) are given by (Honeycombe 1985):

$$1 \quad \gamma = \frac{1}{\sin\chi_0}\left(\sqrt{(1+\varepsilon)^2 - (\sin\lambda_0)^2} - \cos\lambda_0\right)$$

$$2 \quad \tau = \frac{L}{A_0}\frac{1}{1+\varepsilon}\sin\chi_0\sqrt{(1+\varepsilon)^2 - (\sin\lambda_0)^2}$$

$$3 \quad \varepsilon = \frac{\Delta l}{l_0}$$

λ : the initial angle between the tensile axis [011] and the slip direction <110>
χ : the angle between the tensile axis [011] and slip plane {111}
L_0 and A_0 : the initial gauge length and cross section, respectively
L : load
Δl : the elongation of specimens
ε : the engineering strain

The resolved yield shear stress was taken to be the stress at a plastic strain of 0.2%. Its change due to irradiation was evaluated as a function of dose and irradiation or testing temperature.

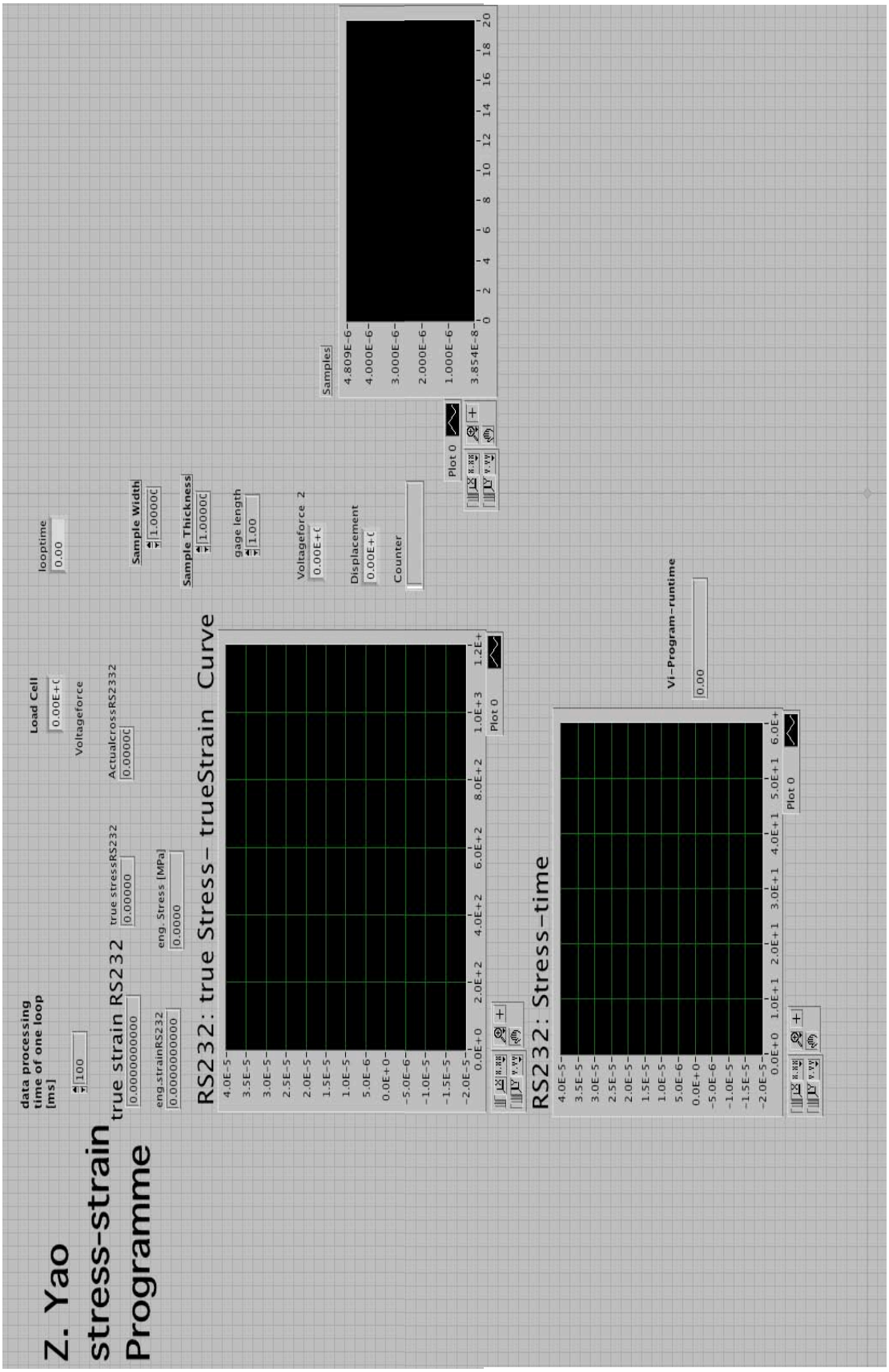

Fig. 2.3.4 The graphical user interface of program 'stress-strain' developed in LabView©.

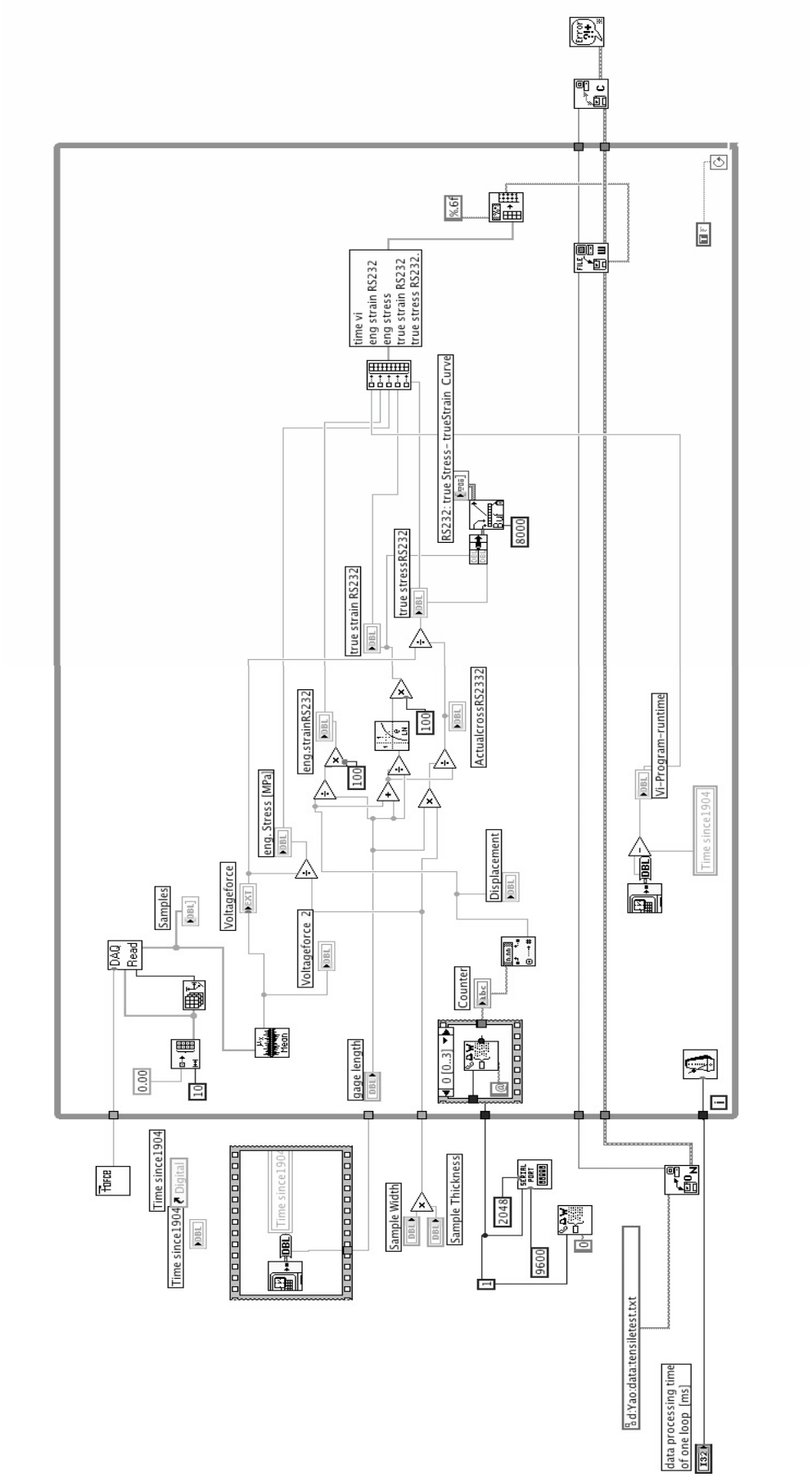

Fig. 2.3.5 The schematical diagram of program 'stress-strain' developed in LabView©.

2.3.2 Stress relaxation experiments

Definition of activation volume and activation energy

When a dislocation moves through a crystal lattice a force is exerted upon it by the obstacles. The force can be separated into two components: a long range force, F_m, which varies slowly with the position of the dislocation on the slip plane, such as the force due to large obstacles and dislocations on the slip planes, and a localized force, F*, which acts over a few atomic distances, such as the force due to the forest dislocations and small irradiation induced defects. The flow stress can then be given by the following relation:

$$\tau = \tau_\mu + \tau^* \qquad (2.3.2.1)$$

When both types of obstacles are present in a lattice, τ_μ can be looked as the athermal component, and τ^* as the thermal component.

The thermal energy that has to be supplied for a dislocation to overcome a given thermal obstacle when an effective stress τ^* is available has been determined by Schoeck (1965) and Gibbs (1965). When a linear segment of dislocation of length *l* moves reversibly and isothermally from its equilibrium position to the saddle-point of an obstacle, the minimum Gibbs free energy that has to be supplied is given by

$$\Delta G = \Delta g - \tau^* lb\Delta x \qquad (2.3.2.2)$$

Δx is the activation distance and Δg represents the change in free energy associated with the localized atomic displacements during activation, and *b* is the Burgers vector. The term ($\tau^* lb\Delta x$) is the work done by the external stress τ^* during the unpinning process.

Differentiating Equation (2.3.2.2) with respect to the effective stress:

$$\left(\frac{\partial \Delta G}{\partial \tau^*}\right)_T = \left(\frac{\partial \Delta g}{\partial \tau^*}\right)_T - lb\Delta x - \tau^* bl\left(\frac{\partial \Delta x}{\partial \tau^*}\right)_T - \tau^* b\Delta x\left(\frac{\partial l}{\partial \tau^*}\right)_T \qquad (2.3.2.3)$$

$(d\Delta G)=0$ for all values of stress and temperature (Gibbs 1964): therefore from equation (2.3.2.2)

$$\left(\frac{\partial \Delta g}{\partial \tau^*}\right)_T = \tau^* lb\left(\frac{\partial \Delta x}{\partial \tau^*}\right)_T + \tau^* b\Delta x\left(\frac{\partial l}{\partial \tau^*}\right) \qquad (2.3.2.4)$$

Thus, from equations (2.3.2.3) and (2.3.2.4)

$$\left(\frac{\partial \Delta G}{\partial \tau^*}\right)_T = -bl\Delta x = -V^* \qquad (2.3.2.5)$$

If it is assumed that $\left(\frac{\partial \tau_\mu}{\partial \tau}\right)_T = 0$, differentiating equation (2.3.2.2) with respect to the applied stress:

$$\left(\frac{\partial \Delta G}{\partial \tau}\right)_T = -bl\Delta x = -V \qquad (2.3.2.6)$$

Here V is defined as the **thermal activation volume**.

The plastic strain rate satisfies the Arrhenius equation: (Christian and Masters 1964)

$$\dot{\varepsilon} = \dot{\varepsilon}_0 \exp\left(-\frac{\Delta G}{\kappa T}\right) \qquad (2.3.2.7)$$

where $\dot{\varepsilon}_0$ is the temperature-independent frequency and entropy factor. From equations (2.3.2.6) and (2.3.2.7), V can be related to experimentally accessible relations between $\dot{\varepsilon}$ and τ as

$$V = kT\left(\frac{\partial \ln \frac{\dot{\varepsilon}}{\dot{\varepsilon}_0}}{\partial \tau}\right)_T = kT\left(\frac{\partial \ln \dot{\varepsilon}}{\partial \sigma}\right)_T \frac{1}{\cos\theta\cos\phi}$$

$$\approx kT\left(\frac{\Delta \ln \dot{\varepsilon}}{\Delta \sigma}\right)_T \frac{1}{\cos\theta\cos\phi} \qquad (2.3.2.8)$$

where $\cos\theta\cos\phi$ is the Schmid Factor, σ is the applied true stress. Therefore V can be estimated by changing the strain rate and measuring the resulting stress increment. For this purpose stress relaxation test or strain rate jump tests are used.

From equations (2.3.2.6) and (2.3.2.7), **thermal activation energy** can be obtained by

$$\Delta G = \int_{\tau_p}^{\tau} V d\tau = \int_{\tau_p}^{\tau_m} V d\tau + \int_{\tau_m}^{\tau} V d\tau = \delta G + \int_{\tau_m}^{\tau} V d\tau \qquad (2.3.2.9)$$

$$\Delta G = kT \ln\left(\frac{\dot{\varepsilon}_0}{\dot{\varepsilon}}\right) = \alpha kT \qquad (2.3.2.10)$$

where τ_p and τ_m are the Peierls effective stress at 0 K and the largest measured stress, respectively. Thus, δG corresponds to the high stress and low temperature contribution to ΔG that is not directly measured. According to equation (2.3.2.10), the activation energy must return to zero at 0 K, then by measuring V at different temperatures δG can be obtained.

Experimental measurement of activation volume

A number of stress relaxation tests have been performed by interrupting the tensile tests to get the correlation between activation volume and shear stress or strain, as shown in the sketch of stress-time curve in fig 2.3.6. The interval between two relaxation tests is random but shorter in the beginning of the tensile curve in order to get the information from the rapid changes of microstructures in this part, especially for irradiated specimens. Except for the softening region, successive relaxation series tests are used to obtain the correction for the effective activation volume. In the yield region the irradiated specimens with no or a small hardening, the first stress level cannot be reached again, without producing additional deformation. Therefore, only single relaxation was performed in this case. In successive relaxations normally three relaxation tests are performed. The duration for each relaxation is about 30 seconds.

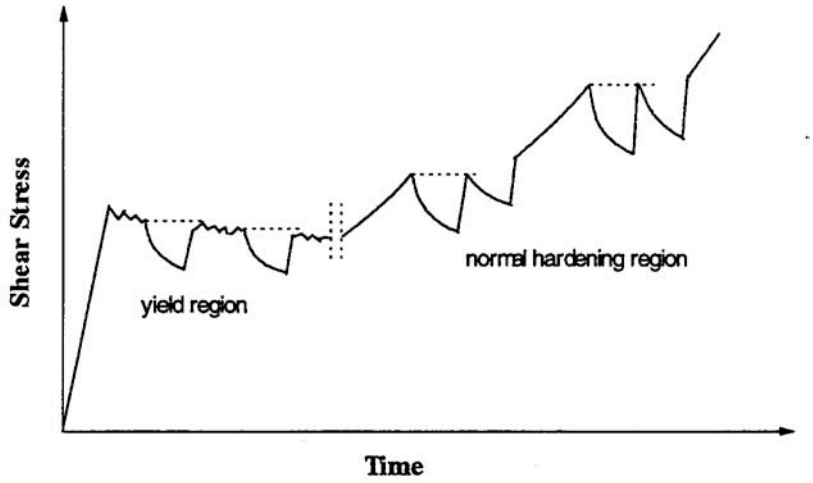

Fig. 2.3.6 Illustration of the stress relaxation method with a constant relaxation time.

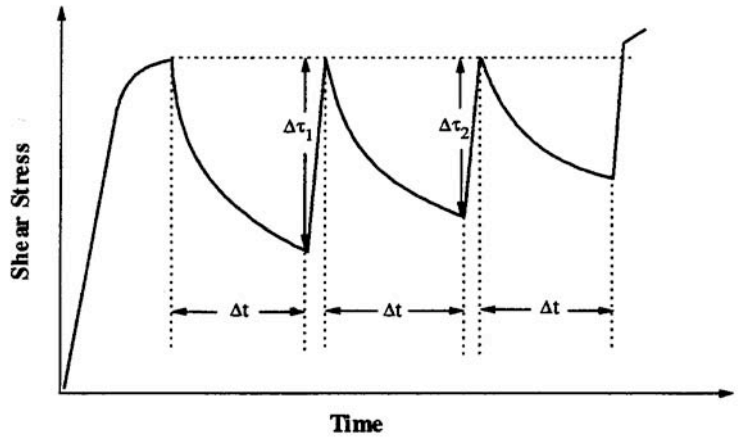

Fig. 2.3.7 Illustration of the repeated stress relaxation method with a constant relaxation time.

The apparent activation volume is given by fitting the following relation (Guiu and Pratt 1964):

$$\Delta\tau = kT/V_a \ln(1+t/c) \qquad (2.3.2.11)$$

where c is an adjustable time constant, t the relaxation time, T the test temperature, k the Boltzmann constant and $\Delta\tau$ the stress drop. A correction to account for the strain hardening is introduced by performing successive relaxations in order to obtain the effective activation volume V_{eff} (Kubin 1974). This correction in our experiments amounts to about 10 %.

The apparent activation volume has to be corrected to obtain the effective activation volume, V_e.

$$V_e = V_a - V_h \qquad (2.3.2.12)_e$$

Where V_h is the correction term, which can be obtained by performing successive relaxations. As shown in Fig. 2.3.7, using the fixed relaxation time method, V_e can be calculated by

$$V_h = \frac{kT}{\sum_{i=1}^{n-1}\Delta\tau_i} \ln\left[\frac{\exp\left(-\Delta\tau_n/\lambda\right)-1}{\exp\left(-\Delta\tau_1/\lambda\right)-1}\right] \qquad (2.3.2.13)$$

Where $\Delta\tau_1$ and $\Delta\tau_n$ are the first and the *n*th stress drop, respectively.

The stress relaxation technique provides unique results about the values of the effective activation volume, which is characteristic of the deformation mechanism. This parameter describes the dependence of dislocation velocity on stress. In that sense, this technique is superior to strain rate jump tests or single relaxation tests in which microstructural changes occur.

2.3.3 The evolution of slip bands during deformation

A digital video camera was used for optical observation of the surface topography evolution in the tensile samples. The camera can run at 25 frames per second. If the specimens are polished well, the accumulated morphology of the slip bands can be recorded. The image was magnified by a magnifying glass (5×) and video camera zoom (10×) configured as Fig. 2.3.8.

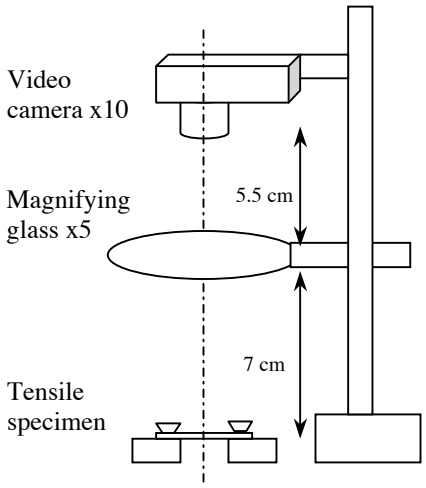

Fig. 2.3.8 The optical observation of the surface evolution during tensile test.

2.4 Electron microscopy

Transmission Electron Microscopy (TEM) was used for investigation of the radiation induced lattice defects microstructure. Special techniques are introduced here for irradiated TEM samples.

2.4.1 TEM disc preparation

As Ni is magnetic and irradiated samples are very active, the volume of the TEM Ni specimen was reduced by the following technique. First, a ring with 3mm outer diameter and 1mm inner diameter was cut. High precision punchers were used to cut the discs of TEM rough samples, as shown in Fig. 2.4.1. The composite TEM specimens are constructed by the above-mentioned stainless steel ring outside and 1mm disc of research materials inside. The ring coheres with inner disc by special glue which was mixed with hardner and solidified. Once the glue becomes hard, the composite specimen is reduced to about 100 μm thin by mechanical polishing. The composite specimens were then jet-electro-polished at -20 °C in a solution of 12% H_2SO_4 in methanol and examined in the electron microscope.

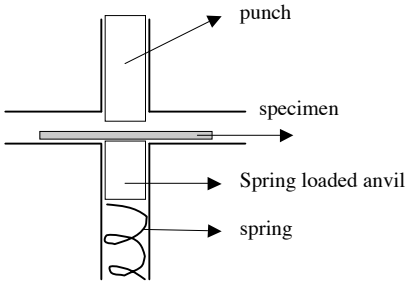

Fig. 2.4.1 Schematical view of a high precision puncher.

In-stu TEM observations of deformation were also performed In Cu single crystal specimens. The in-situ straining specimens strictly follow the geometry and size designed to fit the Gatan Straining Sample Holder (Cold Stage). Three different stages for preparing the specimen were used as shown in fig 2.4.2. The in-situ TEM specimens should employ a lacomit painting technique. First, the in-situ TEM specimens are cut into such the shape shown in Fig. 2.4.2a. The middle width after cutting the neck shape is kept at a value larger than 1 mm. The second step is to paint with lacomit around the neck region, then to dig a rectangular hole on the lacomit surface as illustrated in Fig. 2.4.2b. The ring in Fig. 2.4.2c is used for covering the rectangular hole, in order to prevent the light from the neck of samples. Fig. 2.4.2d shows a well-polished in-situ sample.

The tensile axis of in-situ specimens is $<0\bar{3}1>$ while the electron beam relatively to the in-situ tensile test specimen is <013>. This eases the observation of dislocations gliding on the {111} plane with the lowest Schmid factor, which is, by design, the most inclined plane. In addition, this orientation allows an operating diffraction vector **g**={200}, which is the most favorable in the observation of stacking fault tetrahedra. Being perpendicular to the traction axis, which is also the tilt axis, the diffraction condition can be adjusted for dark field weak beam observations, from **g**(4**g**) to **g**(6**g**). While the electron beam being close to <001> SFTs image is close to a square. In-situ tests have been performed at temperatures below room temperature (183 K) in order to improve spatial resolution during weak beam observations in thicker regions. In effect, inelastic scattering being reduced relatively to room temperature, contrasts from thicker regions remain sharp. Thicker regions allow, on the one hand, increasing the probability to observe dislocation-defects interaction events and, on the second hand, reducing the influence from TEM sample free surfaces on such events.

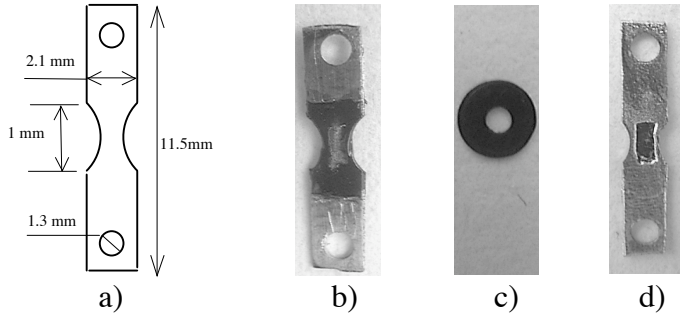

Fig. 2.4.2 The in-situ straining sample preparation. a) the geometry of in-situ sample, b) a sample with lacomit painting, and c) the ring which is put above the samples during electro-polishing. d) a well-polished sample after removing the lacomit painting.

2.4.2 TEM Sample Holders

In TEM experiments, three types of sample holders are used. In the following figures, normal double tilt stage, cold straining stage and heating stage are illustrated, respectively.

1. Normal Double Tilt Stage from JEOL.

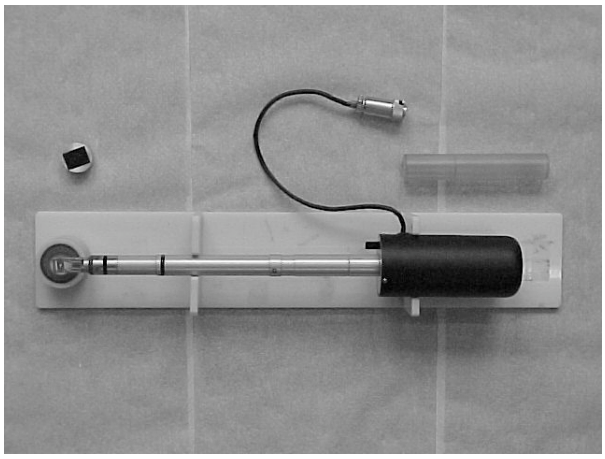

Fig. 2.4.3 The double tilt stage from JEOL company.

The normal double tilt stage shown in fig. 2.4.3 is commonly used for TEM observation. The purposes of specimen tilting are: 1) tilting specimens by fractions of a degree to obtain optimum contrast, 2) for taking stereo pairs, 3) tilting specimens by relatively large angles to perform particular experiments in contrast, e.g. the determination of Burgers vectors of dislocations.

2. Single Tilt Straining Cooling Stage

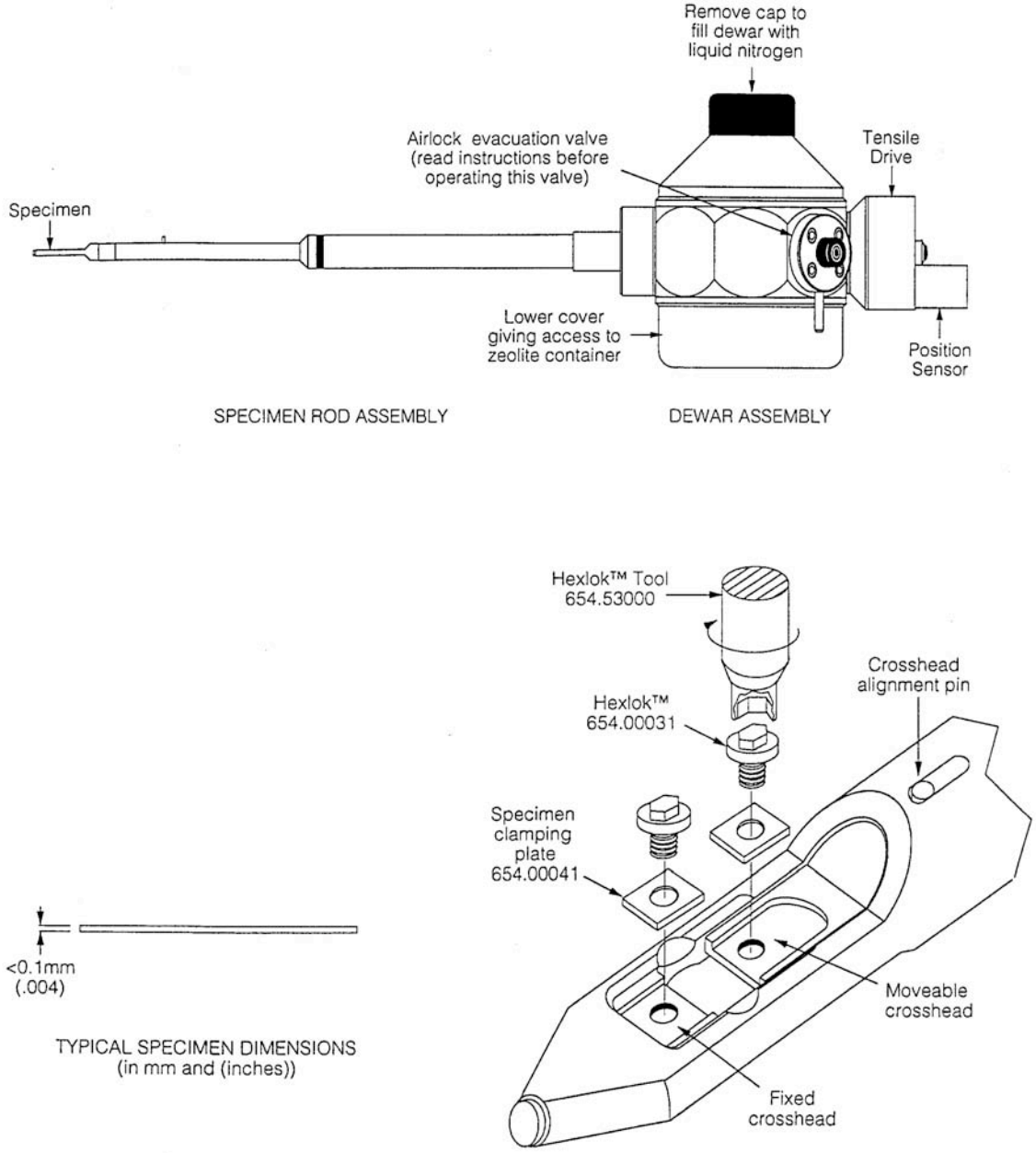

Fig. 2.4.4 The Model 671 single tilt strain cooling holder from Gatan company and its tip.

The straining cooling stage shown in fig. 2.4.4 is used in the transmission electron microscope to observe dislocation activity, such as multiplication or glide, in thin foils, with a controlled low strain rate. The temperature control of this stage allows cooling the specimen to liquid nitrogen temperature. At such a low temperature specimen contamination can be reduced and the observation for a relatively thick region is improved by the reduction in inelastic electron contribution in the image. Before the holder is used at low temperatures, it has to be degassed at 373 K and pumped in order to achieve a vacuum thermal insulation of the holder.

3. Double Tilt Heating Stage

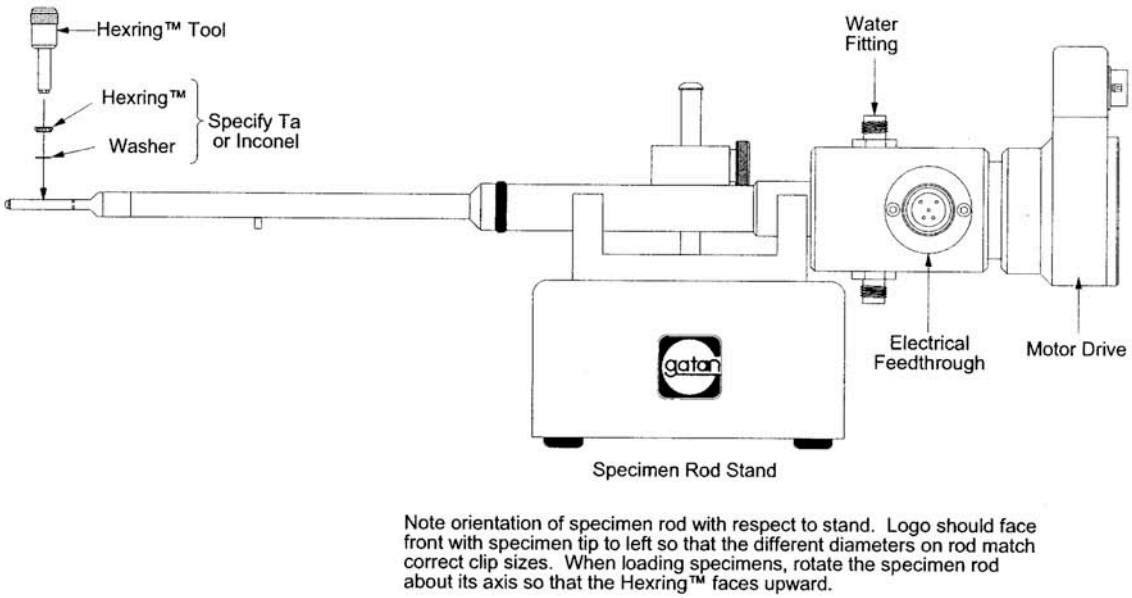

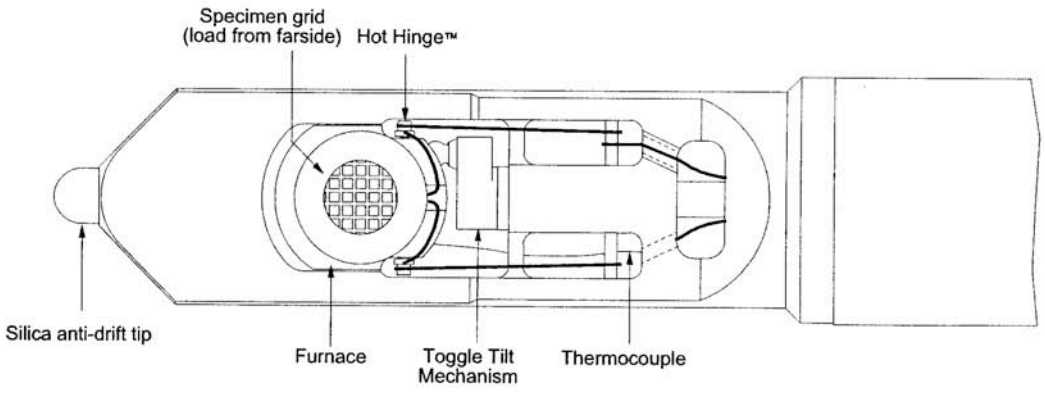

Fig. 2.4.5 The Model 652 double tilt heating holder on stand, from Gatan company, and its tip.

Commonly heating stages have been used for two general types of experiments. The first type of experiments concerns the changes in structure of the specimen during heating, in as stepwise manner, through isochronal anneals. In the type of experiments picture are acquired on a slow scan CCD camera or on classical photographic negatives. The second type of experiments involves the continuous observation of a given high temperature reaction, e.g. surface oxidation or a disordering process. In this framework, the double tilt heating stage shown in fig. 2.4.5 was used in the first class, for the annealing of stacking fault tetrahedra and dislocation loops..

2.4.3 TEM observation methods

The contrast of small clusters is very dependent on the contrast mechanism used to get their density and nature.

Phase contrast

The specimen introduces local changes in the phase of the electron wave. The local phase variations are converted into amplitude variations produced by the microscope over which the operator has control by defocusing. Voids in out of focus conditions are imaged by this mechanism.

Z contrast

The scattering of the electron wave by atoms is proportional to their atomic mass, or Z, the atomic number. The higher the atomic number the higher the intensity at large scattering angles. Allowing incoherent imaging of materials, it represents a new approach to high-resolution electron microscopy. The Z-contrast high-resolution transmission electron microscopy technique provides directly interpretable images - maps of scattering power of the specimen. There are no phases in a Z-contrast incoherent image, therefore, no phase problem for structure determination. Location of atom column positions in an image is simplified. In addition, the resolution is higher than in a coherent image, the information is more highly localized, the intensity of atom columns directly reflects their mean square atomic number (Z), and there are no contrast reversals with crystal thickness. It is also the only means to achieve spectroscopy from individual atomic columns. The Z-contrast image is obtained by scanning an electron probe of atomic dimensions across the specimen and collecting electrons scattered to high angles. The resolution of the technique is determined by the size of the electron probe.

Diffraction contrast

In the microscope, the objective aperture allows forming an image by selecting only the transmitted beam (bright field mode) or one of the diffracted beams (dark field mode). The resulting contrast is named diffraction contrast. Structural defects in the specimen are imaged by the diffraction contrast arising from their elastic strain fields. The defect elastic strain field causes a local change in the diffraction condition; for example, the local bending of plane causes the amplitude changes of the diffraction beam used to form the image. This is the most common contrast mechanism used in radiation damage studies to image irradiated induced defects. The image feature depends on the diffraction condition chosen.

2.4.3.1 Two-beam condition

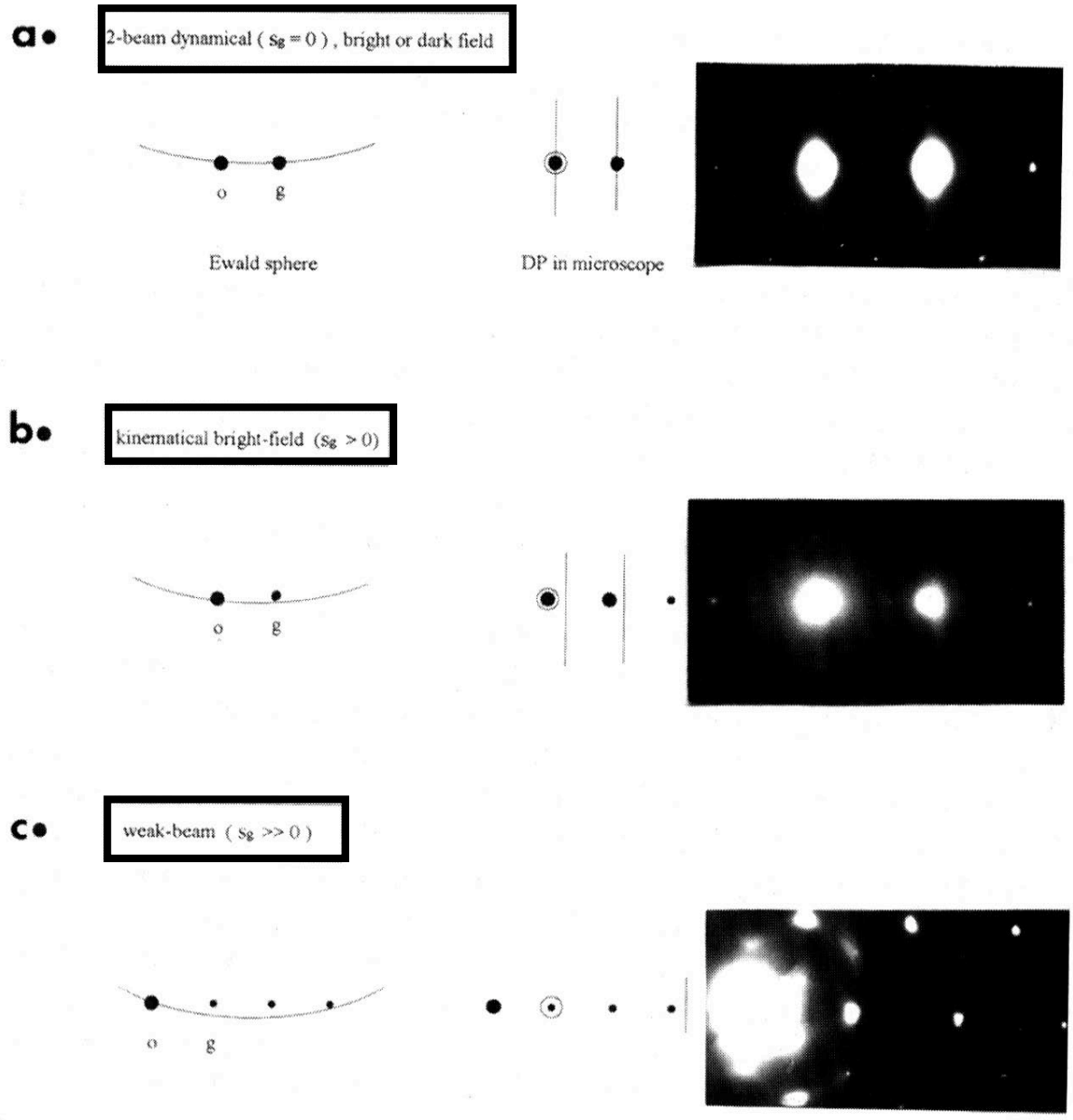

Fig 2.4.6 Three different diffraction conditions used in diffraction-contrast imaging: a) two-beam dynamical, b) two beam kinematical, c) weak-beam. In each case the Ewald sphere is sketched on the left-hand side, a schematic diffraction pattern (DP) showing the position of the relevant Kikuchi lines is shown at the centre, and an actual diffraction pattern is shown on the right-hand side. The curvature of the Ewald sphere is exaggerated for clarity. The open circle represents the objective aperture. (Jenkins 1994)

Under two-beam dynamical condition, the foil is tilted so that one set of crystalline planes (h k l) is at or close to Bragg condition as illustrated in figure 2.4.6.

The Ewald sphere construction is displayed in figure 2.4.7 (left). The reciprocal lattice vector **g** corresponds to the diffraction vector from (0 0 0) to (h k l) spot in the diffraction pattern. The radius of Ewald sphere k ($k=1/\lambda$) is much bigger than **g**.

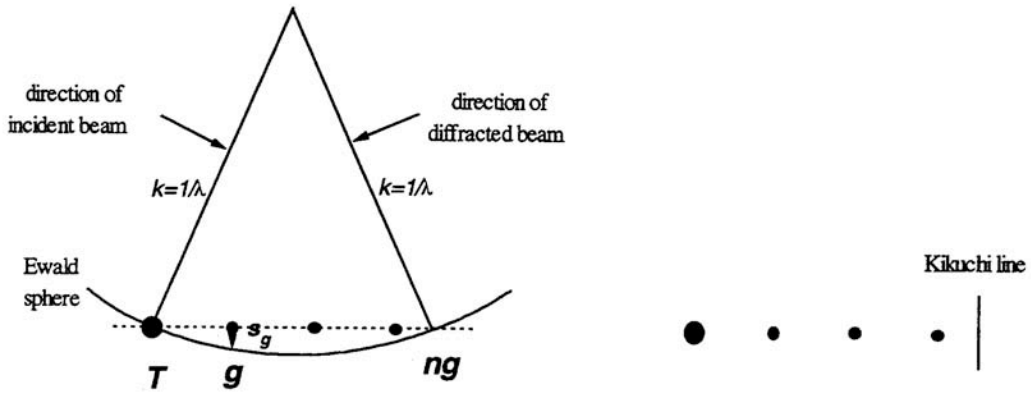

Figure 2.4.7 Sketches showing the diffraction condition **g**(n**g**). The position of Ewald sphere shown on the left side and the position of the relevant Kikuchi line shown on the right side.

The 'deviation parameter', s_g, is the distance from diffraction vector **g** point to the Ewald sphere in the direction of the normal of the foil. In case of the dynamical two beam condition, s_g is very small. The diffraction condition is specified by 'ng(mg)', where ng is the beam selected to form the image and mg is the beam intersecting with the Ewald sphere. The deviation parameter is then given geometrically by $s_g = n(n-m)g^2 \lambda/2$. In radiation damage studies conditions range typically from g(3g) to g(6g).

The effective extinction distance is given by (Hirsch et al 1977)

$$\xi_g^{eff} = \frac{\xi_g}{\sqrt{1+\omega^2}} = \frac{\xi_g}{\sqrt{1+\xi_g^2 \bullet s_g^2}} \qquad (2.4.3.1)$$

Under strong two-beam conditions, there is a strong dynamical interaction between the two beams, or beating. Note that the distance amplitude of this beating is the extinction distance, as illustrated in Fig. 2.4.8. When this condition is used for small dislocation loops located close to the foil surfaces they show so-called black-white contrasts, consisting of pairs of black and white lobes. This technique allows deducing the Burgers vector and habit planes of the loops.

Usually this condition is used for small dislocation loops located close to the foil surfaces show so-called black-white contrast, consisting of pairs of black and white lobes. It is able to deduce the Burgers vector and habit planes of the loops.

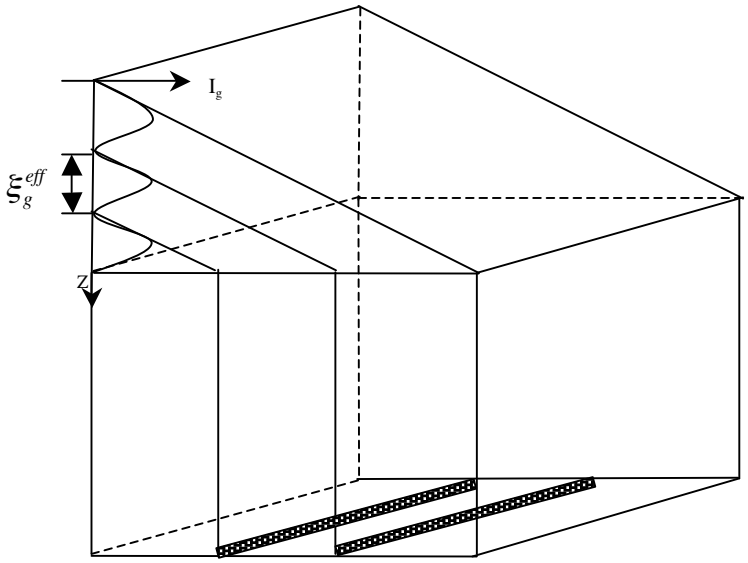

Fig. 2.4.8 The thickness fringes formed in diffraction contrast by a wedged specimen, where Z is the thickness of specimen and I_g is the intensity of the transmitted beam.

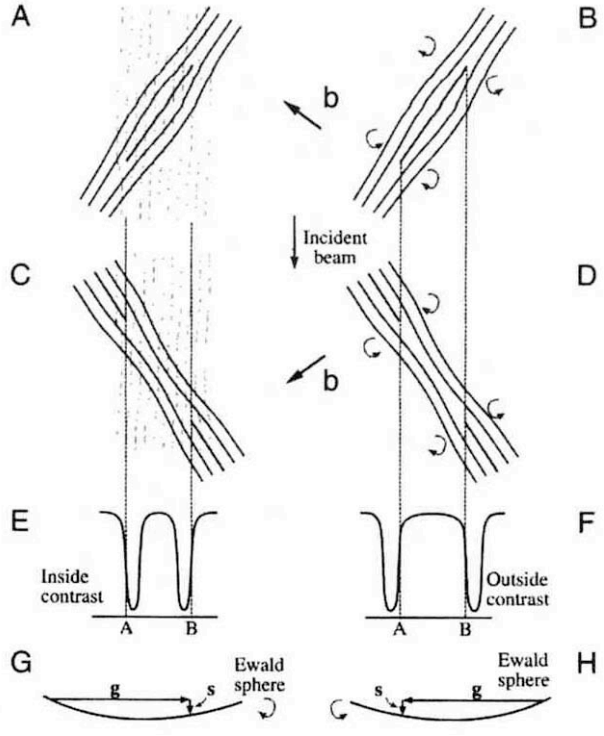

Fig 2.4.9 The inside-outside technique for loop nature determination. An inclined interstitial loop with diffraction planes (faint lines) is shown in (A) with the sense of plane rotations indicated in (B). The same is shown for a oppositely-inclined vacancy loop in (C) and (D). The position of image contrast with respect to the projection of the loop dislocations is shown in (E) and (F) for the diffraction conditions shown in (G) and (H), respectively. (Jenkins and Kirk 2001)

For example, an inside-outside technique is used to determine the loop nature, under the two beam dynamical condition. In Fig. 2.4.9, the inside-outside technique is schematically described, (H) the sign of g is reversed, but in both (G) and (H) s_g is positive. Inside contrast results when clockwise rotation of the diffracting planes bring them into the Bragg condition (G). outside contrast results for the counterclockwise case (H). Everything is reversed if the loops are positively inclined with respect to the electron beam, or if s_g is negative. Formally, inside contrast arises when $(g \bullet b)s_g < 0$, outside contrast when $(g \bullet b)s_g > 0$.

2.4.3.2 Kinematical bright field

Bright field kinematical conditions are used when it is desired to avoid the dynamical contrast effects seen in strong two-beam images. The typical bright field conditions are shown in fig. 2.4.6b. A two beam condition is set up with a small positive deviation parameter, i.e. $s_g > 0$. The magnitude of deviation parameter is not specified explicitly. We tilt the foil just sufficiently away from the Bragg condition that the image loses most of its dynamical features. This condition has been used to image small loops.

2.4.3.3 Weak-beam dark-field conditions

The weak beam technique was discovered and developed since 1969 (Cockayne et al.).

The deviation parameter is larger than in the case of two-beam dynamic conditions. The foil should be tilted sufficiently away from the Bragg condition, so that the image gets rid of its dynamical features. The contrast in the weak beam image arises from regions of large lattice strain close to the cores of defects.

In the past (Cockayne et al. 1969), it was recommended to use the following diffraction conditions in order to ensure a single image per dislocation, thus avoiding spurious multiple images. They were established for Cu and for a microscope operated at 100 kV and corresponded to a diffraction condition g(3g). It was said that the weak beam imaging should be carried out with the dimensionless deviation parameter $\omega = s_g\xi_g$ equal or larger than 5, and that | sg | should be 2×10^{-1} nm^{-} larger. For Ni, at 200 kV, this results in a ξ_g^{eff} of about 5 nm. At present the diffraction condition is controlled by g(ng). Interestingly, for Ni, the conditions of Cockayne are fulfilled for a diffraction condition g(6g), which is indeed the one that was usually applied in this work. The effective extinction distance as a function of the diffraction condition in Ni, Cu, Al, Ag and Au is given in the appendix tables.

Fig. 2.4.10 shows a crystalline foil containing an edge dislocation. The lattice columns close to the dislocation core can be considered as consisting of three parts. The central parts contains the dislocation, the two side parts are perfect structure. The lattice planes in the central part are inclined with respect to their orientation of perfect parts. Thus somewhere closer to the dislocation core the local deviation parameter s_g is much smaller than in perfect part, as shown in Fig 2.4.10. The beam intensity scattering originates from this region, producing a bright peak on a dark background in the dark field weak beam image. This implies that the dislocation image position is shifted relatively to the real image position as depicted in Fig. 2.4.10. It should be noted that the width of the dislocation contrast in a diffraction contrast image is about $\frac{1}{3}\xi_g^{eff}$ (Cockayne 1969).

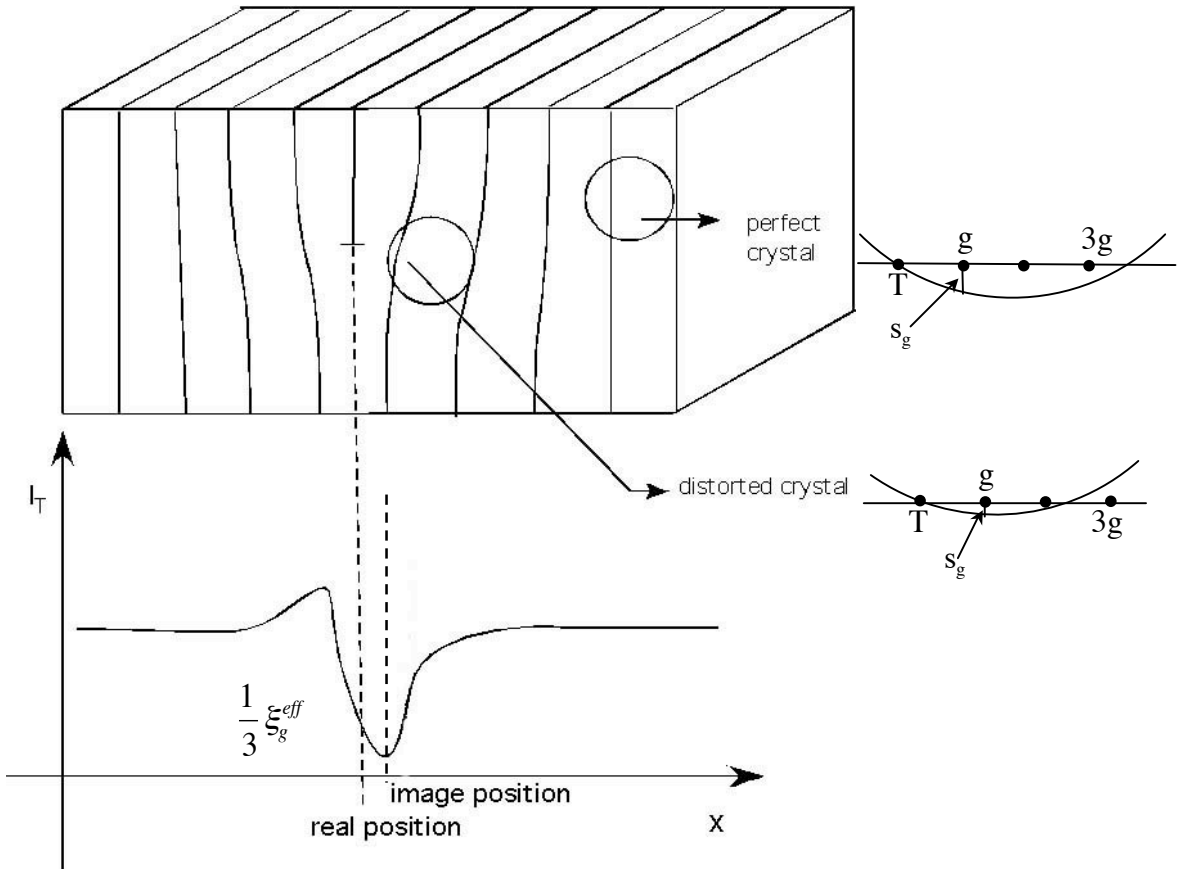

Fig. 2.4.10 Schematically representation of the formation of the image of a dislocation in diffraction contrast. Top: crystal containing an edge dislocation. Left: Sketches showing the diffraction condition far from the defect and close to it. Bottom: Intensity profile across the resulting bright field image.

2.4.4 Determination the thickness of specimen

The measurement of foil thickness is important in electron microscopy due to the need for quantitative measurements of the density of irradiation induced defects and dislocation density.

2.4.4.1 stereo pair method

Nankivell (1962) has investigated this technique and has shown that it is workable under certain conditions. The stereo pair images are achieved by using the different tilt condition with the same diffraction condition in microscope, shown in fig. 2.4.11. The tilt angle α should be around 15 degree. The thickness can be calculate as following:

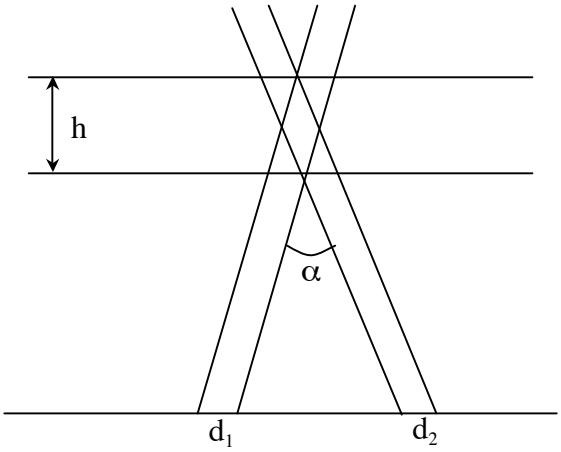

Fig. 2.4.11 The stereo pairs method to measure the foil thickness.

Goniometer angle: from (x_1, y_1) to (x_2, y_2);
Angle $\gamma_1 = x_2 - x_1$, $\gamma_2 = y_2 - y_1$.
$\alpha = \text{acos}(\cos\gamma_1 \bullet \cos\gamma_2)$
parallax: $d = d_1 + d_2$,
Thickness: $h = d/2\sin(\alpha/2)$

2.4.4.2 Extinction contour method

This method consists in counting the number of thickness fringes from the edge of the crystal to the location of measurement. In bright-field micrographs white fringes occurs at $h/\xi_g^{eff} = 0, 1, 2$, etc., while dark fringes occur at $h/\xi_g^{eff} = 1/2, 3/2, 5/2$, etc., where h is the thickness of the foil and ξ_g^{eff} is the effective extinction distance given in 2.4.3.3. The ξ_g^{eff} values are enclosed in appendix.

2.4.5 Observation techniques

In the present work the irradiation induced microstructure is observed in TEM in areas relatively thin (20-70 nm) in order to be suitable for dark field weak beam observations. The defect density and size distribution are obtained by measuring the visible defects under a DF-WB image condition **g**(5**g**) or higher, with g={200}.

1) Characterization of irradiation induced defects

The observation condition is a critical factor in order to obtain quantitative information on the irradiation induced defects. There is in the open literature a large discrepancy on the density and type of defects is observed. One of most likely reason for that is the difference in the TEM techniques and specimen preparation deployed for these studies.

As explained earlier the nature of an SFT can be generally described as four triangular {111} faulted planes bounded by six stair-rod partial dislocations. This specific three dimensional structure cannot be simply and unambiguously determined from a single classical bright field or dark field picture. In principle, a stereoscopic observation can be applied to characterize the SFT (Saldin et al. 1979). This would allow, with the appropriate viewing equipment such green-red glasses or a stereoscope, observing the SFT in three dimensions. However, it is in practice difficult to make such an observation for SFTs of size about 2 to 3 nm, which is just above the limit of

resolution of the TEM in diffraction contrast.

Starting with the nature of the SFT, Kojima et al. (1989) reported a method which relies on the asymmetry of stacking fault contrast under a dark-field condition, for a deviation parameter $|\mathbf{s}_g| \neq 0$. It allows determining the vacancy or interstitial nature of the SFT. The typical recommended condition is **g**(2**g**) along a <112> direction using a {220} reflection. Kojima et al. (1989) found that the SFT in various materials (Au, Cu, Ag, Ni) produced by electron, neutron and ion irradiation are invariably vacancy in nature.

Coene et al. (1985) proposed to use high resolution TEM (HRTEM) imaging for determining the nature of the SFT. The experimental images are formed with the foil normal orientated along a <110> direction. The SFT is visible as a V-shaped open triangle bounded by two {111} planes. From the comparison between the intensity profile of the bright dots in the experimental image and in the simulated one, the SFT was determined to be of vacancy type (Coene et al. 1985).

It should be noted that these methods from Kojima et al. (1989) and Coene et al. (1985) are only used to determine whether an SFT is of vacancy type or interstitial type. One of the important parameters in the identification of the detailed SFT configuration, which plays a crucial role in the interaction with a mobile dislocation (Wirth et al. 2003, Osetsky et al. 2004). In effect, it appears that perfect SFTs are strong/weak obstacles to dislocations, while truncated ones are weak/strong obstacles. In order to identify the SFT morphology, the following methods are used.

One of the techniques is based on a principle similar to that of a stereoscopic observation. It consists in obtaining two images along two different and well characterized viewing directions. In the case of the SFT the most fruitful directions are <110> and <001>.

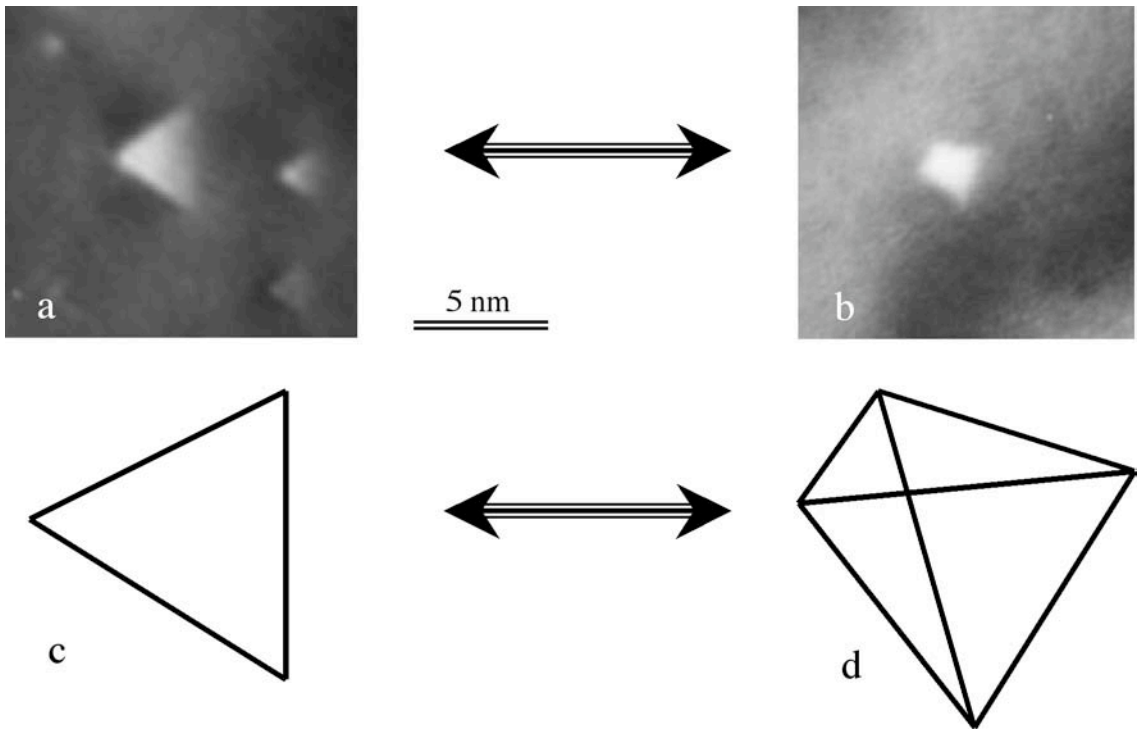

Figure 2.4.12 TEM DFWB, **g**(5**g**), **g** = {200}, micrographs in irradiated Ni under two different orientations showing SFT contrasts. (a) Close to a zone axis <011>, (c) wire frame of a tetrahedron oriented in the same way. (b) Close to a zone axis <001>, and (d) wire frame of a tetrahedron oriented in the same way.

Effectively, it appears that if the tetrahedron is viewed along a <011> orientation, the structure projected on the viewing screen has a triangular shape. In Fig. 2.4.12a, the DFWB contrast of SFTs exhibit a triangular shape, similarly to that of c), which is the wire frame of an SFT projected in the same direction. The triangular contrast shows a strong contrast apex and decreasing to a weak contrast along the base. Beside the apex, dark wings, or a 'moustache', appear with an intensity lower than the one of the background. These SFT contrast features are well reproduced in the simulation of the TEM image of an SFT produced by molecular dynamics simulation (Schäublin et al. 2000b). Among the four SFTs present in Fig. 2.4.12, the largest SFT, of about 4nm in size, clearly shows these typical characters, while for those SFTs smaller than 2 nm in size, various contrasts are present, as the one in the right corner of the image with only a triangular profile. The contrast of the SFT is also variable with its depth in the TEM sample, and can appear as a triangle darker than the background as examplified in Fig. 2.4.13 in the white circle. In addition, it should be noted that TEM image simulations showed that it may be difficult to distinguish SFTs smaller than 2 nm from dislocation loops of the same size (Schäublin et al. 2000b).

When the tetrahedron is viewed along a <001> direction, the structure projected on the viewing screen has a trapezoidal shape. In Fig. 2.4.12b, the experimental SFT contrast shows such a a similar trapezoid shape with the same orientation. The intensity of the trapezoidal contrast is relatively homogenous. Therefore this condition $\mathbf{g}(5\mathbf{g})$, $\mathbf{g} = \{200\}$, close to a zone axis <001> has been regarded as an efficient complementary condition to the classical condition $\mathbf{g}(5\mathbf{g})$, $\mathbf{g} = \{200\}$, close to a zone axis <011>.

The condition $\mathbf{g}(5\mathbf{g})$, $\mathbf{g} = \{200\}$, close to a zone axis <011>, is the most commonly used for identifying and counting the SFTs. Note that Dai (1995) reported that 10% of the irradiation induced defects in Au consists in triangular dislocation loops. It should be noted however that the formation energy of such loops, presenting sharp corners, is higher than loops with more rounded shapes. Based on this simple argument it seems that these loops are rather unlikely, relatively to hexagonal loops for example, or even SFTs. Later in the text a more detailed discussion is presented on the energetic of possible clusters.

Although the identification of the morphology of the SFTs by combining the two abovementioned conditions becomes possible, defects smaller than 2 nm remain difficult to identify for their contrast strongly depends on various parameters, such as sample thickness, depth and diffraction condition (Schäublin et al. 2000b). In the condition $\mathbf{g}(5\mathbf{g})$, $\mathbf{g} = \{200\}$, close to a zone axis <011>, those defects will probably show a round shape, similar to that of small dislocation loops. This can be one of the reasons for the discrepancy in the measured ratio of SFT to dislocation loops reported in the open literature.

2) DFWB condition: deviation parameter

Other studies (Satoh 1989, Proennecke 1992) also showed how the visibility of small defects varies with imaging conditions. They concluded that the visibility increases while the image size decreases when the deviation parameter is increased. Dai (1995) made observations under a condition $\mathbf{g}(4\mathbf{g})$, $\mathbf{g} = \{200\}$, close to a zone axis <011>, and also under a condition $\mathbf{g}(6\mathbf{g})$, $\mathbf{g} = \{200\}$. He concluded from this comparison that about 7% of the defects observed under $\mathbf{g}(4\mathbf{g})$ were not seen under $\mathbf{g}(6\mathbf{g})$. It seemed that the difference would be larger if more imaging conditions were used. It appears that in the literature not a single data is corrected for the fact that part of the defects is invisible depending on the imaging condition.

3) Foil thickness

The foil thickness is commonly estimated by counting the number of thickness fringes from the edge of the thin foil. While the accuracy of this method is at most 10 %, it is extensively used because of its simplicity. In addition, Zinkle (1987) compared the visible defects size distribution in regions about 30 nm thick and in regions over 100 nm in thickness. He found that the mean size was larger in the thicker regions and concluded that most of the defects smaller than 2 nm are not visible in thicknesses greater than 100 nm. This implies that the defect density in thick region is under-estimated. Moreover, the defects in the thick region visible in the left of the image in Fig. 2.4.13 start to overlap one another. Therefore, a classical density measurement misses invisible defects and overlapping ones. It implies that the thickness of the region selected for the quantification of defects should be smaller than 100 nm.

On the other hand, if the region is too thin, say below 20 nm, a large fraction of the glissile loops might escape to the foil surface due to image forces. This can induce an artificial decrease in the loop density measurement. In addition, in the thin regions the thickness contrast oscillation is stronger than in thicker regions (Schäublin et al. 2000c). This implies that in these very thin regions the contrast of irradiation induced defects will vary more strongly with their depth in the foil and will have a higher probability to present an absent contrast, thus further decreasing the measured apparent defect density. Schäublin et al. (2000c) proposed a technique consisting in applying a moderate beam convergence of about 5 mrad in order to smooth thickness oscillations in weak beam convergence. It proved successful in the measurement of dislocation dissociation distances in Ni3Al (Meng et al. 1997). This allows for a homogeneous contrast of the nanodefects throughout the thickness of the foil, for thicknesses comprised between about 40 and 80 nm.

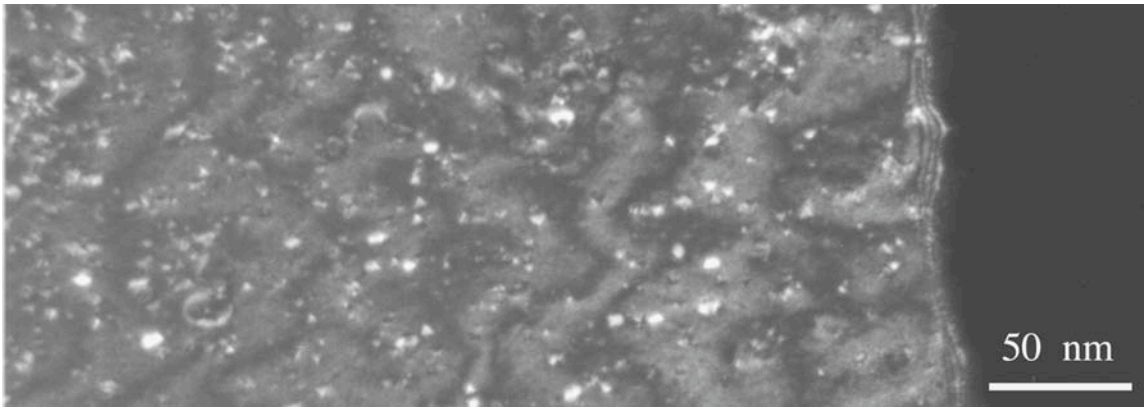

Fig. 2.4.13 The defect micrograph under DFWB, **g**(5**g**), **g** = {200}, close to a zone axis <011> in Ni irradiated at 250 °C to 0.09 dpa.

4) Difference between real size and image size of defects

The relation between image size and real size of defects depends on a number of factors, such as the diffraction condition, foil thickness and the depth of defects in the foil (Schäublin et al. 2000b). In section (3), it was already reported that Zinkel found that the defect mean size is larger in thick region (~100 nm) relatively to the one found in the thin region (~30 nm). The contrast of loops, similarly to SFTs, changes with the depth at which they reside in the thin foil (Schäublin et al. 2000b). It appeared that the dislocation loop image and the SFT image size saturates to about 1 nm

when size is decreased below 1 nm (Schäublin et al. 2000). This relates to the fact that the objective aperture placed in the diffraction plane in order to form a diffraction contrast on the viewing screen limits spatial frequencies. For the usual aperture sizes used in this kind of studies, which are about one third of the length of a usual g such as {200} at 200 kV, this spatial resolution is degraded to about 7 Å in a 200 kV TEM. This represents a degradation of a factor of about 3 relatively to the nominal resolution of the microscope which is 2.3 Å for the JEOL2010.

In this quest of a better understanding of the relationship between the mechanical properties and the microstructure of irradiated materials, and in particular metals, transmission electron microscopy is widely used. The point defects, interstitials, vacancies or impurities, generated by the impinging particles can condense to form three dimensional defects or clusters that eventually may transform in stacking fault tetrahedra (SFT), dislocation loops or cavities. Parameters to determine are the size, or number of point defects constituting the defect, its type and its morphology (loop, SFT, cavity). The difficulty in this kind of studies is the defect size that is generally at the limit of the spatial resolution using diffraction contrast. The resolution limits are explored through image simulations and experimentally through the development of a new objective aperture.

TEM image simulation of dislocation loops in Ni and Al, as typical materials with different atomic masses, are being performed, using the EMS code (Stadelmann 1987). A simple dislocation loop, made of an interstitial platelet placed between <111> planes, is considered. The loop is then relaxed using molecular dynamics with a sample made of 0.5 million atoms. Only one potential (Al) is considered for both materials in order to identify contrast differences resulting only from scattering differences between materials, and not differences in elastic properties. Image simulations are performed for the case of a dark field weak beam diffraction condition of $\mathbf{g}(5\mathbf{g})$, for $\mathbf{g} = \{200\}$, at an acceleration voltage of 200 kV. Fig. 2.4.13 illustrates the fact that TEM image simulations allow reproducing the thickness oscillation of the contrast of a small dislocation loop. In Fig. 2.4.14a the loop appears as a strong black and while contrast while in Fig. 2.4.14b, the loop, for a different thickness, shows a weak coffee bean contrast. The dislocation loop contrast oscillates between these two extremes as thickness, or equivalently depth, is increased.

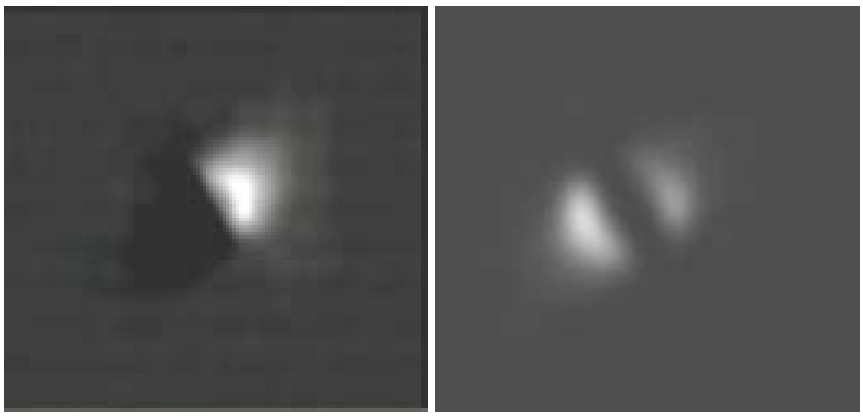

Fig. 2.4.14 The multi slice image simulation of an interstitial loop, in the samples with different thickness. A) Thickness: 10 nm; b) Thickness: 12 nm.

Results indicate that image contrasts increase with increasing size of loops, then reach saturation at a size of about 30 interstitials corresponding to a size of about 2 nm. The loop image contrast in the case of Al is similar to the case of Ni (Figure 5.1.3 left and middle, respectively), although the scattering power is lower (Figure 5.1.3 right).

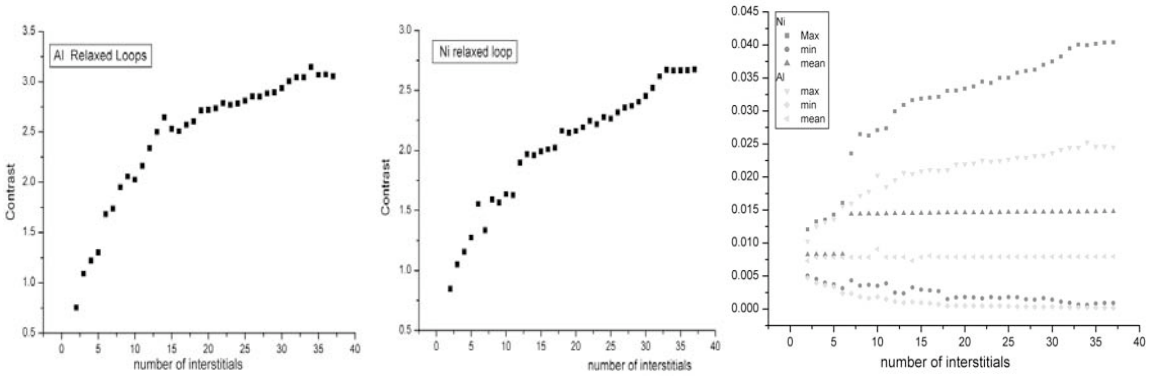

Fig. 2.4.15 Contrast of the simulated TEM image of an interstitial loop as a function of the number of interstitials contained in the loop, in Al (left) and in Ni (middle). Contrast is defined as the ratio of the difference between the maximum and minimum intensity reported to the mean intensity of the image. Right: maximum, minimum and mean intensities of the simulated TEM weak beam image of the interstitial loop as a function of the number of interstitials. Intensities are reported to the incident electron beam intensity, which is 1.0.

A new objective aperture has been developed in order to improve spatial resolution. Following a simulation study, it appeared that a larger directional objective aperture should result in a higher spatial resolution in bright field or dark field imaging, and in particular dark field weak beam imaging. The present aperture provides a resolution of about 6 Å in Cu. The new aperture, rectangular in shape, provides a resolution of about 3 Å. This new aperture was focused ion beam milled in a 15 μm thick Mo foil (Figure 5.1.4 top right) and is applied perpendicular to the operating diffraction vector **g**. The use of the new aperture allows identifying the details of the corners of the SFTs, which appear sharper (Figure 5.1.4 bottom right). The left SFT is in fact not truncated on its left wing, contrary to what the first left image taken with with the smallest aperture seems to indicate. This is also the case in the image with the usual aperture of 40 μm (Figure 5.1.4 bottom right). It should be noted that the overall diffraction contrast is reduced because of the larger aperture. This is clearly visible in the upper right corner of the image. This reduction in contrast is not detrimental to spatial resolution, on the contrary. In addition to improvement of resolution brought by the acceptance of higher spatial frequencies, the larger aperture allows for a higher image intensity implying a reduced exposure time and hence a reduced drift of the image (which degraded resolution with the 30 μm aperture). This new aperture is very promising in the analyses by diffraction contrast imaging of nano-crystalline defects.

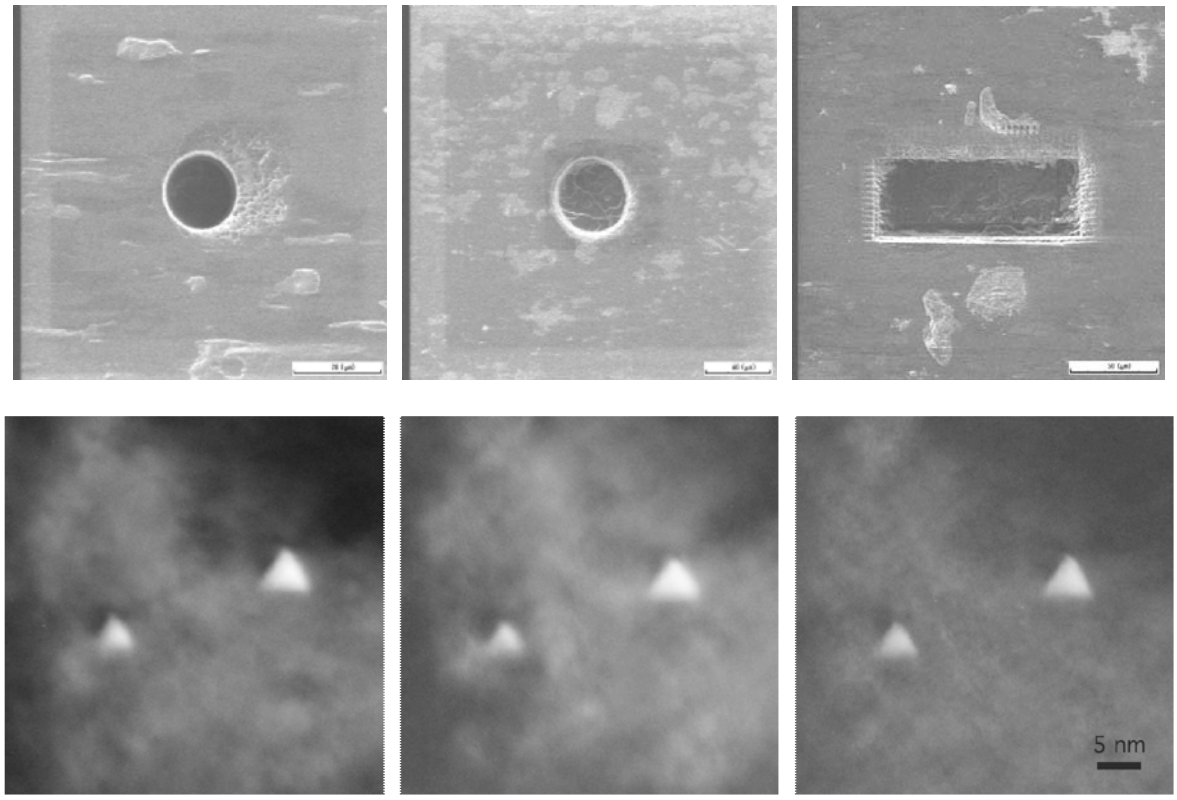

Fig. 2.4.16 SEM images of the apertures cut by FIB in a 15 μm thick Mo foil (ø15, ø40 and 40x100 μm apertures from left to right). Au quenched in water from the melting temperature. TEM dark field weak beam **g**(6**g**), **g** = {200}, at 200 kV, as a function of objective aperture size (ø15, ø40 and 40x100 μm apertures from left to right).

5) Surface oxidation

Pure Ni is generally regarded as a stainless metal in air at room temperature. In fact, in contrast to its appearance, oxidation of pure nickel takes place at a very high rate. The very thin oxide layer is compact and as the oxygen cannot penetrate it the surface keeps a shiny appearance. When performing TEM observations, this thin oxide layer should be seriously considered. Robertson et al. (1991) reported that their TEM specimens were stored in a vacuum system (10^{-3} Pa) after they were electro-polished in order to minimize oxidation. Fig. 2.4.17a shows a TEM specimen with a large quantity of oxide on the surfaces, in comparison to Fig. 2.4.17b showing a TEM specimen free of surface oxide. The oxide particles or flakes reveal their presence by thinly fringed patterns, similar to finger prints.

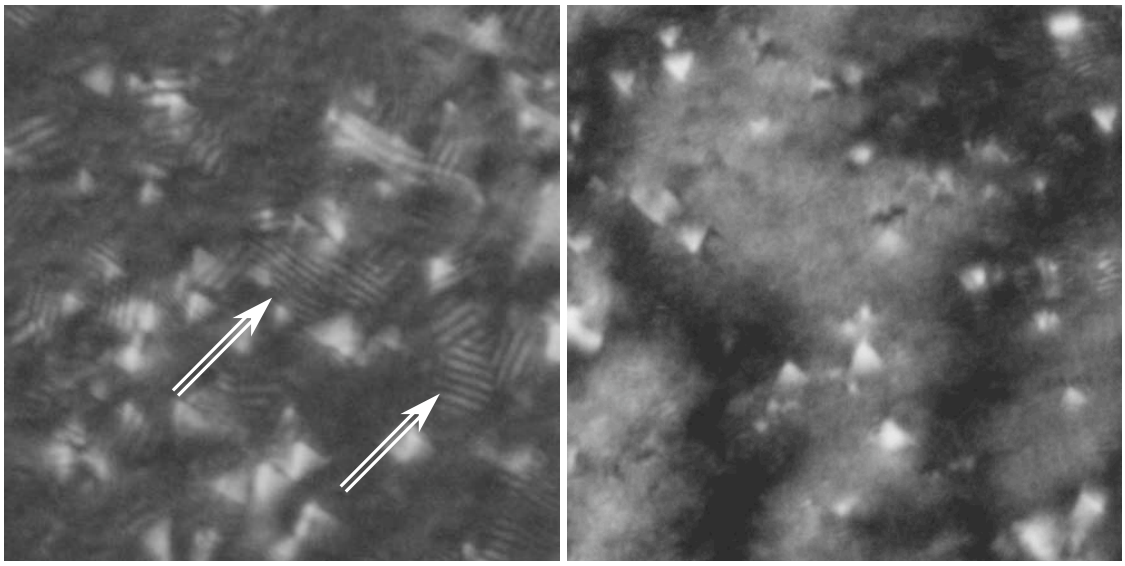

a) b)

Fig. 2.4.17 The DFWB micrographs of (a) a largely oxidised irradiated Ni sample and (b) a clean irradiated Ni sample.

The diffraction contrast of oxide under DFWB conditions is larger than that of small irradiation induced defects. In the present experiments, it was found that the oxide contrast increases with increasing diffraction condition, such as **g**(6**g**) or higher, while the contrast of irradition induced defects decreases. As their size is larger their contrast will cover the one of the defects of interest. It should be noted that in the observation of cavities under brigh field kinematical conditions, the classical technique based on defocusing is used as it gives rise to a Fresnel contrast at the interface between the cavity and the matrix. Unfortunately these oxides present a similar contrast, that is to say a Fresnel contrast. This surface oxidation is thus a very critical factor and will tend to an underestimation of the SFT and dislocation loops density and adds difficulties in the quantification of these nanodefects.

One of the effective methods to reduce the oxide density is to shorten the time between the sample preparation and the TEM observation to minutes or less. Another method is to use a **g**(5**g**) or even a **g**(4**g**) condition, at the expense of spatial resolution, in order to avoid using larger deviation parameters that enhance oxide contrast.

2.4.6 TEM image simulation

TEM image simulation are used to close the gap between the molecular dynamics simulations and the experimental images.

Then a widely adopted approach, to determining the Burgers vectors and habit-planes of loops for example, is to match the experimental images with computer-generated images. Here, the images of the defect clusters are simulated using the multislice method to obtain their weak beam image at 200 kV. On the imaging side the parameters of importance are the objective aperture size, the spherical aberration, the beam convergence, and the defocus spread. Regarding the sample itself, its thickness and the depth of the defect cluster are the main parameters.

The image simulation is performed with EMS code (Stadelmann 1987) that applies the multislice technique (Cowley and Moodie 1957) that is schematically depicted in Fig. 2.4.18. Basically, the sample is cut perpendicular to the electron beam direction in slices 0.2 nm thick. The diffraction condition is inherently chosen by the beam direction that is normal to the slices. Slices have to be periodic because the multislice method is based on Fourier transform. In order to comply with this rule the cut direction is chosen to be a crystallographic direction.

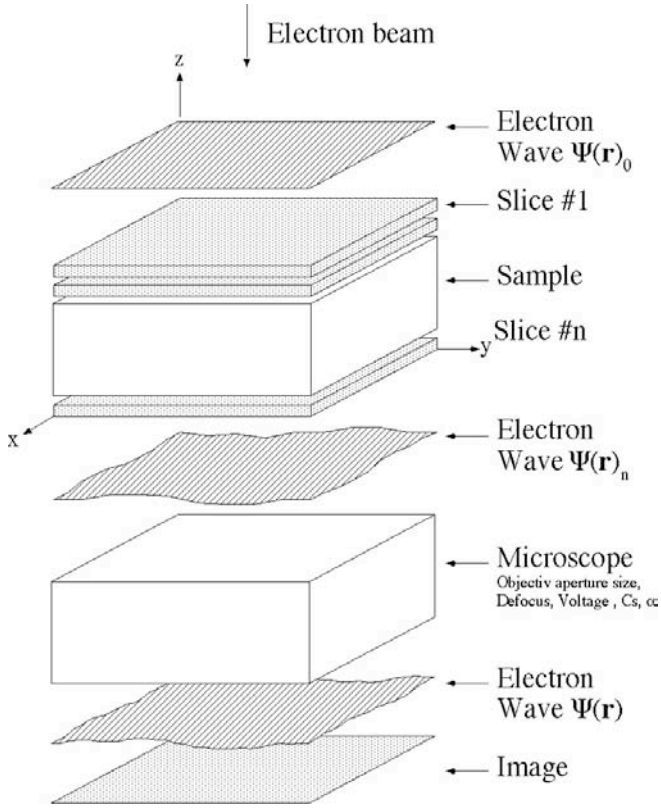

Fig. 2.4.18 The simulation sample is cut for the electron wave transform through slices one by one. $\Psi(r)_j = [\Psi(r)_{j-1} \bullet q_j] \otimes p_j$->j+1; $\Psi(r)_j$: Wave function entering slice j+1, q_j : Function of the transmittance of the slice j, p_j > j+1 : Function of propagation (propagator) from slice j to slice j+1. (Cowley and Moodie1957).

Thus the diffraction condition is selected by the slicing direction. In present work, one cutting slice contains about 2000 atoms. The number of slices depends on the simulation box size.

The weak beam conditions are selected between **g**(3.1**g**) and **g**(6.1**g**) with **g** = {200} to simulate a stacking fault tetrahedron or an interstitial loop in our Ni and an interstitial loop in Al. Here an objective aperture size of 2.5 nm^{-1} is selected. The imaging of the exit wave is achieved by taking into account the convergence, focus and spread of defocus. The diffraction condition with **g**(200) set with a slicing direction perpendicular to <032> (11.3° from <011>), or <015> (11.3 ° from <001>).

Chapter III

Numerical methods

3.1 MD simulation

Computer simulation becomes more and more important in materials science as a complementary tool to experiments. The displacement cascade process occurs in length and time scales of the order of nanometer and picosecond, respectively, and is ideally studied by molecular dynamics (MD) simulation. It should be noted again that there is at present no direct experimental information on the structure and dynamics energetic displacement cascades, that last less than 20 ps in volumes smaller than thousands cubic nanometers. Thank to the development of computer technology, simulation box length and time scales can reach now reasonable sizes to simulate the time evolution of the cascade to its complete cool down and to avoid self annealing effects due to periodic boundary conditions.

Molecular dynamics consists of the study of the evolution in time of an N-body system. It is based on a deterministic interpretation of nature where the behavior of a system can be computed if we know the initial conditions and forces of interaction.

The methodology consists of identifying or constructing a model for the interaction of the particles in the system, computing the trajectories of those particles and finally analyzing those trajectories to obtain observables.

Although in principle a very simple method to implement its foundations reside on:
–classical mechanics
–classical nonlinear dynamics
–kinetic theory
–statistical mechanics
–sampling theory
–conservation principles
–solid state physics
as we will see in the description of the method.

Newton's second law relates the motion of a particle to the force acting on it:

$$F_i = m\ddot{r}_i \qquad (3.1.1)$$

where m is the mass of the molecule. The acceleration of the particle is given by:

$$\ddot{r}_i = \frac{d^2 r_i}{dt^2} \qquad (3.1.2)$$

where $\mathbf{r}_i$ is a vector that locates the position of the particle with respect to the laboratory coordinates. If we have N molecules, then Newton's second law represents 3N second-order, ordinary differential equations of motion.

If we have an isolated system, the total energy of the system will be conserved, that is the sum of the potential energy and kinetic energy will be constant. In that case we identify the total energy with the Hamiltonian of that system with the form:

$$H = \sum_{i=1}^{N} \frac{P_i^2}{2m_i} + U(r_i), \qquad \text{for i=1,….,N} \qquad (3.1.3)$$

where r_i and p_i are the coordinates and momentum, respectively, N is the number of atoms, m_i is the mass of ith particle. The potential energy *U* comes from molecular interactions. Deriving this equation we can obtain the equation of motion for N particles in an isolated system and we will find that:

$$\dot{p}_k = \frac{\partial H}{\partial r_k}, \quad \dot{r}_k = \frac{\partial H}{\partial p_k} \qquad \text{for k=1,….,f} \qquad (3.1.4)$$

which are the Hamilton's equations of motion, equivalent to Newton's second law:

$$F_i = m\ddot{r}_i = \frac{-\partial H}{\partial r_i} = \frac{-\partial U}{\partial r_i} \qquad (3.1.5)$$

The Hamiltonian above is only valid for an isolated system. If the system was not isolated, then the Hamiltonian will still be conserved, however additional terms will appear and the value of the Hamiltonian will not be equivalent to the total energy of the system. *H* will be conserved but not *E* in a non-isolated system.

As stated at the beginning, the goal of molecular dynamics is to obtain the trajectories of a set of N molecules interacting through a potential function *U* by solving the above equations of motion. In an isolated system the derivative of the potential with respect to atom positions will give the force of that particle. Given a value of the force, the new position of that particle can be obtained from Newton's second law. The key component is the interatomic potential since it will define the properties of our system. Before going into details about how the equations of motion are integrated or how we can extract macroscopic properties from particle trajectories, we will review some of the basic interatomic potential functions used in the literature, and what they represent, since they will define our model system.

Interatomic potentials

An interatomic potential $U(\mathbf{r}^N)$ can be approximated to the sum over two-body to N-body contributions of the form:

$$U(r^N) = \sum_i U_1(r_i) + \sum_{i<j} U_2(r_i, r_j) + \sum_{i<j<k} U_3\left(r_i, r_j, r_k\right) + \ldots \qquad (3.1.6)$$

where the first term represent external forces, and the rest are interactions between molecules. The most important is the second term: the pair potential. This pair potential depends only on the separation between two molecules, r_{ij}.

Lennard-Jones (1931) introduced a model for a soft-sphere pair potential of the form:

$$U_2(r_{ij}) = k\varepsilon\left[\left(\frac{\sigma}{r_{ij}}\right)^n - \left(\frac{\sigma}{r_{ij}}\right)^m\right] \qquad (3.1.7)$$

where he introduced a short-range, repulsive force and a longer range attractive force. The short range force prevents the system from collapsing and the long range attractive interaction maintains the structure bonded. The range and strength of the forces depend on the values of n and m. The main choices are m = 6 and n = 12. The value of m = 6 comes from London's theory for dispersion but there is no justification for the value of n = 12.

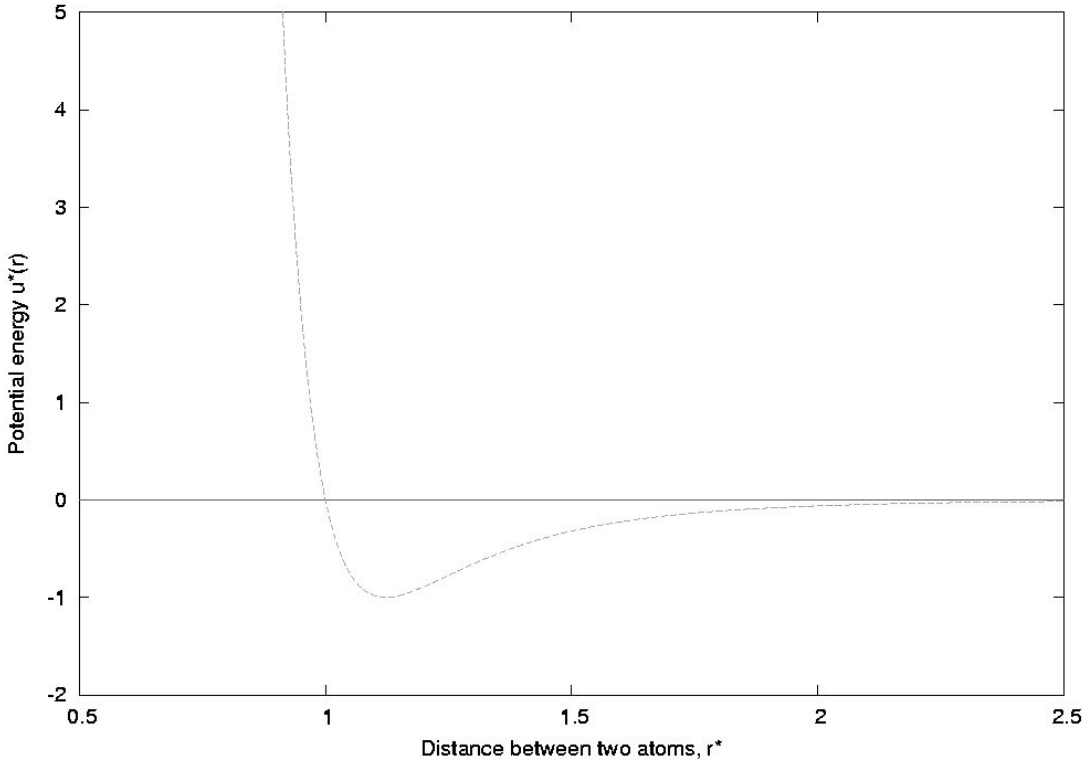

Figure 3.1: Lennard-Jones pair potential in reduced units (Caturla 2003).

The Lennard-Jones potential will then be:

$$U_2(r_{ij}) = 4\varepsilon\left[\left(\frac{\sigma}{r}\right)^{12} - \left(\frac{\sigma}{r}\right)^6\right] \qquad (3.1.8)$$

This potential is a good representation of noble gases and it has been used also for metals. For example in the case of copper the parameters are s = 2.3151 A and for e = 0.167 eV. Figure 1 shows the potential energy in reduced units (u* = u/e and r* = r/s) for a Lennard-Jones potential.

For the case of metals, an interatomic potential introduced by Daw and Baskes in 1984 is probably the most widely used and successful. This potential considers that a metallic bond occurs due to the immersion of a ion in a free electron gas. Under this assumption, the energy of N atoms is given by:

$$U(r^N) = \frac{1}{2}\sum_{i,i\neq j}\Phi_{ij}(R_{ij}) + \sum_i F_i(\rho_{h,i}) \qquad (3.1.9)$$

This so called 'embedded atom potential' consists of two terms. The first term is a two body potential that represents the repulsion between the ion and the rest of the ions in the system. The second term is a multi-body function that represents the energy to embed an atom in the position *i* where there is an electron density $\rho_{h,i}$ that comes from the linear superposition of spherically averaged atomic electron densities.

One of the advantages of this potential is that it is environmental dependent, since a change in coordination of an atom will result in a different electron density and therefore it will change the bond energy. The embedding function, electron density and pair potentials can be obtained either from *ab initio* calculations or from fitting to experimental properties, such as the atomic volume, the elastic constants or the ground state structure.

When angular-dependent interactions contribute significantly to the bonding, pair potentials like those described above are not sufficient and three-body or higher order terms must be included in the potential energy. That is the case of covalently bonded systems like silicon or transition metals.

Integration algorithms (predictor-corrector algorithms)

Predictor-corrector algorithms constitute another commonly used class of methods to integrate the equations of motion. Those more often used in molecular dynamics are due to Gear, and consists of three steps:

1. *Predictor*. From the positions and their time derivatives up to a certain order *q*, all known at time *t*, one ``predicts" the same quantities at time $t+\Delta t$ by means of a Taylor expansion.

2. *Force evaluation*. The force is computed taking the gradient of the potential at the predicted positions. The resulting acceleration will be in general different from the ``predicted acceleration". The difference between the two constitutes an ``error signal".

3. *Corrector*. This error signal is used to ``correct" positions and their derivatives. All the corrections are proportional to the error signal, the coefficient of proportionality being a ``magic number'' determined to maximize the stability of the algorithm.

The goal of molecular dynamics is to compute the phase-space trajectories of a set of molecules. Given the interatomic potential we can compute the force on each atom. From the force, and using Newton's second law we can compute the acceleration on each particle. Integrating those equations we can obtain the next position due to the applied force. One of the standard forms to solve these ordinary differential equations is the finite difference approach. In general it is based on the idea that given a set of positions, velocities and accelerations at time t we compute the positions, velocities

and accelerations at time t+Δt within a certain accuracy. $x(t)$ = coordinate, $u_1 = x'(t)\Delta t$, $u_2 = (1/2)\, x''(t)\, \Delta t^2$, and $u_3 = (1/6)\, x'''(t)\, \Delta t^3$, where Δt is the time step.

$$
\begin{aligned}
x(t+\Delta t) &= x(t) + u_1 + u_2 + u_3, \\
u_1(t+\Delta t) &= u_1(t) + 2u_2 + 3u_3, \\
u_2(t+\Delta t) &= u_2(t) + 3u_2, \\
u_3(t+\Delta t) &= u_3(t),
\end{aligned}
\qquad (3.1.10)
$$

These are predicted values of the new positions, accelerations, etc. With this values, however we will not get the correct trajectories because we have not introduced the equations of motion. Using the predicted values of the positions at time t+Δt we can calculate the new values of the acceleration, and then compare to the calculated above to estimate the error in the predicted value.

$$\phi = (1/2)\,(F/m)\,(\Delta t)^2 - u(t+\Delta t), \qquad (3.1.11)$$

Using this error we can correct the predicted values of positions, etc.

$$
\begin{aligned}
x^c(t+\Delta t) &= x(t+\Delta t) + c_0\phi, \\
u_{1c}(t+\Delta t) &= u_1(t+\Delta t) + c_1\phi, \\
u_{2c}(t+\Delta t) &= u_2(t+\Delta t) + c_2\phi, \\
u_{3c}(t+\Delta t) &= u_3(t+\Delta t),
\end{aligned}
\qquad (3.1.12)
$$

The coefficients c_0, c_1, c_2 were calculated by Gear and the values depend on the number of derivatives included and the order of the differential equation being solved. For example, for the case above, a predictor-corrector algorithm of 4-th order, the values of the coefficients are: $c_0 = 19/120$, $c_1 = 3/4$, $c_2=1$, $c_3=1/2$, $c_4=1/12$.

This type of algorithm is called a predictor-corrector. The procedure in molecular dynamics using this algorithm consists of (1) predict the positions, velocities and accelerations at time t + Δt, (2) evaluate the forces for the new positions and (3) correct the predicted positions using the new values of the acceleration.

Boundary conditions

Even with the most powerful computers only a small number of molecules can be followed with molecular dynamics simulations. Those molecules on the surface of the simulation cell will experience very different forces than those in the bulk. In many situations it is important to avoid the effect of the surfaces on the variables computed. We, therefore, would like to immerse our system into an infinite medium. This can be achieved using periodic boundary conditions. This method consists of making infinite replicas of the original simulation box. Implementation is very simple: those atoms leaving the box will enter on the opposite site of this simulation box.

As shown in Fig. 3.2, the central box is the original simulation box and the surrounding are replicas of it. When an atom leaves the simulation box on one side one of its images will enter the box on the other side, keeping always the total number

of atoms constant. At the same time, when computing energies or forces on every atom, the periodic images must be taken into account.

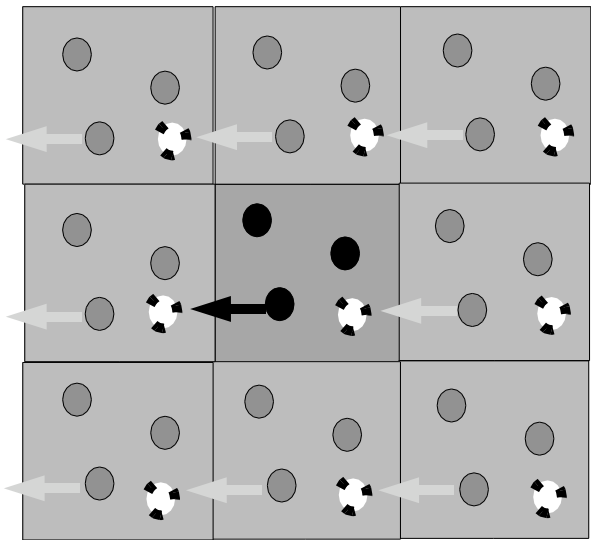

Fig. 3.2 Schematic interpretation of periodic condition of the simulation box (Caturla 2003).

If we are considering a short-range interatomic potential, that is, if we define a cut-off radius such that for distances further apart than that given cut-off the interaction between particles is zero, we can use the idea of periodic boundary conditions to compute the interaction between the particles of the principal simulation box and all the surrounding images. This is done using the minimum image convention: each molecule interacts only with those molecules in a region equal in size to the main simulation box and centered around that particle. If the interatomic potential is not short-ranged then this approximation cannot be used and the total contribution of all the images must be included. Such is the case of Coulombic interatomic potentials.

It is important to understand the limits of this approximation. When using short range potentials the the dimensions of the simulation box can be set such that one atom does not 'sense' the presence of its periodic image. However, for the case of long range potentials that will not be true. Periodicity can also be a problem for modeling amorphous systems. They also inhibit the occurrence of long wavelength fluctuations. If the length of the box is L, no density waves with a wavelength larger than L will exist. However, they are still appropriate for short range interactions and equilibrium thermodynamic properties. Repeating the simulation for different cell sizes could give an assessment on the validity of this boundary condition.

Neighbor lists

To compute the forces over a set of N atoms we have to loop over the j neighbors of each particle i for all N particles. If the distance between those two particles is smaller than the cut-off of the interactomic potential we go to the next atom. This implies a total of N^2 calculations. There are techniques to improve the calculation of the neighbors of each atom for the case of short-range interactomic potentials, where we have a defined cut-off for the interaction. One of those algorithms is the 'link cell list'. This method consists of computing a set of cells on top of the simulation box with dimensions such that the length of those link cells are as close as possible to the cut-

off of the interatomic potential. Once these cells are defined, computing the number of neighbors of a given atom is done taking into account only those atoms within its link cell and those in the next nearest neighbor link cells,

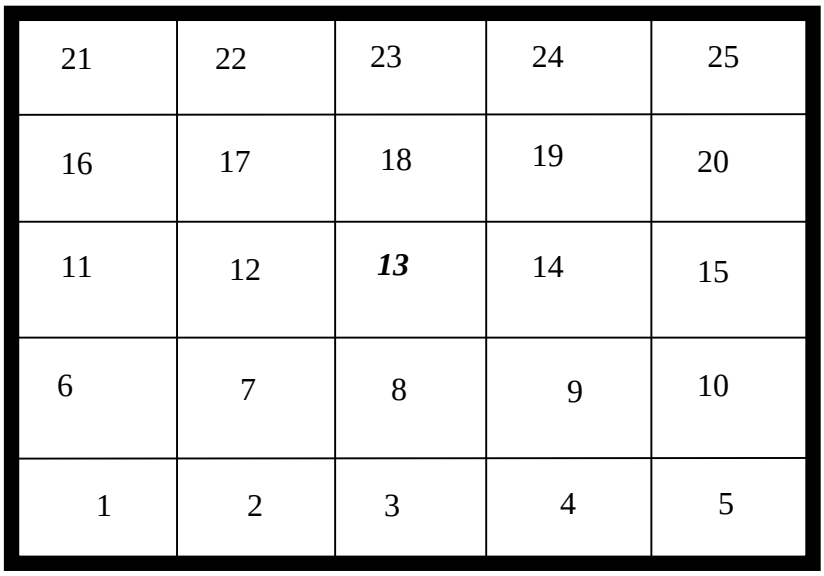

Fig. 3.3 In this example of Link Cell map, eight neighbors (7, 8, 9 , 12, 14, 17, 18, 19) are considerable around cell 13 (Caturla 2003).

For example in Figure 3.3 we have a system divided into 25 cells. In order to find the neighbors of atoms in cell 13, we would look only to those in cells 7,8,9,12,14,17,18,19 and its own cell 13.

Using this method in three dimensions we have to compute $27*N*N_c$ interactions, where N_c is the number of particles on each cell. The number of calculations has been reduced significantly.

3.2 Common neighbor analysis method

We employ the method of common neighbor analysis (Honeycutt and Andersen 1987) to characterize local atomic environments within the clusters. This code calculates the number of vacancies, interstitials and replacements using the Wigner-Seitz cell for fcc and bcc lattices. We identify a given atom's nearest neighbors as simply those closer to it than an appropriately chosen distance r_c, which we take from Wigner-Seitz cell, midway between the nearest- and next-nearest-neighbor shells in fcc Ni. Results from this analysis for these clusters are insensitive to the precise value of r_c. We speak of each pair of nearest neighbor atoms as being ''bonded'' and being connected by a ''bond,'' but this merely denotes a geometrical relationship and not a chemical one. CNA fundamentally operates by categorizing such bonds. Each of a bond's two atoms has a set of nearest neighbors; the intersection of those two sets comprises the neighbors that the two atoms have in common. CNA characterizes the bond by examining this set of common neighbors and specifying three numbers: the total

number of atoms in the set, the total number of bonds between atoms in it, and the number of bonds in its largest contiguously bonded subset. While in general a given CNA bond signature may correspond to more than one possible common-neighbor configuration, in practice this is not a problem in this study. Thus in a fcc bulk crystal, each nearest-neighbor pair shares four common neighbors, among those common neighbors two disjointed bonds are found so that the longest chain of bonds has only one member. Thus the CNA signature of the bond is 421. Since all 12 of the bonds of each atom in a fcc crystal are the same, we say that the local environment of an atom with 12 nearest neighbors each of which has a 421 CNA signature is that of fcc bulk. Similarly an atom in a hexagonal-close-packed bulk crystal or equivalently one on a twinning plane in a fcc crystal. Table I lists the CNA signatures for some of the interesting atomic environments considered in this study. Note that classification of an atomic environment as described above is inherently conservative in the sense that if only one bond fails to match a possible signature, that signature is entirely rejected. In order to find configurations that are near that of fcc bulk, for example, it is necessary to explicitly catalog any signatures one wants to characterize as having that property and track them separately.

Chapter IV

RESULTS

In this chapter the detailed results of this work will be presented in five sections:

i) Mechanical tests
ii) Deformation microstructure
iii) Irradiation induced defects
iv) TEM image simulations
v) MD simulations

Irradiation conditions

The list of samples irradiated in PIREX with the different irradiation conditions and time is given in Table 4.1.1. For most of the specimens (otherwise specified) a beam current of 15 to 20 μA was used. A total of 67 specimens was irradiated in PIREX to various doses and temperatures. There are 49 Ni single crystalline specimens, 13 Cu single crystalline specimens, 3 Al polycrystalline specimens and 2 Ag polycrystalline specimens. The irradiation dose for Ni specimens ranges from 10^{-3} dpa to 1 dpa, for irradiation temperatures ranging from RT to 350 °C. 4 Cu specimens were irradiated to 0.01 dpa and 3 Cu specimens to 0.001 dpa at RT. The 6 Cu in-situ specimens were irradiated to 0.0004 dpa at RT. The 3 Al specimens were irradiated to 0.001 dpa, with a particularly low beam current of 1 μA in order to reduce heating. In effect, in previous PIREX irradiation of pure Al no irradiation induced defects but cavities were visible. This was attributed to a too high beam current that would have led to a temperature sufficient for glide and annihilation of irradiation induced defects such as dislocation loops. Due to time limitation not all irradiated specimens have investigated. The focus of the present study is single crystal Ni.

The actual irradiation dose received by a given specimen can be estimated from the actual proton fluence that impeded on that specimen. However, a more accurate dose value is derived from the measurement of the gamma emission of the irradiated specimen. Gamma spectrometry has been performed on all specimens that have been tested mechanically. It should be noted that the variation in irradiation dose between specimens irradiated in the same batch can yield a difference by a factor of two. The reason for this fluctuation could be that the six specimens may not have been precisely aligned along the beam direction.

The results of mechanical testing of the irradiated and unirradiated Ni and Cu single crystals are given in table 4.1.2. In the following sections the results will be described in detail.

Table 4.1.1 Irradiation conditions for the Ni, Cu, Al and Ag specimens.

Material	Specimen	Number	Irradiation Temperature	Dose rate	Dose (dpa)	Type	Irradiation date
Ni single crystal	I40T01	2	RT	5×10^{-7}	0.1	Tensile	15.10.00
	I40T02	2	RT	5×10^{-7}	0.1	Tensile	15.10.00
	I40T03	2	RT	5×10^{-7}	0.1	Tensile	15.10.00
	I40T04	2	250	5×10^{-7}	0.1	Tensile	23.10.00
	I40T05	1	250	5×10^{-7}	0.1	Tensile	23.10.00
	I40T06	1	250	5×10^{-7}	0.001	Tensile	11.07.01
	I40T07	2	250	5×10^{-7}	0.001	Tensile	11.07.01
	I40T08	1	250	5×10^{-7}	0.01	Tensile	17.08.01
	I40T09	2	250	5×10^{-7}	0.01	Tensile	17.08.01
	I40T10	2	RT	5×10^{-7}	0.01	Tensile	01.09.01
	I40T11	1	RT	5×10^{-7}	0.01	Tensile	01.09.01
	I40T12	2	RT	5×10^{-7}	0.001	Tensile	14.09.01
	I40T13	1	RT	5×10^{-7}	0.001	Tensile	14.09.01
	I40T14	2	RT	5×10^{-7}	0.3	Tensile	21.07.02
	I40T15	2	RT	5×10^{-7}	0.3	Tensile	21.07.02
	I40T16	2	RT	5×10^{-7}	0.3	Tensile	21.07.02
	I40T17	2	RT	5×10^{-7}	0.001	Tensile	06.10.02
	I40T18	1	RT	5×10^{-7}	0.001	Tensile	06.10.02
	I40T20	1	RT	5×10^{-7}	0.01	Tensile	03.11.02
	I40T21	2	RT	5×10^{-7}	0.01	Tensile	03.11.02
	I40T23	2	250	5×10^{-7}	0.001	Tensile	13.12.02
	I40T24	2	250	5×10^{-7}	0.001	Tensile	13.12.02
	I40T25	2	250	5×10^{-7}	0.001	Tensile	13.12.02
	I40T26	2	350	5×10^{-7}	0.1	Tensile	07.12.02
	I40T27	2	350	5×10^{-7}	0.1	Tensile	07.12.02
	I40T31	2	RT	5×10^{-7}	1.0	Tensile	30.09.03
	I40S01	2	RT	5×10^{-7}	0.001	In-situ	13.09.02
	I40S02	2	RT	5×10^{-7}	0.001	In-situ	13.09.02
	I40S03	2	RT	5×10^{-7}	0.001	In-situ	13.09.02
Cu single crystal	I05T01	2	RT	5×10^{-7}	0.01	Tensile	01.09.01
	I05T02	1	RT	5×10^{-7}	0.01	Tensile	01.09.01
	I05T03	1	RT	5×10^{-7}	0.001	Tensile	14.09.01
	I05T04	2	RT	5×10^{-7}	0.001	Tensile	14.09.01
	I05T05	1	RT	5×10^{-7}	0.01	Tensile	03.11.02
	I05S01	2	RT	5×10^{-7}	0.001	In-situ	04.05.01
	I05S02	2	RT	5×10^{-7}	0.001	In-situ	04.05.01
	I05S03	2	RT	5×10^{-7}	0.001	In-situ	04.05.01
Al	I00T01	1	RT	5×10^{-7}	0.001	TEM	06.10.02
	I00T02	2	RT	5×10^{-7}	0.001	TEM	06.10.02
Ag	I47T01	2	RT	5×10^{-7}	0.01	TEM	03.11.02

4.1 Mechanical Properties

Results of tensile tests for unirradiated samples and for samples irradiated at RT are presented in Fig. 4.1.1, and results for samples irradiated at 250 °C and 350 °C are presented in Fig. 4.1.2. It appears that there is a significant hardening in Ni. In the case of tensile test at RT, all irradiated specimens, irrespective of the irradiation dose or irradiation temperature, present a much higher yield shear stress than the unirradiated ones. For specimens irradiated at a same temperature the yield shear stress increases with dose. At the same time the uniform strain decreases but only for doses higher than 0.01 dpa. At 0.1 dpa, the flow stress after yielding increases continuously up to a maximum at $\gamma \approx 0.06$, where strain softening sets in up to $\gamma \approx 0.21$. Strain hardening takes place at higher strain level. Notice that the corresponding stress at which this happens is already higher than the stress for transition into stage III in the unirradiated material.

In Fig. 4.1.1 for example irradiation hardening is already present at the lowest dose of 3.5×10^{-3} dpa. In the present dose range, the following characteristics of the irradiation effects on the mechanical properties are observed.

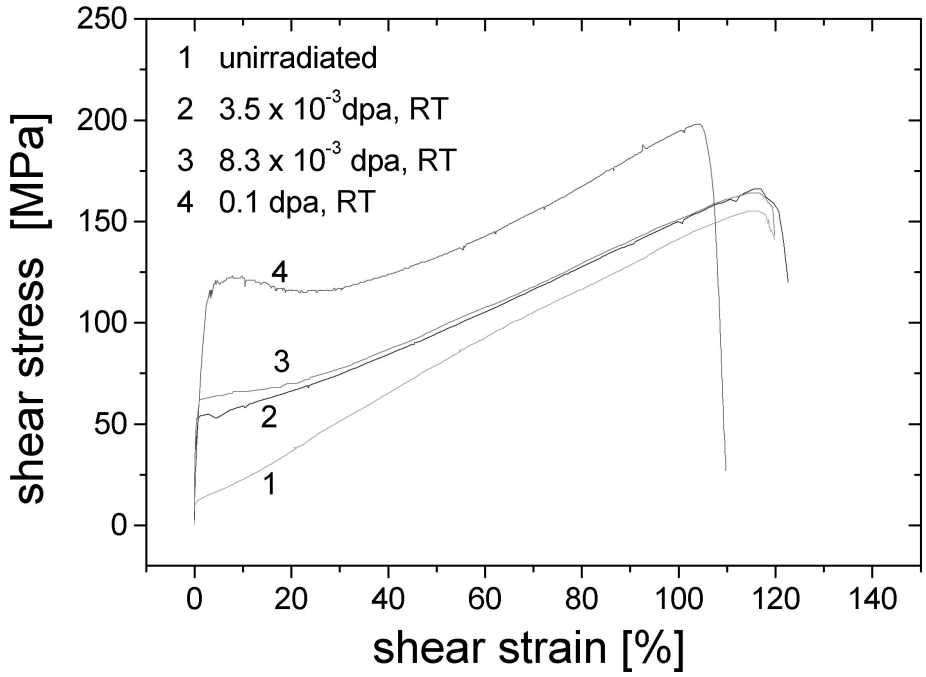

Fig. 4.1.1 Shear stress-shear strain curves as a function of dose for single crystal Ni, tested at RT.

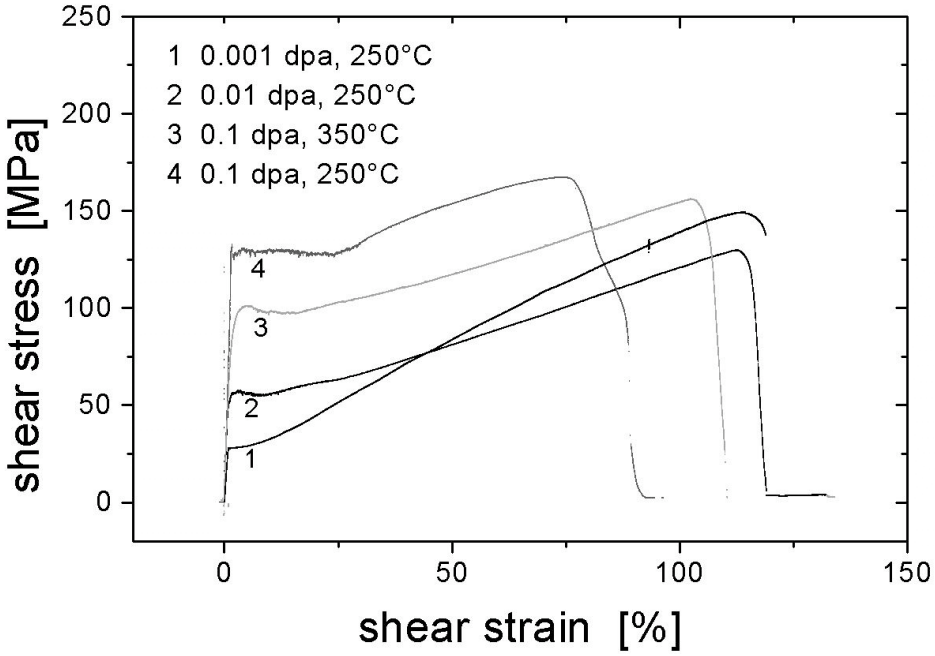

Fig. 4.1.2 Shear stress-shear strain curves as a function of dose for irradiated single crystal Ni, tested at RT.

1) An upper-yield point followed by a yield region with slight hardening or even softening at the higher doses over 0.01 dpa. Both the upper yield point and the length of the yield region are more pronounced with increasing dose.

2) A serration phenomenon appears during the yield region. The serration increases with the increasing dose and diminishes at the end of yield region. Figures 4.1.3-6 show the magnitude and appearance of the stress serration for examples of 0.0035 dpa tested at RT, 0.097 dpa tested at 430 K, 0.097 dpa tested at RT and 0.097 dpa tested at 77 K, respectively. The mean magnitude of stress serration shows an obvious dependence on the irradiation dose and the mechanical testing temperature. The higher the dose, the larger the stress serration (Fig. 4.1.4, as compared to Fig. 4.1.3). The lower the testing temperature, the smaller stress serration(Fig. 4.1.6, as compared to Fig. 4.1.5).

3) Work hardening appears after the yield region in irradiated specimens, and is unlike the unirradiated case that shows a parabolic hardening region.

4) The work-hardening rate in the linear hardening region decreases in the cases of 3.5×10^{-3} and 8.3×10^{-3} dpa compared to unirradiated one, but in the case of 9.7×10^{-2} dpa, the work hardening rate starts to increase at a shear strain 0.7 until interrupted.

5) The elongation of irradiated specimens does not degrade except at a high dose of 9.7×10^{-2} dpa, which decreases from 122 % for unirradiated to 102 %.

6) For samples irradiated at 250 °C and 350 °C, irradiation hardening appears like that in RT irradiation. During yield region stress serration also happened and become more pronounced with increasing dose. At a similar dose level of 0.1 dpa, 250 °C irradiation presents a higher yield stress hardening than 350 °C

irradiation. 250 °C irradiation to 0.085 dpa shows the shortest elongation of, about 77 %.

7) The work-hardening rate of samples irradiated at high temperature after yield region decreases at all doses, relatively to the unirradiated case.

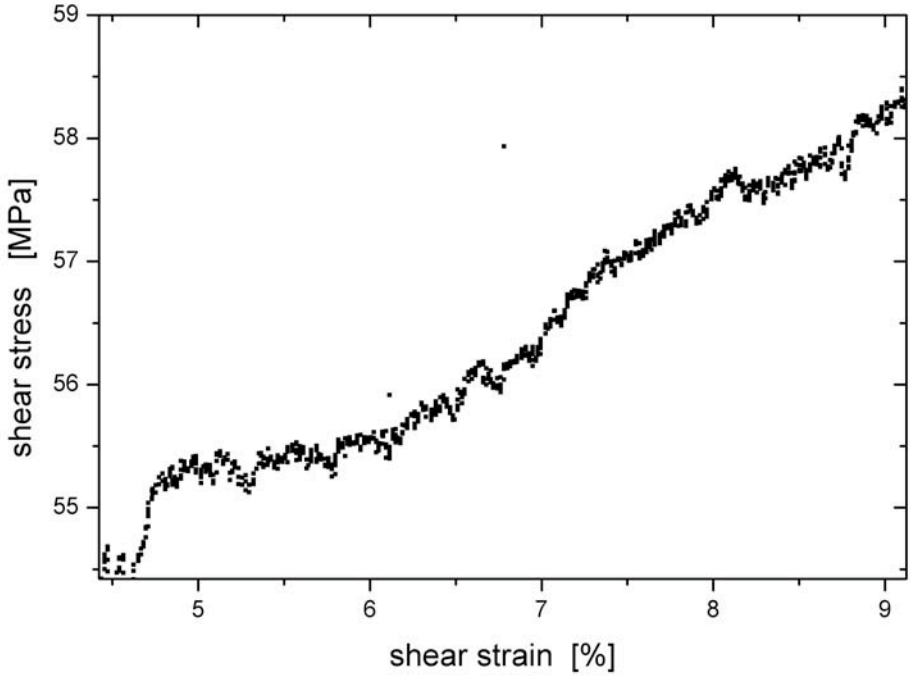

Figure 4.1.3 Stress serrations appearing during the testing of a specimen irradiated to 0.0035 dpa at RT, tested at RT.

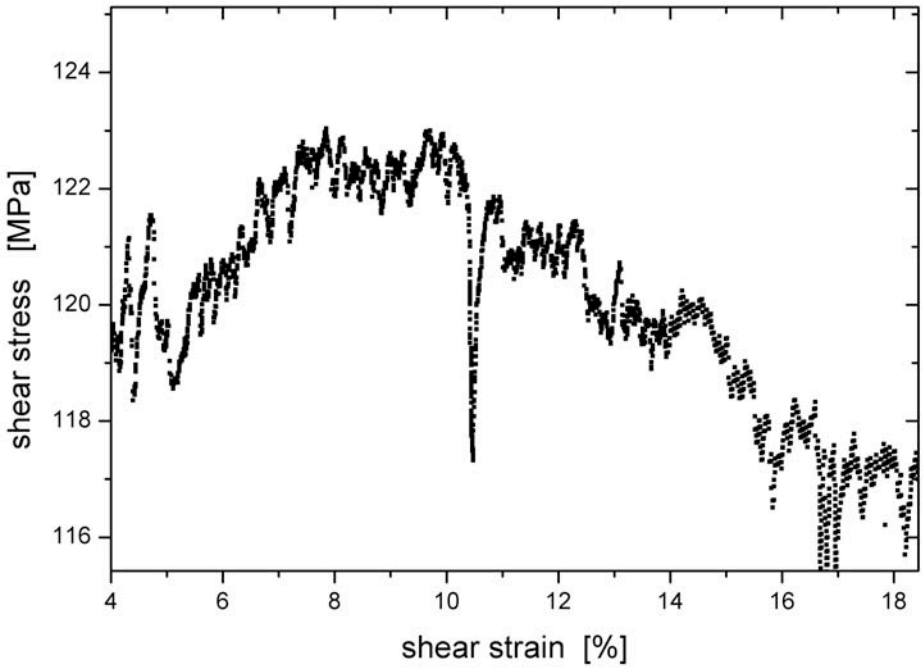

Figure 4.1.4 Stress serrations appearing in the testing of a specimen irradiated to 0.1 dpa at RT, tested at RT.

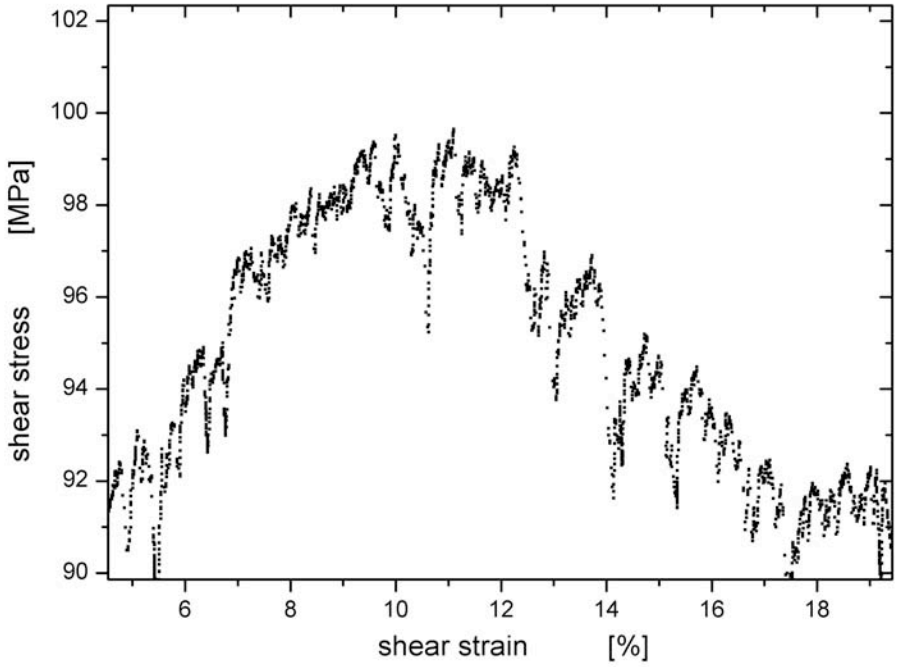

Figure 4.1.5 Stress serration appearing in the testing of a specimen irradiated to 0.1 dpa at RT, tested at 430 K.

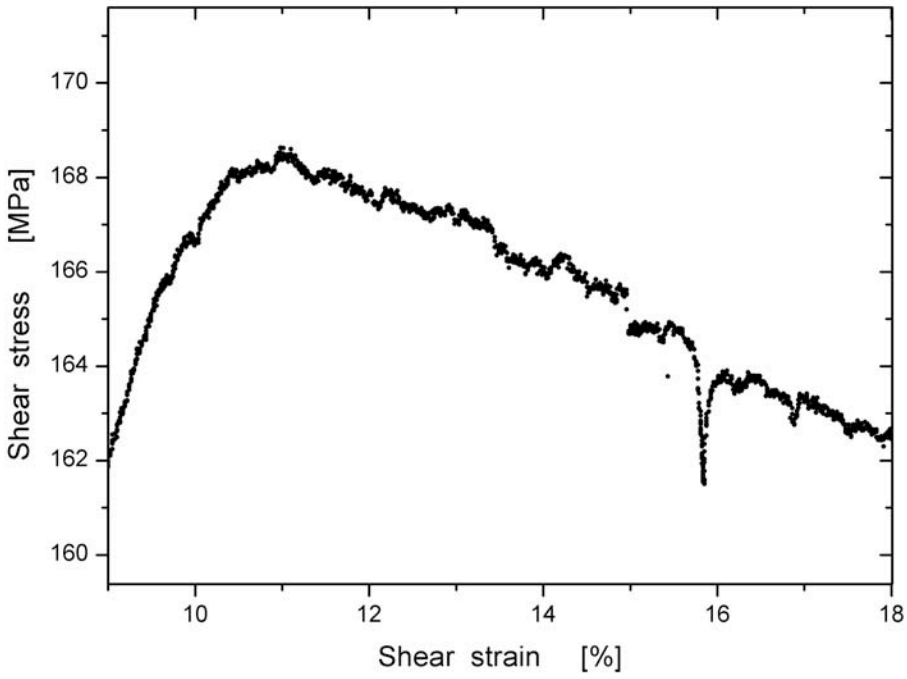

Figure 4.1.6 Stress serrations appearing in the testing of a specimen irradiated to 0.1 dpa at RT, tested at 77 K.

4.1.1 The temperature dependence of the flow stress in tensile tests

Ni

To investigate the temperature dependence of flow stress, tensile tests on unirradiated and irradiated Ni single crystal to a dose of 0.1 dpa at RT were carried out at 77 K, 173 K, 233 K, 293K and 423 K. Here it is noted that samples irradiated to 0.1 dpa were chosen for those tests at different temperatures, because in such samples the defects density has reached saturation according to the above description, and the irradiation effects are expected to be representative of high doses.

In an effort to save the scarce and thus expensive irradiated specimens, one of the tensile tests at 233 K was stopped soon after yield and used for a composite experiment covering various temperatures to get the yield stress at each temperature. Firstly, the sample was deformed at 293K up to the yield point and then partially unloaded below the elastic limit. Secondly, the sample was deformed again at 77 K up to the yield point and then once again unloaded. The third step was done at 233 K in the same way. Finally the sample was deformed at 173 K to failure. The intermediate deformation steps increased the yield stress on returning to RT by less than 5 MPa.

The shear stress-shear strain curves are shown in Figs. 4.1.7 and 4.1.8, and results are summarized in table 4.1.3, together with the shear modulus at the different temperatures (Mader et al. 1963).

The yield shear stress increases linearly with decreasing temperature from 13 MPa at 423 K to 20 MPa at 77 K (see Fig. 4.1.7). The tensile curve at 77 K shows a stage I that extends for about 0.17 shear strain. There is an observable increase in the work hardening at about 0.4 shear strain as the testing temperature decreases.

Samples irradiated at a dose of 0.1 dpa were deformed at the same temperatures as the unirradiated material. The yield shear stress of the irradiated Ni is more strongly dependent on the test temperature than the unirradiated material (Fig. 4.1.8), as it increases with decreasing temperature from 80 MPa at 423 K to 160 MPa at 77 K.

Table 4.1.2 The mechanical tests and the results of irradiated and unirradiated specimens.

Material	Specimen	Dose (dpa)	Irradiation temperature (K)	Thickness (μm)	T_{test} (K)	YSS (MPa)	γ_{total} (%)	Usage	Remark (grips)
Ni	Ni-23#	0	-	173	293	8	120	Tensile	Short
	Ni-32#	0	-	288	293	11	118	Tensile	Short
	Ni-33#	0	-	310	77	20	131	Tensile	Long
	Ni-34#	0	-	290	293	13	122	Tensile	Long
	Ni-39#	0	-	300	173	19	122	Tensile	Long
	Ni-40#	0	-	275	233	16.5	128	Tensile	Long
	Ni-64#	0	-	275	293	12	121	Tensile	Short
	Ni-72#	0	-	311	173	18.5	123	Relaxation	Long
	Ni-74#	0	-	310	77	21	132	Relaxation	Long
	Ni-77#	0	-	260	423	13	129	Relaxation	Long
	I40T01-03	0.1	RT	296	293	105	102	Relaxation	Long
	I40T01-04	0.1	RT	286	293	100	105	Tensile	Long
	I40T02-01	0.1	RT	310	77	160	82	Relaxation	Long
	I40T02-10	0.1	RT	250	293	153	115	TV(strain rate: $10^{-4}s^{-}$)	Short
	I40T03-05	0.1	RT	280	173	135	103	Relaxation	Long
	I40T03-06	0.1	RT	286	423	80	111	Relaxation	Long
	I40T04-07	0.1	523	282	293	129	76	Tensile	Short
	I40T06-21	0.001	523	214	293	26	1.3	Tensile	Short
	I40T07-13	0.001	523	257	293	28	118	Relaxation	Short
	I40T07-15	0.001	523	260	293	26.5	120	Tensile	Short
	I40T09-27	0.01	523	215	293	50.5	116	Tensile	Short
	I40T10-12	0.01	RT	154	293	62.5	120	Tensile	Short
	I40T10-28	0.01	RT	210	293	65	118	Tensile	Short
	I40T11-14	0.01	RT	125	-	-	-	TEM	-
	I40T12-20	0.001	RT	241	-	-	-	TEM	-
	I40T12-26	0.001	RT	291	293	48.5	119	Tensile	Short
	I40T13-18	0.001	RT	210	293	45	121	Relaxation	Short
	I40T15-25	0.3	RT	230	293	-	-	Tensile(failed)	Short
	I40T15-29	0.3	RT	196	-	-	-	TEM	
	I40T27-51	0.1	623	280	293	88.5	103	Tensile	Short
	I40T27-65	0.1	623	255	-	-	-	TEM	-
Cu	Cu-13	0	-	260	77	27	136	Tensile	Long
	Cu-14	0	-	155	233	21.5	123	Tensile	Long
	Cu-15	0	-	300	173	25	130	Tensile	Long
	Cu-16	0	-	405	233	22	124	Relaxation	Long
	Cu-17	0	-	400	293	14	120	Relaxation	Long
	Cu-18	0	-	370	293	16	121	Tensile	Long
	I05T01-3	0.01	RT	223	77	28	138	Relaxation	Long
	I05T01-1	0.01	RT	245	173	24	129	Relaxation	Long
	I05T02-2	0.01	RT	270	233	22	121	Relaxation	Long
	I05S01-1	0.004	RT	100	120			In-situ	-

In the case of unirradiated Ni, the total elongation at 77 K is 5 % more than those at other higher temperatures. The temperature dependence of shear stress becomes more pronounced at 40 % plastic deformation.

In the case of irradiated Ni to 0.1 dpa, the total elongation of samples decreases with decreasing temperatures, from 111 % at 430 K to 82 % at 77 K. The flow stress indicates a strong temperature dependence from the beginning of yield to the starting of fracture.

Table 4.1.3 Tensile tests results for the unirradiared and irradiated single crystal Ni as a function of temperature. (Shear modulus from Mader et al. 1963)

	Test Temperature	Yield shear stress [MPa]	Shear modulus [GPa]*	Maximum Stress [MPa]	Total elongation [%]
Unirradiated Ni	430 K	13	76.1	121	129
	293 K	13	80.5	128	122
	233 K	16.5	82.3	141	128
	173 K	19	84	154	122
	77 K	20	86.1	198	131
Ni, 0.1 dpa	430 K	80		146	111
	293 K	105		198	102
	233 K	122		-	-
	173 K	135		233	103
	77 K	160		229	82

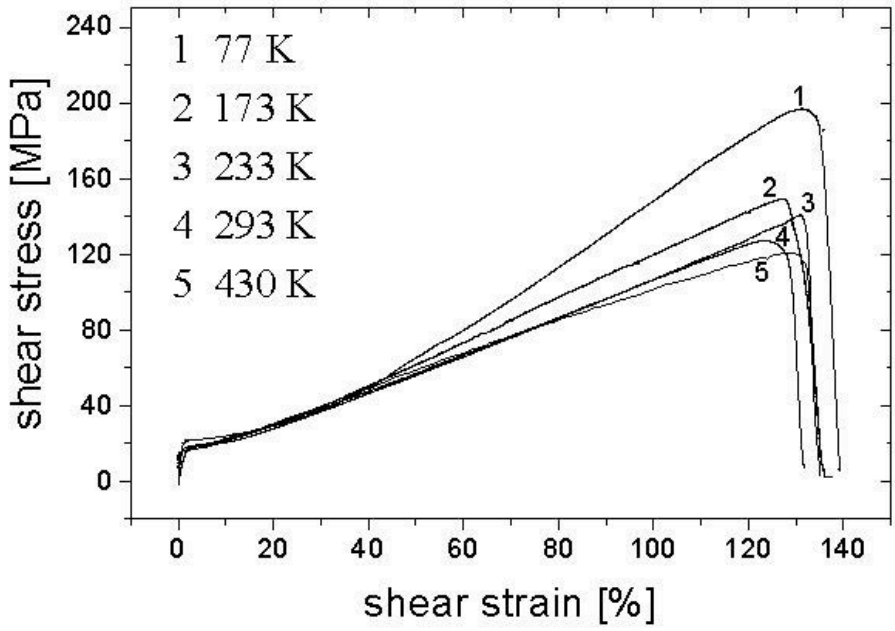

Fig. 4.1.7 Shear stress-shear strain curves as a function of testing temperature for unirradiated single crystal Ni.

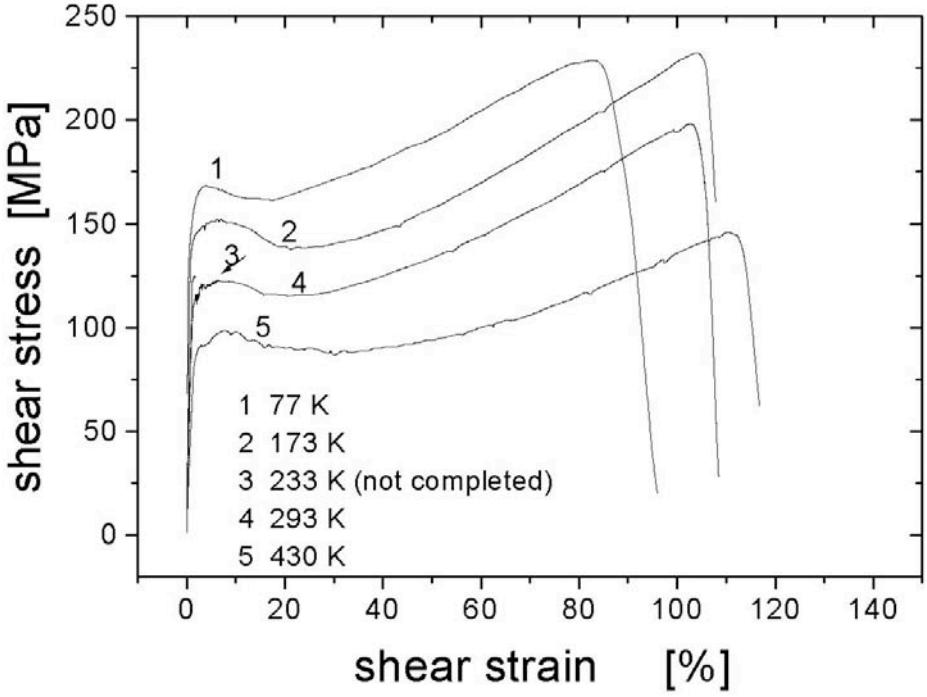

Fig. 4.1.8 Shear stress-shear strain curves as a function of testing temperature for single crystal Ni irradiated at RT.

Cu

To compare with the temperature dependence of the flow stress in Ni, tensile tests on unirradiated Cu single crystal and irradiated ones to a dose of 0.01 dpa at RT were carried out at 77 K, 173 K, 233 K and 293K. For Cu samples irradiated to 0.01 dpa the defects density nearly reaches saturation, according to the previous research (Dai et al. 1995). Here the testing temperatures are selected between 77 K and 293 K (RT), not the same as those for Ni which are between 77 K and 430 K. It is thought that the melting point of Cu (1362 K) is much lower than that of Ni (1730 K). Thus such a temperature range much below 400 K (0.3 T_m) can sustain the stability of irradiation induced defects (SFT domination microstructure).

The shear stress-shear strain curves are shown in figures 4.1.9 for unirradiated samples and 4.1.10 for samples irradiated to 0.01 dpa at RT. The yield shear stress of unirradiated samples increases linearly with decreasing temperature from 14 MPa at 293 K to 27 MPa at 77 K (see Fig. 4.1.9).

The yield shear stress of irradiated Cu is more strongly dependent on the test temperature than the unirradiated material (see Fig. 4.1.9), as it increases with decreasing temperature from 37 MPa at 293 K to 83 MPa at 77 K. At 293 K and 233 K, once yielding starts, the plastic deformation proceeds without hardening or softening up to ~20 % plastic strain. When deformed at 173 K, the obvious softening appears and at the lowest temperature, 77 K, the shear stress-shear strain curve shows a larger softening rate than that of 173 K.

After yield, the flow stress also indicates a temperature dependence similar as that of the yield shear stress, up to the starting of fracture.

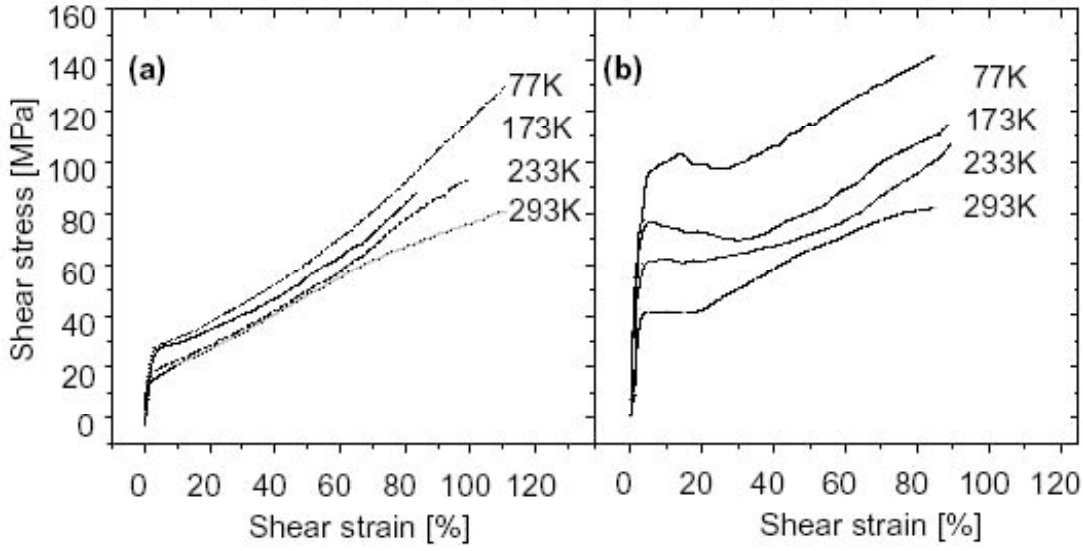

Fig. 4.1 9 The shear stress responses to shear strain for the testing results of (a) unirradiated Cu samples and (b) for the testing results of Cu samples irradiated to 0.01 dpa at RT.

4.1.2 The correlations between work hardening and shear strain, shear stress.

As described in Chapter I, work-hardening is normally ascribed to the increasing density of dislocation forest. Here the work-hardening rates ($\theta=d\tau/d\gamma$) are plotted as a function of shear stress (Fig. 4.1.10).It appears that, contrary to the case of the unirradiated material, the work hardening rate of the irradiated Ni is less dependent on testing temperature.

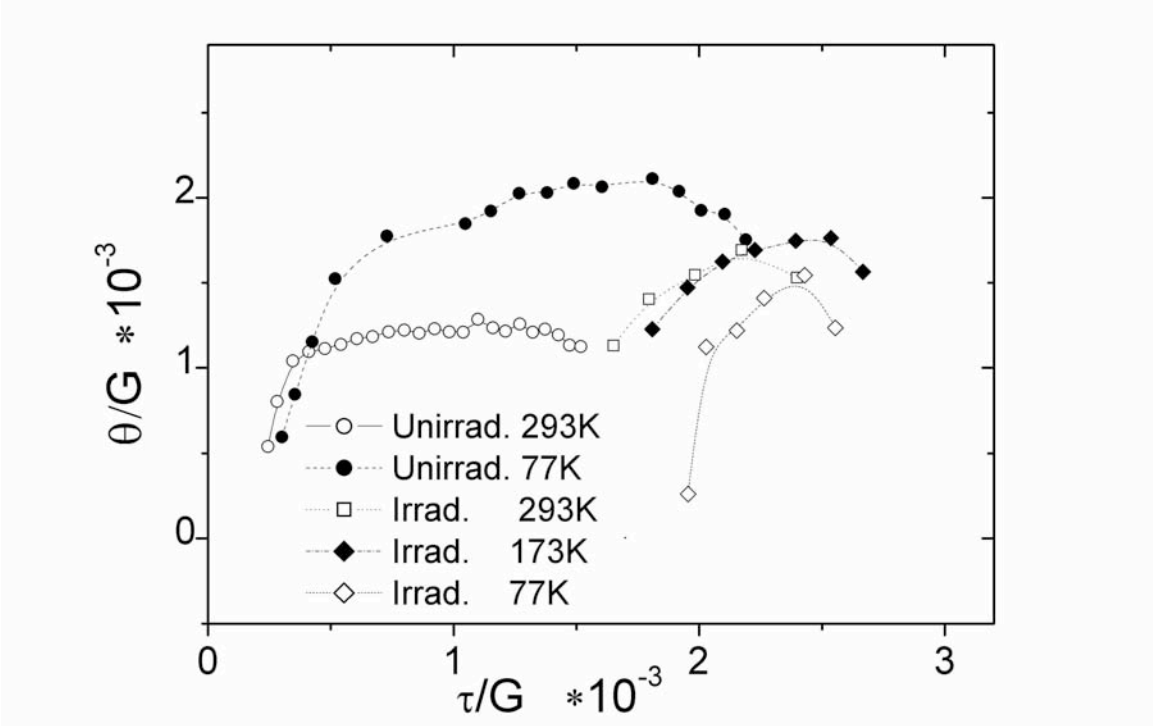

Fig. 4.1.10 Work hardening as a function of shear stress of unirradiated Ni tested at RT and 77 K, and Ni irradiated to 0.1 dpa tested at RT, 173 K and 77 K.

4.1.3 Thermal activation volume and energy

The stress drop-time curves from the stress relaxation tests can be represented by the relationship $\Delta\tau = kT/V_a \ln(1+t/c)$, where V_a is the apparent activation volume. This apparent activation volume can be precisely determined.

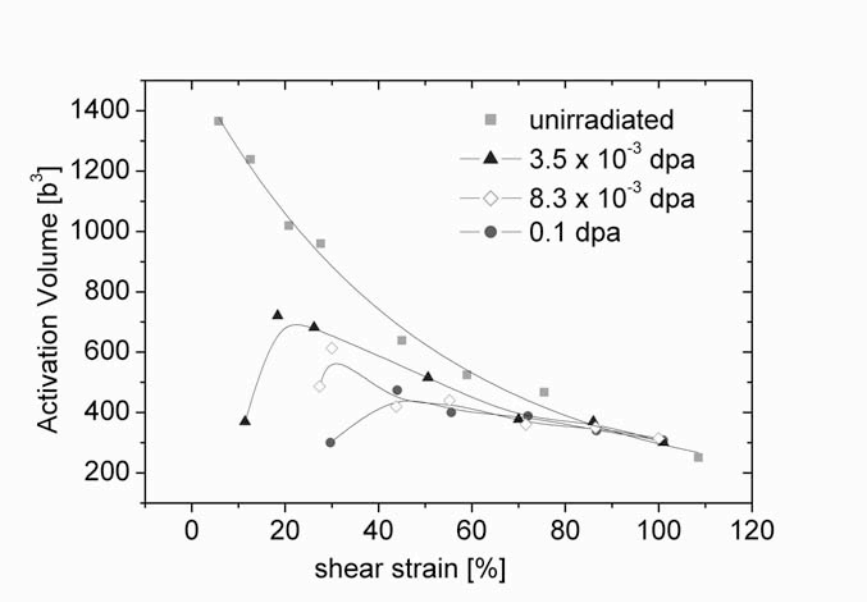

Fig 4.1.11 Effective activation volume responses to shear strain as a function of dose in irradiated and unirradiated Ni, tested at RT.

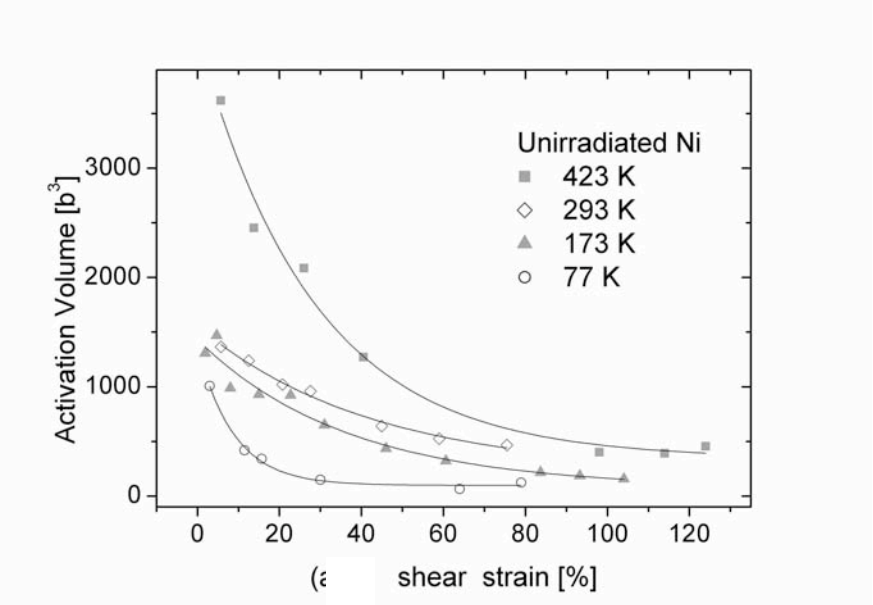

Fig 4.1.12 Effective activation volume response to shear strain as a function of temperature in unirradiated Ni.

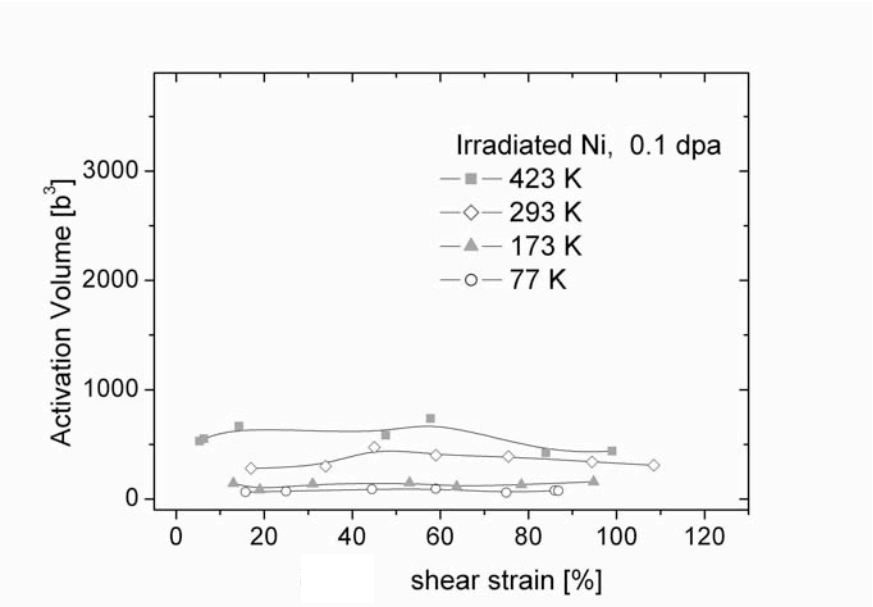

Fig 4.1.13 Effective activation volume-shear strain response as a function of temperature in irradiated Ni.

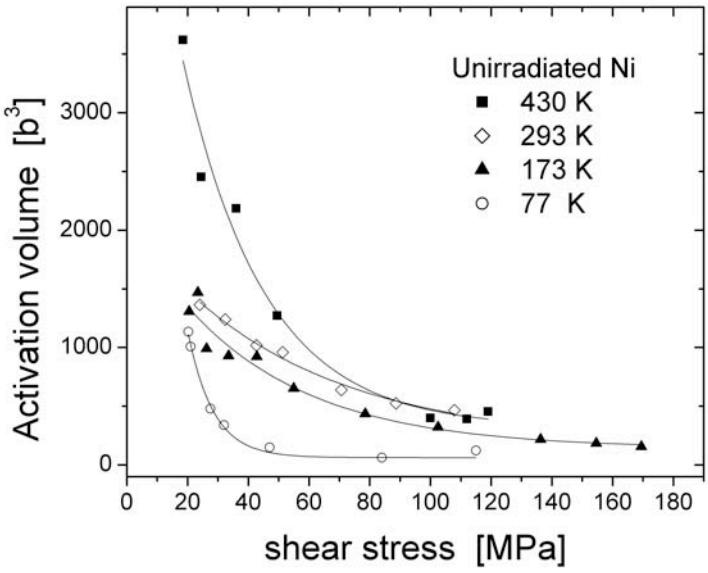

Fig 4.1.14 Effective activation volume-shear stress response as a function of temperature in unirradiated Ni.

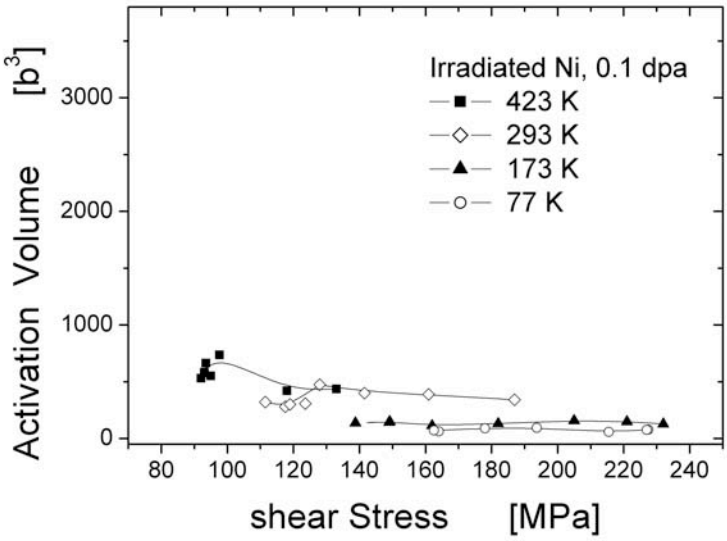

Fig 4.1.15 Effective activation volume-shear stress response as a function of temperature in irradiated Ni.

Fig. 4.1.11 shows the activation volume as a function of shear strain for measurement of different doses for tests performed at room temperature. The activation volumes derived for the unirradiated and irradiated Ni as a function of shear strain, shear stress at the different temperatures are shown in Fig. 4.1.12, 13, 14 and 15, respectively. In the unirradiated Ni the activation volume decreases rapidly with strain at all testing temperatures. Moreover, the starting value decreases with decreasing temperature and asymptotic approaches a value between 60 b^3 and 120 b^3 at 77K. Conversely, in the irradiated case it remains almost constant at all temperatures. Values between 100 b^3 to 150 b^3 and 60 b^3 to 90 b^3 are found at 173 K and 77 K, respectively. It should be noted that no measurements were performed in the irradiated material for $\gamma \leq 0.1$ because the stress level at which the relaxation is started is not well defined due to the stress serration at these strain levels.

4.2 Slip band evolution in irradiated and unirradiated specimens during deformation

Fig. 4.2.1 shows optical micrographs of the surface of the tensile test specimen made during a tensile test together with the corresponding stress-strain curve.

Fig. 4.2.1 clearly shows that slip bands appear as soon as the specimen yields and start to spread over the whole gage length. As deformation proceeds, the density of slip bands increases. Interestingly these slip bands remain thin and well defined up to failure of the specimen. This is contrary to the case of the unirradiated specimen, not shown here, where at about 10 % elongation the slip bands start to smear out and the surface of the specimen start to present bumps, while the irradiated specimen surface remains flat.

Once slip bands appear, deformation is inhomogeneous and localized in these slip bands. Between the slip bands are undeformed regions. Figs. 4.2.2a-d are SEM observations made at the vicinity of the neck of broken irradiated and unirradiated samples.

From the SEM observations a mean distance between the primary slip lines on the surface is measured to be about 400 nm. Taking the tensile axis into consideration, a mean value of about 700 nm is observed which is equivalent to the mean space between channels in the microstructure of samples, as described later. In addition, it can be observed that the slip lines indeed remain thin and well defined, as traces of {111} planes, in the case of the irradiated specimen, contrary to the unirradiated specimen that shows smeared slip lines with undefined crystallographic directions.

Figs. 4.2.2c and d show no obvious difference in the morphology of the failure face of unirradiated and irradiated samples and presents typical features (dimples) of ductile fracture. It implies that ductile fracture still occurs in the deformation of irradiated pure metals.

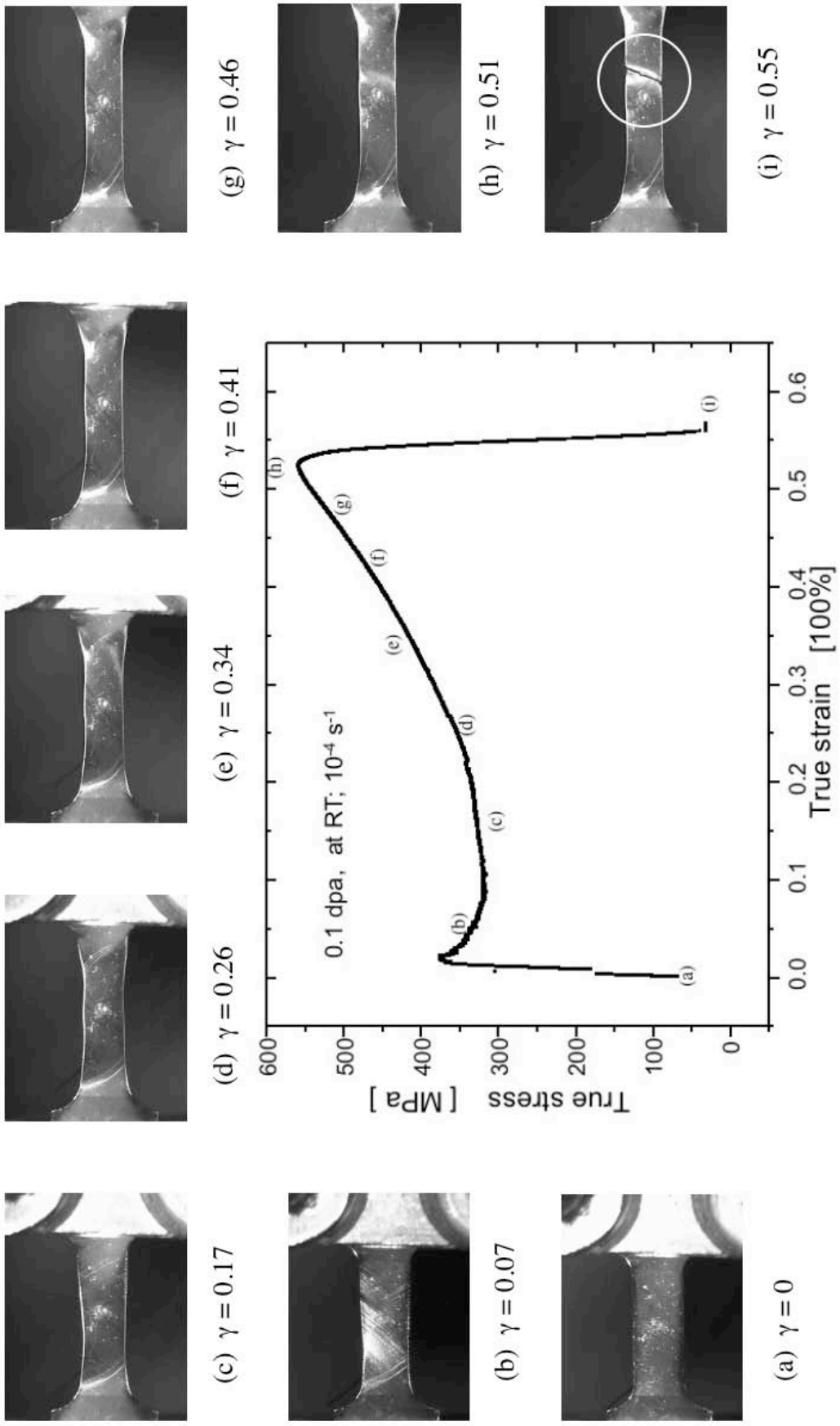

Fig. 4.2.1 Slip lines evolution in a Ni single crystal with a dose of 0.1 dpa. The corresponding strain of each photo from (a)-(i) is marked on the tensile stress-strain curve.

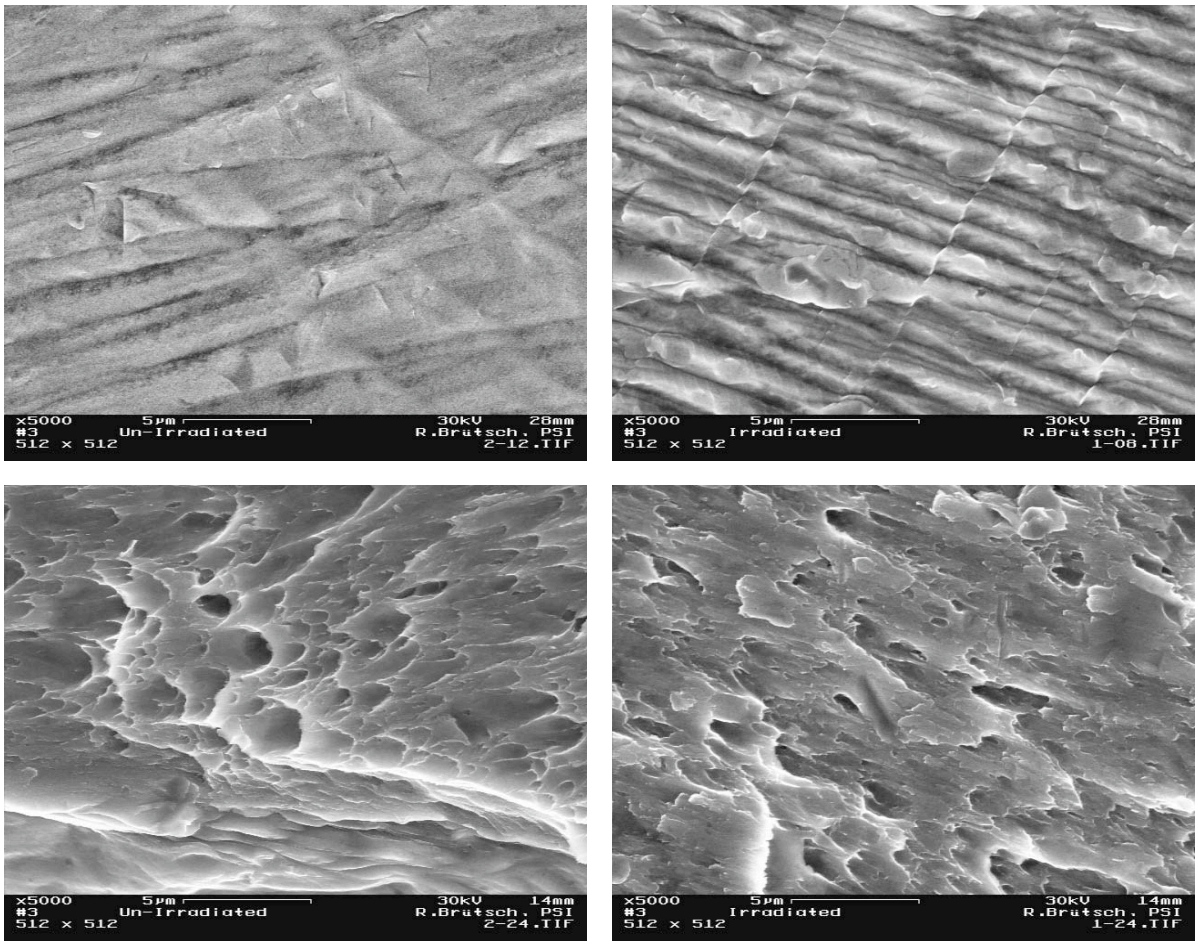

Figure 4.2.2 The surface morphology of Ni samples unirradiated (left) and irradiated (right) to a dose of 0.1 dpa in SEM micrographs. The upper images show the neck region, while the lower images show the failure region.

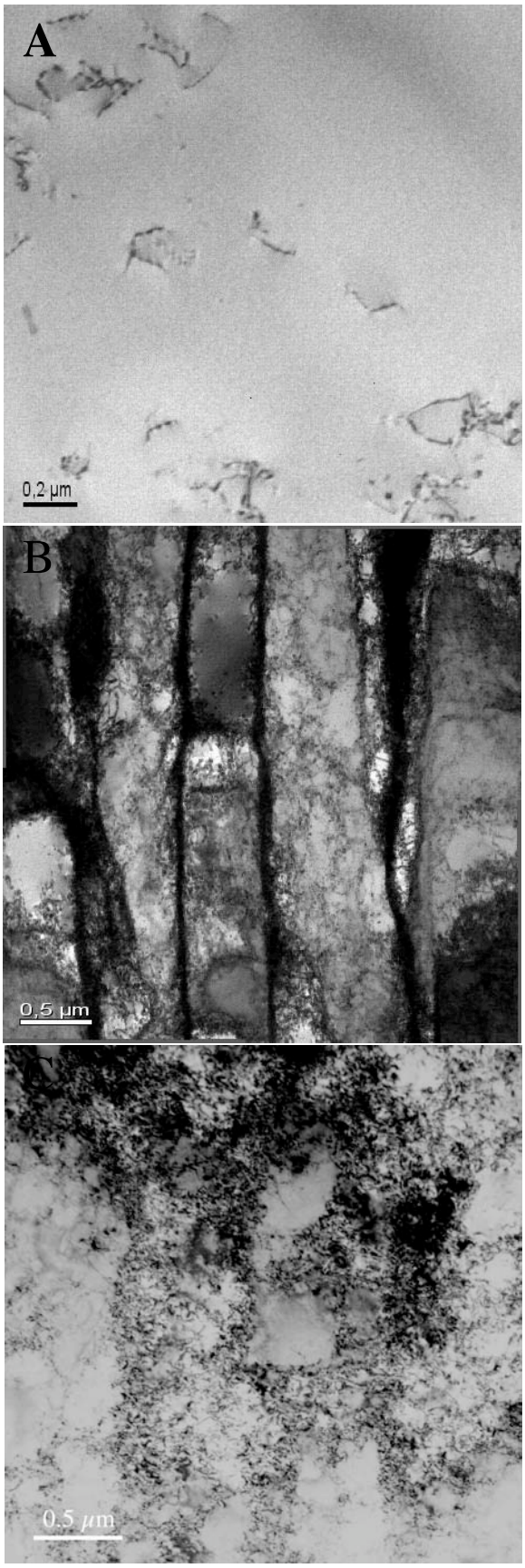

Figure 4.3.1 The microstructure of a) an undeformed Ni sample, b) a Ni sample deformed to failure at RT and c) a Ni sample deformed to failure at 77 K. All Ni samples are unirradiated.

Unirradiated Cu

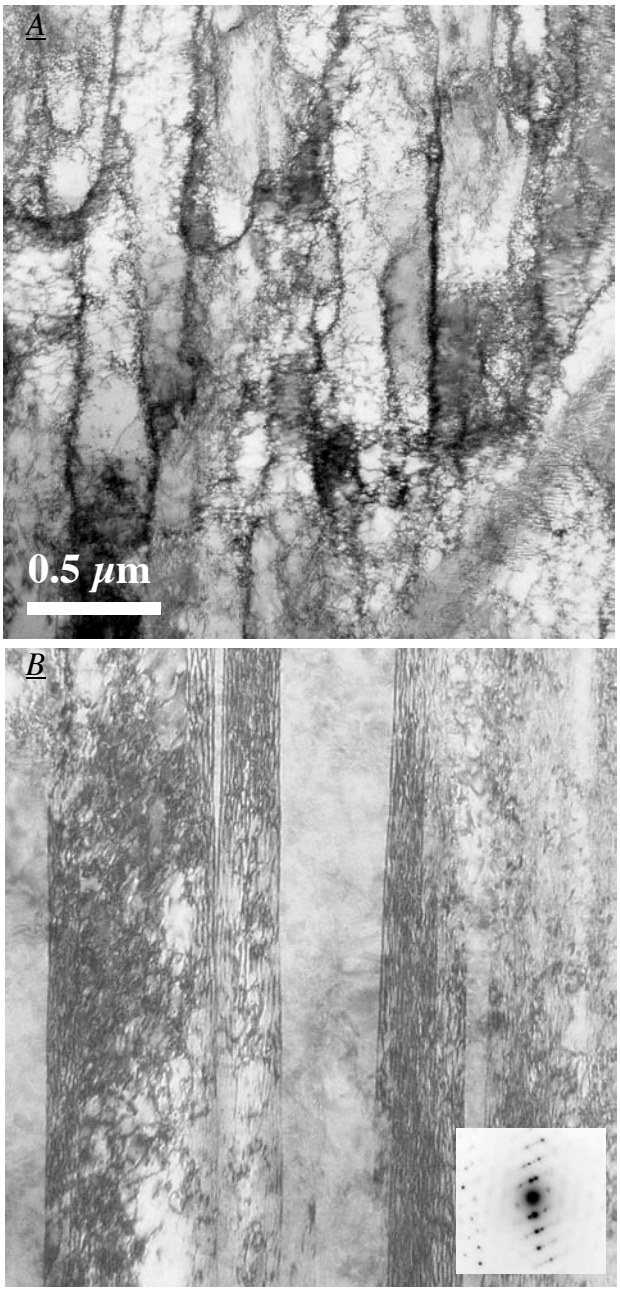

Figure 4.3.2 The microstructure of a) a deformed Cu sample at RT, b) a Cu sample deformed to failure at 77 K. Both of them are not irradiated.

4.3 Deformation microstructure

In this part, the investigation of the microstructure of deformed, unirradiated and irradiated specimens will be presented. The main features studied include dislocation structures in the deformed specimens either in the shoulder region, or gage region after fracture in both unirradiated and irradiated Ni and Cu specimens.

4.3.1 Unirradiated Ni

The micrographs in Fig. 4.3.1 summarize the microstructure of unirradiated samples observed by TEM. Fig. 4.3.1a corresponds to microstructure of an as-annealed unirradiated Ni without deformation. The grown-in dislocation density is estimated to be about 1×10^{11} m^{-2}.

In the unirradiated case at 293K a dislocation cell structure (Fig. 4.3.1b) characteristic of stage III is formed. At 77 K, open dislocation braids typical of stage II (Prinz and Argon 1979) are observed (Fig. 4.3.1c).

Fig. 4.3.2 shows the microstructure of unirradiated Cu specimens deformed at 293 K (Fig. 4.3.2a) and 77 K (Fig. 4.3.2b). The microstructure observed in the samples deformed at 233 K and 173 K shows a similar elongated dislocation cell structure as that of fig. 4.3.2a, characteristic of stage III. At 77 K, twin lamellae are observed (fig. 4.3.2b), as indicated by the diffraction pattern inserted at the bottom right in fig. 4.3.2b.

4.3.2.1 Defects free dislocation slip channels

Fig. 4.3.3 shows defect-free dislocation slip channels with a length of about 20 μm in Ni irradiated to 0.1 dpa at room temperature. These bright field micrographs were taken with a diffraction vector **g** = {200} close to zone axis <011>. The inserted diffraction pattern in Fig. 4.3.3 shows that the channels are parallel to {111} plane, which is the glide plane. The TEM sample was cut in the shoulder region of a tensile specimen pulled to failure. It was assumed that this shoulder region was slightly deformed during the tensile tests, so that there the dislocation free channels could still be the dominant microtructural feature in the deformation. In TEM, it means a higher probability to observe these channels.

Usually, the edges of channels are well defined in TEM, as in fig. 4.3.4a. The width of these channels is about 100 nm and their separation distance between them is about 1 μm, which is equivalent to the mean distance between the primary slip lines on the specimen surface shown in Fig. 4.2.2. In the channels, most of crystal volume seems clean but for some few dislocations and remaining debris (Fig. 4.3.4b).

Between the channels, defect density is high indicating limited contribution to further plastic deformation of these regions.

In Fig. 4.3.3, a few channels intersect the main channels. The intersecting channels correspond to the traces of the other {111} slip planes.

It should be noted that there are some dislocation cell-like structure appeared along the long-range channels.

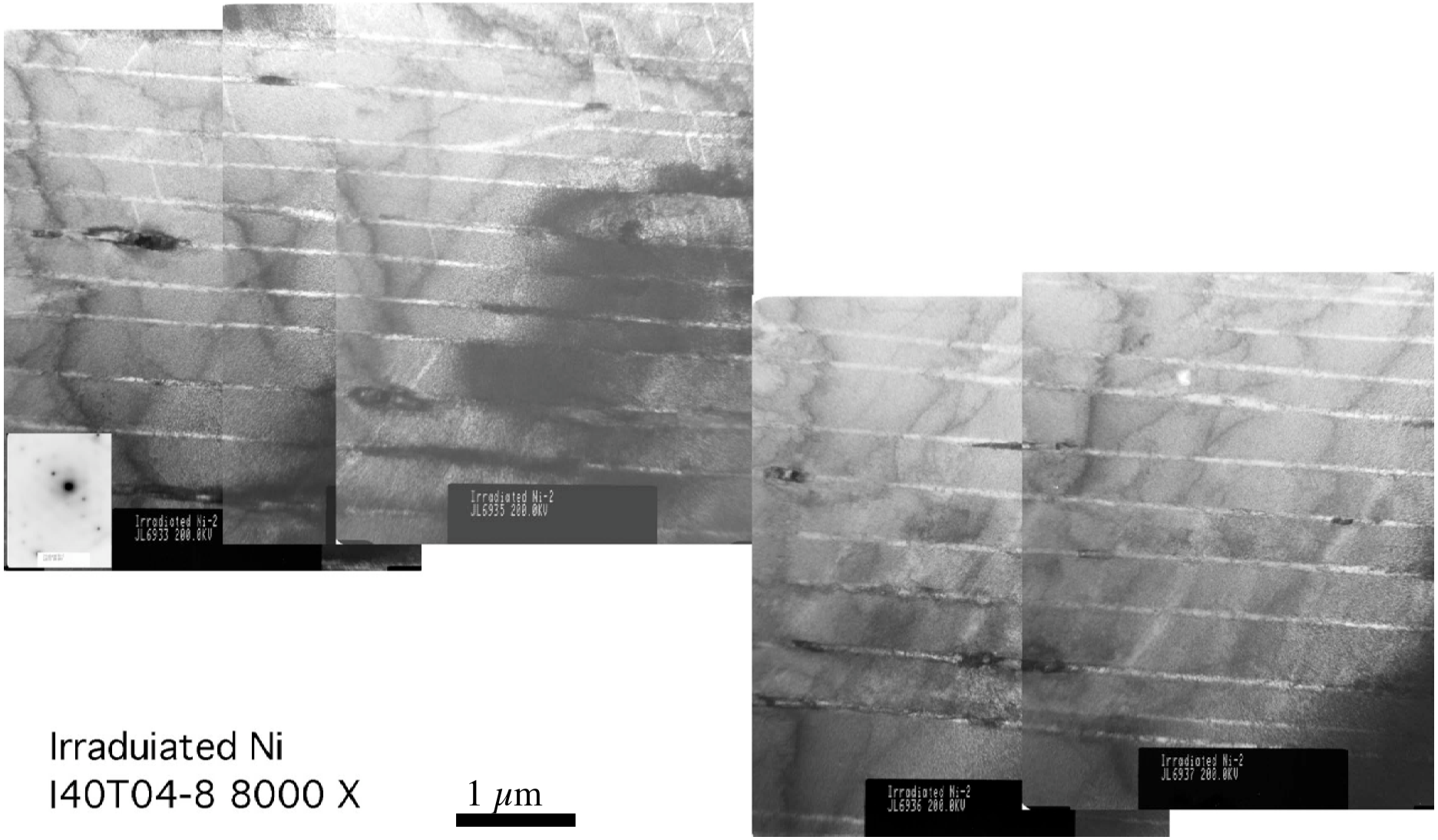

Fig. 4.3.3 Low magnification BF micrographs showing defects-free channels in a Ni specimen irradiated to 0.1 dpa at RT and deformed

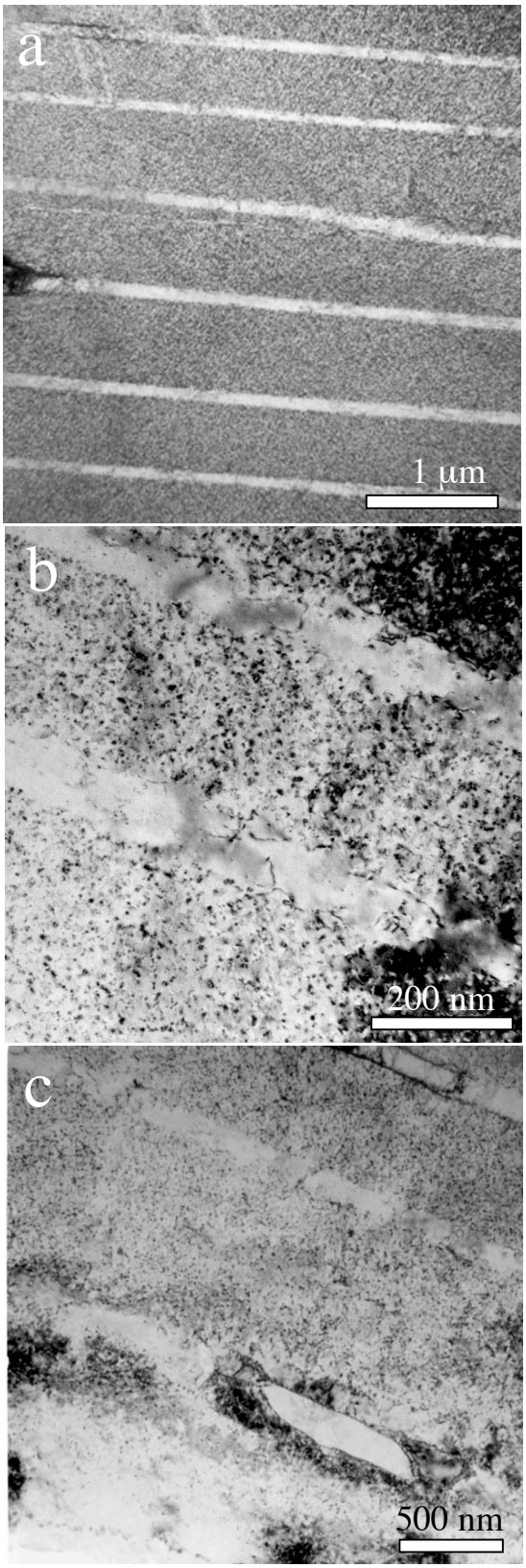

Fig. 4.3.4 The deformation microstructure of Ni irradiated to 0.1 dpa at RT. A) Defect free channels with a mean spacing around 1μm and mean width around 100 nm, b) dislocations in channels (arrows), c) dislocation cells formation starting (arrows) in channels.

4.3.2.2 Initial dislocation cell structure

When deformed at 293K, the highly strained gage section of the irradiated material contains dislocation cells but no channels or dislocation braids or bands (Fig. 4.3.5a). At 77K, a mixed structure of defect-free channels together with a dislocation cell structure comparable to that found in stage III exists (Fig. 4.3.5b). Defect-free channels formed earlier in the test are presumably replaced by dense dislocation cells, while a high density of defect clusters subsists in the region between the channels. The microstructure in the shoulder region of the same irradiated specimen (Fig. 4.3.5c and 5d) consists, at both 293 K and 77 K, of defect free channels and undeformed structure containing the original high density of irradiation induced defects (Fig.4.3.5d).

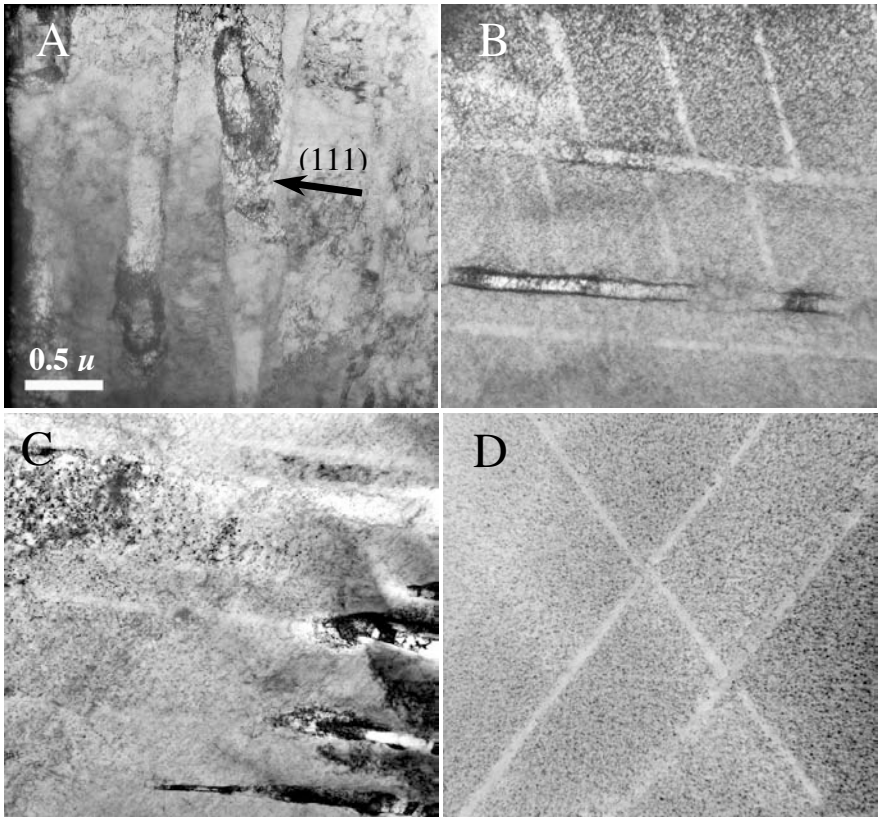

Fig. 4.3.5 TEM micrographs showing deformation microstructure in Ni irradiated to 0.1 dpa at RT. Top and bottom row of images relate to specimens deformed at RT and 77 K, respectively. A), B), C) and D) show the microstructure of deformed Ni irradiated to 0.1 dpa. A) and B) show regions of the gauge length and C) and D) show regions close to the shoulder of tensile specimens.

4.4 Irradiation induced defect microstructure

Microstructures of irradiated Ni specimens have been studied in this section. The information on the irradiation dose and temperature dependences of the defect structure has been obtained.

The defects induced by irradiation below 250 °C consist in SFTs and loops, as well as black dots which are smaller than 1 nm and produce relatively weak contrast. At temperatures higher than 250 °C, another kind of defect, the voids, starts to appear and becomes clearly observable in the case of irradiation at 350 °C. All results are collected in table 4.4.1.

Table 4.4.1 Defects densities and mean sizes of irradiated Ni single crystals measured from weak beam dark field (DFWB) **g**(5**g**~6**g**) = {200} micrographs, as well as bright field (BF) micrographs for the identification of voids. (-) denotes no voids and (?) denotes no visible voids although they are expected (Kojima et al. 1988).

Specimen # Irr. Temp.	Dose (dpa)	Total defects density ($10^{22}m^{-3}$)	Mean image size of total defects (nm)	SFT proportion (%)	Mean size of SFTs (nm)	Loop proportion (%)	Mean size of Loops (nm)	Voids proportion	Mean size of Voids (nm)
I40T12 RT	0.0035	11	2.59	46.3	2.2	39.1	3.74	-	-
I40T10 RT	0.083	24	2.03	50.5	1.69	30.6	3.28	-	-
I40T02 RT	0.101	70	1.89	42.5	1.7	41.1	2.53	-	-
I40T15 RT	0.29	87	1.81	55	1.56	33	2.61	-	-
I40T07 250°C	0.002	0.29	3.9	51	3.4	42	5.07	?	?
I40T09 250°C	0.0096	1.72	3.8	44	3.2	51	4.8	?	?
I40T04 250°C	0.085	16.4	4.04	52.6	3.8	35	5.5	?	?
I40T27 350°C	0.105	5.4	5.06	13.8	5.1	36	6.7	50	3.9

4.4.1 TEM observation condition

The SFT is one type of crystal defect frequently observed in fcc metals. The structural configuration of SFT will be described in detail in relation with molecular dynamics simulation. It is worth noting that it is very efficient to observe SFTs with weak beam imaging technique, usually with **g**(>5**g**) condition. In the present TEM work, the DFWB **g**(5.1**g**) has been extensively applied to study SFTs. On the contrary, to study voids, the technique of under-focus and over-focus in BF is used, with a defocus of ±512 nm. The oxidation of fresh surface of pure metals during the TEM observation seems inevitable even though great efforts have been made to minimize it. According to our experience, the effects of this kind surface oxidation may degrade the efficiency in identification of defects but mainly for those smaller than 2 nm.

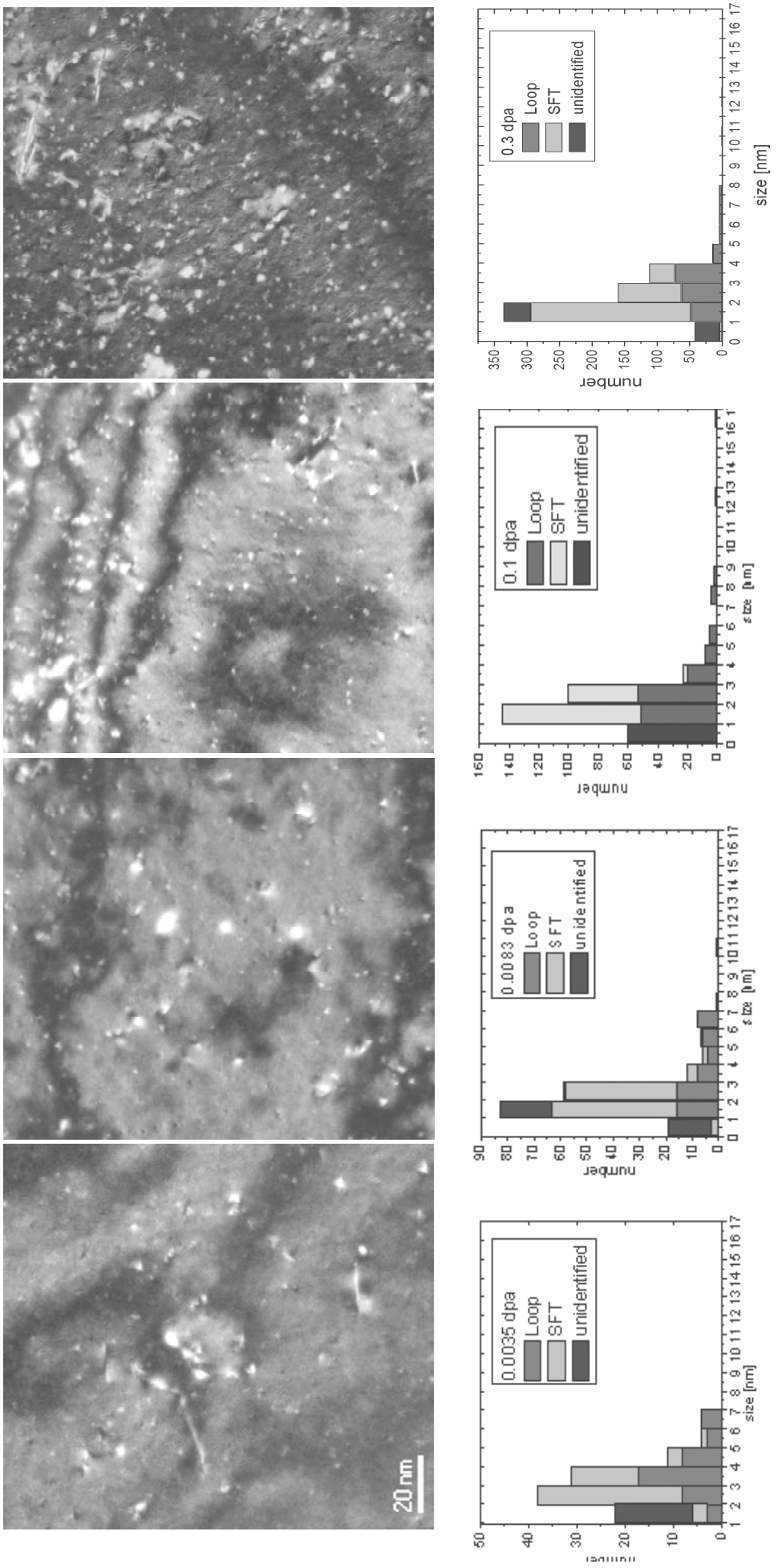

Figure 4.4.1 Irradiation induced defects in Ni irradiated to 3.5×10^{-3} dpa, 8.3×10^{-3} dpa, 9.7×10^{-2} dpa and 2.9×10^{-3} dpa at RT.

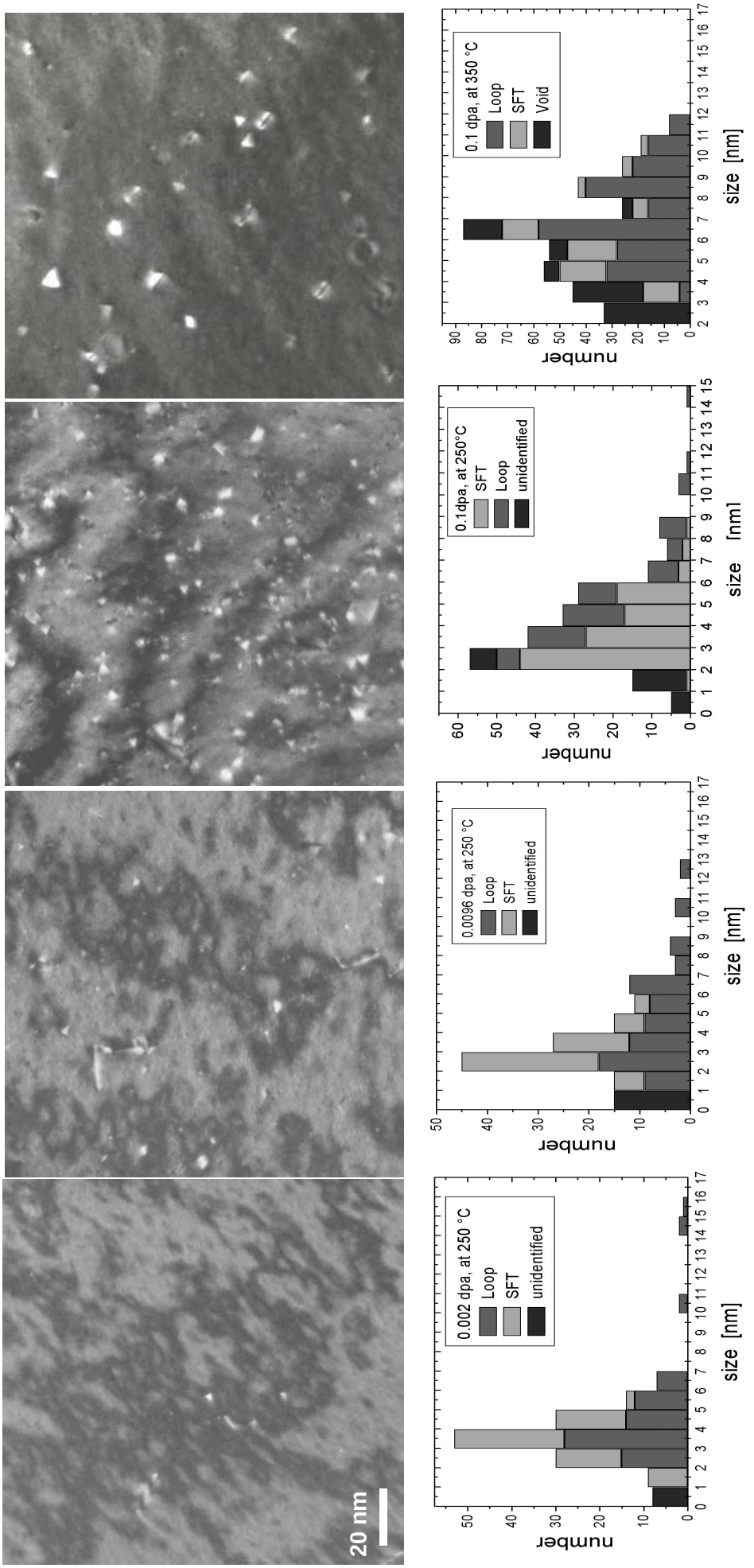

Figure 4.4.2 Irradiation induced defects in Ni irradiated to 2.0×10^{-3} dpa, 9.6×10^{-3} dpa, 8.5×10^{-2} dpa at 250 °C and 1.05×10^{-1} dpa at 350 °C.

4.4.2 Defect structures induced by irradiation

Fig. 4.4.1 presents the results for the RT irradiation. It appears that the mean size of SFTs measured from samples irradiated to the dose level between 0.003 dpa and 0.3 dpa varies between 1.5~2.2 nm, slight decreasing with increasing dose between 0.001 and 0.3 dpa. In other words, taking into account any possible systematic errors, one can conclude that the mean size of SFTs remains approximately constant with a value of about 2 nm for different irradiation dose levels, i.e. SFT size is dose independent.

In the same dose range, the mean size of dislocation loops varies between 2.6 nm and 3.7 nm. The portion of loops larger than 10 nm remains only a few percent but an increase with dose is observable.

Fig. 4.4.2 presents the results for the irradiation at 250°C and at 350°C. The mean size of SFTs between 0.002 dpa and 0.1 dpa varies between 3.2 and 3.8 nm. The average size of SFTs remains around 3.5 nm and is not dependent on dose at 250°C. The mean size of loops in the same dose range is between 4.8 and 5.5 nm at 250°C. At 350°C the mean size of SFTs is about 5 nm. The mean size of loops at this dose is about 6.7 nm and voids appear, as seen in Fig. 4.4.3, with a mean size of about 3.9 nm.

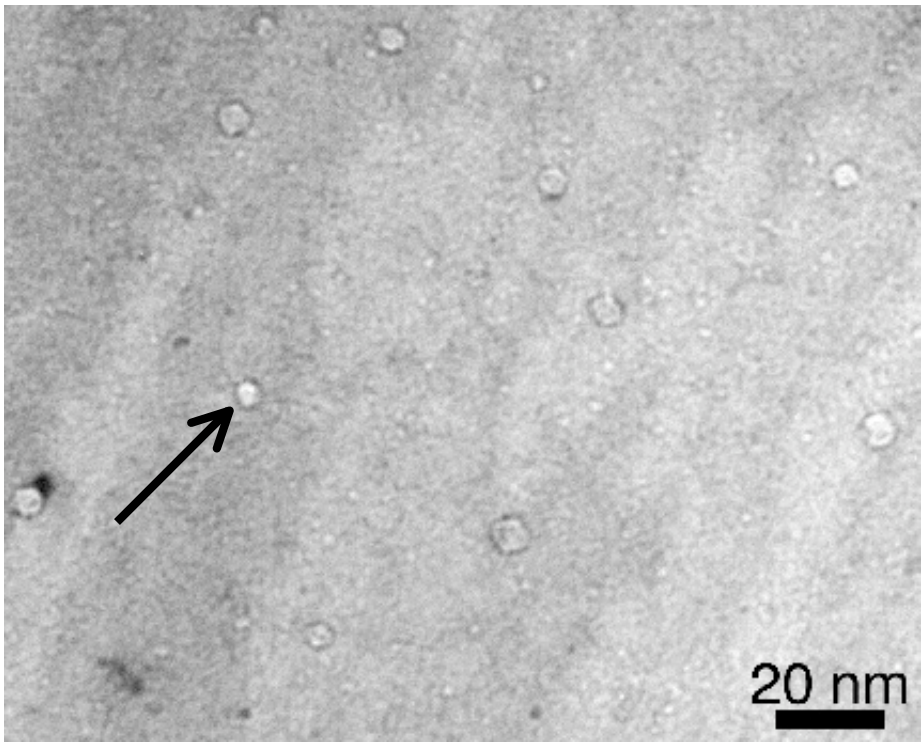

Under-focus

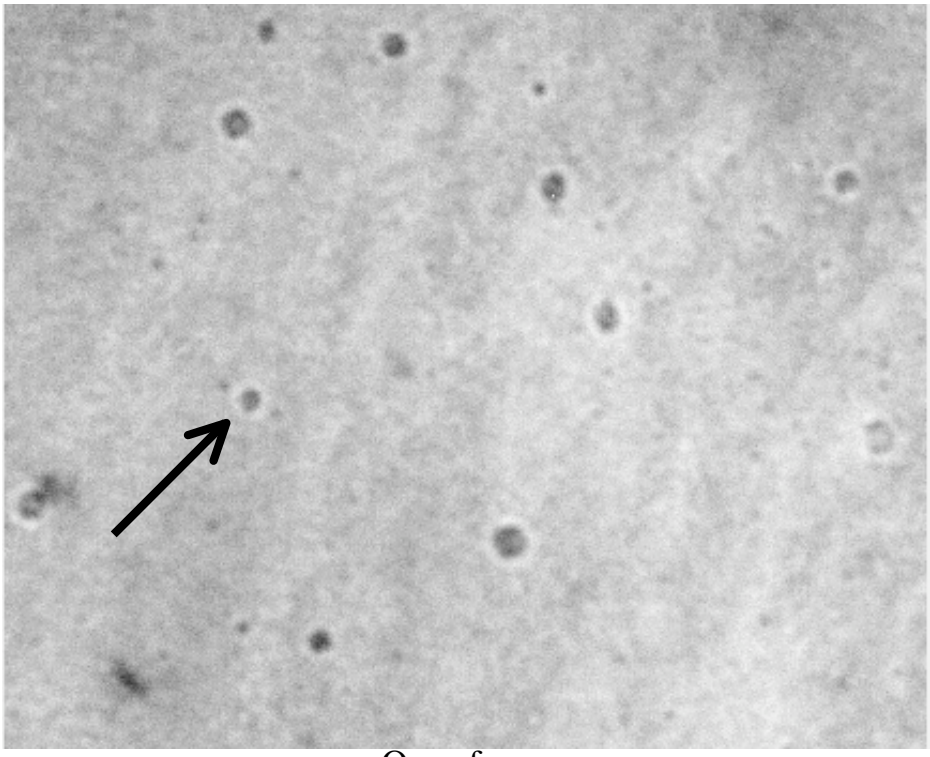

Over-focus

Figure 4.4.3The Bright Field images showing under-focus and over-focus contrast of the voids in a sample irradiated at 350 °C.

4.5 TEM in-situ straining tests

As the uniaxial tensile tests of Cu irradiated to 10^{-2} dpa showed at room temperature a yield shear stress of 37 MPa relatively to the 14 MPa of the unirradiated Cu, it is not implausible to relate the irradiation hardening to numerous radiation induced defects. In order to identify the basic mechanisms at the origin of irradiation hardening, in-situ deformation in transmission electron microscope has been performed,

The Cu specimens prepared for in-situ straining were irradiated to 4.5×10^{-4} dpa. As already reported in literature (Dai 1995) that, in this condition, the radiation induced defect density is around 5×10^{22} m^{-3} and nearly 90 % of them are SFTs.

4.5.1 Interaction between dislocation and irradiation induced defects

4.5.1.1 Dislocation movements in unirradiated materials

Here Fig. 4.5.1 shows a sequence of two dark field micrographs taken with a TV camera, during the in-situ deformation at RT. Fig. 4.5.1(a) shows in the center a dislocation line of a total of about 80 nm. It is interesting to note that, the upper part of this dislocation line shows a very slight curvature while the lower part gives a more pronounced bulge-out towards the right, generating a “hook” in the centre. In the second frame of this sequence (Fig. 4.5.1(b)), the whole dislocation line becomes more smooth and from the line tension of this dislocation segment that, under the applied stress. From the relative positions of these white spots on the two frames, one may also notice that the ends of this dislocation line shows no observable change between the them.

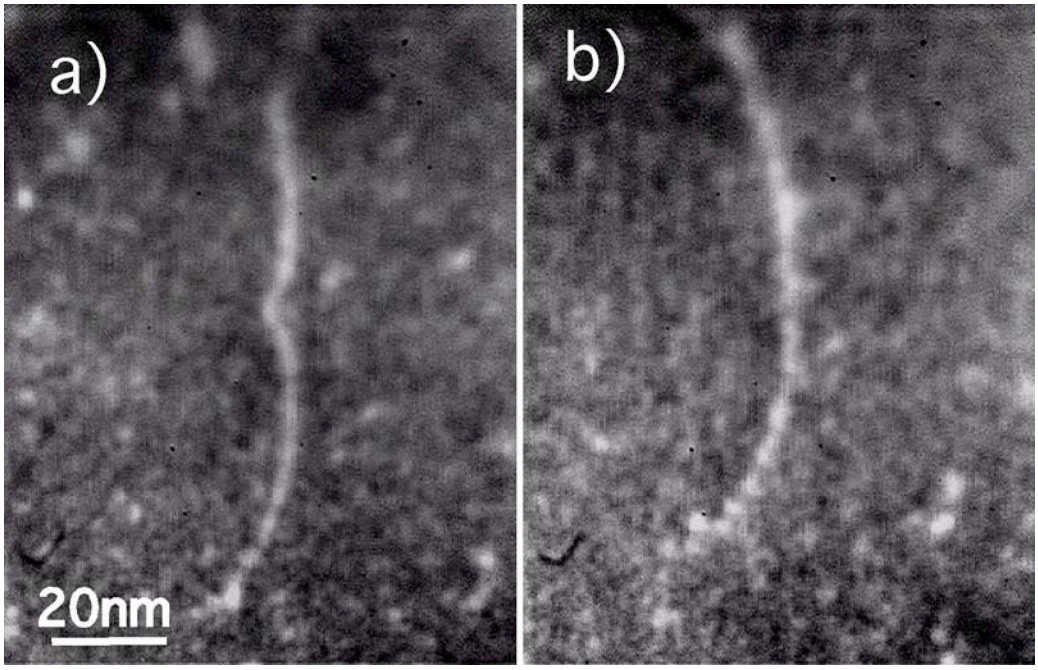

Fig. 4.5.1 Two frames taken during the in-situ deformation of an unirradiated Cu sample showing dislocation movement in a region about 80 nm thick. (a) The dislocation was pinned locally. (b) The dislocation broke away from the obstacle.

One plausible explanation of this observation is that, under the applied stress, this dislocation

line which has been blocked or locally pinned in the middle of the segment broke away from its blockage/pinning point towards the right.

Due to the relatively limited spatial resolution of TV camera, the nature of the local pinning point could not be resolved successfully. In the following observations, a slow scan charge coupled device (CCD) camera system was used instead of the TV camera in order to obtain a better spatial resolution, at the expense of time resolution.

4.5.1.2 Dislocation movements in the irradiated materials

In-situ straining tests of irradiated Cu have been performed at a low temperature (183K). Fig. 4.5.2 shows a sequence of dark field micrographs taken during the in-situ deformation at 183 K of the Cu sample irradiated to 0.0004 dpa at room temperature. The region is about 100 nm thick where irradiation induced defects appear as black dots while a number of dislocations cut through them. It shows one dislocation, as shown by small white arrows, was pinned by defects and was bowing out and escaping from the cloud of defects. In addition, some defects seem to be stronger than others, as described in what follows. One dislocation is shown in this sequence as impinging on an obstacle (large white arrow) and was unable to escape during the time of the experiment.

Fig. 4.5.3 shows the histogram of the critical stresses deduced from the measurement of the breaking angle on weak dark field micrographs. Following the model of Foreman and Markin (1966), the shear stress can be estimated with the following formula:

$$\tau_c = Gb(cos\phi_c)^{3/2}/l \qquad (4.5.1)$$

where G is shear modulus, b is the magnitude of Burgers Vector, and ϕ_c is the half breaking angle of dislocation for unpinning, l is the distance between pinning positions.

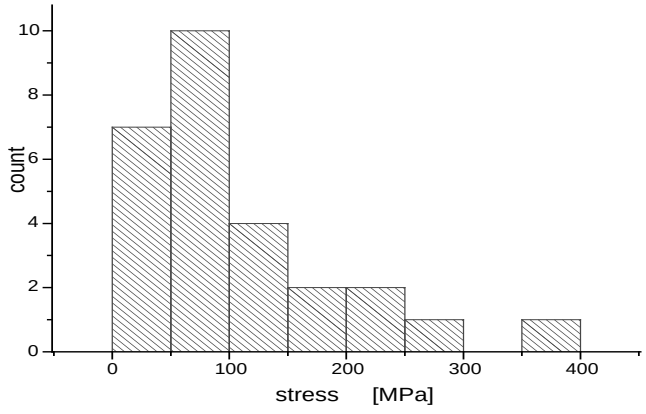

Fig. 4.5.3 Histogramme of the critical shear stress for dislocations escaping defects.

The measurement shows a peak at about 100 MPa with a mean distance between obstacles of 80 nm. Robach et al. (2003) did a similar experiment and found a value of 40 MPa but a similar escape angle. In addition, the obstacle strength of Robach et al. is 0.67, which matches the one of the present study of about 0.6. The lower critical shear stress relatively to our

measurements relate to the fact that the density of defects they have is much lower. It should be noted that this value of 100 MPa is much higher than the critical shear stress of 40 MPa measured in single crystal Cu bulk sample irradiated to the same dose level and tested at RT (see Fig. 4.1.9b compared to Fig. 4.1.9a). However, it is close to the one measured at 77 K, with a value of 82 MPa (see Fig. 4.1.9b).

Fig. 4.5.4 shows a sequence of weak beam dark field micrographs taken during the same in-situ experiment as for Fig. 4.5.2 showing one dislocation pinned, pulling a dislocation segment, and then escaping and leaving behind a debris about 30 nm long. Such remaining debris ('dislocation string'), about 20 nm to 40 nm long, have been observed to be homogeneously distributed in the strained regions. It is not clear at this point the nature of these strong pinning defects but this type of event constitutes only part of the observed dislocation-defect interactions. Most of the dislocation-defect interactions resulted in the disappearance of the defect from its original position.

Fig. 4.5.5 shows another sequence of weak beam dark field micrographs taken during the in-situ deformation of a Cu irradiated to 0.0004 dpa. It exhibits a dislocation band in motion that originates from the TEM sample edge. One SFT, as marked with the circle, interacts with one of the moving dislocations. This interaction results in a strong bowing of the dislocation, which indicates that SFT can be strong obstacles. At this temperature the formation of debris could not be repeated.

Activation volumes deduced from mechanical testing (Yao et al. 2004) at the onset of yielding have values much lower than in the unirradiated material, which correlate well qualitatively with a dislocation-defect interaction relatively to a dislocation-dislocation one. An activation energy was tentatively extracted from the activation volume but the relatively high value obtained, of 3.1 eV, and the poor quality of the necessary linear fit in the analysis had led to the conclusion that multiple dislocation-defect interaction mechanisms were operative, which impedes the type of analysis used in (Yao et al. 2004). The present in-situ experiments may support this conclusion, by the fact that the formation of debris was observed only at low temperatures.

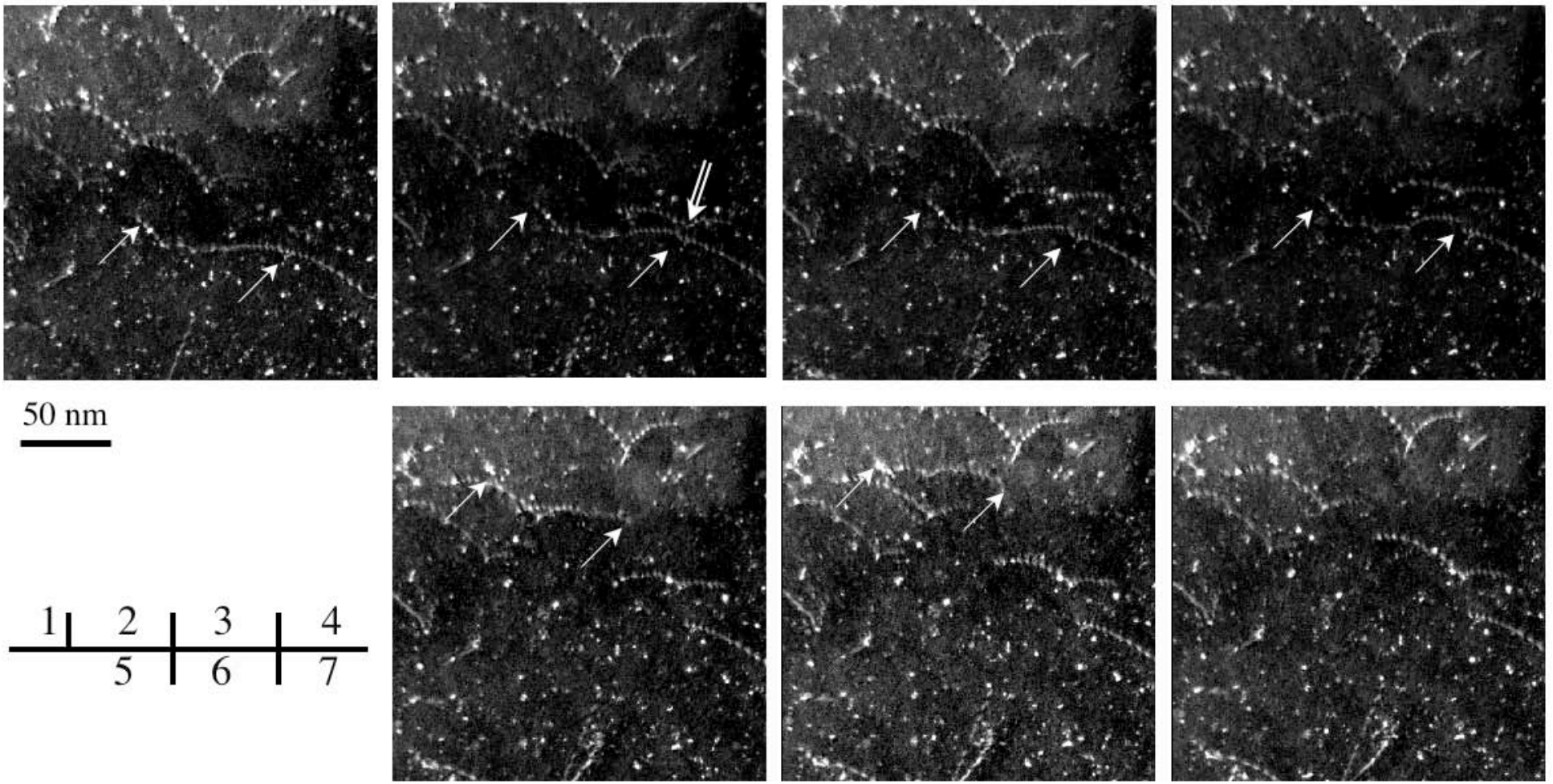

Fig. 4.5.2 In situ TEM straining of Cu irradiated to 0.1 dpa at RT, showing a pinned dislocation (thin white arrows) bowing out between pinning points and then escaping. One dislocation is strongly pinned (thick white arrow). The sequence follows the order from left to right and from top to bottom, as indicated in the table on the left.

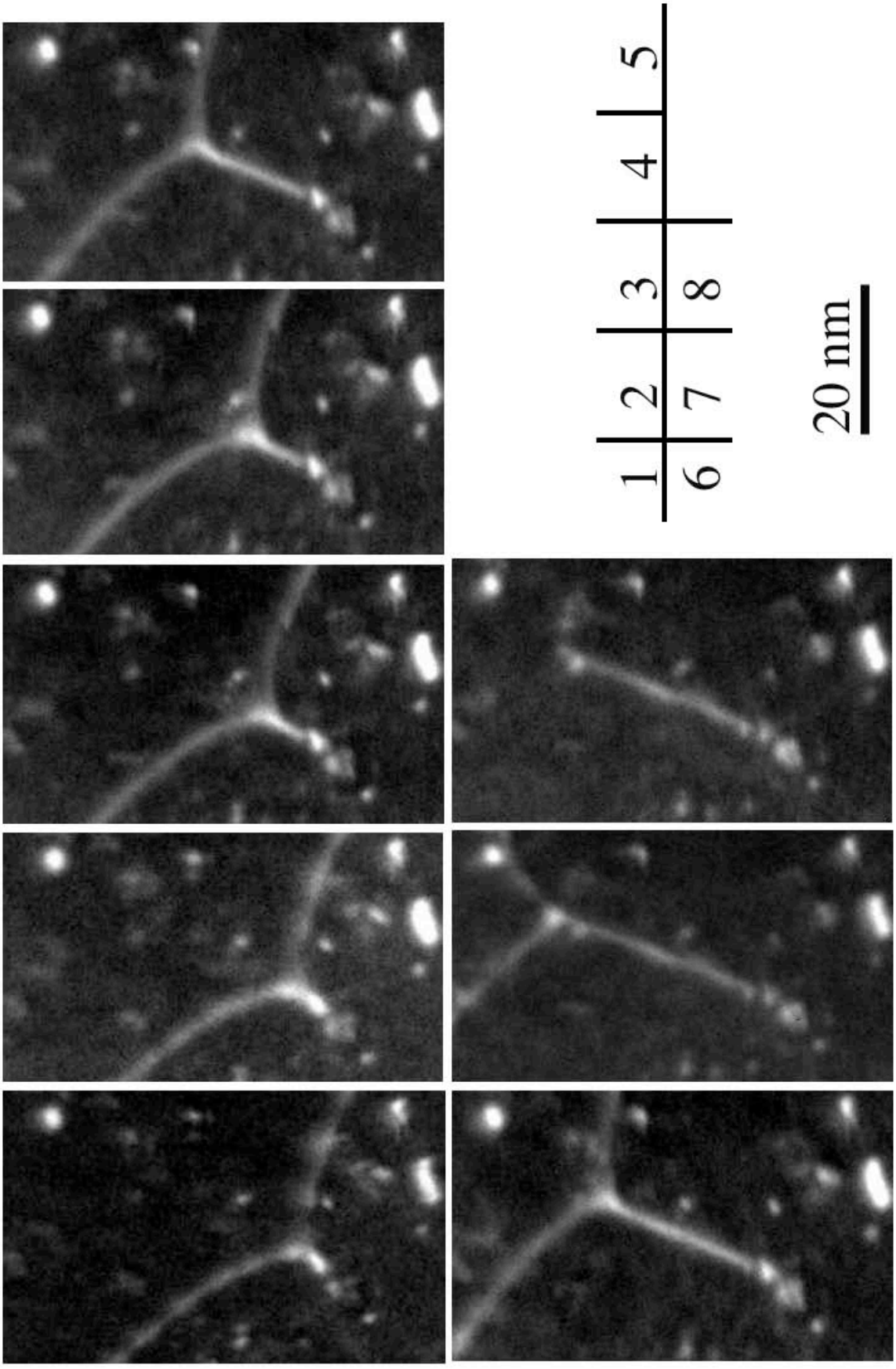

Fig. 4.5.4 In situ TEM straining experiment in Cu irradiated to 0.1 dpa at RT showing a dislocation pinned by a defect, probably an SFT, at 120 K. A dislocation string or dipole is pulled and left behind after the gliding dislocation escapes. The sequence follows the order from left to right and from top to bottom, as indicated in the table on the right.

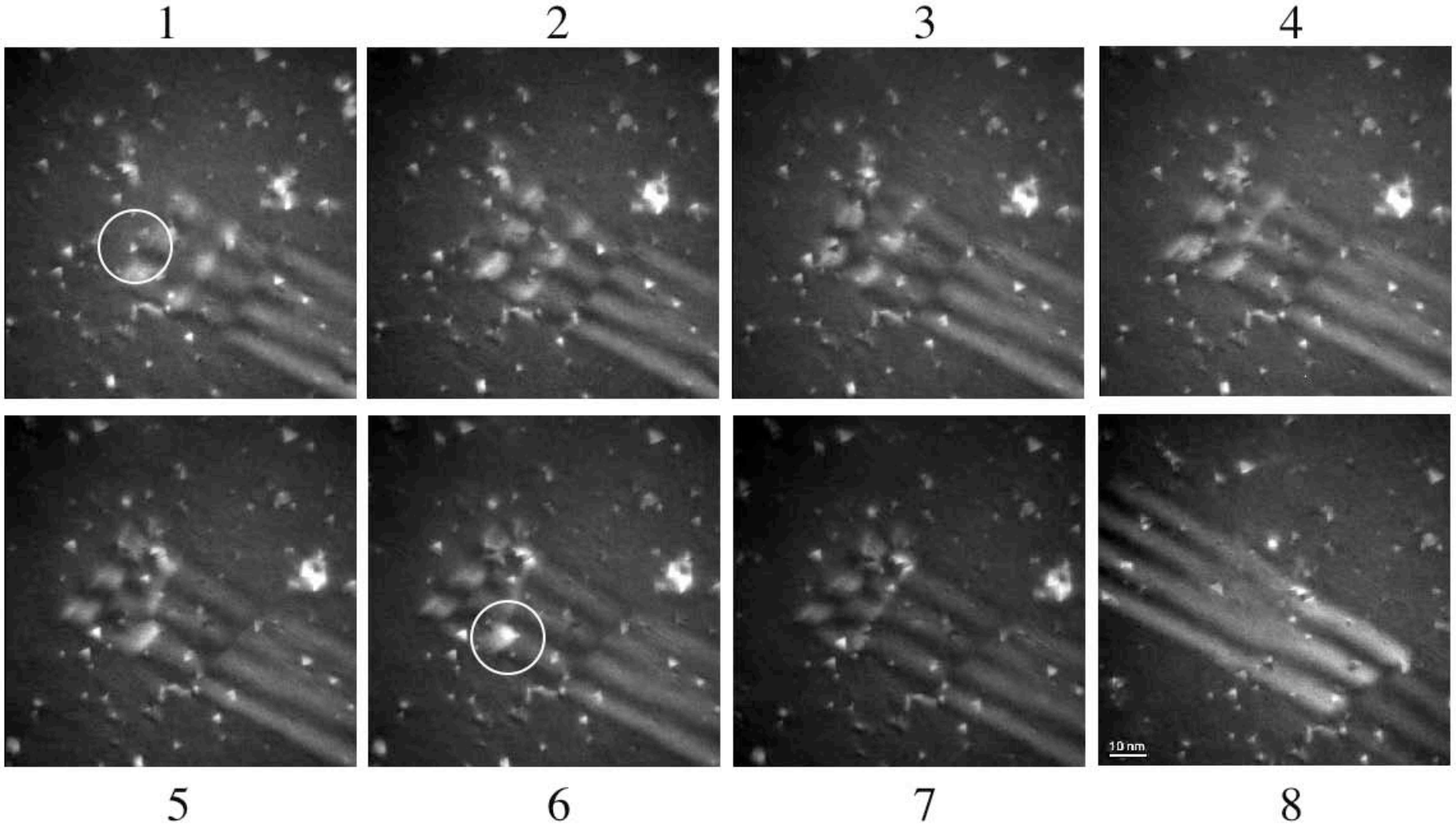

Fig. 4.5.5 In situ TEM straining experiment in Cu irradiated to 0.1 dpa at RT showing a dislocation band and SFTs at 370 K. One of the dislocation interactss with one of the SFTs (circled in white), is strongly pinned and then escapes. The SFT is destroyed.

4.6 MD simulation of displacement cascades

In the present work four different EAM potentials were employed for the MD simulations. These potentials were selected in order to investigate the effect of the stacking fault energy (γ). Table 4.6.1 summarizes the characteristics of these potentials as compared to experimental values. The reported values are the lattice parameter (a_0), the radius of cut off of the potential (r_{cut}), the displacement threshold energy (E_d), the elastic constants C_{11}, C_{12} and C_{44}, the bulk modulus (B) and the stacking fault energy (γ). The displacement threshold energy was deduced from simulations by starting pka(s) in random crystallographic directions with increasing energies until the atom was displaced from its lattice site and would not return to it after cooling. The indicated range of values in the table corresponds to the minimum and maximum displacement threshold energies obtained in the simulations, corresponding to the softer (<100>) and harder (<110>) crystallographic directions, respectively.

The so-called Farkas-1 and Farkas-2 potentials (Mishin et al. 1999) were tailored to specific stacking fault energy values corresponding to half and to exactly the experimental value, respectively. While the so-called Cleri-Rosato is an earlier potential (Cleri and Rosato, 1993) frequently used in this area with a stacking fault energy that is more than twice as large as the experimental value. The Cleri-Rosato-AA is a modified Cleri-Rosato potential in order to take into account high energy collisions more accurately (Caturla et al. 2000). This is done by using the universal potential of Ziegler et al. (1985) instead of the Cleri-Rosato potential for interatomics distances between 0 and 1 to 2 Å. The smooth connection between the two potentials is made by fitting a spline. The resulting displacement threshold energy is closer to the experimental value than the one given by the original potential. The elastic properties and the stacking fault energy remain the same, as they are related to interatomic distances beyond the range of the part modified by the universal potential.

Table 4.6.1 The basic parameters of the four potentials:

	a_0/r_{cut} [Å]	Threshold energy [eV]	C_{11}	C_{12}	C_{44}	B [10^{11}Pa]	γ [mJ•m^{-2}]
Experimental	3.523	40	2.47	1.47	1.25	1.81	125
Farkas-1	3.519 / 4.7895	30-60	-	-	-	-	61
Farkas-2	3.523 / 5.8038	15-25	2.47	1.48	1.25	1.81	125
Cleri-Rosato	3.523 / 5.8714	90-300	2.33	1.54	1.28	1.80	300
Cleri-Rosato-AA	3.523 / 4.6485	40-80	2.33	1.54	1.28	1.80	300

4.6.1 Constructing an SFT by MD

Among irradiation induced defects in Ni and Cu, the SFT is one of the most extensively studied recently because of its specific configuration and of the scientific curiosity in understanding its role in the irradiation induced hardening mechanisms. Silcox and Hirsch (1959) proposed an SFT formation mechanism. A vacancy disc nucleates on a {111} plane, changes its shape to a triangular one with <110> edges and subsequently collapses into an SFT.

An SFT can be achieved using the same mechanism in MD simulation (Osetsky et al. 1999, Wirth et al. 2001). A triangular platelet of vacancies is placed onto a {111} plane by removing atoms from it. Then the sample containing the vacancy platelet of a given size is annealed at a given temperature and time until it collapses to an SFT, provided the potential and conditions (size, temperature and time) allow it.

According to the present experimental work the observed mean SFT size in irradiated Ni remains approximately 1.5 nm in RT irradiation over a wide irradiation dose and grows to 3.5 nm in 250 °C irradiation. So the size scale of the simulated SFTs was selected from ~ 0.7 nm to ~ 3 nm. Here, according to the above mentioned mechanism with three steps, a triangular vacancy platelet was used to form SFT by MD simulation, as shown in fig. 4.6.1A. The size of SFT is pre-defined by the size of this triangle: a triangle of 6 vacancies leads to an SFT of 0.7 nm, 15 vacancies lead to 1.5 nm and 66 vacancies lead to 3 nm.

A simulation box of 24×24×24 (in lattice units) was used for the relaxation at temperatures from 500 K to 800 K. The duration of annealing took about 1 to 2 ps. After annealing the system potential energy is minimized by using the conjugate gradient method.

In order to identify the defect configuration we used the so-called 'common neighbor analysis' (CNA) method presented in section 3.2 (see Fig. 4.6.1 for example).

The main results are summarized as following:

i) The platelet of 6 vacancies did not collapse to SFT regardless of the annealing conditions, but formed a void in fig. 4.6.1B while relaxing above 800K, for all selected potentials, but below this temperature it remains a platelet shape without any transformation.

ii) The platelet of 15 vacancies collapsed into an SFT (fig. 4.6.1D) when simulated with Farkas-I and Farkas-II potentials at 500 K. It remains the original platelet shape when Cleri-Rosato and Cleri-Rosato-AA potentials are used.

iii). The platelet of 66 vacancies much easily collapsed to an SFT at 500K as shown in Fig. 4.6.1E, for all the four potentials applied. The collapse occurred even with the very high stacking fault energy Cleri-Rosato potential.

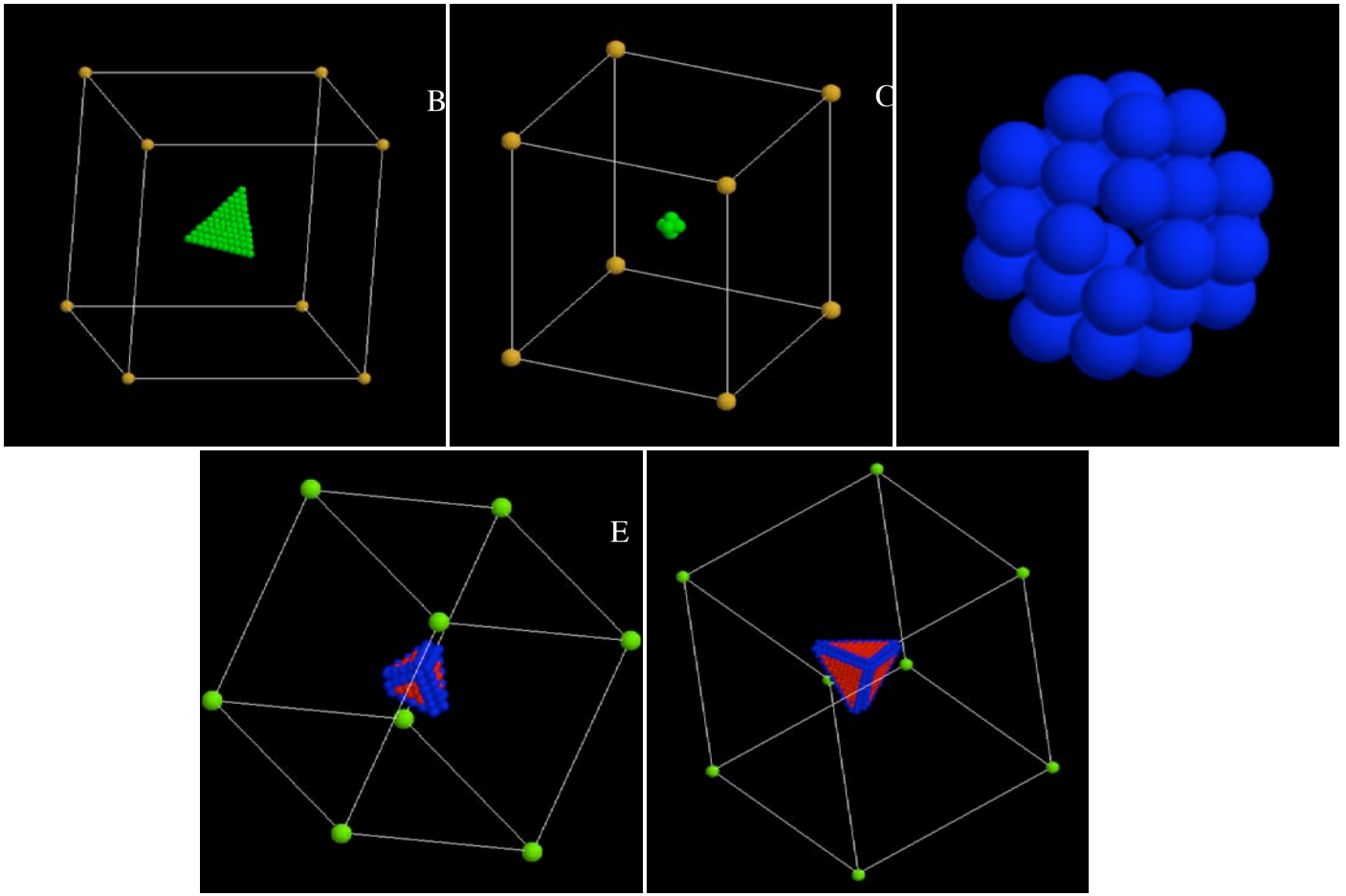

Fig. 4.6.1 The MD relaxation of a triangular platelet. A) a triangular platelet with 66 vacancies, habiting at the centre of box. B) a void formed by relaxing a 6v platelet. C) a void formed by relaxing a 15v platelet with Cleri-Rosato potential. D) A SFT was collapsed from a 15v platelet with Farkas-I potential. E) A SFT was collapsed from a 15v platelet with Cleri-Rosato-AA potential. The green balls represent the vacancies, and red balls are atoms with hcp structure, and blue balls are atoms with non fcc, non hcp structure.

4.6.2 Cascade simulation

In present work, a number of calculations of cascades with different conditions have been carried out. Before launching a PKA, the simulation box was annealed for about 1ps, in order to get a relative equilibrium condition of the system, in particular for what concerns the phonon spectrum. One atom of system was selected as the PKA, with an ideal shooting angle and position. The angle should not be too close to a crystallographic direction to avoid channeling.

After shooting the PKA, a thermal bath residing in boundary layers starts to operate to simulate a real situation, where the sample is embedded in a large matrix or bulk that has a fixed temperature. The temperature in the thermal bath is reset to a fixed value every 100 steps (100 fs) to mimic thermal conduction to the bulk. Fig. 4.6.2a-c shows typical cross sectional views of a Ni specimen in which a 40 keV cascade evolves. Fig. 4.6.2.d and e indicate that temperature and potential energy change with time, and a thermal spike appears within 1.5 to 2 ps after the PKA.

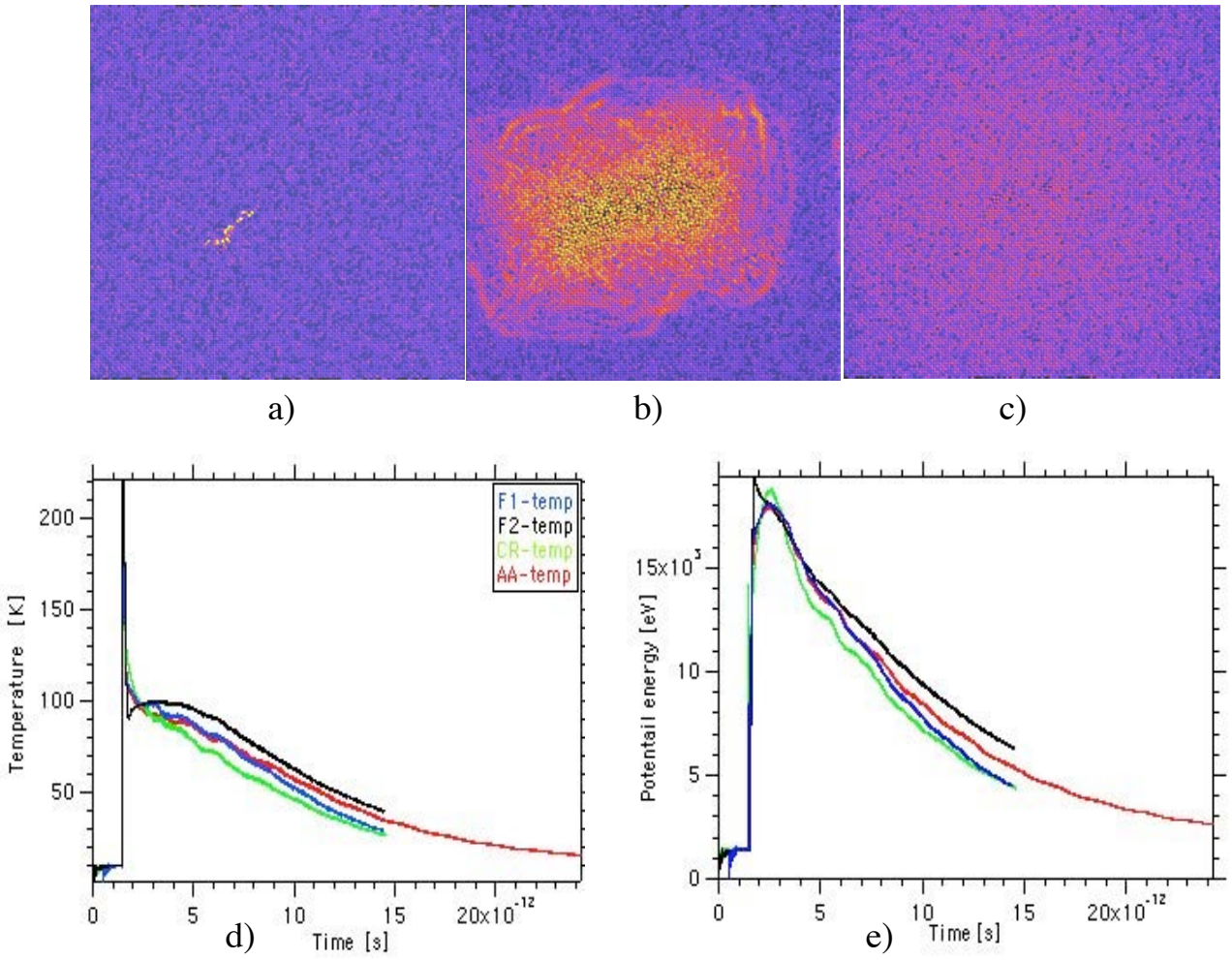

Fig. 4.6.2 View in cross section of a developing 40 keV cascade in Ni at 0.1ps (a) showing first collisions, at 0.8 ps (b) showing shock wave propagation and hot core and at 25 ps (c) showing the cool down and the recrystallization of the molten core, respectively, after the first collision. Sample is 1 million atoms and side length is 22.9 nm. Color represents kinetic energy (blue: cold, yellow: hot). (d) Temperature and (e) potential energy as a function of time and of the potentials used.

4.6.2.1 Cascade simulation with four different potentials

30 keV cascades are selected to compare the influence of the four potentials on the resulting damage. The CNA analysis is shown in table 4.6.2 and Fig. 4.6.3 and summarized as following:

i) Farkas-I and Farkas-II potentials give rise to similar defect structures. No large clusters are formed and defects are scattered, in the form of small clusters or individual point defects. Farkas-II gives a higher density of defects than Farkas-I. Farkas-I gives rise to small loops. Surprisingly, there is no SFT or SFT-like structures visible, even though the stacking fault energy is low. However, Farkas-I, with the lowest stacking fault energy, does produce more hcp atoms, which relate to a stacking fault.

ii) In fig. 4.6.3c and d, produced with the Cleri-Rosato potential as received and modified respectively, SFT-like structures appear close to the core of cascades. Also, an isolated interstitial loop is found in fig. 4.6.3c.

iii) The maximum number of Frenkel pairs is reached with the Cleri-Rosato potential, which has the largest displacement threshold energy (90~200 eV). As HCP atoms reflect information on stacking fault areas, it appears that Fig. 4.6.3c shows a large number of stacking faults, even though the potential presents the highest stacking fault energy (300 $mJ \bullet m^{-2}$).

Table 4.6 2 The statistic numbers of vacancies and interstitials, and clusters resulted from cascade with a 30 keV PKA input.

	Number of interstitials	Number of vacancies	Number of Clusters(I/v)	HCP atoms / Non FCC atoms
FI	66	66	13 / 7	97 / 1363
FII	141	141	15 / 21	12 / 3522
Cleri-Rosato	169	169	30 / 31	931 / 1723
Cleri-Rosato-A.A	129	129	25 / 20	174 / 1902

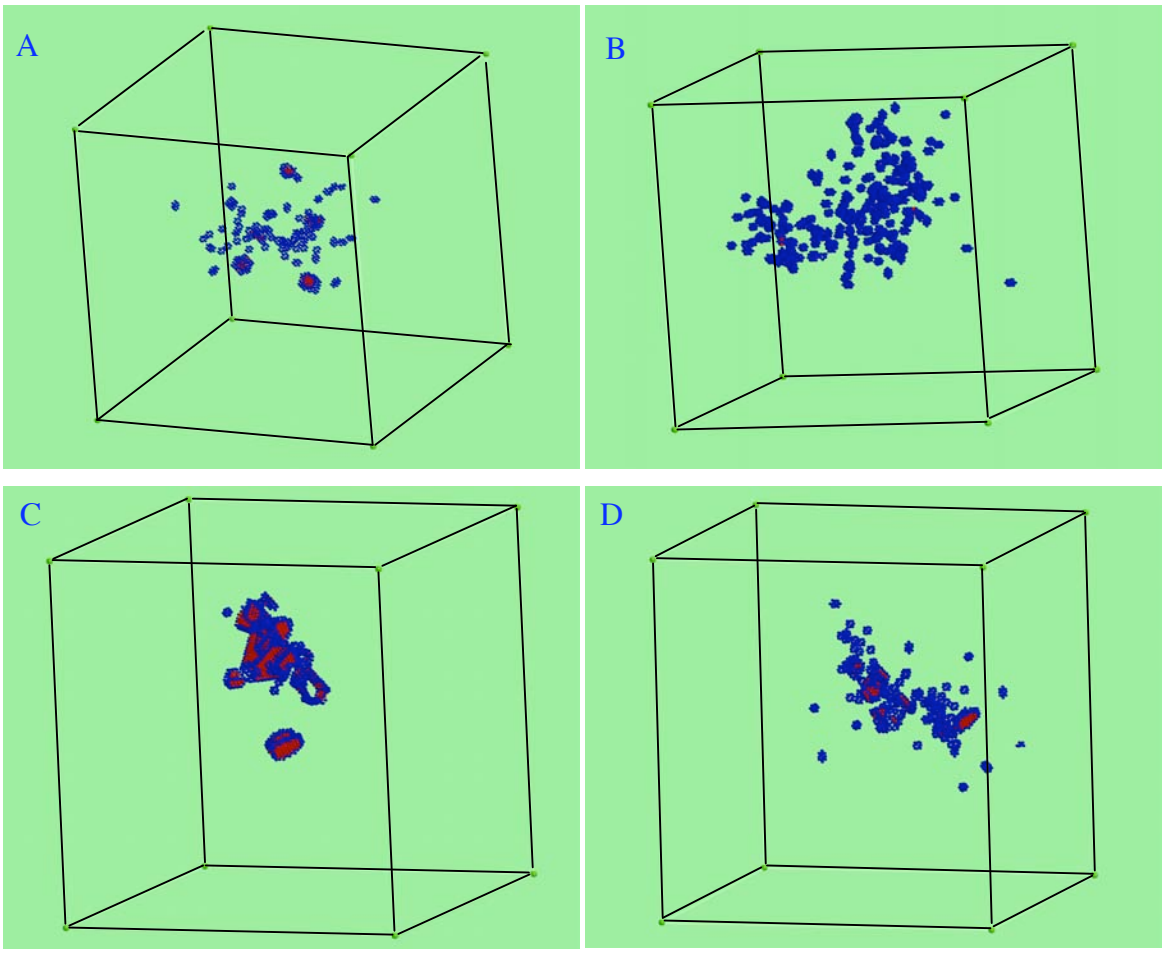

Fig. 4.6.3 The red balls show atoms with hcp structure, and blue balls are atoms with non fcc, non hcp structure. A), B), C) and D) are results by using Farkas-I, Farkas-II, Cleri-Rosato and Cleri-Rosato-AA potentials, respectively

4.6.2.2 Energy dependence of N_{FP}

The dependence of the number of the defects or Frenkel pairs produced for PKA energies from 5 keV to 40 keV, at different temperatures and potentials is reported in table 4.6.3, together with the number of Frenkel pairs evaluated using NRT model (see equation 1.1.1.3), shown in the parenthesis ().

Table 4.6.3 The number of resulting Frenkel pairs (N_{FP}) produced by MD with different PKA energy and potentials. The NRT values are reported in parenthesis.

	Farkas I			Farkas II			Cleri-Rosato			Cleri-Rosato-AA		
	10K	100K	300K	10K	100K	300K	10K	100K	300K	10K	100K	300K
5keV	6 (50)	8	-	47 (100)	44	42	-(20)	-	-	9 (50)	5	12
10keV	17 (100)	14	15	76 (200)	96	80	369 (40)	-	-	49 (100)	23	30
20keV	37 (200)	38	30	107 (400)	120	114	74 (80)	-	-	104 (200)	44	65
30keV	66 (300)	61	45	141 (600)	201	160	169 (120)	-	-	129 (300)	139	70
40keV	-(400)	61	52	266 (800)	205	181	1335 (160)	-	-	272 (400)	171	124

Chapter V Discussion

Results will be discussed in six sections:

(i) Irradiation induced defects,
(ii) Molecular dynamics simulation of displacement cascades,
(iii) Irradiation induced hardening,
(iv) Work hardening during plastic deformation,
(v) In-situ TEM deformation,
(vi) Synthesis of hardening modeling.

In the first two parts the case of irradiated Ni will be discussed. In the third and fourth parts the discussion is not only on the results obtained for Ni but also on the ones obtained for Cu. In the fifth section the TEM in-situ deformation of Cu is discussed and in the last part an attempt to synthesize results in a hardening model is presented.

5.1 Irradiation induced defect formation and accumulation

5.1.1 Irradiation induced defects microstructures

The results on the irradiation induced defects in Ni single crystal are presented and are critically compared to existing results in the open literature. They are characterized by their mean size, size distribution, density and nature as a function of irradiation dose and temperature. In addition, these results are compared to the ones obtained in Cu.

5.1.1.1 The dose dependence of defect density and size distribution.

Experimental results show that the defect density depends linearly on the irradiation dose at low doses, at which there is no cascade overlap and, after a transition regime, tends to saturation at high doses. It should be mentioned that this dependence is discussed for a single irradiation temperature, as the temperature dependence is beyond the scope of this discussion.

Earlier studies show that in Ni in particular, for a given irradiation temperature, a similar dependence on dose was found. Kirk et al. (1987) and Robertson et al. (1991) performed these experiments by ion implantation. Both of them used 100 keV Ni^+ to irradiate pure Ni. In their work, the dose and defect density are represented in units of ions m^{-2} and units of m^{-2}, respectively. Kirk et al (1987) show that when the dose changes from 5×10^{16} to 7×10^{16} ions m^{-2} the defect density reaches saturation after a linear increase with increasing dose. The saturation value was identified to be at a dose of about 5.3×10^{15} m^{-2}. Robertson et al. (1991) shows that such a transition appears between 7.5×10^{16} ions m^{-2} and 1.3×10^{17} ions m^{-2}, with a saturation occuring at a dose of about 8×10^{15} m^{-2}.

In this work, in order to compare these results to results obtained by other irradiation methods where the dose is measured in dpa, the units were converted from ions m^{-2} to dpa. A simulation programme called SRIM (Biersack and Ziegler 1998) was deployed in this frame. This programme allows simulating the damage resulting from impinging particles by a simplified Monte Carlo scheme, which allows deducing the number of Frenkel pairs resulting from such an interaction. The results from Kirk et al. (1987) and Robertson et al. (1991) were in this way scaled to dpa and are reported in Fig. 5.1.1. Fig. 5.1.1 contains also results from this work and other research groups obtained by other irradiation techniques. It appears that these data are comparable to the results and previous data reported by Kiritani et al (1987, 1990) and Zinkle and Snead (1995) (Fig. 5.1.1).

It is clearly shown that the defect density in the irradiated thin foil is more or less 50 % of that found in bulk material. In the latter case, where bulk specimens are irradiated, saturation of the defect density (~ 2×10^{23} m^{-3}) appears at a dose of around 0.01 dpa. In the previous case, where thin specimens are irradiated, the saturation (~ 5×10^{23} m^{-3}) appears at a higher dose of around 0.03 dpa. This discrepancy between thin foil and bulk is certainly caused by the image forces induced by the presence of the free surfaces in the thin foil relatively to the bulk case, allowing interstitials or interstitial clusters escaping the foil. Given that this is the sole factor that accounts for the lesser defect density observed in thin foils, one might expect that the

SFT fraction on the total defect population in thin foil should be much higher in thin foil than that in bulk. Assuming that in bulk a constant fraction, say 40 %, of the total defects consists in SFT, then assuming that in thin foil only interstitials (about 50 % of total defects) escaped to the foil surface, the fraction of SFT should reach nearly 80 % relatively. Unfortunately, Robertson et al. (1991) carefully checked a population of 539 loops at DFWB g(200) from zone axis <011>, even assuming that all unassigned defects are SFT, a maximum fraction that could be present is 40 %.

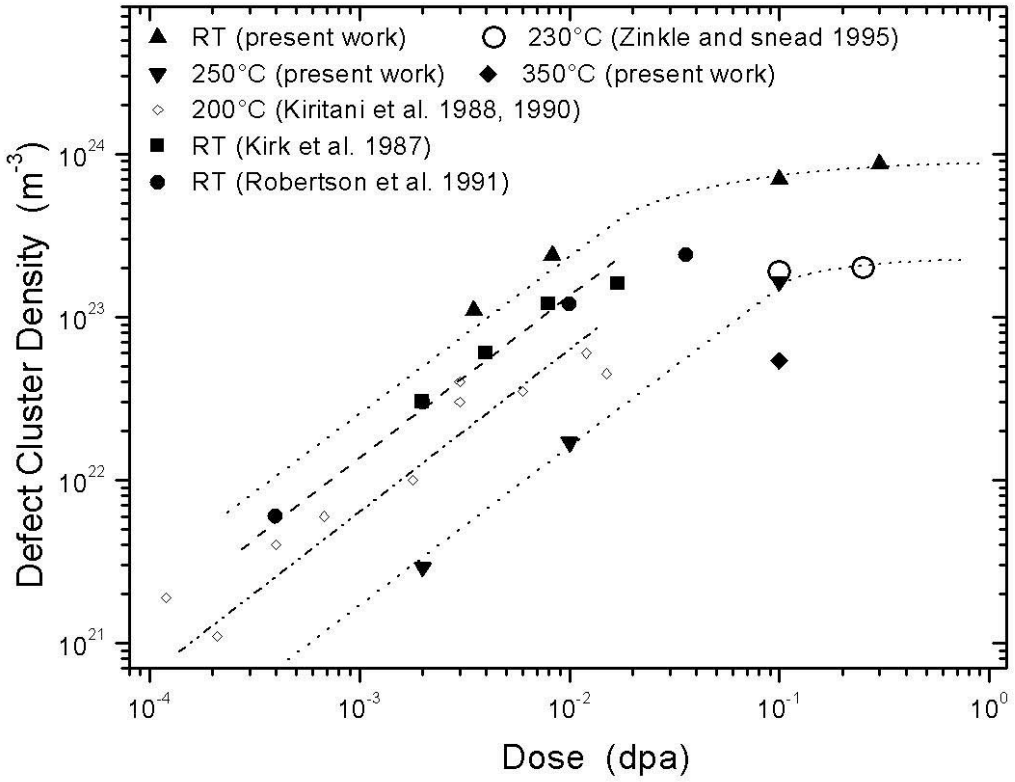

Fig. 5.1.1 The dose dependence of defect density in pure Ni irradiated by protons, ions and neutrons, respectively.

5.1.1.2 Irradiation temperature dependence of defect density and size distribution

In Fig. 5.1.1, the data for Ni irradiated at 200 °C by Kiritani et al. (1987, 1990) and Ni irradiated at 230 °C by Zinkle and Snead (1995) are plotted. With increasing temperatures, the defects density decreases. It is 3 times less at 250 °C than at RT. In the case of the 250 °C irradiation, these numbers decreases to less than 50 % of that of the 200 °C irradiation. The defect density due to the 350 °C irradiation decreases to one third of the one of the 250 °C irradiation. The reduction of defect density can be explained by the fact that with increasing temperature the mobility of interstitials and vacancies increases, which induces agglomeration of free interstitials and vacancies to larger clusters, a the expense of smaller ones, thus decreasing the defect density. In table 4.4.1, the mean size of defects increases from ~ 2nm at RT to ~ 4 nm at 250 °C and ~ 5 nm at 350 °C. While a high density of voids appears at 350 °C, the SFT concentration and fraction decrease to large extent. The mean size of SFTs meanwhile tends to be larger than that at 250 °C.

Kojima et al. (1988) observed a small number of voids in bulk Ni irradiated at 200 °C. He claimed that two mechanisms operate at different temperatures: 1) at 300 K free interstitials play a major role; 2) at higher temperatures, single vacancies are mobile, and the stability of vacancy clusters becomes an important factor in the microstructure evolution. Their results show a rapid decrease of SFT stability when reaching high temperatures. Kojima noted that SFTs can still absorb single vacancies at 200 °C. This mechanism was used to explain the observation that voids did not grow until a temperature of 623 K was reached.

Kiritani et al. (1990) concluded that in Ni thin foil voids formed at 673 K, while more recently Yoshiie et al. (2002) showed that vacancies start to aggregate at a low dose of 0.0026 dpa at 300 °C. From our observation, voids do not appear as visible defects at 250 °C, but become visible and promptly grow over 250 °C, as shown in Fig. 4.4.3. Following the size distribution of SFTs, and with the idea of Kojima in mind, it appears that SFTs do not shrink, but grow too. However, it should be mentioned that the fraction of SFTs decreases from 40~50 % to about 10 % only, when going from RT to 350 °C. The concentration of SFT is hence decreased by more than 90 % relatively to the 250 °C irradiation, while the total defect density at 350 °C is one third of that at 250 °C. In fact SFTs do not show shrinking, but a reduction in their number density. This will be discussed together with our annealing in-situ TEM experiments. It appears that SFTs in Ni need a higher temperature than 350 °C for shrinking or collapsing.

It should be noted however that in our case, where samples are irradiated with 590 MeV protons, a high proportion of He is generated by transmutation during the irradiation. These He atoms will contribute to the stabilization of defects, and in particular the defects formed by vacancies, that is to say SFTs and voids.

The void density measured in Ni irradiated at 350 °C is approximately one order of magnitude larger than that reported in the literature (Muroga et al. 1988). One plausible reason could be the high production of Helium in PIREX (Marmy et al. 1990), which has a He production rate ~150 appm per dpa. Thus in this sample at least 15 appm He should be produced, which can significantly facilitate the nucleation of voids.

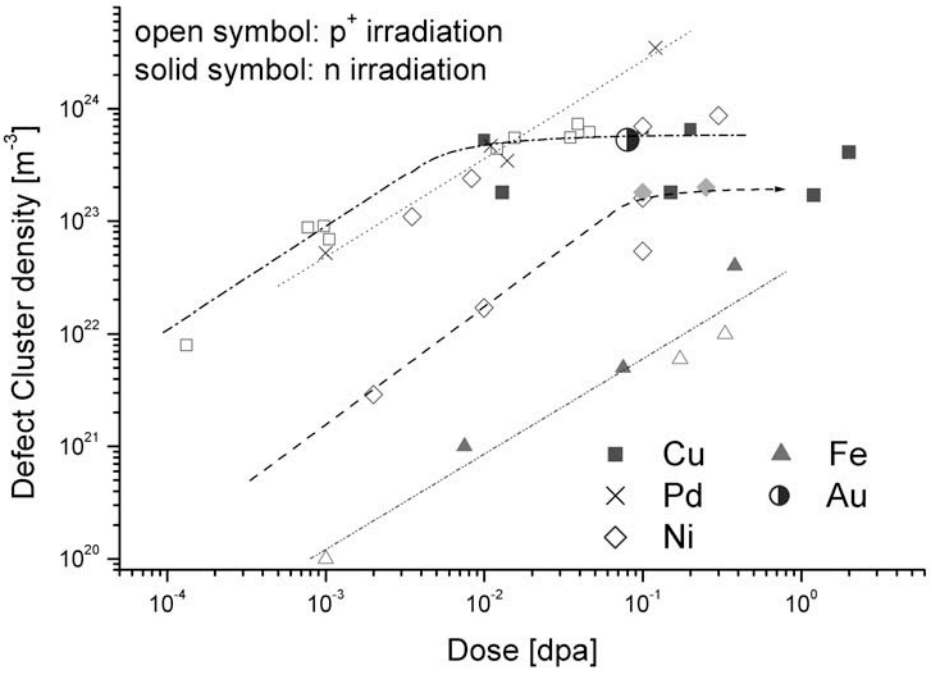

Fig. 5.1.2 The dose dependence of defect density, including Ni (present work), Cu (Dai 1995, Zinkle 1992), Pd (Baluc 1999), Au (Dai et al. 1995) and bcc metal Fe (Luppo et al. 2000).

5.1.1.3 Comparison between irradiation induced defects in Ni and those in other fcc and bcc metals

In Fig. 5.1.2, the defect density of Ni is compared with other pure fcc metals, Cu, Au, Pd and a typical bcc metal, pure Fe following RT irradiation. We will focus on two questions:
1) Does Ni have a different defect production rate from other fcc metals ?
2) Does SFT formation relate to the stacking fault energy (SFE) ?

Singh et al. (1993), Zinkle and Snead (1995) concluded, from a large collection of previous data, that Ni has a different behaviour of defect accumulation than Cu. They reported that the total defect density observed in copper at homologous temperatures below 0.3 T_M (for Cu it is 135 °C, and for Ni it is 245 °C) is a factor of 5 to 10 higher than that observed in irradiated nickel. Several authors tried to use the thermal spike model of displacement cascades to explain this difference. But no solid evidence shows that displacement cascades in nickel would be expected to be quenched more rapidly than in copper. One may consider a difference in electron-phonon coupling (Caro and Victoria) between these two materials that would lead to a difference in the cooling rate of the thermal spike, but no quantitative argument can be raised at this point.

As the present work shows, the 590 MeV protons irradiations at RT in nickel as compared to copper (Dai 1995) do not induce a very different density of defects, as show in Fig. 5.1.2, even when comparing to the data from neutrons irradiation of Cu. In fact, as shown in Fig. 5.1.2, the other fcc metals, palladium and gold, do show a similar defect density when irradiated to similar dose levels at room temperature.

The 250°C irradiation in Ni gives a defect density that is much lower than the one at RT irradiation. The results at 250°C irradiation in Ni do match the ones of Zinkle and Snead (1995) of their 230°C irradiation. Obviously $0.3T_M$, corresponding to 245°C, cannot be strictly taken as the temperature of occurence of stage V, and probably stage V occurs at a temperature between RT and $0.3T_M$. Thus when comparing the defect accumulation between two metals, the temperature regime, in terms of annealing stage, has to be precisely the same. In other words the metals should be irradiated at the same homologous temperature. These results imply that actually the defect accumulation is very sensitive to irradiation temperature.

Defects are accumulated more efficiently in all these fcc metals than in bcc iron. This was interpreted by Nordlund et al. (2000) by saying that interstitials arising from cascades in bcc Fe are more mobile than the ones in fcc Cu. They would then be more prone to annihilation with neighbouring vacancies, thus reducing the final defect density.

The SFT fraction is still an open issue for these fcc metals. In irradiated Cu (Victoria et al. 2000), more than 90 % of total defects are recognized as SFTs. In irradiated Pd (Schaeublin et al. 2004), nearly 50 % of defects are SFTs. Al is generally not considered in this issue, as until very recently no SFT were ever observed after irradiation by neutrons, protons or ions at RT, but only loops. It is only recently that Satoh et al. (2003) observed SFTs in Al after a low temperature electron irradiation. It was recognized that the stacking fault energy, γ, is one of key parameters to the formation of SFTs (Coulomb 1978). Nevertheless, Pd, which has a γ of 180 mJ m^{-2}, does exhibit a significant ratio of SFTs, while Al, which has a similar γ, of 200 mJ m^{-2}, shows generally exclusively dislocation loops. In this respect Pd is closer to Cu, which has a γ value of 70 mJ m^{-2}. Schaeublin et al. (2004) calculated the elastic energy of a number of defect configurations including the SFT, in order to identify other key parameters.

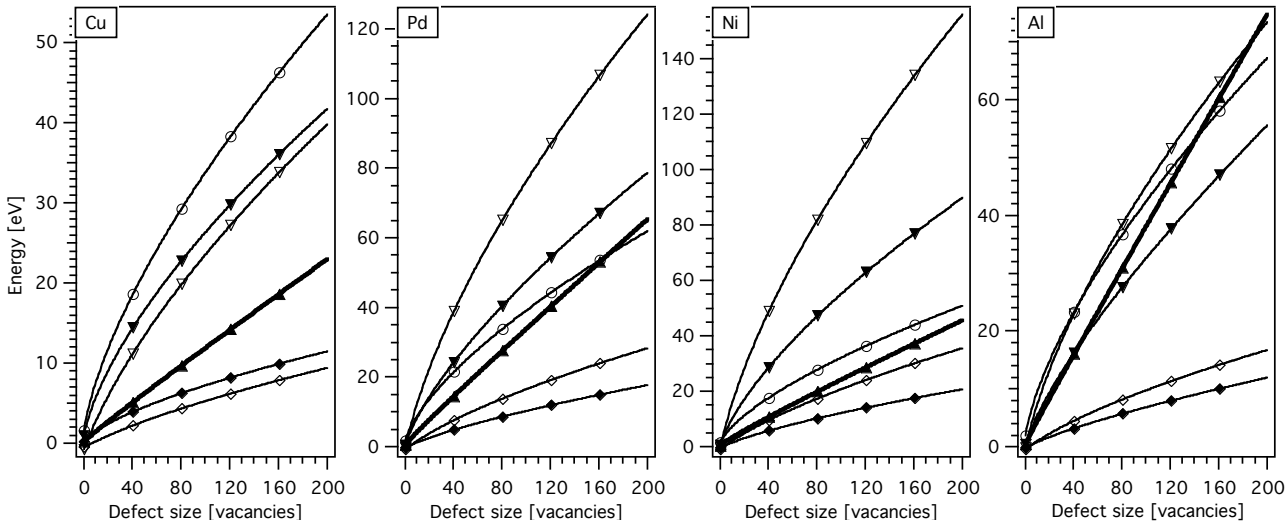

Fig. 5.1.3 Elastic energy in Cu, Ni, Pd and Al as a function of the number of vacancies of (▲) an SFT, a Frank (▼) triangular and (◆) hexagonal loop, a perfect (∇) triangular and (◊) hexagonal loop and (O) a void.

The elastic energy of a range of defect configurations formed by vacancies has been calculated according to the analytical relations given in Hirth and Lothe (1982). As only a qualitative analysis was sought after the detail of dislocation core energy, whose quantitative influences can be found for instance in Condat and Fayard (1978), was left aside.

One the most striking features of these calculations is the fact that Al has the highest relative SFT elastic energy. When analyzing in Fig. 5.1.3 the influence of the different parameters used in the calculations, reported in table 1, it appears that the key parameters for SFT elastic energy are the shear modulus, μ, and m. This was recognized earlier (Czjzek et al. 1962) and reported by Friedel (1967). It is said that when the reduced stacking fault energy, m/μb, where b is the Burgers vector of the perfect dislocation, is smaller than 1/80 SFTs are more favorable than circular Frank loops, and hence more favorable than perfect ones. For Cu, Ni, Pd and Al m/μb is equal to 1/192, 1/170, 1/66 and 1/38, respectively. From our experimental results showing SFTs in Pd, the value suggested by Friedel of 1/80 appears to be too conservative, by a factor of about two as it should be somewhere between the one of Pd and the one of Al.

Table 5.1 Material parameters used in the elastic energy calculation of various defect configurations. Data from Hirth and Lothe (1982) apart from the stacking fault energy of Ni from Carter and Holmes (1982).

	Stacking fault energy	Shear modulus	Poisson's ratio	Lattice parameter	Burgers vector **b** [10^{-9} m]		
	γ [10^{-3} J/m^2]	m [10^{10} N/m^2]	n	a_o [10^{-9} m]	a_o/2<110>	a_o/3<111>	a_o/6<110>
Ni	140	9.47	0.276	0.3524	0.2492	0.2034	0.0831
Cu	73	5.46	0.324	0.3615	0.2556	0.2087	0.0852
Pd	180	4.77	0.385	0.3887	0.2479	0.2244	0.0916
Al	200	2.65	0.347	0.4049	0.2863	0.2338	0.0954

The interplay between γ and μ means, in other words, that when the material is hard and even in the case of a high γ, it might be more favorable to form the SFT by accommodating the smaller displacement field required for the tiny dislocations bordering it, than to form the loop by forcing the way for the broader displacement field of the larger dislocation that bounds it. However, while this may hold in the frame of the Silcox-Hirsch mechanism of formation of SFTs, it does not give indications on the kinetic path of formation of the SFT by a displacement cascade. Furthermore, our elastic energy calculations show that the triangular loop necessary in this mechanism has a much higher energy than the SFT and the hexagonal loop. This suggests that the SFTs result from a local adjustment of adjacent and coherent nanocrystallites that form simultaneously in the solidifying core of the cooling cascade.

5.1.1.4 In situ TEM annealing

In order to investigate the influence of temperature on the defect stability, in-situ TEM annealing has been performed. It may help explaining the situation in the bulk, such as why in the case of 350°C irradiation Ni SFTs still grow, while a high density of voids appear. Some authors (Kojima 1988) thought single vacancies would preferentially migrate to voids than to SFTs.

Ni was left aside for this type of test as magnetism renders this type of experiments difficult. Cu TEM samples irradiated to 10^{-2} dpa with 590 MeV protons were used for this testing. In-situ heating test has been described in Chapter II. The experiment consisted in isochronal anneals and at each temperature a series of micrographs were acquired. Resulting micrographs are displayed in Fig. 5.1.4.

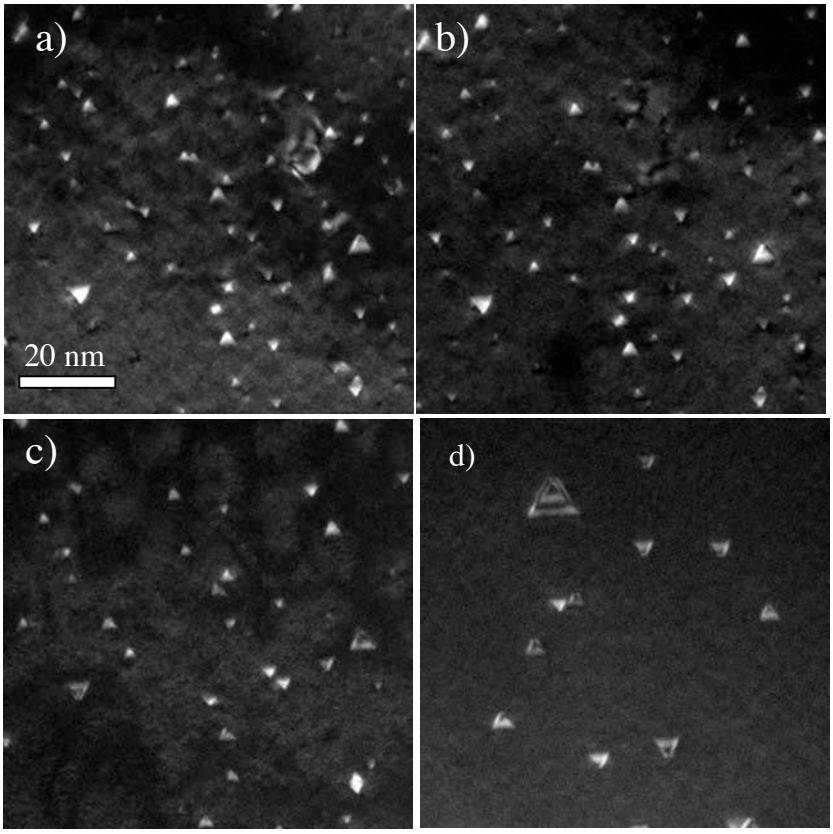

Fig. 5.1.4 Sequence of TEM DFWB micrographs taken in Cu irradiated to 0.01 dpa during in situ isochronal anneals. a) 200°C for 20 minutes, b) 300°C, c) 300°C for 2 hours, d) 400°C for 20 minutes.

As shown in Fig. 5.1.2, at 100°C, the interstitials are already escaping to the surface, and at 200°C only SFTs survive. Between a) and d), it appears that small SFTs dissolve while big SFTs remain in the sample, or even grow. This agrees well with the results presented in section 5.1.3 showing that the mean size of SFTs in Ni irradiated at 350 °C tends to become larger than the ones in Ni irradiated at lower temperatures. In this temperature regime, around 0.37 T_M, equal to 230 °C of Cu, the SFTs with sizes around 1 nm will dissolve. This will provide a number of free vacancies to grow larger SFTs and voids. It can be also be concluded that SFTs grow at the same time as voids grow, so that in the case of Ni irradiated at 350 °C both large SFTs and voids appear.

5.1.2 MD results

5.1.2.1 Small size defects

As described in chapter IV, it appears that at temperatures higher than 200 °C irradiation leads to the formation of voids or vacancy clusters. Of the total defects, about 10 ~20 % are unidentified group, and consists mainly in defects smaller than 1 nm. Moreover, due to the TEM conditions and specimen qualities, a number of small defects are invisible. At such a size level, it is very difficult to use the TEM technique to characterize the nature of defects. To characterize these small defects is still a challenge to the microscopist.

Experimentally, however, nanovoids have been detected and were found by Kojima et al. (1988) in Ni irradiated at 200 °C. MD simulations allow describing defects clusters of size below the resolution of the TEM in diffraction contrast.

5.1.2.2 Cascades simulation

The results have been summarized in table 4.6.3. It appears that:

1) The NRT model provides the number of Frenkel pairs induced by irradiation, which is described in equation 1.1.1.3. This equation depends on the displacement threshold energy. Because of the variety in the displacement threshold energies resulting from the selected potentials, a variable Frenkel pair number will result from the same introduced PKA energy.

In the case of Cleri-Rosato potential, at 10 K, the PKAs with energies from 5 keV to 40 keV produce a large number of Frenkel pairs, which is higher than what is obtained by NRT. According to the literature (Bacon et al. 1995), the Frenkel pair number produced in MD simulation is a fraction of about 30 % of the NRT number, when the PKA energy is larger than 5 keV. Therefore, the Cleri-Rosato potential can be excluded as an adequate choice. It should be noted though that, in Fig. 4.6.3, a SFT-like structure and an interstitial loop are observed, which approaches the irradiation induced microstructure observed in the TEM.

The NFP does not show an explicit dependence on the temperature.

2) Stacking fault energy (SFE) is one of the key factor, as discussed in section 5.1.1.4, in cooperation with the elastic shear modulus, which values are summarized in table 4.6.1, for SFT formation.

In section 4.6.1, it was shown that the platelet of 15 vacancies did not collapse to an SFT in the cases of Cleri-Rosato and Cleri-Rosato-AA potentials, but did with Farkas I and II potentials, at 500 K. The different SFEs (see table 4.6.1) could explain this phenomenon. Lower SFE implies that Shockley partials emission is favoured to form the stacking faults on other {111} planes, eventually to form a SFT.

3) The temperature independence of NFP in fact is still unclear. It is suggested however that during such a short time, 20 ps, the thermal diffusion of atoms may be neglected.

4) The PKA energy dependence of NFP is clearer. With increasing PKA energy, NTP increases, except in the case of the Cleri-Rosato potential. Table 5.2 shows the remaining percentage of Frenkel pairs after the complete cool down. It is difficult at this point to link the NFP with NRT. According to the recent work, the correlation between the PKA energy and NFP can be fitted by the power law from Bacon et al. (1997).

5.1.2.2 Cascade overlap on SFT

When irradiation reaches a certain dose, displacement cascades start to overlap each other. In order to investigate the effect of this overlap on existing defects, simulations of cascade overlap on SFT in Cu are carried out using the potential of Mishin et al (1999). An SFT including 66 vacancies, about 2.6 nm in size, is put in the centre of the simulation box. Three

consecutive displacement cascades were shoot on the SFT, with a pka energy of 20 keV, then 15 keV and eventually 10 keV. The result is shown in Fig. 5.1.5 as a sequence of snap-shots in the time evolution of the vents. Clearly the pre-existing perfect SFT is destroyed already by the first cascade, and a new structure is subsequently formed, which presents characteristics of an SFT. It shows in Fig. 5.1.5f two platelets of hcp-coordinated atoms that form stacking fault planes, borded by <011> directions, typical of SFT. This defect structure does not however form a complete and perfect SFT. It implies that thermal diffusion should be the main mechanism to form the perfect SFTs observed experimentally. These may be formed from structures similar to the ones seen in Fig. 5.1.5f.

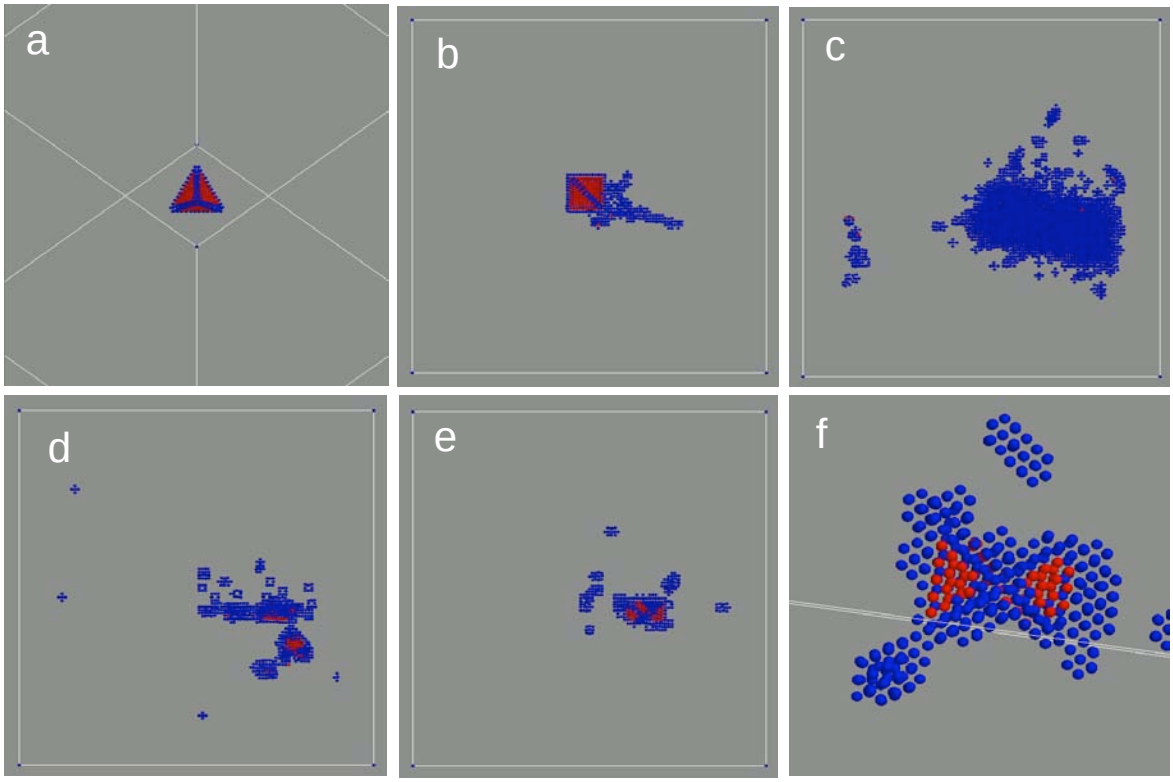

Fig. 5.1.5 The cascades overlap on top of SFT in Cu. Red atoms are in hcp sites, and blue are neither hcp nor fcc sites. a) A perfect SFT that contains 66 vacancies. b) A 20 keV cascade on the top of SFT after 0.4 ps, c) after 5ps. e) A 15 keV cascade on the top of SFT after 16 ps and f) a 10 keV cascade on top of SFT after 16 ps with a (100) view, f) rotated and enlarged.

5.2 The dislocation defect interaction deduced from in-situ TEM straining tests

The interaction between defects and moving dislocations in situ observations can help in clarifying what may happen during the plastic deformation of irradiated fcc metals. In effect, with this type of information, and by taking into account the interactions with loops as described section 1.5, one may be able in the future to describe the microstructural evolution upon deformation. This implies that this evolution is fully described by these interactions, that is to say the interaction between a dislocation and a SFT and the interaction between a dislocation and a dislocation loop. However, this is not all, as in our observations, the interaction between a dislocation and possibly a SFT lead to the production of a string along <110>, with a length around 30 nm as displayed in Fig. 4.5.4. This debris, similar to that observed by Johnson and Hirsch (1980), will also play a role in the microstructure evolution upon deformation.

In the following we review the results from in situ TEM straining experiments. Johnson and Hirsch (1980) performed in situ straining experiments in TEM of neutron irradiated copper crystals. They observed that dislocation slip bands formed as defect free channels. When the leading dislocations swept up impeding obstacles, then dislocations that follow can move on but only in the channels created by these leading ones. They also observed a number of elongated debris.

More recently Schaeublin et al. (2002b) performed similar in situ TEM straining tests in Au. They show an interaction between an SFT and a dislocation. A gliding dislocation impinged onto a perfect SFT, reacted with it and the resulting structure seemed to move, indicating the possible formation of a loop, then annihilated and the dislocation finally escaped.

Matzukawa and Zinkle (2004) performed in situ straining experiments and observed the collapse of a SFT by dislocations. In Fig. 5.2.3, during about 306 seconds, one after another, three moving dislocations interact with the same SFT of a size of about 30 nm. This SFT seems to be split into two pieces after the passage of the first two dislocations. After the third dislocation intersected the SFT, one part is annihilated while the remaining one ends up as SFT smaller than the original one.

In Fig. 4.5.2, moving dislocations could free themselves from obstacles (mainly SFTs) without large reaction strings, they did not show a dragging process as taking place in case of straining at 100 °C in Fig. 4.5.5.

Fig. 5.2.1 shows a region with a number of deformation induced dislocation strings with lengths of about 30 nm. These result from the interaction between gliding dislocations and defects, which are mainly SFTs in this case. The scattering of these string suggests that the destruction of SFTs, the major obstacle to gliding dislocations, may depend on various parameters such as the size of the SFT, the intersection height relative to the size of the SFT, the properties of the impinging dislocation, and maybe the testing temperature. Of course at this point of the study these are only suggested parameters.

Wirth et al. (2001), have simulated an edge dislocation interacting with overlapping, truncated SFT and show that under an applied stress of 300 MPa, the defect absorption by the dislocation resulted in climb and the formation of a pair of jogs. But they did not give a more

quantitative estimation for this mechanism.

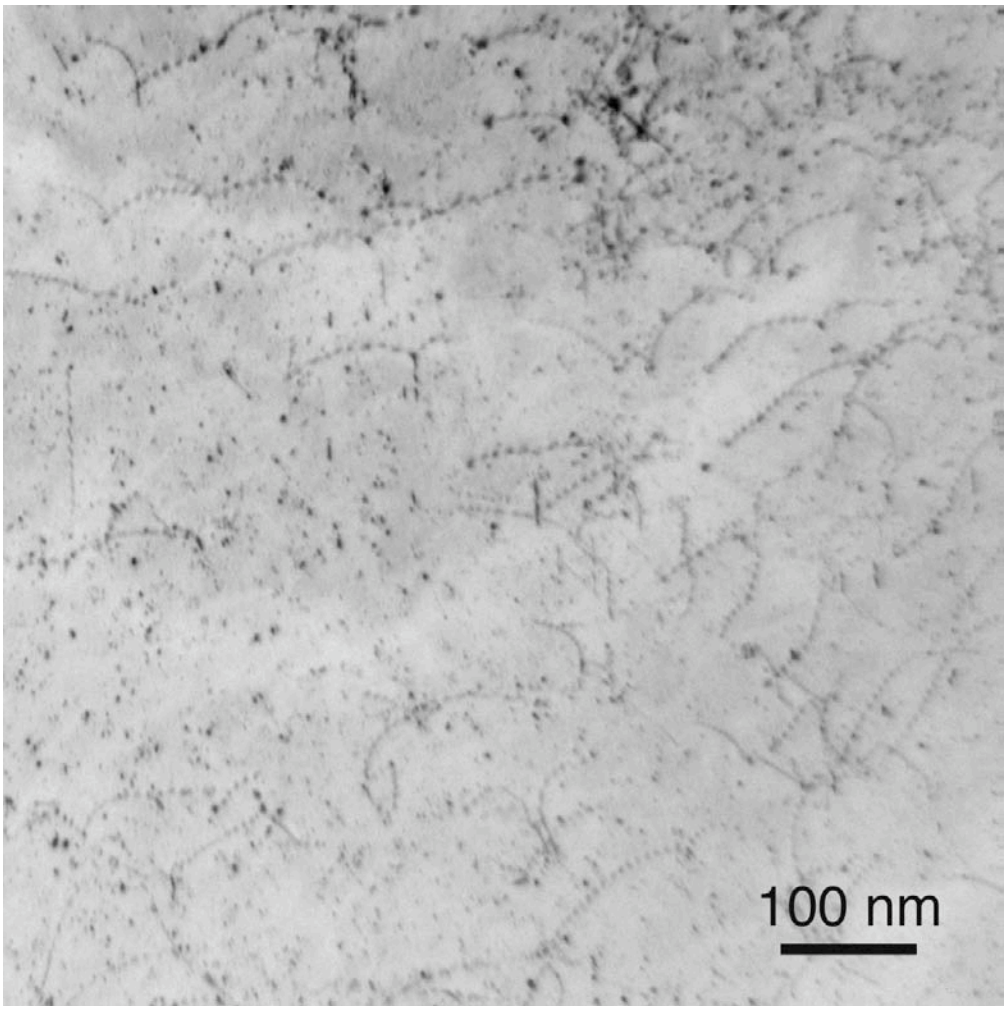

Fig. 5.2.1 The remaining strings distributed in the deformed region.

The aim of this section is to analyses the possibilities that exist for the interaction between a dislocation and a SFT. Based on our experiments and numerical modeling reported in the literature, the following mechanisms can be proposed. Osetsky et al. (2004) performed an MD simulation of the interaction between a pure screw dislocation and a perfect SFT (~3 nm), which intersects the SFT at half of its height. In Fig. 5.2.2 this sequence clearly shows that the moving dislocation cuts the SFT into two pieces by a complicated process, consisting in one smaller SFT and one truncated SFT portion. This simulation is nicely supported by Matsukawa and Zinkle's observations reported in Fig. 5.2.3.

SFT can collapse by interaction with a moving dislocation and the resulting structure can be dragged away by the same dislocation. This took place at 100 °C and is shown in Fig. 4.5.5. When compared to the case of Matsukawa, it implies that the collapse of the SFT is temperature dependent, as they did not observe such a phenomenon at room temperature.

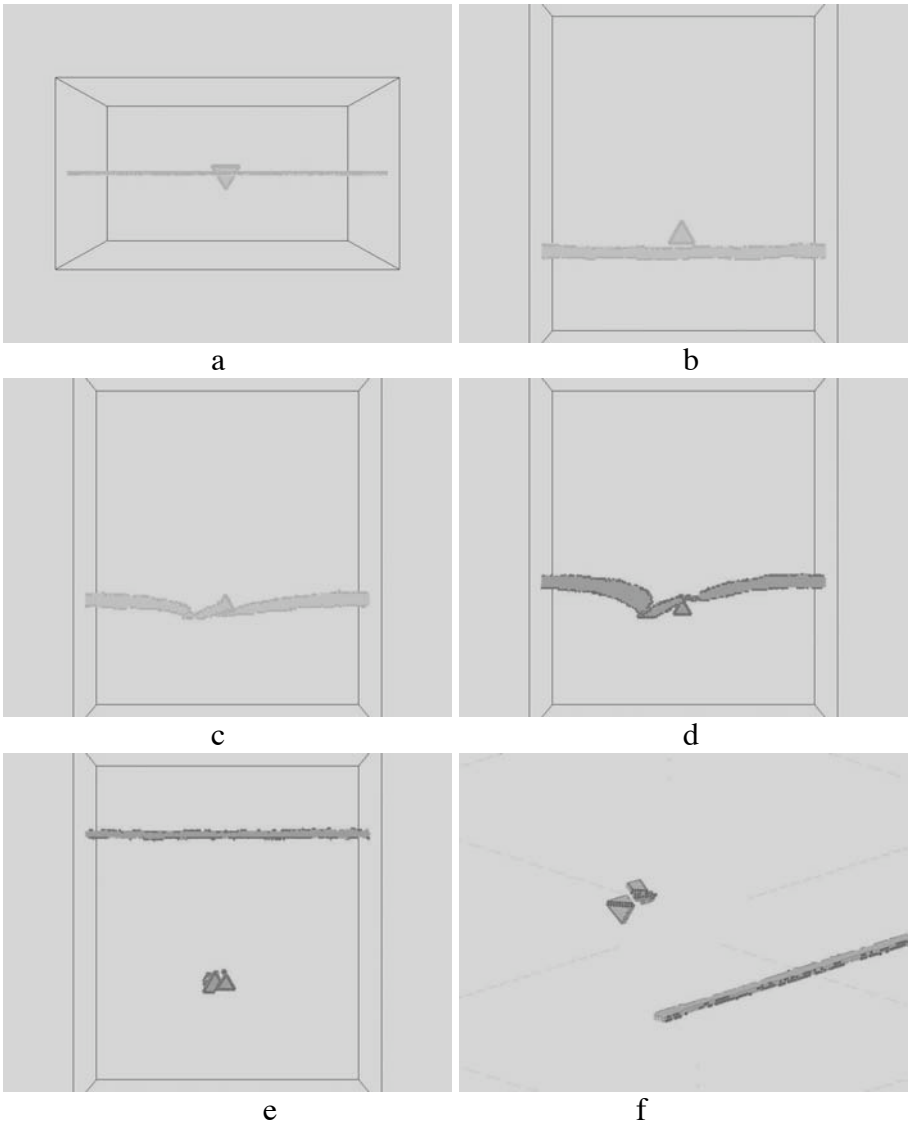

Fig. 5.2.2 Interaction between a pure screw dislocation and an SFT, by MD simulation (Osetsky et al. 2004). Time evolution from (a) to (e). (f) presents (e) under a different viewing direction.

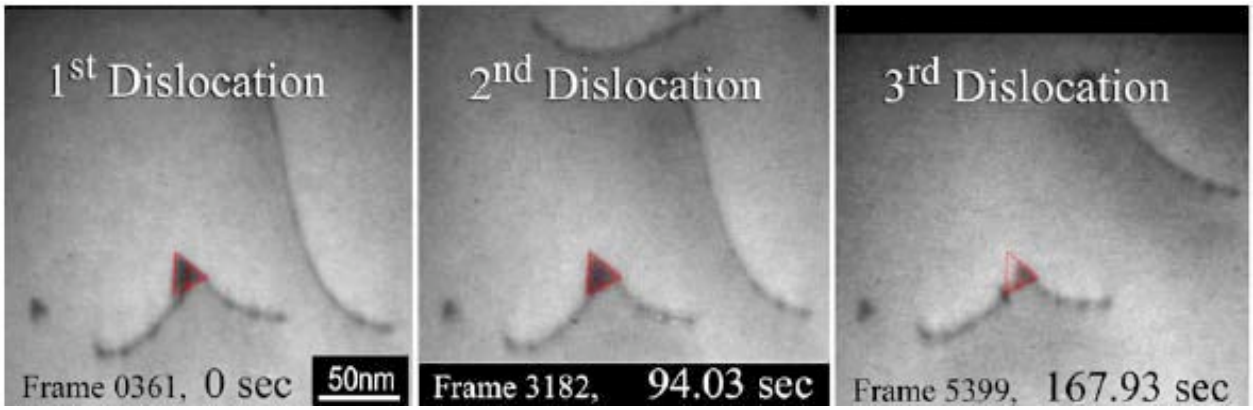

Fig. 5.2.3 Interaction between dislocations and an SFT, by in-situ TEM tests (Matsukawa and Zinkle 2004). Analysis of the position of the ends of dislocation line intersected by foil surface and the position of SFT interacted with the dislocations provide the following information about geometry of the interaction process: (1) The first moving dislocation interacts with the SFT relatively close to the top, compared with the second and the third ones. (2) The second and the third dislocations glide on almost the same (111) plane.

In order to understand the formation of the string we observed in the straining at low temperature we suggest the following mechanism. a) The SFT collapsed into a Frank loop by the stress applied by the approaching dislocation; b) it transformed into a perfect loop; c) the moving dislocation will react with this perfect loop as Saada described (1963) (see section 1.5). With this modified structure, the string can be induced by the jog formed on the moving dislocation and pulled out as the dislocation moves away. At some point the dislocation may escape. This is summarised in Fig. 5.2.4.

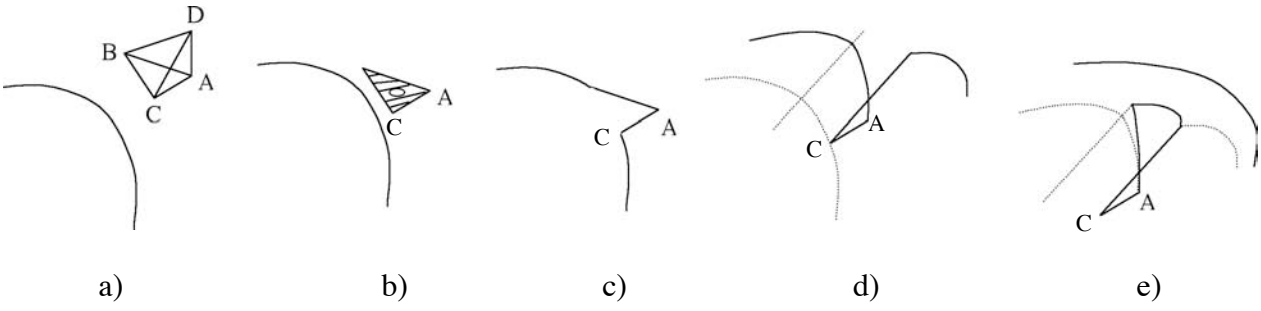

Fig. 5.2.4 The possible interaction between an SFT and moving dislocation. a) A dislocation glides on the plane BCD. b) SFT collapsed to a Frank loop, then this Frank loop is transformed into a perfect loop (Saada 1962), with a burgers vector 1/2<110> directed along BD. c) One section BC will annihilate with gilding dislocation, then form a jogged dislocation. d) Because the section AC is not mobile on its resident plane {100}, the other dislocation parts will continue to glide on their {111} plane, including section AB gliding on plane ABD. e) After the dislocation glides some distance until impeded by other defects on the gliding plane, a possible annihilation take place again between two wing sections. Therefore, such a string is left, while the dislocation recovers and continues to glide. The dash line in d) and e) indicate the traces of dislocation.

5.3 Irradiation induced hardening

In this section, the results of the mechanical tests will be discussed with an emphasis on the Ni results. First, the irradiation dose dependence of irradiation hardening will be discussed. Second, a correlation between the irradiation hardening and the defect structure will be attempted.

It should be emphasized that we have to analysis two types of tensile tests:
1) Tensile tests at room temperature of samples irradiated at different irradiation temperatures where the initial defect microstructure is different. These are shown in Figs. 5.3.1 and 5.3.2.
2) Tensile tests at different temperatures of samples irradiated at a fixed irradiation dose and temperature. The starting microstructure is here the same, but one looks at the temperature dependence of the operating mechanisms. These are shown in Figs. 5.3.4 and 5.3.5.

5.3.1 The dose dependence of yield shear stress

The changes of yield shear stress at different irradiation temperatures as a function of dose are shown in figure 5.3.1. The slope of the fitting curve is about 1/4 for samples irradiated at RT and about 1/2 for high temperature (HT), 250 °C irradiation.

Certainly, this difference implies that the defects accumulation mechanism from RT regime to HT regime over 250 °C has changed significantly. In chapter IV, the microstructure of irradiation induced defects of these samples has already been indicated. The density of defects at HT irradiation decreases, but mean size of defects increases. The following paragraphs discuss the correlation between the change of yield shear stress when the defect density and size are factors that determine the mechanical properties.

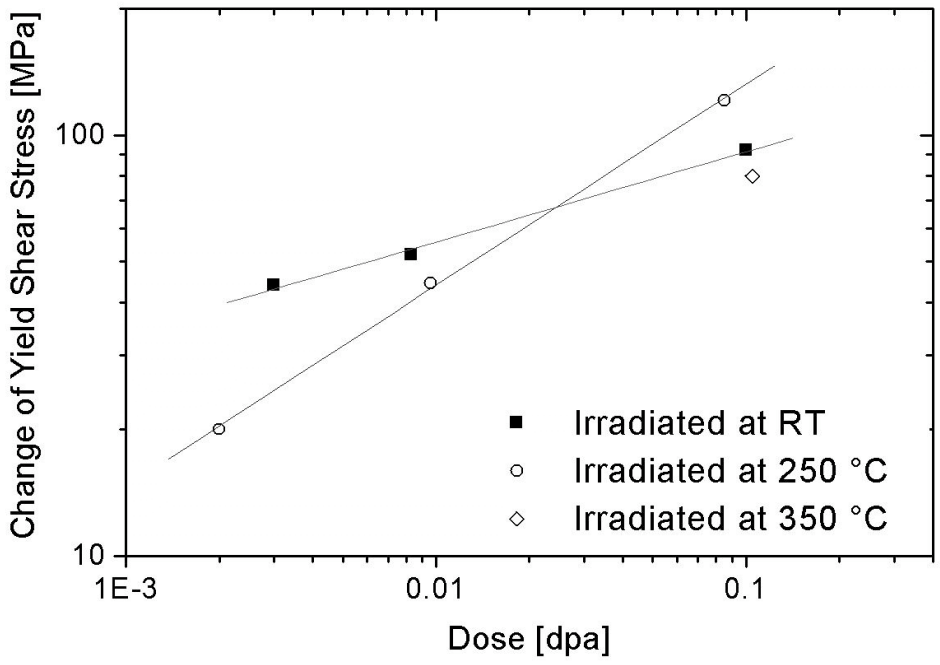

Fig. 5.3.1 The dose dependence of the change of yield shear stress in Ni irradiated at various temperatures.

5.3.2 The radiation hardening: dependence on the irradiation temperature

To explain the large changes of yield shear stress induced by irradiation, as shown in Fig. 4.1.1 and 4.1.2, two models are generally proposed, namely the dispersed barrier hardening (DBH) model and the cascade induce source hardening (CISH) model (Singh et al. 1997).

In the description of the DBH model, the yield shear stress change is expressed by the following expression (Bement 1970):

$$\Delta\tau = \alpha\mu b(Nd)^{1/2} \qquad (5.3.1)$$

where $\Delta\tau$ is the change of yield shear stress, μ is the shear modulus which for Ni is 80.5 GPa at 293 K, b is the Burgers vector, which is 2.49 Å for Ni, and N is the defect number density and d the defect mean equivalent diameter. The mean size of defects, at the lowest dose of 3.5×10^{-3} dpa is 2.6 nm and at the highest dose of 0.1 dpa is approximately 1.9 nm. Fig. 5.3.2 shows the dependence of the yield shear stress with the square root of Nd at RT. The data can be linearly fitted, with a slope of approximately 2.5×10^{-6} for RT irradiation cases and 4.5×10^{-6} for 250 °C and 350 °C irradiation cases.

According to equation (4.5.1) and (5.3.1), assuming an average pinning efficacy for defect types, then a relation between α and the breaking angle ϕ_c can be obtained as:

$$\alpha = 0.9\ (\cos\phi_c)^{3/2} \qquad (5.3.2)$$

The value of α can be evaluated accordingly to be about 0.13 for RT irradiation cases and about 0.23 for high temperature irradiation cases, which correspond to breaking angles of about 149° and 133 ° calculated from equation (5.3.2), respectively. These angles can be compared with a breaking angle of 150 ° in irradiated Cu at RT (Dai 1995), to conclude that during RT deformation the RT irradiation induced defects in Ni are weak obstacles, but HT (250 °C and 350 °C) irradiation induced defects are stronger toward impeding the moving dislocations.

In section 4.4, the TEM observation shows the following differences in the microstructure following RT irradiation or HT irradiation: 1) the ratio of SFTs to interstitial loops remains constant while their sizes increase with irradiation temperature; 2) voids appear in HT irradiation.

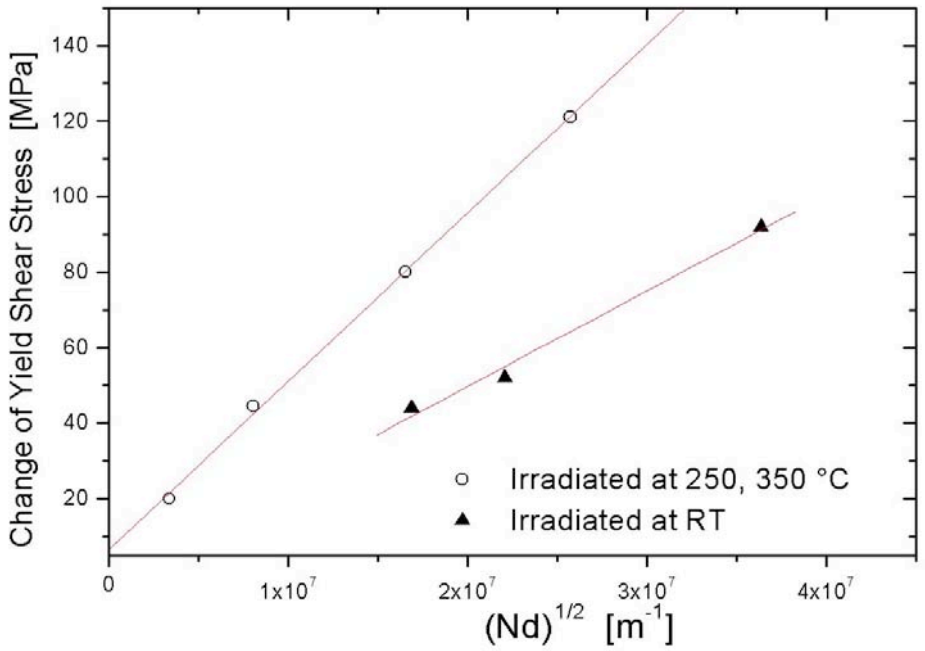

Fig. 5.3.2 Variation of the change of yield shear stress with the square root of the defect density and size.

In section 5.2, the different possible interactions between moving dislocation and SFT were discussed. Even when a moving dislocation intersects with the SFT of various sizes, the reaction may present different unpinning mechanisms, which provide us with different impeding efficiency. Moreover, the pinning obstacles in our irradiated samples consists of three types defects, namely SFT and dislocation loops, and voids in the case of high temperature irradiation. For estimating their hardening efficiency, these three types defects have to be discussed separately.

1) SFT

In the previous section, the interaction between a SFT and a moving dislocations was discussed in detail. A critical stress for unpinning the SFTs of about 100 MPa was deduced in our work. It should be noted that the tests were performed at a low temperature, 120 K. Robach et al. (2004) and Matsukawa and Zinkle (2004) also have done similar TEM in situ observation in irradiated Cu and quenched Au, respectively. The detailed situation was discussed in previous section. Robach et al. (2004) obtain a mean critical shear stress of 43 MPa for their irradiated Cu.

Osetsky et al. (2004) could simulate by MD the interaction between an edge dislocation and a SFT, and with different interaction geometries. They apply a constant strain rate and measure the stress response. The stress level they obtained is reported in Fig. 5.3.3 and express the strong temperature and interaction geometry dependences.

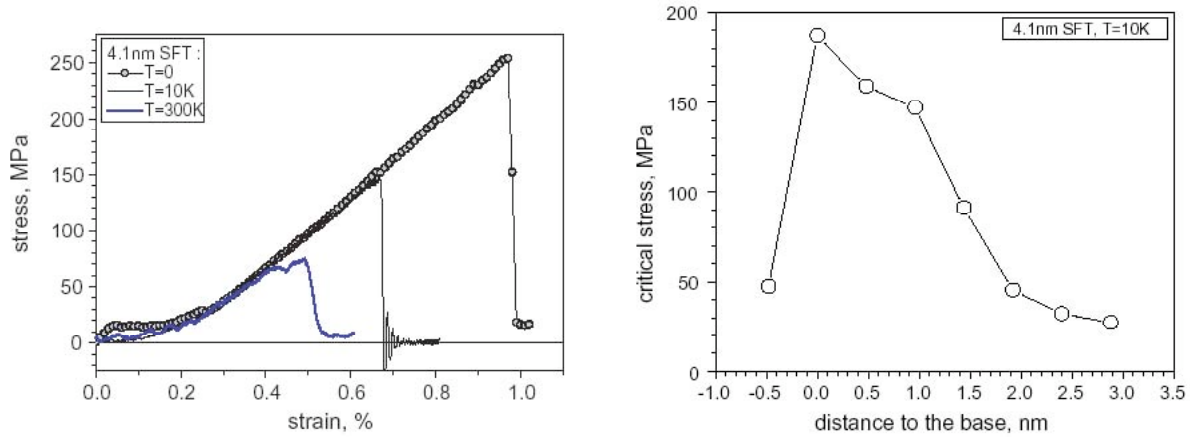

A) B)

Fig. 5.3.3 A) Applied stress as function of strain containing a dislocation gliding through a row of 4.1 nm (136 vacancies) SFT at h = 0.96 nm. B) Dependence of the value of critical resolved shear stress on distance between the dislocation glide plane and the base of a 4.1 4,1 nm SFT at T = 10 K (Osetsky et al. 2004).

2) Dislocation loop

Saada (1962) did the analysis for the interaction between the moving dislocations and loops, perfect or faulted type, as presented in the literature review (section 1.5). He reported that in case of stacking fault loops, small sized ones are probably more efficient to impede the movement of dislocations. More recently, the estimation of stress level of these interactions was performed by Rodney et al. (2004). They used MD to simulate the interaction between moving dislocations and interstitial dislocation loops in single crystalline Ni. Two representative interactions were considered:

I. An edge dislocation interacts with glissile loops. The simulation indicates that the dislocation absorbed and dragged glissile loops, with a very weak interaction. They apply a constant stress and measure the strain. There was no significant pinning, as denoted by a bow out, when interacting with the loops.

II. A screw dislocation interacts with a Frank loop. In case of a hexagonal Frank loop

(6~10nm) on the cross slip plane of the moving dislocation, the cross-slipped partials remove the 1st stacking fault and two other partials appear spontaneously and remove the 2nd fault. Eventually the unfaulted half loops are weak obstacles. They are dragged by the dislocation in the direction of their Burgers Vector. The applied stress was 300 MPa and the simulation performed at 100 K. In case of such a hexagonal Frank loop, of which habit plane is not on the cross slip plane of the moving dislocation, a sessile helical turn was formed on the screw dislocation. Unpinning this helical turn required a stress of 425 MPa. The interaction with other shape and size of loops were also calculated, and it turned out that the unpinning stress level is strongly dependent on those factors.

3) Void

The MD simulation or TEM observation of such interaction have not been done yet for fcc metals. Nevertheless, in our experiments the hardening induced by voids can be estimated. In Fig. 5.3.2, the fitting by a linear relationship between the yield stress change and $(ND)^{1/2}$ is much different. Obviously the difference is in the size distribution of SFTs and loops, or voids. The hardening effects from various sizes of SFTs and loops have been already estimated by Osetsky et al. (2004) and Saada (1962). In their modelling, a size effect exists, but faint. Even the smaller Frank loops are thought to be strong obstacles. The reason for the strong hardening of HT irradiation is that voids are more efficient to impede the moving dislocations than others, SFT and loops. In other words, voids may be stronger obstacles than SFTs and loops.

The factor α implies an average efficacy of the defects on impeding the moving dislocations. For SFTs and interstitial loops in irradiated Ni, α is around 0.1, similar as in Cu (Dai 1995). For voids, α is suggested here to be much larger.

5.3.3 Temperature dependence of the irradiation hardening

In this section, the temperature dependence of critical yield shear stress will be discussed. It is well known from the theory of thermally activated dislocation glide (Evance and Rawlings 1969), that the force on a dislocation can be separated into two components, a long range force, F_m, which varies slowly with the position of the dislocation on the slip plane, such as the force due to large obstacles and dislocations on the slip planes, and a localized force, F*, which acts over a few atomic distances, such as the force due to the forest dislocations and small irradiation induced defects.

The thermal activation energy has been calculated from equation (2.3.2.9) and (2.3.2.10). ΔG can be determined by requiring that $\Delta G=0$ at 0 K. Fig. 5.3.4a shows the correlations between reduced shear stress, temperature and activation energy for unirradiated samples. In this case ΔG is indeed linear with temperature. Conversely, in the irradiated case ΔG is not linear with temperature (Fig. 5.3.4b). It indicates that the microstructural process of yielding may change with testing temperature, or, that multiple processes are operating.

In the unirradiated case an activation energy of approximately 0.3 eV at RT can be extrapolated from Fig. 5.3.4a. It should be noted that the shear modulus μ change with temperature should be taken into account in the calculation. However, with a difference between 77 K and 423 K of only 13 % in the value of μ (Mader et al. 1963) and a linear

behavior in the plot of the activation volume with temperature (Fig. 5.3.4a), the derivation of the values of ΔG-δG and ΔG is straightforward.

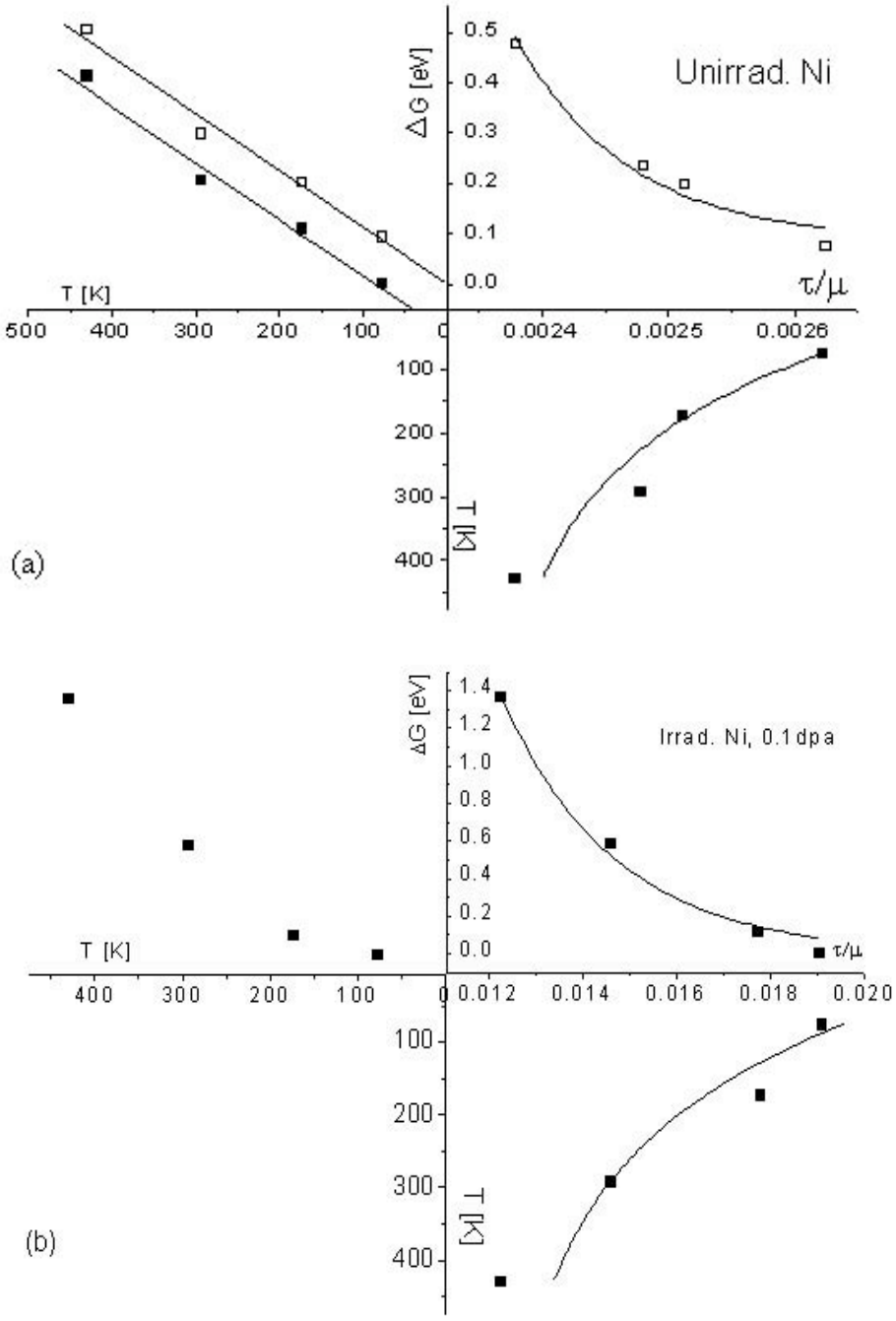

Fig. 5.3.4 Stress and temperature dependence of the activation energy along with the temperature dependence of the reduced yield shear stress for (a) unirradiated Ni and (b) Ni irradiated to 0.1 dpa.

Contrary to the unirradiated case, the critical yield stress of the irradiated samples show a strong temperature dependence from 293 K to 423 K and suggests an additional mechanism, related to the irradiation induced defects, to be operating during the deformation of the irradiated material. This result is comparable to that of Blewitt et al. (1960), who found a similar temperature dependence of the yield stress of irradiated Cu single crystals at doses higher than ~10^{-3} dpa.

The temperature behavior of the critical yield shear stress of irradiated material has been shown by Seeger (1958) and Foreman and Makin (1966) to correspond to the thermally activated movement of a dislocation through a random square arrangement of obstacles and the dependence is calculated

$$\left(\frac{\tau}{\tau_0}\right)^{2/3} = 1 - \left(\frac{T}{T_0}\right)^{1/2} \qquad (5.2.2)$$

Where τ_0 is the stree at absolute zero, and T_0 is the temperature at which the stress becomes vanishingly small and thermal activation over barriers occurs unaided. A plot of $\tau^{2/3}$ vs $T^{1/2}$ should then be a straight line. This is found in the present results (Fig. 5.3.5) indicating then that above assumptions are obeyed in the measured temperature range.

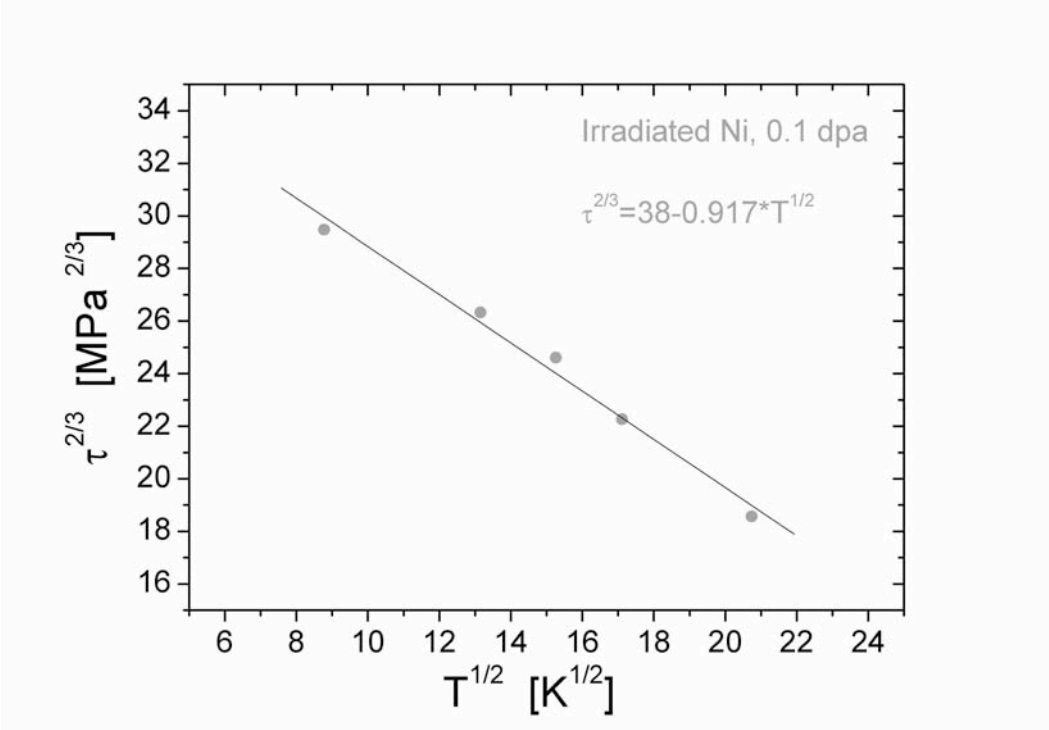

Fig. 5.3.5 Relation between yield shear stress and test temperatures in Ni irradiated to 0.1 dpa.

Through the data fitting as this plot, $\tau_0 \approx 234$ MPa and $T_0 \approx 1717$ K could be obtained, respectively.

As equation (5.3.1) does not have an explicit temperature dependence, one possible approximation is to suppose that the dislocation-defect interaction strength, α, is temperature dependent, $\alpha=\alpha$ (T). In present TEM in-situ observation of strain tests, the different interactions were observed at the different temperature –90 °C and 100 °C, respectively (in Figs. 4.5.4 and 4.5.5). The interaction between an SFT and moving dislocation at low temperature presents a stronger behaviour than at high temperature, i.e. that the factor α at high temperature should be larger than that at low temperature.

5.4 Evolution of the microstructure on deformation

5.4.1 The flow stress and work hardening rate

In Fig. 4.1.10, the work hardening of samples deformed at different temperatures is shown. The work hardening is induced by dislocation forest interaction that leads to dislocation entanglement. As described in Chapter I, the work hardening rate at a same temperature regime should only depend on the applied stress. This is a key point in order to investigate the differences between the unirradiated and irradiated materials.

Softening appears at the beginning of deformation in irradiated Ni and diminished soon afterwards. The initial deformation of irradiated Ni is constrained in local regions, in the so called defect free channels. Once these channels are created, the shear stress will be released by the moving of dislocations in these channels. Following this mechanism, a softening appears after the yield point, as shown in Figs. 4.1.1 and 4.1.2. When considering an ideal situation where no more defects remain in these channels, one may envisage that deformation could be maintained in such soft regions up to failure of the specimen, that is, failure in the soft region to a stress level much below the one of the yield point. However, results show that softening disappears at a strain of about 0.2 and hardening starts again on further deformation.

Conversely, it is true that it is difficult to understand that at such a high stress level the deformation can be sustained by a single slip system, which is the primary slip system. More recently this issue was considered by Veyssière et al. (2004). They tried to investigate the self –patterning in a single slip system and found that two moving 1/2 <110> dislocations forming a dipole annihilate in places to generate loop strings. An impacting dislocation could then be captured by the string. Sooner or later, the dislocation annihilates with an impacting dislocation forming a second string, and a gradual thickening into a loop wall is observed by the repetition of this manoeuver. In fact, this mechanism allows interpreting the initiation of small cells formed in channels as seen in Fig. 4.3.4c. This single slip induced dislocation tangling, and the possible subsequent cell formation in the channels, plays an important role in stopping the softening and in increasing the work hardening rate.

A large difference of work hardening rate at different temperatures is observed during deformation of unirradiated samples, but it is smaller in the case of irradiated samples. In case of unirradiated Ni, the situation is shown in Fig. 5.4.1. The dislocations start to tangle each other even in stage I, during single slip deformation, then at the stage II, following the activation of secondary slip systems, the work hardening rate increases rapidly, as shown in Fig. 4.1.10. The different temperature dependences of work hardening rate for unirradiated samples is clear, while the irradiated ones show a similar behaviour of the work hardening rate, with almost parallel increases as a function of shear strain, as shown in Fig. 4.1.8. Because the dynamical recovery is a thermally activated mechanism, it needs a higher stress level at a lower temperature to overcome the Lomer-Cotrell barriers at a same strain of samples. It follows that, as we have a higher stress level, the work hardening rate is larger.

In case of irradiated Ni, the microstructural mechanisms of the deformation can then be rationalized in the following scenario, which is schematically represented in Fig. 5.4.1. As dislocation sources of decreasing lengths are activated, dislocation channels form simultaneously in more than one region of the gauge length, as observed in this work and in (Dai 1995), and softening is observed in the yield region, for example following irradiation to

0.1 dpa. At the end of this initial yield region, which amounts to about 0.21 at 293 K, the deformation microstructure consists of a distribution of channels of ~ 100 nm width separated ~ 1 μm from each other. It should be noted that the regions between channels retain the original cluster density (Fig. 4.3.4a). As secondary slip systems become active, the deformation starts to be controlled by the intersection, within the channels, between dislocations from various slips systems. Cell (Fig. 4.3.4c) formation initiates from mobile dislocation (Fig. 4.3.4b) in the already formed channels. The interaction takes place then within the thickness of the channel (100 nm), which lowers the probability of the interaction and explains why a lower work hardening rate than in the unirradiated Ni is observed in the region of $\varepsilon>0.2$. The process extends into the rest of the volume of the crystal to produce the cell structure observed at the end of deformation by the formation of additional channels in the region between the original channels. The eventual cell configuration would then retain part of the dimensionality of the channels, for at least their width of 100 nm for the cell size, because of the geometrical constraint.

It is observed that a higher stress appears for irradiated Ni than for unirradiated Ni just before failure. Comparing Fig. 4.3.1b (unirradiated) with 4.3.5a (irradiated), the cell size statistics show that in the irradiated material, a smaller size is present than in the unirradiated Ni. This mechanism already was discussed in the above paragraph. In Fig. 5.4.1, the deformation in unirradiated and irradiated Ni is schematically shown with the difference of the cell initiation. In failed irradiated samples, there still remains a large density of defects observed between the cell walls. This implies that the flow stress at large strains is still controlled by the defect microstructure produced by the irradiation. Moreover, at the point where the work hardening θ reaches a maximum value (Fig. 4.1.10), θ is still smaller than for the unirradiated in stage II (Fig. 4.1.10), but happens at stresses (Fig. 4.1.1) that are already those of stage III of the unirradiated specimen (Fig. 4.1.1).

Table.5.2 Deformation cells of Ni tested at room temperature, unirradiated and irradiated samples.

	Unirradiated	I40T07 (0.002 dpa, 250 °C)	I40T01 (0.1 dpa, RT)
Length of Deformation Cells (μm)	1-4	0.6-2	0.6-2
Mean Width Deformation Cells (nm)	700	500	400

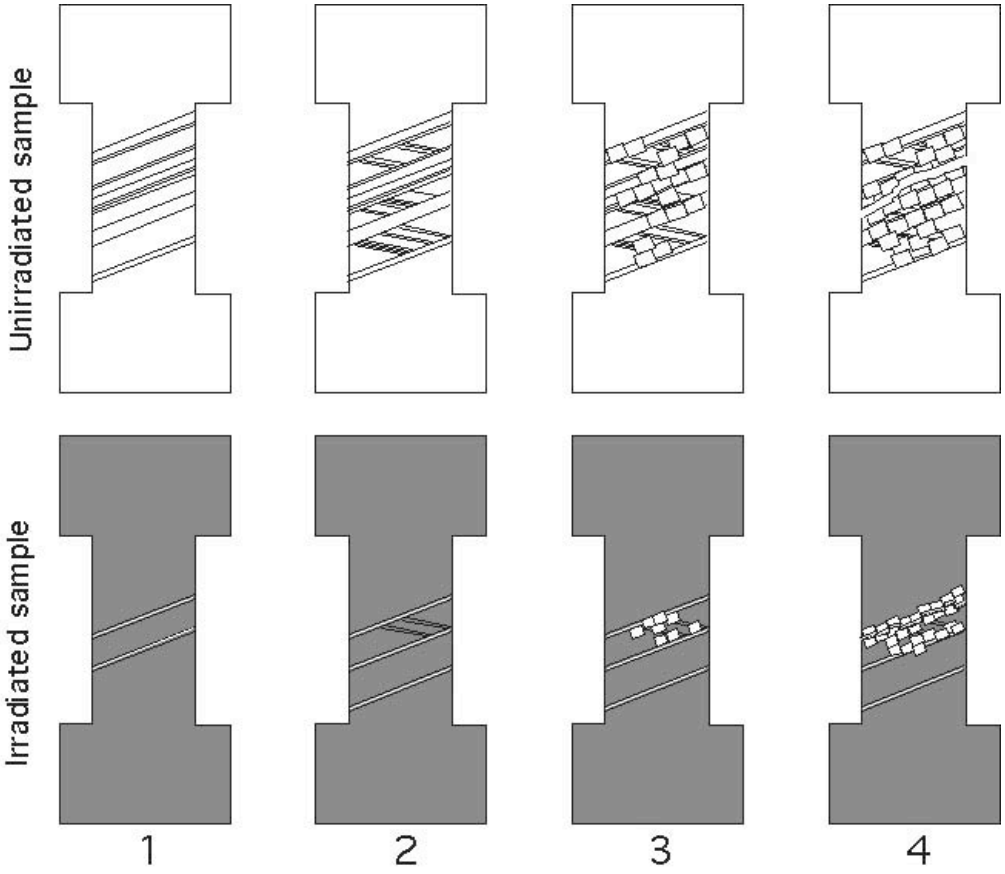

Fig. 5.4.1 Schematic representation for the deformation microstructure evolution during the plastic deformation, in case of unirradiated and irradiated samples. (1) at the onset of yielding, (2) secondary slip activation, (3) cell formation, (4) failure.

Conclusion

Ni single crystal specimens have been irradiated with 590 MeV protons to doses ranging from 10^{-3} dpa to 0.3 dpa, at room temperature, 250°C and 350°C. The irradiation induced microstructure has been characterized by transmission electron microscopy, and the mechanical properties have been assessed by mechanical testing. Molecular dynamics simulations have been conducted in Ni and Cu in order to understand the defect formation and accumulation following a displacement cascade. The following conclusions are established.

Following irradiation at room temperature, it appears that 43% to 55% of the irradiation induced defects in Ni consists in SFTs, 31%~41% in loops and about 10 % in unidentified black dots. In the case of Ni irradiated at 250 °C, 44%~53% of the irradiation induced defects consists in SFTs, 35%~51% in loops, and less than 5% in black dots. In the case of Ni irradiated at 350 °C, 50% of the irradiation induced defects consists in voids. The remaining 50% include ~ 14% SFTs and 36% loops. Moreover, it appears that these ratios are independent of the irradiation dose, contrary to what was found in the literature. These results allow clarifying this long standing issue, that in fact in Ni there is no transition in the ratio between SFTs and loops with increasing dose.

In addition, it appears that in fact the irradiation induced defect density is similar to that found in other irradiated fcc metals for RT irradiation. The data of the irradiation at 250°C are in agreement with previous published results on a neutron irradiation at 230 °C (By Kiritani 1987).

It appears that the size of SFTs is independent of the irradiation dose, similar to what is found in irradiated Cu. It depends, however, on the irradiation temperature.

MD simulations have been performed to try to understand the formation of defects following displacement cascades, by using different embedded atomistic potentials. The results of SFT collapse tests show that i) the platelet of 6 vacancies did not collapse to SFT regardless of the annealing conditions, but formed a void above 800K, for all selected potentials; ii) the platelet of 15 vacancies collapsed into an SFT when simulated with Farkas-I and Farkas-II potentials; iii) the platelet of 66 vacancies much easily collapsed to an SFT at 500K for all applied potentials, even with a high stacking fault energy (SFE) of 300 $mJ \bullet m^{-2}$.

The common neighbor analysis and Wigner-Seitz defects analysis codes are used for studying the MD files after complete cooling, and results are discussed and show that the large number of stacking faults is obtained with the highest stacking fault energy (300 $mJ \bullet m^{-2}$). An SFT-like structure appears close to the core of cascades and also an isolated interstitial loop was found with the Cleri-Rosato potential. With the Farkas-II potential, no big cluster appears. The Frank pair numbers increases with the increasing PKA energy, and depends less on the box temperature.

Irradiation hardening was assessed by tensile testing, associated with TEM in situ strain tests.

It appears that a significant irradiation hardening occurs starting at the lowest dose of 10^{-3} dpa, at room temperature and 250°C. With increasing dose, the yield shear stress increases. The dose dependence of this increase varies on an irradiation temperature from room temperature to 250°C, showing a significant temperature dependence.

The thermal activation energy was calculated by measuring the activation volume, which is obtained from relaxation tests. In unirradiated Ni, an activation energy of about 0.3 eV can be extrapolated at RT. In the case of irradiated Ni, the unsuccessful fitting with a linear relationship between the thermal energy and temperature suggests that multiple deformation mechanisms are operating, simultaneously or in turn, over the considered temperature range of –196 °C to 423 °C. If they operate simultaneously they would be thermally activated.

The DBH model is used to interpret the irradiation induced hardening in irradiated Ni. According to the equation, $\Delta\tau = \alpha\mu b(Nd)^{1/2}$, with α, the obstacle strength. It appears that α is 0.12 for the room temperature irradiation induced hardening, similar to what was previously found for irradiated Cu, and is 0.22 for the hardening following irradiation at 250°C, which is much larger than previous values. This difference in α is suggested to be related to the presence of voids at high temperatures, suggested that they are stronger obstacles than SFTs or dislocation loops.

In situ TEM observations were made in irradiated Cu, in order to assess the strength of irradiation induced defects as obstacle to gliding dislocations. It appeared that the strength of obstacles is approximately 100 MPa. Considering that 90% of the damage consists in SFTs, it is suggested that these obstacles presenting a resistance of 100 MPa are SFTs. In particular, the pulling out of a string from the interaction between what was assumed to be an SFT and a moving dislocation could be recorded for the first time. This reaction, of relatively high frequency, implies that the gliding dislocation is strongly pinned by SFTs.

TEM observation of the microstructure of the irradiated Ni following plastic deformation shows that defects-free channeling is the deformation mechanism at the beginning of yielding. The channeling allows explaining the observed softening.

As deformation proceeds, a dislocation cell structure is created. It takes different forms depending on whether the sample is irradiated or not. In the irradiated case, cell formation initiates from mobile dislocations in the defect free channels. This implies that the eventual cell configuration will retain part of the dimensionality of the channels, namely their width of 100 nm, because of the geometrical constraint. In unirradiated Ni the dislocation cell size is larger. The higher flow stress observed in the irradiated case is thus related to the dislocation cell size.

Prospective

The present work could be extended in the following directions:

In order to explore the behaviour of Ni at higher doses, which are more relevant to fusion reactor applications, TEM observations and mechanical testing should be performed on samples irradiated at 1 dpa or more. In addition polycrystalline Ni should be considered in order to understand the role played by the grain boundaries in the plasticity of the irradiated material.

It appears clearly from this study that the next step is simulation. Extensive MD calculations on the interaction between SFTs, dislocation loops and voids and moving dislocation in Ni are needed in order to understand its temperature dependence are its relative impact on hardening. For the damage accumulation kinetic Monte Carlo, or alternately kinetic rate theory, calculations are needed in order to simulate the time evolution of the irradiation induced microstructure. Defect size and density could be derived and compared to experimental ones in order to test models of defect formation deduced from MD calculations.

Appendix I S_g and ξ_g^{eff} values of Ni, Cu and Au under different imaging conditions

Ni	1g(1g)		1g(2g)		1g(3g)		1g(4g)		1g(5g)		1g(6g)		1g(7g)		1g(8g)		1g(9g)		1g(10g)	
	Sg	ξ_g^{eff}	Sg	ξ_g^{eff}	Sg	ξ_g^{eff}	Sg	ξ_g^{eff}	Sg	ξ_g^{eff}	Sg	ξ_g^{eff}	Sg	ξ_g^{eff}	Sg	ξ_g^{eff}	Sg	ξ_g^{eff}	Sg	ξ_g^{eff}
(111)	0	31.8	0.032	22.11	0.065	13.8	0.097	9.75	0.13	7.47	0.162	6.035	0.195	5.06	0.228	4.34	0.26	3.818	0.29	3.394
(200)	0	36.7	0.043	19.52	0.086	10.9	0.130	7.51	0.173	5.69	0.217	4.57	0.260	3.82	0.303	3.278	0.347	2.87	0.39	2.55
(220)	0	53.5	0.086	11.26	0.173	5.728	0.26	3.836	0.347	2.877	0.434	2.302	0.521	1.918	0.608	1.644	0.694	1.44	0.78	1.28

$S_g = n(n-m)\, g^2\, \lambda/2$;
λ (200 KV) $= 2.5079 * 10^{-3}$ nm ;
$g = 1/d$

Cu	1g(1g)		1g(2g)		1g(3g)		1g(4g)		1g(5g)		1g(6g)		1g(7g)		1g(8g)		1g(9g)		1g(10g)	
	Sg	ξ_g^{eff}	Sg	ξ_g^{eff}	Sg	ξ_g^{eff}	Sg	ξ_g^{eff}	Sg	ξ_g^{eff}	Sg	ξ_g^{eff}	Sg	ξ_g^{eff}	Sg	ξ_g^{eff}	Sg	ξ_g^{eff}	Sg	ξ_g^{eff}
(111)	0	30.6	0.029	23.0	0.058	15.1	0.086	10.8	0.115	8.4	0.144	6.8	0.173	5.7	0.202	4.9	0.23	4.3	0.259	3.8
(200)	0	35.5	0.038	21.0	0.077	12.3	0.115	8.5	0.153	6.4	0.191	5.2	0.230	4.3	0.268	3.7	0.306	3.3	0.345	2.9
(220)	0	52.7	0.077	12.6	0.154	6.5	0.23	4.3	0.307	3.2	0.384	2.6	0.461	2.2	0.537	1.9	0.614	1.6	0.691	1.4

Au	1g(1g)		1g(2g)		1g(3g)		1g(4g)		1g(5g)		1g(6g)		1g(7g)		1g(8g)		1g(9g)		1g(10g)	
	Sg	ξ_g^{eff}	Sg	ξ_g^{eff}	Sg	ξ_g^{eff}	Sg	ξ_g^{eff}	Sg	ξ_g^{eff}	Sg	ξ_g^{eff}	Sg	ξ_g^{eff}	Sg	ξ_g^{eff}	Sg	ξ_g^{eff}	Sg	ξ_g^{eff}
(111)	0	20.2	0.023	18.4	0.045	14.9	0.068	11.9	0.09	9.7	0.113	8.1	0.136	6.9	0.158	6.0	0.181	5.3	0.204	4.8
(200)	0	22.7	0.030	18.7	0.060	13.4	0.09	9.9	0.121	7.8	0.151	6.4	0.181	5.4	0.211	4.6	0.241	4.1	0.271	3.6
(220)	0	31.5	0.060	14.7	0.121	8.0	0.181	5.4	0.241	4.1	0.302	3.3	0.362	2.8	0.422	2.4	0.482	2.1	0.543	1.8

References

Alurrade, M., Caro, A., Victoria, M., *J. Nucl. Mater.*, 183 (1991) 33.

Almazouzi, A., Caturla, M.J., Alurralde, M., Diaz de la Rubia, T., and Victoria, M., *Nucl. Instr. and Meth. B*, **153** (1999) 105.

Almazouzi, A., Caturla, M.J., Diaz de la Rubia, T., and Victoria, M., *Mater. Res. Soc.*, **735** (1999) 685.

Andrade, E.N., Henderson, C., *Phil. Trans. Roy. Soc.*, **244** (1951) 177.

Bacon, D.J., Calder, A.F., Gao, F., Kapinos, V.G., Wooding, S.J., *Nucl. Instr. and. Meth. B*, **102** (1995) 37.

Bailat, C., EPFL *thesis*, Lausanne, **2011** (1999).

Bailat, C., Almazouzi, A., Baluc, N., Schäublin, R., Groeschel, F., Victoria, M., *J. Nucl. Mater.*, **283-287** (2000) 446-450

Baluc, N.L., Dai, Y., Victoria, M., *Mater. Res. Soc. Symp. Proc.* **540** (1999) 555.

Bement, A. L., 1970, *Proc. 2nd Int. Conf. On Strength of Metals and Alloys*, 693.

Biersack, J.P., Haggmark, L.G., *Nucl. Instru. Methods*, **174** (1980) 257.

Biersack, J.P., Ziegler, J.F., 'SRIM', 1998.

Blewitt, T.H., Coltman, R.R., Jamison, R.E., Redman, J.K., *J. Nucl. Mater.*, **2** (1960) 277.

Bloom, E., Martin, W. R., Stiegler, J. O. and Weir, J. R., *J. Nucl. Mater.*, **22** (1967) 68.

Caturla, M.J., *A Short Course in Molecular Dynamics Simulations with Empirical Potentials*, Dept. Fisica Aplicada, Universidad de Alicante, (2003)

Christian, J.W., Masters, B.C., *Proc. Roy. Soc.* **A281** (1964) 233.

Cockayne, D.J.H., Ray, I.L.F. and Whelan, M.J., *Phil. Mag.,* **20** (1969) 1265.

Coene, W., Bender, H., Amelinckx, S., *Phil. Mag. A*, **52** (1985) 369.

Coleman, W.A., Armstrong, T.W., *Oak Ridge National Lab. Rept.*, ORN-64606 (1970).

Condat, M., Fayard, M., *Phil. Mag. A*, **37 (5)** (1978) 683.

Coulomb, P., 1978, *J. Microsc. Spectrosc. Electron.*, **3**, 295.

Cowley, J.M., Moodie, A.M., *Proc. Phys. Soc.* **B70** (1957) 486.

Cleri, F., Rosato, V., *Phys. Rev.,* **B48** (1993) 22.

Czjzek, G., Seeger, A., Mader, S., *Phys. Stat. Sol.*, **2** (1962) 558.

Dai, Y., personal communication.

Dai, Y., EPFL *thesis*, Lausanne, **1388** (1995).

Dai, Y., Victoria, M., Mater. *Res. Soc. Symp. Proc.* **439** (1996) 319.

Daw, M.S., Baskes, M.I., *Phys. Rev.* B, **29** (1984) 6443.

De la Rubia, T., Averback, R.S., Horngming, H., *J. Mater. Res.*, **4** (1989) 579.

De la Rubia, Guinan, M.W., *J. Nucl. Mater.* **174** (1990) 151.

Diehl, J., Mader, S. and Seeger, A.K., *Z. Metallk.*, **46** (1955) 650.

Diehl, J., *Z. Metallk.*, **47** (1956a) 331, **47** (1956b) 411.

Diehl, J., Schilling, W., *Third Intern. Conf. On Peaceful Uses Atomic Energy*, (1965) 72.

English, C.A., Foreman, A.J.E., Phythian, W.J., Bacon, D.J., Jenkins, M.L., *Materials Modeling*: From Theory to Technology, eds. English, C.A., et al. (Inst. Of Phys. Bristol, 1992) 105.

Evance, A. G., and Rawlings, R. D., *Phys. Stat. Sol.*, **34** (1969) 9.

Finnis, M.W., *MOLDY6 – A Molecular Dynamics Program for Simulation of Pure Metals, Harwell Report AERE-R-13182*, (1989).

Fleischer, R.L., *Acta Metll.*, **10** (1962) 835.

Fleischer, R.L., *Appl. Phys.*, **33** (1962) 3504..

Foreman, A.J.E., Makin, M.J., *Phil. Mag.*, **14** (1966) 911.

Friedel, J, *Dislocations*, Pergamon Press, (1967) 149.

Gavillet, D., EPFL *thesis*, Lausanne, **652 (**1986).

Gavillet, D., *PSI-Bericht Nr.85*, Paul Scherrer Institute, Switzerland, 1991.

Gelles, D., and Schäublin, R., *Materials Science and Engineering* **A309-310** (2001) 82.

Gibbs, G.B., *Phys. Stat. Sol.*, **5** (1964) 693.

Gibbs, G.B., *Phys. Stat. Sol.,* **10** (1965) 507.

Greenwood, L.R., Smithers, R.K., *Argonne National Lab. Rept.*, ANL/FPP/TM-197 (1985).

Guiu, F., Pratt, P.L., *Phys. Stat. Sol.*, **6** (1964) 111.

Haasen, P., *Phil. Mag.*, **3** (1958) 384.

Head, A.K., Humble, P., Clarebrough, L.M., Morton, A.J. and Forwood, C.T., *Computed Electron Micrographs and Defect Identification,* North-Holland Publishing Company, Amsterdam, (1973).

Heinisch, H.L., Singh, B.N., *Phil. Mag.* A, **67** (1993) 407.

Heinisch, H.L., Singh, B.N. and Diaz de la Rubia, T., *J. Nucl. Mater.*, **127-31** (1994) 212.

Heyes, D.M., Smith, W., in: Information Quarterly for Computer Simulation of Condensed Phases, No 26 (Science and Engineering Research Council, Daresbury Laboratory, Daresbury, Warrington WA4AD, England. 1987) p.68.

Hirsch, P.B., in: *Vacancies 76,* eds. Smallmann, R.E., Harris, J.E., The Metals Society, (1977) 95.

Hirsch, P.B., Howie, A., Nicholson, R.B., Pashley, D.W. and Whelan, M.J., *Electron Microscopy of thin crystals* (Malabar, FL: Krieger) ISBN 0-88275-376-2 revised edn, first published 1965, second revision 1977.

Hirth, J.P., Lothe, *Theory of Dislocations*, Wiley-Interscience Publication, (1982) 332.

Honeycombe, R.W.K., *The plastic deformation of metals*, London, (1985) 21.

Honeycutt, J.D., Andersen, H.C., *J. Phys. Chem.*, **91** (1987) 4950.

Howie, A., Whelan, M.J., *Phil. Trans. Roy. Soc.*, **252** (1960) 499.

Hsieh, H., Diaz de la Rubia, T., Averback, R.S., Benedek, *R., Phys. Rev.*, **B40** (1989) 9986.

Jenkins, M.L., Kirk, *Characterization of Radiation Damage by Transmission Electron Microscopy*, Institute of Physics Publishing, ISBN =-7503-0748-X (hbk), (2001) 77.

Jenkins, M.L., *J. Nucl. Mater.*, **216** (1994) 124.

Johnson, E., Hirsch, P.B., *Phil. Mag.* A **43** (1981) 157-170.

Johnson, M.D., Caturla, M.J. and Diaz de la Rubia, T., *J. Appl. Phys.* **84** (1998) 1963.

Kinchin, G.H., Pease, R.S., *Rep. Prog. Phys.*, **18** (1955) 1.

King, W.E., Benedek, R., *Phys. Rev.*, **B23** (1981) 6335.

Kiritani, M., Yoshida, N., Ishino, S., *J. Nucl. Mater.*, **122 & 123** (1984) 602.

Kiritani, M., *Mater. Sci. Forum*, **15-18** (1987) 1023.

Kiritani, M., Yoshiie, T., Kojima, S., Satoh, Y., *Radiation Efeects and Defects in Solids*, **113** (1990) 75.

Kirk, M.A., Robertson, I.M., Jenkins, M.L., English, C.A., Black, T.J. and Vetrano, J.S., *J. Nucl. Mater.*, **149** (1987) 21.

Kitagawa, K., Yamakawa, K., Fukushima, H., Yoshiie, T., Hayashi, Y., Yoshida, H., Shimomura, Y. and Kiritani, M., *J. Nucl. Mater.* 133-134 (1985) 395.
et al. (1985)

Kojima, S., Satoh, Y., Taoka, H., Ishida, I., Yoshiie, T. and Kiritani, M., *Phil. Mag.* A, **59** (1989) 519.

Kojima, S., Yoshiie, T., Hamada, K., Satori, K. and Kiritani, M., *J. Nucl. Mater.* **191-194** (1992) 1155.

Kubin, L.P., *Phil. Mag.,* **30** (1974) 705.

Lennard-Jones, J.E.*, Proc. Camb. Phil. Soc.*, **27** (1931) 469.

Lindhard, J., Scharff, M., Schitt, H.E., *K. Dan. Vidensk. Selsk. Mat. Fys. Medd.*, **33** (14) (1963).

Luppo, M.I., Bailat, C., Schäublin, R. and Victoria, M., *J. Nucl. Mater.*, **283-287** (2000) 483-487.

Mader, S., *Z. Phys.* **149** (1957) 73.

Mader, S., Seeger, A.K. and Leitz, C., *J. Appl. Phys.*, **34** (1963) 3368.

Makin, M.J., Whapham, A.D., Minter, F.J.*, Phil. Mag.*, **6** (1961) 465.

Marmy, P., EPFL *thesis*, Lausanne, **949** (1991).

Marmy, P., Daum, M., Gavillet, D., Green, S., Green, W. V., Hegedus, F., Proennecke, S., Rohrer, U., Stiefel, U., and Victoria, M., *Nucl. Ins. and Meth. In Phy. Res,* **B47** (1990) 37.

Matzukawa, Y., Zinkle, S.J., *J. Nucl. Mater.*, **329-333** (2004) 919-923.

Meng, X., Schäublin, R.E. and Stobbs, W.M., *Phil., Mag., Letters*, **75 (4)** (1997) 179-185.

Metropolis, Rosenbluth, A.W., Rosenbluth, M.N., Teller, A.H., Teller, E., *J. Chem. Phys.,* **21** (1953) 1087.

Mishin, Y., Farkas, D., Mehl, M.J., Papaconstantopoulos, D.A., *Phys. Rev. B*, **59** (5) (1999) 3393-3407.

Muroga, T., Watanabe, H., Araki, K., Yoshida, N., *J. Nucl. Mater.*, **155-157** (1988) 1290.

Nankivell, J.F., Brit. *J. Appl. Phys.*, **13** (1962) 126.

Nordlung, K., Averback, R.S., *J. Nucl. Mater.*, **276** (2000) 194.

Norgett, M.J., Robinson, M.T. and Torrens, I.M., *Nucl. Eng. Des.*, 33 (1974) 50.

Osetsky, Yu. N., Stoller, R.E., Matsukawa, Y., *J. Nucl. Mater.*, **329-333** (2004) 1228-1232.

Parrinello, M., Rahman, *J. Appl. Phys.*, **52** (1981) 7182.

Paschoud, F., EPFL *thesis***,** Lausanne, **834** (1990).

Prinz, F., Argon, A.S., *Phys. Stat. Sol.* **57** (1979) 741.

Proennecke, S. EPFL *thesis*, Lausanne, **1067** (1992).

Robach, J.S., Robertson, I.M., Wirth, B.W. and Arsenlis, A., *Phil. Mag.*, **A83** (2003) 955.

Robertson, I.M., Vetrano, J.S., Kirk, M.A. and Jenkins, M.L., *Phil. Mag.,* **A63** (1991) 299.

Robinson, M.T., *J. Nucl. Mater.*, **216** (1994) 1.

Robinson, M.T., Torrens, I.M., *Phys. Rev.*, **B9** (1974) 5008.

Robinson, M.T., Jenkins, M.L., *Phil. Mag.*, **A43** (1981) 999.

Rodney, D., *Acta Materialia*, **52**, 3-9 (2004) 607.

Saada, G., Washburn, J., *Report UCRL 10213, Berkeley*, 1962.

Saada, G. *Proc. Int. Conf. Cryst. Latt. Def.* (1962).

Saada, G., Washburn, J., *J. Phys. Soc. Japan Suppl. 1*, **18** (1963) 43.

Saldin, D.K., Stathopoulos, A.Y. and Whelan, M.J., *Phil. Tran. R. Soc.* **292** (1979) 524.

Sasaki, S., Kiritani, M., Iwase, A., Iwata, T. and Fujita, F.E., *Point defects and defect interactions in metals*, (1982) 903.

Satoh, Y., personal communication.

Schäublin, R., and Victoria, M., *J. Nucl. Mater.*, **283-287** (2000a) 339-343.

Schäublin, R., Almazouzi, A., Dai, Y., Osetsky, Yu. N. and Victoria, M., *J. Nucl. Mater.*, **276 (1-3)** (2000b) 251-257.

Schäublin, R., Meng, X. and Stobbs, W.M., *Ultramicroscopy*, **83** (2000c) 145-157.

Schäublin, R., Gelles, D., Victoria, M., *J. Nucl. Mater.*, **307-311** (2002a) 197-202.

Schäublin, R., Caturla, M. J., Wall, M., Felter, T., Fluss, M., Wirth, B. D., Diaz de la Rubia,

T. and Victoria, M., *Presentation in ICFRM-10, Baden-Baden, Germany,* (2002b)

Schäublin, R., Yao, Z., Victoria, M., *Phil. Mag.,* in press (2004)

Schilling, W., Ullmaier, H., *Materials Science and Technology*, eds. Cahn, R.W., Haasen, P., Kramer, E.J., Vol.**10b**, (1994) 179.

Schoeck, G., *Phys. Stat. Sol.*, **8** (1965) 499.

Schoeck, G., Seeger, A.K., *Report Bristol Conference on defects in Crystalline solids* (London: Physics society) (1955) 340.

Schule, W., *Effects of Radiation on Materials*; *Savannah; Ga,* (1981) 166.

Seeger, A.K., *Phil. Mag.,* **46** (1955) 1194.

Seeger, A.K., Diehl, J., Mader, S. and Rebstock, H., *Phil. Mag.*, **2** (1957) 323.

Seeger, A.K., *Sec. Intern. Conf. on Peaceful Uses Atomic Energy*, vol.**5**, (1958) 250.

Seeger, A.K., Essman, U., in: *Radiation damage in solids*, eds. Billinton, D.S., (1962) 717.

Silcox, J., Hirsch, P.B., *Phil. Mag.* **4** (1959) 72.

Singh, B.N., Zinkle, S.J., *J. Nucl. Mater.*, **206** (1993) 212.

Singh, B., Foreman, A. J. E., and Trinkaus, H., *J. Nucl. Mater.*,**249 (**1997) 103.

Smidt, F.R., *Dislocation channelling in irradiated metals*, Report NRL-7078, Naval research Lab. (1970).

Soneda, N., Diaz de la Rubia, T., *Phil. Mag.* A, **78** (1998) 995.

Spaczer, M., EPFL *thesis*, Lausanne, **1340** (1995).

Spätig, P., Schäublin, R., Gyger, S. and Victoria, M., *J. Nucl. Mater.*, **258-263** (1998) 1345.

Stadelmann, P.A., *Ultramicroscopy*, **21** (1987) 131.

Theis, U., Wollenberg, H., *J. Nucl. Mater.*, **88** (1980) 121.

Victoria, M., Baluc, N., Bailat, C., Dai, Y., Luppo, M. I., Schäublin R. and Singh B. N., *J. Nucl. Mater.,* **276** (2000) 114.

Veyssière, P., Chiu, Y., Grégori, F., '*International Symposium on Advanced Structural and Functional Materials Design*', Osaca, Japan, (2004).

Vincotte, F., *Thesis*, University of California, Berkeley (1962)

Wirth, B.D., Caturla, M.J., Diaz de la Rubia, T., Khaishi, T., Zbib, H., *Nucl. Inst. Met. Phys. Res. B* **180** (2001) 23-31.

Yao, Z., Schäublin, R. and Victoria, M., J. Nucl. Mater., **329-333** (2004) 1127.

Yoshida, N., Muroga, T., Watanabe, H., Araki, K. and Miyamoto, U., *J. Nucl. Mater.* **155-157** (1988) 1222.

Yoshiie, T., Ishizaki, T., Xu, Q., Satoh, H., Kiritani, M., *J. Nucl. Mater.*, **307-311** (2002) 924.

Ziegler, J. F., Biersak, J. P., Littmark, U., in: *Stopping and Range of Ions in Solids*, **vol.1**, Pergamon, New York, (1985).

Zinkle, S.J., *J. Nucl. Mater.*, **155-157** (1988) 1201.

Zinkle, S.J., Snead, L.L., *J. Nucl. Mater.*, **225** (1995) 132.

ACKNOWLEDGMENTS

I am grateful to Drs Robin Schäublin and Maximo Victoria of the Fusion Technology – Materials Group of the CRPP for their great guidance and helpful discussions during my thesis. Also, I would like to thank them for their encouragement and help in the completion of the present manuscript and for their patience during this period.

I would also like to thank Professor Minh Quang Tran, Professor Andreas Mortensen and Dr. Wolfgang Hoffelner for their constructive criticism and valuable remarks as members of the examining committee.

I also wish to heartfully thank Dr. M. J. Caturla for her kind and excellent guidance in the world of molecular dynamics simulations during my stay at the University of Alicante, Spain.

I am grateful to Drs. N. Baluc and P. Spätig for helpful discussions along these years of my thesis. Also, I would like to thank Drs. D. Rodney and P. Veyssière for the fruitful discussions.

For their great and indispensable help at some point or another during my PhD work, I wish to express my gratitude to R. Stoenescu, R. Bonade, G. Yu, A. Ramar, C. Gavillet, A. Kramer, R. Wetter, Dr. F. Dalla Torre, Dr. P. Almeida, Dr. C. Bailat, Dr. T. Leguey, Dr. N. Nita, Dr. D. Hamaguchi, Dr. P. Marmy, Dr. Y. Dai and Dr. X. Jia, which are past, present or close members of the CRPP materials group in PSI.

I would like to give my thanks to P. Bugnon and Dr. T. Kruml of the IPMC of the EPFL for their help in the preparation of specimens.

I wish to express my gratitude to A. Ramar and Dr Y. Chiu for proof reading the manuscript.

The Swiss National Science Foundation (grants number 20-061837 and 20-100557) and the CRPP are acknowledged for financial support, as well as the Paul Scherrer Institute, where this work was achieved, for the provision of the facilities.

CURRICULUM VITAE

Mr. Zhongwen Yao

Né le 13 October 1971 à Gansu, République Populaire de Chine

1990 –1994	Etudes de physique Université de Wuhan, République Populaire de Chine Diplome obtenu: Bachelor of Science
1994 – 2000	Etudes en Science des Matériaux, Laboratoire de Génie Atomique China Institute of Atomic Energy, République Populaire de Chine Diplome obtenu: Master of Science
2000 – 2004	Assistant doctorant du Centre de Recherches en Physique des Plasmas, Ecole Polytechnique Fédérale de Lausanne à l'institut Paul Scherrer, Villigen

Scientific publications

'Dislocation defect interaction in irradiated Cu'
R. Schäublin, Z. Yao, P. Spaetig and M. Victoria, submitted to Dislocations 2004 conference. Accepted for publication in Materials Science and Engineering A.

'*Irradiation induced stacking fault tetrahedra in FCC metals'*
R. Schäublin, Z. Yao, N. Baluc and M. Victoria , Philosophical magazine, Volume 85, 2005, page 769-777.

'TEM diffraction contrast of nano-crystalline defects to the resolution limits and beyond'
R. Schäublin, Z. Yao and N. Nita, Proceedings of the 13th European Microscopy Congress, Ed. G. Van Tendeloo, Belgian Society for Microscopy, 2004, Pages 261-262.

'*Mechanical properties of irradiated single crystal Cu and their temperature dependence*'
Z. Yao, R. Schäublin and M. Victoria, Journal of Nuclear Materials, Volumes 329-33, 2004, Pages 1127-1132.

'Mechanical properties of irradiated single crystal Ni and their temperature dependence'
Z. Yao, R. Schäublin, P. Spätig and M. Victoria, Philosophical magazine, Volume 85, 2005, page 745-755.

'*Irradiation behavior of pure Ni single crystal irradiated with high energy protons*'
Z. Yao, R. Schäublin and M. Victoria, Journal of Nuclear Materials, Volumes 323, 2003, Pages 388-393.

'*The microstructure and tensile properties of pure Ni single crystal irradiated with high energy protons*'
Z. Yao, R. Schäublin and M. Victoria, Journal of Nuclear Materials, Volumes 307-311, Part 1, 2002, Pages 374-379.